

2015

Simultaneous Counter-Ion Codeposition: A Technique Enabling Matrix Isolation Spectroscopy Studies Using Low-Energy Beams of Mass-Selected Ions

Ryan Michael Ludwig
Lehigh University

Follow this and additional works at: <http://preserve.lehigh.edu/etd>

 Part of the [Chemistry Commons](#)

Recommended Citation

Ludwig, Ryan Michael, "Simultaneous Counter-Ion Codeposition: A Technique Enabling Matrix Isolation Spectroscopy Studies Using Low-Energy Beams of Mass-Selected Ions" (2015). *Theses and Dissertations*. 2697.
<http://preserve.lehigh.edu/etd/2697>

This Dissertation is brought to you for free and open access by Lehigh Preserve. It has been accepted for inclusion in Theses and Dissertations by an authorized administrator of Lehigh Preserve. For more information, please contact preserve@lehigh.edu.

Simultaneous Counter-Ion Codeposition:
A Technique Enabling Matrix Isolation Spectroscopy Studies
Using Low-Energy Beams of Mass-Selected Ions

by

Ryan Michael Ludwig

A Dissertation

Presented to the Graduate and Research Committee

of Lehigh University

in Candidacy for the Degree of

Doctor of Philosophy

in

Chemistry

Lehigh University

May 2015

© 2015 Copyright
Ryan Michael Ludwig

Approved and recommended for acceptance as a dissertation in partial fulfillment
of the requirements for the degree of Doctor of Philosophy

Ryan Michael Ludwig

Simultaneous Counter-Ion Codeposition: A Technique Enabling Matrix Isolation
Spectroscopy Studies Using Low-Energy Beams of Mass-Selected Ions

Defense Date

Approved Date

Dr. David T. Moore
Dissertation Director

Committee Members:

Dr. Gregory S. Ferguson

Dr. James E. Roberts

Dr. Christopher J. Kiely

ACKNOWLEDGMENTS

In order to thank everyone that has shaped my life to this point, I would need to write another dissertation. I am a believer that you never know how much impact you have in a person's life. Henry Adams said it best, "A teacher affects eternity; he can never tell where his influence stops." Thank you to all my teachers who laid the foundation of my knowledge.

Thank you to my dissertation committee. Dr. Ferguson, Dr. Roberts, and Dr. Kiely, I thank you for your time and guidance these past five years.

A special thanks to my research advisor Dr. Moore: You've formed how I view and question science. Thank you for your guidance, instruction, arguments, and teaching me that "you "gotta" want it."

To my parents and grandparents: I could not have gotten to where I am today without your influence. You have taught me the values of integrity and hard work. I have you to thank for the person I have become.

To my wife Meg: I could not have gotten to this point without your unconditional love and support. You continue to make me a better person every day. I thank you for standing next to me throughout the crazy ride of graduate school.

Finally, to God who has made a universe so wonderful that it's worth investigating, and for giving me the intellect and curiosity to do so.

TABLE OF CONTENTS

Copyright.....	ii
Certificate of Approval.....	iii
Acknowledgements.....	iv
List of Figures.....	xii
List of Tables.....	xxii
Abstract.....	1
Chapter 1: Freeze-Frame Spectroscopy: using matrix isolation as a means to study reactive intermediates.....	4
1.1 Overall research goals.....	4
1.2 Matrix isolation.....	7
1.2.1 Crystal structure and rigidity.....	7
1.2.2 Trapping sites and probability of isolation.....	10
1.2.3 Spectral effects.....	13
1.2.4 Energy Dissipation.....	15
1.3 Species identification.....	18
1.4 Previous matrix-ion deposition methods.....	21
1.4.1 Photoionization and chemiionization - <i>in situ</i> generation.....	21
1.4.2 Plasmas.....	23
1.4.3 Mass-selected ion deposition.....	24
1.4.4 Ion-codeposition method.....	26
1.5 Dissertation outline.....	26

Chapter 2: Experimental methodologies.....	28
2.1 Introduction.....	28
2.2 Matrix-isolation system.....	29
2.2.1 System overview.....	29
2.2.2 Metal-ion generation and mass selection.....	32
2.2.3 Charge balance and ion-energy measurements.....	36
2.2.4 FT-IR and UV-Vis detection methods.....	38
2.3 Gas preparation and delivery.....	40
2.4 Data collection and manipulation.....	43
2.5 Appendix.....	46
Chapter 3: Formation of ionic complexes in cryogenic matrices: a case study using co-deposition of Cu⁺ with rare gas cations in solid argon.....	49
3.1 Abstract.....	49
3.2 Introduction.....	50
3.3 Experimental.....	51
3.4 Results.....	52
3.4.1 UV-Vis spectroscopy.....	52
3.4.2 FTIR spectroscopy.....	54
3.4.3 Peak assignments.....	56
3.4.4 CO concentration dependence.....	58
3.4.5 Dependence on deposition temperature.....	60
3.4.6 Time-dependent vs. temperature-dependent neutralization.....	62
3.5 Discussion.....	64

3.5.1	Complex formation.....	67
3.5.2	Neutralization.....	69
3.5.3	Nature of counter-cations.....	71
3.6	Conclusions.....	73
3.7	Appendix.....	74
3.7.1	Description of minor spectral differences for 10 K vs 20 K deposition.....	77
3.7.2	Ion abundance calculation.....	77
Chapter 4: Cold chemical reactions triggered using electrons photodetached from “clean” distributions of anions in cryogenic matrices via counter-ion co- deposition.....		79
4.1	Abstract.....	79
4.2	Introduction.....	80
4.3	Experimental.....	81
4.4	Results.....	83
4.4.1	Visible irradiation followed by annealing.....	83
4.4.2	Annealing followed by visible irradiation.....	85
4.4.3	Wavelength-dependent photodetachment.....	87
4.5	Discussion.....	88
4.5.1	Electron-induced C-C bond formation.....	88
4.5.2	Wavelength-dependent trends.....	90
4.5.3	New spectroscopic peak identification.....	92
4.6	Conclusions.....	94

4.7 Appendix.....	95
Chapter 5: High-temperature deposition: intermediate anionic complex formation upon annealing and trapping of subsequent transient photodetachment products.....	99
5.1 Abstract.....	99
5.2 Introduction.....	100
5.3 Experimental.....	101
5.4 Results.....	102
5.4.1 Annealing followed by irradiation.....	102
5.4.2 Irradiation before annealing.....	106
5.4.3 High-temperature assessment.....	107
5.5 Discussion.....	109
5.5.1 $\text{Cu-CO}^- \rightarrow \text{Cu-CO}$	110
5.5.2 $\text{Cu(CO)}_2^- \rightarrow \text{Cu(CO)}_2$	111
5.5.3 $\text{Cu(CO)}_3^- \rightarrow \text{Cu(CO)}_3$	113
5.5.4 Possible explanations for anionic transient formation.....	115
5.5.5 Vertical detachment products: an explanation for neutral transients..	116
5.6 Conclusions.....	117
5.7 Appendix.....	118
Chapter 6: Identification of $(\text{CO})_2^+$ in argon matrices.....	122
6.1 Abstract.....	122
6.2 Introduction.....	123
6.3 Experimental.....	125

6.4 Results.....	126
6.4.1 High energy Ar ⁺ bombardment.....	126
6.4.2 Isotopic studies.....	129
6.4.3 Temperature dependent differences.....	130
6.5 Discussion.....	132
6.5.1 Cationic dimer, (CO) ₂ ⁺	132
6.5.2 Cationic monomer, CO ⁺	134
6.5.3 Anionic CO complexes.....	134
6.5.4 Complex formation and anomalous temperature concentrations.....	135
6.6 Conclusions.....	137
6.7 Appendix.....	138

Chapter 7: The coldest example of chemical equilibrium: reversible conformational rearrangement of O₄⁺ in an argon matrix at 10 K.....140

7.1 Abstract.....	140
7.2 Introduction.....	140
7.3 Experimental.....	143
7.4 Results.....	145
7.4.1 Cu ⁻ Ar ⁺ deposition in a 0.5% O ₂ matrix.....	145
7.4.2 Isotopic study.....	146
7.4.3 High energy Ar ⁺ formation.....	148
7.4.4 Dependence on deposition temperature.....	149
7.4.5 Thermally-induced reversible conformational change.....	151
7.4.6 Radiation-induced reversible conformational change.....	153

7.5 Discussion.....	155
7.5.1 Thermodynamic equilibrium at 10 K.....	155
7.5.2 Quantitative assessment.....	157
7.5.3 Qualitative assessment.....	160
7.5.4 Isotopic substitution.....	161
7.5.5 Photochromic conformational changes at 10 K.....	162
7.6 Conclusion.....	163
7.7 Appendix.....	164
7.7.1 Peak fitting and error analysis.....	164
7.7.2 ¹⁶ O ₂ system.....	166
7.7.3 ¹⁸ O ₂ system.....	169
7.7.4 Deposition temperature anomalies.....	172
Chapter 8: Silver and nickel anionic carbonyl systems: an investigation of the counter-ion codeposition method versatility.....	175
8.1 Abstract.....	175
8.2 Introduction.....	176
8.3 Experimental.....	177
8.4 Results and discussion.....	178
8.4.1 Anionic nickel deposition.....	178
8.4.2 Anionic silver deposition.....	184
8.6 Conclusion.....	187
8.7 Appendix.....	188

Chapter 9: Conclusions and future directions.....	190
9.1 Conclusions.....	190
9.2 Future directions.....	193
9.2.1 Mass-selected cations.....	193
9.2.2 Ionic-cluster deposition.....	195
9.2.3 Formation and deposition of gas-phase carbonyls.....	197
9.2.4 Wavelength dependent studies.....	198
9.2.5 Pump-probe technique.....	199
Chapter 10: List of references.....	201
Curriculum Vita.....	218

LIST OF FIGURES

- Figure 1.1** Physical size ranges for substitution sites created by the removal of matrix atoms in solid Ne, Ar, and Kr using the model of hard spheres 11
- Figure 2.1** Ultra-high vacuum system for deposition of mass-selected ions into rare gas matrices. Some interior components, such as collars and housings, have been made transparent for clarity. The system stand, internal gas lines, and wires not shown.....30
- Figure 2.2** Magnetron sputter source containing a spent copper target: A) fully assembled, B) anode removed, and C) cathode removed.....33
- Figure 2.3** Extraction nozzle assembly, completely disassembled showing: A) nozzle attachment plate, B) nozzle with 6.25 mm opening, C) inner, sacrificial gasket, and D) outer gasket. Aggregation tube in E with nozzle completely assembled and attached.....34
- Figure 2.4** Copper sputtering target used for matrix isolation experiments: A) new B) after ~20 hours of sputtering..... 35
- Figure 2.5** Mass spectra of copper anions from sputter source: A) high-resolution, isotopically resolved monomer and dimer, and B) high-throughput for matrix experiments.....36
- Figure 2.6** Ion energy distributions derived from stopping-potentials of metal-anion beams detected at the Faraday plate.....38
- Figure 2.7** Close-up illustration of the deposition chamber showing the FTIR beam path. The beam is produced by a Nicolet 6700 spectrometer (not shown), directed into the vacuum chamber, through the matrix, and detected by an external MCT-A detector.....39
- Figure 2.8** Gas rack used for making matrix gas mixtures. Stock solutions are diluted into aluminum gas mixing bottles and stored until needed for an experiment. Baseline pressure in the rack is measure by a Pirani gauge (mTorr) while low and high pressures during gas mixing are measured with a piezo transducer gauge (Torr) and Bourdon gauge (MPa), respectively.....41
- Figure 2.9** Matrix line used to introduce gas mixtures into the deposition region. The gas is sent from the gas to a mass flow controller which regulates the gas flow. The gas is dehydrated and purified by a liquid N₂, ethanol-bath before being introduced into the deposition region via a 1/16" tube.....42

Figure 2.10	Baseline correction performed in Origin software: A) raw data is taken which contains an upward slope, B) a 9 th -order polynomial is fit to the raw data, and C) the poly fit is subtracted from the raw data to give a baseline-resolved spectrum.....	43
Figure 2.11	Picture through Kodial glass viewport showing IR window after 4 hours of matrix deposition.....	44
Figure 2.12	Argon only matrix deposited at 10 sccm, 20 K for: A) 2 hours, and B) 4 hours. As the matrix increases in thickness, the observed etaloning increases in frequency and decreases in amplitude.....	45
Figure 2.13	Baseline-resolved mass spectrum showing copper isotopes as well as a large contamination peak. This peak is likely due to Cu-O or Cu-H ₂ O which is slightly off from the calculated m/z due to improper spectrometer calibration.....	46
Figure 2.14	Silver and nickel high-resolution spectra. The silver anion is similar to copper in that single atoms are relatively easy to produce, but larger clusters are much more difficult. The nickel anion produced the most abundant dimer and trimer, both of which were easily baseline resolved.....	47
Figure 2.15	Measured stopping potentials for Ar ⁺ versus bias set on ionizer extraction plate. Measured cation energies vary nearly linearly with the applied bias.....	48
Figure 3.1	UV spectra of anionic copper monomer balanced by krypton cation deposited in a 20K argon matrix for one hour. After deposition (blue) bands associated with neutral copper monomer are seen for both stable (300.2 nm, 304.6 nm, 309.0 nm) and secondary trapping sites (315.6 nm, 319.6 nm, 323.7 nm). Upon annealing to 25 K for 30 min (red), thermally unstable bands are irreversibly converted to the stable bands. Both spectra are taken at 10 K.....	53
Figure 3.2	FTIR spectra obtained using co-deposition of Cu ⁻ and Kr ⁺ ion-beams (8 nA each) for two hours with 0.02% CO in argon at 20 K, with subsequent annealing steps; all spectra recorded at 10 K. Broad feature marked with † assigned to [Cu(CO) ₃ •(CO) _n] ⁻ species. Peaks marked with * are assigned to metal-carbonyl impurities.....	56
Figure 3.3.	CO concentration dependence on copper carbonyl formation for varying CO concentrations: A) 0.02%, B) 0.1%, and C) 0.5%. Samples were deposited at 20 K for 2 hours with ~10 nA Cu ⁻ balanced by Ar ⁺ ; all spectra recorded at 10 K.....	59

- Figure 3.4** FTIR spectra obtained following 2 hours of co-deposition of Cu^- and Ar^+ at 10 K with: A) 0.1% CO in argon, ~ 7 nA Cu^- & Ar^+ and B) 2% CO in argon, ~ 3 nA Cu^- & Ar^+ ; spectra for subsequent annealing steps are also shown. All spectra recorded at 10 K.....61
- Figure 3.5** Difference spectra emphasizing changes during A) 5 K annealing steps for data shown in Figure 3.2 and B) time-dependent neutralization of a similarly prepared sample maintained at 10 K.....64
- Figure 3.6** Control experiment of Cu^- deposition with no counter-ion in a 0.02% CO/Ar matrix deposited at 20 K. Note that there are no signs of copper complexes upon deposition at 20 K or upon annealing to 30 K showing the necessity of the counter-ion for the deposition process.....74
- Figure 3.7** Deposition of Cu^- into a 0.02% CO in argon matrix at 20 K followed by 30 K annealing during two separate experiments using Kr^+ and Ar^+ as counter-ions as shown. Note that both counter-ions lead to virtually the same spectrum. The same neutralization events occur in both cases upon annealing with the exception of the larger $\text{Cu}(\text{CO})_3^-$ species persisting longer in the Kr^+ case.....75
- Figure 3.8** Deposition of Cu^- into a 0.02% CO in argon matrix at 20 K during two separate experiments using Kr^+ and Ar^+ as counter-ions as shown. Spectra are zoomed in on the $\text{Cu}(\text{CO})_3^-$ and $[\text{Cu}(\text{CO})_3 \cdot (\text{CO})_n]^-$ regions to emphasize the reproducibility of fine structure contained within the broad feature.....75
- Figure 3.9** Time-lapse study using sample with ~ 7 nA Cu^- & Ar^+ co-deposited in a 0.02% CO in argon matrix at 20 K. Sample was maintained at 10 K over the course of 8 hours with scans taken every two hours. Spectra show neutralization attributed to long-range photodetachment mechanism....76
- Figure 3.10** Unprocessed data from Figure 3.3 of main text showing low-frequency etaloning from interference in the matrix. Using index of refraction of bulk argon (1.77),¹⁴⁴ fringes correspond to matrix thickness of ~ 60 μm76

Figure 4.1	FTIR spectra from co-deposition of Cu ⁻ and Ar ⁺ ion-beams (3 nA each) for two hours with 2% CO in argon at 10 K, with subsequent annealing steps; all spectra recorded at 10 K. A) Spectrum following deposition, showing only anionic copper carbonyl bands. B) spectrum following photodetachment of the anions by visible irradiation; new bands correspond to neutral copper carbonyl complexes, as well as <i>trans</i> -OCCO ⁻ near 1515 cm ⁻¹ C-F) Spectra following annealing steps at 15, 20, 25 and 30 K, respectively.....	84
Figure 4.2	Cu ⁻ Ar ⁺ co-deposited (4 nA each) for 4 hours with 2% CO in argon at 10 K. A) 10 K deposition, B) 15 K annealing, C) 20 K annealing, D) 25 K annealing, E) 30 K annealing, F) low intensity irradiation, G) high intensity irradiation, and H) 30 K annealing after irradiation. All spectra taken at 10 K.....	86
Figure 4.3	Cu ⁻ Ar ⁺ co-deposited (4 nA each) for 4 hours with 2% CO in argon at 10 K. A) 10 K deposition, B) 735 nm light, C) 660 nm light, D) 590 nm light, and E) 30 K annealing. All spectra taken at 10 K.....	88
Figure 4.4	Cryochemistry scheme based on using electrons photodetached from the anionic monocarbonyl complex to induce formation of the <i>trans</i> -OCCO ⁻ by electron attachment to the van der Waals CO-dimer, which results in C-C bond formation. Positions of corresponding IR bands in Fig. 4.1 and 4.7 are indicated.....	89
Figure 4.5	UV-visible spectrum of emission from tungsten-filament bulb used for broad-band photodetachment studies.....	95
Figure 4.6	LED spectra used for narrow-band photodetachment studies. Neither the 470 nm nor the 365 nm centered LEDs were used in this study, but are used in later chapters and have been included for completeness.....	95
Figure 4.7	IR spectrum of the CO stretching region showing concentration dependence of the associated bands. Note the prevalence of the band at 2140 cm ⁻¹ for the van der Waals CO-dimer ⁵⁹ in the more concentrated 2% CO matrix used for the current study. The peaks near 2150 cm ⁻¹ arise from H ₂ O-(CO) _n van der Waals complexes. ^{140,141}	96
Figure 4.8	Difference spectra emphasizing changes during 5 K annealing steps and irradiation steps for data shown in Figure 4.1.....	96
Figure 4.9	Tungsten-filament source on during deposition of 3 nA Cu ⁻ balanced by Ar ⁺ in 0.02% CO doped argon matrix. As expected, no anionic copper compounds are observed after a 2 hour deposition. A) 10 K deposition, B) 15 K, C) 20 K, D) 25 K, and E) 30 K annealing. All spectra recorded at 10 K.....	97

Figure 4.10	Cu ⁻ Ar ⁺ codeposited with a 1% ¹² CO + 1% ¹³ CO in Ar matrix at 10 K: A) deposition, B) visible irradiation, C) 30 K annealing after irradiation.....	98
Figure 5.1	Cu ⁻ Ar ⁺ co-deposited (4 nA each) for 4 hours with 0.02% CO in argon at 20 K: A) 20 K deposition, B) 25 K annealing, C) 30 K annealing, D) 590 nm irradiation, E) 470 nm irradiation, F) 30 K annealing, and G) 35 K annealing. All spectra taken at 10 K. Subtraction spectra included to emphasize changes.....	103
Figure 5.2	High resolution (0.125 cm ⁻¹) spectra of Figure 5.1 after 30 K annealing of A) anionic region and B) neutral region. C) neutral region after 470 nm irradiation. In order to get spectrum A, the high resolution 30 K scan was subtracted from the irradiation scan in order to remove atmospheric water lines across this region. No anionic species remain after irradiation, so subtraction only removes water lines. Since the atmospheric peaks are only present up to ~1800 cm ⁻¹ , spectra B and C are both raw data with no background interferences.....	105
Figure 5.3	Cu ⁻ Ar ⁺ co-deposited (4 nA each) for 4 hours with 0.02% CO in argon at 20 K: A) 20 K deposition, B) 590 nm irradiation, C) 470 nm irradiation, D) 30 K annealing, and E) 35 K annealing. All spectra taken at 10 K....	106
Figure 5.4	Cu ⁻ Ar ⁺ co-deposited (4 nA each) for 2 hours with 0.02% CO in argon at 20 K: A) 20 K deposition, B) 30 K annealing, C) 40 K annealing, D) 470 nm irradiation, and E) 30 K annealing. All spectra taken at 10 K (data taken by Michael Goodrich).....	107
Figure 5.5	Cu ⁻ Ar ⁺ co-deposited (4 nA each) for 4 hours with 2 ppm CO in argon at 30 K: A) 30 K deposition, B) 35 K annealing, C) 590 nm irradiation, D) 30 K annealing, E) 40 K annealing, and F) 470 nm irradiation. All spectra taken at 10 K.....	109
Figure 5.6	Reaction scheme for the copper carbonyl complex. The asterisks denotes a transient complex. A curved arrow is used to emphasize that the “back” process happens only at 40 K.....	110
Figure 5.7	Reaction scheme for the copper dicarbonyl complex. The asterisks denotes a transient complex. A curved arrow is used to emphasize that the “back” process happens only at 40 K.....	113
Figure 5.8	Subtraction data from Figure 5.3 showing differences for B-A) 590 nm irradiation, C-B) 470 nm irradiation, D-C) 30 K annealing, and E-D) 35 K annealing.....	118

Figure 5.9	Subtraction data from Figure 5.4 showing differences for: B-A) 30 K annealing, C-B) 40 K annealing, D-C) 470 nm irradiation, and E-D) 30 K annealing.....	120
Figure 5.10	Cu ⁻ Ar ⁺ co-deposited (4 nA each) for 4 hours with 0.002% CO in argon at 30 K. A) 30 K deposition, B) 35 K annealing, C) 590 nm irradiation, and D) 30 K annealing.....	120
Figure 5.11	Cu ⁻ Ar ⁺ co-deposited (4 nA each) for 6 hours with 0.02% ¹² CO + 0.02% ¹³ CO in argon at 20 K. A) 20 K deposition, B) 25 K annealing, C) 30 K annealing, D) 590 nm irradiation, E) 470 nm irradiation, F) 30 K annealing, and G) 35 K annealing.....	121
Figure 6.1	400 eV Ar ⁺ deposition into 0.5% CO in excess Ar matrix, deposited for 4 hours at 20 K. A) 20 K, 0.125 cm ⁻¹ resolution, B) 20 K, 0.5 cm ⁻¹ resolution, C) 735 nm, D) 660 nm, E) 590 nm, F) 470 nm, and G) 365 nm. All spectra taken at 10 K. Irradiation performed for 5 minutes with specified LEDs while sample at 10 K.....	128
Figure 6.2	Same sample as Figure 6.1 showing a low intensity band blue-shifted from the main CO peak. This is near where CO ⁺ should show up and follows the same irradiation trends as the other ionic peaks. A) 20 K, 0.125 cm ⁻¹ resolution, B) 20 K, 0.5 cm ⁻¹ resolution, C) 735 nm, D) 660 nm, E) 590 nm, F) 470 nm, and G) 365 nm. All spectra taken at 10 K.....	128
Figure 6.3	400 eV Ar ⁺ deposition into 0.02% ¹² CO + 0.02% ¹³ CO in excess Ar matrix, deposited for 4 hours at 20 K: A) 20 K deposition, B) 735 nm, C) 660 nm, D) 590 nm, E) 470 nm, F) 365 nm, and G) 30 K annealing.....	129
Figure 6.4	400 eV Ar ⁺ deposition into 2% CO in excess Ar matrix, deposited for 4 hours at 10 K. Note that only one peak for the (CO) ₂ ⁺ is present at 2047.8 cm ⁻¹ . Due to the high CO concentration, the ¹³ C ¹⁸ O species is observable at 2038.9 cm ⁻¹	131
Figure 6.5	Deposition-temperature comparison. Both samples deposited under high energy argon for 4 hours using argon matrices doped with 2% and 0.5% CO for 10 K and 20 K deposition, respectively.....	132
Figure 6.6	Anionic CO-dimer region from Figure 6.1B showing low-intensity peaks at 1514.7, 1519.9, and 1526.4 cm ⁻¹	138

- Figure 6.7** 0.02% CO in argon matrix deposition at 20 K of 70 eV Ar⁺ balanced by A) Cu⁻ and B) Ag⁻. The (CO)₂⁺ behaves the same regardless of counterion. All spectra taken at 10 K.....139
- Figure 6.8** Deposition-temperature comparison of 2180 cm⁻¹ band. Both samples deposited under high energy argon for 4 hours using argon matrices doped with 2% and 0.5% CO for 10 K and 20 K deposition, respectively.....139
- Figure 7.1** Cu⁻ Ar⁺, 20 K deposition in a 0.5% O₂ in Ar matrix showing a survey scan of ionic complexes formed upon deposition. Note that the Cu(O₂)₂ is the only copper derived peak formed. The sharp line in the baseline near 1385 cm⁻¹ is due to a difference in the background and the irregular baseline is due to the KBr window cracking from repeated use.....146
- Figure 7.2** Cu⁻ Ar⁺ deposition for 6 hours at 20 K in a 0.5 % ¹⁶O₂ + 0.5% ¹⁸O₂ in argon showing *trans*-O₄⁺ and cyclic-O₄⁺. Spectra are taken with sample at 10 K and 14 K, respectively. Peak at 1337.2 cm⁻¹ is due to an isotope of the O₆⁺ complex.....147
- Figure 7.3** Deposition condition comparison for 0.5% O₂ in argon at 20 K formed from deposition of A) 70 eV Ar⁺ with Cu⁻ and B) 400 eV Ar⁺ only. Note the lack of the O₄⁻ in the high energy deposition.....149
- Figure 7.4** Temperature deposition comparison using 400 eV Ar⁺ for: A) 10 K deposition of 2% O₂, B) 20 K deposition of 0.5% O₂, and C) 25 K deposition of 0.02% O₂.....150
- Figure 7.5** FTIR spectra of O₄⁺ in argon matrices: A) spectrum recorded at 10 K following 10 K deposition, showing bands assigned to *trans*- (1119 and 1186 cm⁻¹) and cyclic (1329 and 1331 cm⁻¹) conformers; B) growth of new cyclic conformer band (1310 cm⁻¹) and concomitant loss of *trans* band (1119 cm⁻¹) upon warming from 11-18 K. Note that only whole-integer temperature values are shown, but scans were taken at 0.25 K intervals, see text; C) Restoration of initial spectrum upon re-cooling to 10 K, demonstrating reversible nature of spectral changes. D) Loss of both 1119 cm⁻¹ and 1310 cm⁻¹ bands following heating to 24 K.....152
- Figure 7.7** Irradiation series showing photochromism between the cyclic-1331 cm⁻¹ and *trans*-1186 cm⁻¹ conformers using different narrow-band LEDs. Spectra are taken at 10 K either with the light on or off as specified.....154

- Figure 7.8** A) Temperature dependence of normalized populations in peaks A (1119 cm⁻¹) and B (1310 cm⁻¹). B) van't Hoff plot reflecting temperature dependence of K_{eq} for *trans*-to-cyclic conversion, derived from population data in part A. The higher temperature line was fit with a linear equation of $y = -280 \pm 8 x + 20.6 \pm 0.5$ with an R^2 value of 0.9886. The lower temperature line was fit with a linear equation of $y = -28.4 \pm 7 x + 0.969 \pm 0.6$ with an R^2 value of 0.5690.....158
- Figure 7.9** Simple schematic showing *trans* and cyclic conformers of O₄⁺ in double substitution sites in a rigid fcc argon matrix (figure created by David Moore).....161
- Figure 7.10** Integrated area of peak A (1119 cm⁻¹) versus integrated area of peak B (1310 cm⁻¹). There is a highly linear dependence between the two peaks across the temperature range with an R-squared value of 0.9749.....166
- Figure 7.11** Conversion from 1119 to 1310 cm⁻¹ upon increasing temperature. High density plot of data condensed in Figure 7.1.....167
- Figure 7.12** High temperature annealing for ¹⁶O₂ system. Note the loss of 1119 and 1310 cm⁻¹ above 22 K as well as growth of the (O₂)₃⁺ species at 1416 cm⁻¹.....167
- Figure 7.13** Area of 1416 cm⁻¹, O₆⁺, as a function of temperature. Integrated area from peaks in Figure 7.7.....168
- Figure 7.14** FTIR spectra of O₄⁺ in argon matrices: A) spectrum recorded at 10 K following 20 K deposition, showing bands assigned to *trans*- (1119 and 1186 cm⁻¹) and cyclic (1329 and 1331 cm⁻¹) conformers, B) 590 nm centered LED, C) dark spectrum, D) broad band visible source, E) dark spectrum, F) 470 nm centered LED, and G) dark spectrum.....168
- Figure 7.15** Cu- Ar+ deposited into a 0.5% ¹⁸O₂ in argon matrix. Note that the Cu⁻ is used here for the sole purpose of charge balance.....169
- Figure 7.16** Two interconverting peaks for the ¹⁸O₄⁺ system. Isotopic substitution shows the same linearity as that of the ¹⁶O₄⁺ system. R-squared value is 0.9317.....169
- Figure 7.17** Thermal population of the ¹⁸O₄⁺ system. There is more cyclic-O₄⁺ at 10 K for the 18-isotope species.....170
- Figure 7.18** Van't Hoff plot for the ¹⁸O₄⁺ system. Note the lower ΔH and ΔS values compared to the ¹⁶O₄⁺ system as well as the divergence from linearity at 10 K and 11 K.....170

- Figure 7.19** Higher temperature annealing of the $^{18}\text{O}_4^+$ system. Upon heating to 25 K, both the 1056cm^{-1} and 1243cm^{-1} peaks are destroyed irreversibly analogous to the $^{16}\text{O}_4^+$ system.....171
- Figure 7.20** Deposition at 25K. Notice the absence of 1119 and 1310cm^{-1} both upon deposition and at 15 K. Photochromism still occurs between the 1186 and 1332cm^{-1} bands that are still present.....172
- Figure 7.21** Deposition at 10 K with initial annealing to 20 K (before temperature series). Both the O_6^+ and $(\text{O}_2)_n$ clusters at 1416 and 1548cm^{-1} , respectively, anneal in with the loss of a small population of *trans*- O_4^+172
- Figure 7.22** Expansion of *trans*- O_4^+ band from Figure 7.1 showing two shoulder bands upon deposition at 10 K. Both bands are annealed away after initial warming of the system to 20 K along with a small population of the main 1119cm^{-1} peak.....173
- Figure 7.23** Deposition of high energy Ar^+ (300 eV) into a 0.5% doped argon matrix with no explicit deposited anion. Note the large O_4^- peak at 953cm^{-1} formed upon deposition to maintain charge balance.....173
- Figure 7.24** $\text{Cu}^- \text{Ar}^+$ deposition for 6 hours at 20 K in a 0.5 % $^{16}\text{O}_2 + 0.5\% ^{18}\text{O}_2$ in argon showing Cu-O_4 and O_4^- . Spectra are taken with sample at temperature shown. Note that this region does not have any temperature dependent trends.....174
- Figure 8.1** $\text{Ni}^- \text{Ar}^+$ co-deposited (4 nA each) for 4 hours with 0.02% CO in argon at 20 K: A) 20 K deposition, B) 25 K annealing, C) 30 K annealing, D) 735 nm irradiation, E) 670 nm irradiation, F) 560 nm irradiation, G) 490 nm irradiation, H) 365 nm irradiation, I) 30 K annealing, J) 35 K annealing, and K) 40 K annealing. All spectra taken at 10K. Major bands labeled for the mono- (1), di- (2), tri- (3), and tetra-carbonyl (4) complexes and unknown species (?)......179
- Figure 8.2** Subtraction data from Figure 8.1, $\text{Ni}^- \text{Ar}^+$, showing stepwise differences that occurred at each processing step labeled accordingly.....185
- Figure 8.3** $\text{Ag}^- \text{Ar}^+$ co-deposited (4 nA each) for 4 hours with 0.02% CO in argon at 20 K: A) 20 K deposition, B) 25 K annealing, C) 30 K annealing, D) 470 nm irradiation, E) 30 K annealing, F) 365 nm irradiation, G) 30 K annealing, and H) 40 K annealing. All spectra taken at 10 K. Literature peaks labeled for di- (2) and tri-carbonyl (3). * denotes a peak near a literature assignment for a mono- and tri-carbonyl species separated by 0.2cm^{-1}185

- Figure 8.4** Subtraction data from Figure 8.2, $\text{Ag}^- \text{Ar}^+$, showing stepwise differences that occurred at each processing step labeled accordingly.....189
- Figure 9.1** $\text{Cu}_2^- \text{Ar}^+$ co-deposited (~400 pA each) for 4 hours with 0.02% CO in argon at 20 K: A) 20 K deposition, B) 25 K annealing, C) 30 K annealing, D) 590 nm irradiation, E) 490 nm irradiation, and F) 30 K annealing. All spectra recorded at 10 K.....196
- Figure 9.2** Normalized area of anionic copper carbonyl complexes at 10 K, subjected to 1 s pulses of 470 nm centered light.....198
- Figure 9.3** Subtraction data showing changes upon different length exposures to 365 nm light. Note the large decrease of the dicarbonyl complex with the concomitant increase of both the tricarbonyl and CO_2200

LIST OF TABLES

Table 1.1	Significant temperatures for rare gas matrix materials (values taken from ref. 28).....	10
Table 1.2	Probability of isolation (adapted from ref. 28).....	13
Table 1.3	Ionization potentials of common molecular species commonly found in matrices (values taken from NIST, ref. 51).....	17
Table 2.1	Vacuum pump and gauge information.....	46
Table 2.2	Typical parameters set on individual electronic optics for the deposition of copper, silver, and nickel anions.....	47
Table 2.3	Natural isotopic abundances for copper, silver, and nickel.....	48
Table 3.1	Vibrational band positions (in cm^{-1}) for $\text{Cu}(\text{CO})_n^q$ [$n=1,2,3$; $q=-1,0$] species in argon matrices.....	55
Table 3.2	Peaks assigned to transitions from metal carbonyl impurities (Figures 3.2-3.4), based on previous spectroscopic assignments (see references contained within refs. 85 and 129). Peaks marked with ‘?’ do not correspond to any previously reported bands, but are still assigned to impurity species based on their absence when using an ethanol cooling bath, and insensitivity to annealing (note their absence in difference spectra in Figure 3.4B).....	78
Table 4.1	Gas-phase photodetachment thresholds for anionic copper clusters and anionic copper carbonyls.....	97
Table 5.1	Peak assignment for high temperature, 20 K and 30 K, deposition. Wherever possible, peak position was based on high-resolution scan (0.125 cm^{-1}).....	119
Table 6.1	Vibrational band positions (in cm^{-1}) for $(\text{CO})_2^q$ [$q=-1,+1$] species in argon matrices.....	127
Table 7.1	Normalized peak areas with calculated errors for the calculation of an equilibrium constant for the $^{16}\text{O}_2$ system.....	166
Table 7.2	Normalized peak areas with calculated errors for the calculation of an equilibrium constant for the $^{18}\text{O}_2$ system.....	171

Table 8.1	Vibrational frequencies observed for the anionic and neutral nickel carbonyl system. Changes at various processing steps are shown accordingly.....	188
Table 8.2	Vibrational frequencies observed for the anionic and neutral silver carbonyl system. Changes at various processing steps are shown either by an increase in the peak (↑) or a decrease in the peak (↓). Assignments based on ref. 198.....	189

Abstract

This dissertation describes the development of a new deposition technique for matrix-isolation studies of metal ions codeposited with selected counter-ions. This method was developed to form and stabilize ionic complexes for spectroscopic characterization in a matrix under controlled conditions. Previous techniques have relied on inherently neutral sources such as plasmas, which use high energy transfer processes to create ionic species. The use of mass-selected cation beams has also been employed, which relies on deposition under high-energy to maintain charge balance. All of these former methods suffer from the fact that they rely on secondary processes to generate counter-ions, which are only coarsely controlled at best. One group before us has attempted to deposit mass-selected beams of both cations and anions selectively, but observed no bands assigned to an ionic species. We have shown for the first time that ions can be isolated in a matrix through the simultaneous deposition of selected cations and anions.

As proof of concept, anionic copper atoms were codeposited with Ar^+ or Kr^+ into argon matrices along with varying concentrations of CO (0.02% up to 2%) at deposition temperatures of 10K or 20K. Both anionic and neutral copper carbonyl complexes $\text{Cu}(\text{CO})_n^q$ ($n=1-3$; $q=0,-1$) were observed in the spectra, with peak positions corresponding to previously reported assignments; new partially resolved bands appearing in the range $1830-1845\text{ cm}^{-1}$ are assigned to larger $[\text{Cu}(\text{CO})_3 \cdot (\text{CO})_n]^-$ aggregates, having additional CO ligands in the second solvation shell.

Deposition in the absence of ambient light at 10 K affords “clean” distributions of matrix-isolated copper carbonyl anions, whereby only the anionic bands are present in the CO-stretching region of the vibrational spectrum. Furthermore, photodetachment by mild

irradiation with visible light was used to initiate complete conversion of the anions into their corresponding neutral species. We demonstrated that the photodetached electrons initiate covalent chemistry in the van der Waals dimer of CO, which forms a C-C bond following electron capture to make trans-OCCO⁻.

After deposition of anionic copper carbonyl precursors at 20 K, annealing led to many new sharp features in the anionic region. These peaks could then be converted into transient neutral bands upon photodetachment. Due to the high level of control afforded by this new deposition method, neutralization events occurred sufficiently far from the copper centers such that the neutral transients formed were stabilized and could be traced back to their anionic precursors. Annealing the system after irradiation gets rid of the neutral transients that seemed to “relax” to previously assigned neutral copper carbonyl species. The phenomenology of these bands suggest that they may represent an unprecedented direct observation of vertical detachment products.

Under high-energy deposition, cationic species form due to secondary charge-transfer interactions between Ar⁺ and dopant molecules. Using this method with CO-doped matrices, (CO)₂⁺ has been identified for the first time in an argon matrix. Likewise, oxygen-doped matrices produce (O₂)₂⁺ species which display remarkable conformational thermal-equilibrium between 10-16 K. Quantitative analysis revealed a weakly endothermic reaction, driven by increased entropy of the matrix for the cyclic product state. Problems encountered with quantitative van't Hoff analysis of the temperature-dependence for the equilibrium constant reveal that the assumptions underlying this standard analysis technique may break down at the very low temperatures of these experiments. Furthermore, two other peaks display conformational photochromic-equilibria at 10 K. It

is likely that one set of peaks arises due to the quartet electronic state, which has been the focus of all previous work, whereas the second set of peaks arises from the doublet electronic state, which is able to be stabilized in the matrix. The advantages of our new deposition technique made the study of this complicated system possible.

Finally, in order to test whether some of the new behavior observed was unique to the copper carbonyl system or whether it was more general and extended to other metal carbonyl systems, nickel and silver anions were tested. Similar to the copper system, both anionic and neutral nickel carbonyl complexes $\text{Ni}(\text{CO})_n^-$ ($n=1-3$) and $\text{Ni}(\text{CO})_n$ ($n=1-4$) were observed in the spectra, with peak positions corresponding to previously reported assignments. There were also many additional sharp bands that have not been previously observed. While the silver system did not produce any anionic carbonyl bands, it did form neutral complexes. Two of these absorbances can be assigned to the di- and tri-carbonyl complexes; the remaining bands do not match well with any previous assignments, which is puzzling for such a simple system. Possible explanations for this discrepancy are explored.

Using selected counter-ions for the deposition of metal anions allows for the deposition and stabilization of ionic complexes in argon matrices. This method affords an unprecedented cleanliness and level of control for matrix isolation studies. The development of this technique has enabled the discoveries presented in this dissertation.

Chapter 1

Freeze-Frame Spectroscopy:

Using matrix isolation as a means to study reactive intermediates

1.1 Overall research goals

Over the past several decades, heterogeneous catalysis, specifically that by supported metal nanoparticles, has transformed the chemical industry and advanced energy applications through reactions such as Fischer-Tropsch synthesis,¹ Haber-Bosch process,² petrochemical reforming,³ methane conversion,⁴ alcohol conversion,⁵ vehicle emission control,² as well as numerous other applications.⁶ Both nanoparticle size as well as metal-oxide support show strong correlations to selectivity and chemical activity,⁷ yet little is known about the precise mechanisms of such heterogeneous catalysts. The reason for poor mechanistic understanding lies with the purpose of a catalyst, namely to lower a reaction barrier, which leads to faster formation of products. Under typical reaction conditions, this rapid formation implies that any intermediate formed must be short-lived and does not become concentrated enough to detect using conventional spectroscopic methods. Consequently, model systems such as size-selected clusters on single-crystal thin films or mass spectroscopic studies of mass selected clusters in the gas phase are often employed. Many reaction intermediates involve either free radicals or molecular ions,⁸ both of which become the center of most gas-phase studies aimed at probing complex reactions.

One of the most studied systems is that of gold nanoparticles supported on TiO₂, which can readily oxidize CO at room temperature,⁹ even though gold is the most inert metal in the bulk state.¹⁰ Many mechanisms have been proposed to explain this reaction, which typically involve both ionic reactants as well as gold in different oxidation states,¹¹

however, no complete catalytic cycle has been agreed upon. Although many groups have studied this system,¹¹⁻¹⁵ a complete listing is beyond the scope of this dissertation. Instead, several key experimental approaches are presented as examples.

There is general agreement that CO adsorbs on the surface of gold nanoparticles (Au NPs) under reaction conditions¹⁶⁻¹⁸ and only adsorbs on the support at low temperatures or under high CO partial pressures.^{17,18} The nature of O₂ binding and the gold oxidation state is much less clear. Behm studied O₂ sites by a technique in which pulses of CO reactively removed O₂ from the support. The effluent gases were then analyzed by a quadrupole mass spectrometer.¹⁹ With this technique, Behm determined that the surface lattice oxygen at the perimeter of the Au-oxide interface reacts with CO.¹⁹ Yates performed experiments at ~120 K aimed at the precise nature of the Au-NP charge-state as well as the metal-oxide role through the use of CO as a spectroscopic probe.^{18,20} These IR studies added insight into CO binding sites, but the exact nature of the oxidation states involved is still unknown. Likewise, computational studies that try to provide evidence for bulk phase catalysts are difficult to perform, and the theoretical structural data of the catalytically active species fall short of experimental measurements.

Through gas-phase, mass spectroscopic techniques, Castleman studied the reactions of ionic gold clusters with O₂ seeded in a helium expansion gas. Mass-selected oxides were then reacted with CO, and reactivity was monitored via the production of CO₂ and depletion of the parent oxide. Both AuO⁻ and AuO₃⁻ species were reactive toward CO to form the product CO₂, in agreement with computational studies.²¹ For anionic gold dimers, those which contained a peripheral oxygen atom were most reactive; theory supported this as well, however, two different pathways toward CO₂ formation were found

that could not be differentiated in the experiment.²² For larger clusters, CO binding depended on the number and location of oxygen atoms.²³ The cationic gold system contained similar effects, whereby AuO^+ and Au_3O^+ were experimentally more reactive than Au_2O^+ , again supported by computationally predicted activation barriers.^{24,25}

Although these findings added important insight into small cluster reactions, no structural data were acquired due to the detection method of mass spectroscopy (i.e., reactions that have occurred were inferred based on CO_2 detection and depletion of precursors). These results still leave uncertainties in the exact mechanism when multiple reaction pathways are predicted, as is the case for most cluster reactions. One way to separate multiple pathways would be by trapping sufficient amounts of intermediate complexes and studying them with FTIR. By observing the frequency of a strong vibrational oscillator, such as CO, which is very sensitive to its environment, quantitative structural details, supported by computational data, can be made.

The work described in this dissertation was aimed toward developing a new technique for spectroscopic observation of intermediates by combining mass spectrometry with matrix isolation to study fundamental, metal-ion cluster interactions with reactants of catalytic importance. By using the energy-dissipating environment of rare-gas matrices, reactive ionic intermediates can be trapped and built up to significant concentrations so that conventional spectroscopies, such as FTIR and UV-Vis, may be used. These intermediates can then be moved along their potential energy surface by the addition of energy, such as heat or light, and their products, which can also be new intermediates, become trapped and observed spectroscopically. This forms the basis of a new technique

developed by the Moore group called Freeze-Frame Spectroscopy, the foundational studies of which are presented herein.

1.2 Matrix isolation

Matrix isolation is a technique whereby a frozen material, typically an inert gas, is used to trap reactive species that are dilute compared to the matrix material so that bimolecular reactions do not occur. By depositing for long periods of time, spectroscopically detectable amounts of reactants become trapped. Pimentel first showed the potential of matrix isolation by trapping the free radical NO_2 as well as several small hydrogen-bond forming compounds.²⁶ He later identified four properties that a matrix should contain: inertness with respect to the isolated species, rigidity at the temperature of study, transparency in the spectral region of interest, and volatility for easy introduction into a vacuum system.²⁷ All of these requirements are fulfilled by forming a matrix from rare gases, in particular neon or argon. Although there are reasons for using molecular species as a matrix material, all experiments presented have been done in argon, so rare gas matrices (RGM) are the focus. Besides being chemically inert, rare gases are transparent at all wavelengths down to vacuum-UV, making them ideal for use in FTIR, Raman, and UV-Vis studies. Furthermore, they do not have any unpaired electrons and do not produce any Electron Spin Resonance (ESR) signals.

1.2.1 Crystal structure and rigidity

When considering crystal structure, three models may be employed: the single crystal, the glassy model, or the microcrystalline model.²⁸ The single crystal, as the name implies, consists of well-ordered arrangements of atoms with few or no defects. Although

single crystals can be formed under rigorous conditions as shown by x-ray crystallographic studies,^{29,30} they are not practical for matrix isolation studies and are most often used as a model for trapping sites due to their simplicity.

The glassy model involves a random arrangement of matrix atoms so that trapped species are in sites that vary in size and coordination. Because of this arrangement, the environments of isolated species should be random and diverse, and one would expect inhomogeneous broadening of peaks. As will be discussed, the opposite situation typically exists; matrix peaks are typically sharp and well resolved, therefore, this model is ruled out.

The microcrystalline model consists of small regions of well-ordered crystals surrounded by regions of random structure and is the most probable model. Due to low temperature deposition, only small regions are able to form crystal structures, several of which may coexist. Both ordered and disordered regions make up approximately the same volume of the overall solid making this model hard to treat quantitatively.²⁸ This model also makes it hard to predict what kind of coordination site a trapped species exists in. For these reasons, detailed analyses begin with assuming a single crystal and treat imperfections as perturbations.

The most stable crystal form for neon, argon, krypton, and xenon is the face-centered cubic structure (FCC).^{28,30} This structure means that a single atom contains 12 nearest neighbors situated in a site of O_h symmetry. At the low deposition temperatures, it is also possible to freeze the less stable hexagonal close-packed (HCP) structure. This structure still consists of 12 nearest neighbors but the site symmetry is reduced to D_{3h} . Impurities have been shown to stabilize the HCP structure and small amounts of O_2 and N_2

make it stable up to the melting point.³¹ As molecular species get larger and/or their concentration in the matrix increases, they induce more polycrystallinity and eventually large amorphous regions that cannot be probed by x-ray crystallography.³²

When depositing reactive species, it is important that diffusion does not occur to an appreciable extent in the depositing layer. This is done by maintaining the deposition substrate at a significantly low temperature generally taken to be lower than 30% of the melting point of the matrix.^{28,33} At this temperature, the matrix is rigid and no changes take place on an appreciable time scale. Between 30% - 50% of the melting point, a process known as annealing occurs, which is atomic level reordering of the matrix atoms to form a more stable crystal.^{28,33} Annealing has the added effect of allowing small trapped species to move to a significant extent, so they become segregated at grain boundaries. Large stationary species cause their surrounding matrix atoms to rearrange and form a more stable cage. Depending on matrix conditions, annealing may cause two trapped species to interact and react; therefore, it is common to use annealing as a way to study reactions in matrices after reactive molecules have been stabilized.

Diffusion only occurs once the matrix is non-rigid, at temperatures near 50% of its melting point. This temperature allows molecules to freely move so that all previously isolated species become segregated at grain boundaries as the matrix forms large, single-crystal domains. If diffusion is allowed for a long enough period, reactions should occur until a large stable cluster is formed. In practice, the vapor pressure becomes high enough that heating the matrix near 50% of its melting point causes significant sublimation and overall matrix loss. We have found the onset of significant matrix loss to be highly

dependent on deposition temperature (Chapters 4 and 5). Table 1.1 contains relevant temperatures for rare gas matrices.

Table 1.1 Significant temperatures for rare gas matrix materials (values taken from ref. 28)

Material	$0.3T_m$ (K)	$0.5T_m$ (K)	$T(P = 10^{-5} \text{ Torr})$ (K)	$T(P = 10^{-3} \text{ Torr})$ (K)
Ne	7.3	12.3	9.2	11.1
Ar	25	42	33	39
Kr	35	58	45	54
Xe	48	82	63	74

1.2.2 Trapping sites and probability of isolation

Assuming a cubic close-packed crystal structure, it is reasonable to consider two types of trapping sites, interstitial or substitution. Interstitial sites are those that occupy the 26% empty volume in a cubic close-packed structure. These sites only become large enough to be relevant for krypton and xenon and, even then, only hydrogen atoms fit well; therefore, only the substitution site is of importance in the matrix isolation experiments described in this dissertation. A substitution site is one in which a matrix atom is replaced by an isolated atom or molecule. Single substitution sites can incorporate most atoms, atomic ions, and very small molecules. As the size of the compound increases, so does the number of substitutions the matrix must make in order to incorporate it. This site is referred to as a multiple substitution site and is necessary for most compounds. Three common sites are presented in Figure 1.1, along with their diameters in neon, argon, and krypton.

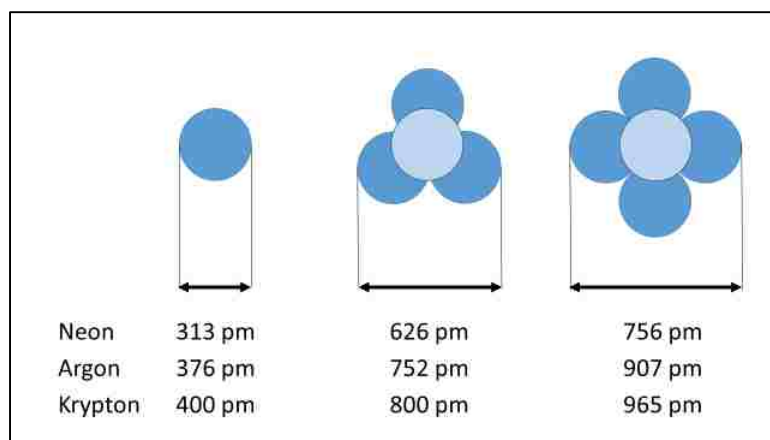


Figure 1.1 Physical size ranges for substitution sites created by the removal of matrix atoms in solid Ne, Ar, and Kr using the model of hard spheres. Adapted with permission from Knozinger, E.; Babka, E.; Hallamasek, D., *J. Phys. Chem. A.* 105, 8177 (2001). Copyright 2001 American Chemical Society.

Based on the above discussion, one can consider the number of neighboring matrix atoms surrounding the isolated species. A single substitution site is surrounded by twelve nearest neighbors, and a double site consists of eighteen. Once a triple-substitution site is reached, multiple geometries can be adopted. A triangular site has 22 neighbors, and a straight row has 24 neighbors. Molecules larger than diatomics are surrounded by at least 20 nearest neighbors and larger molecules, much more. These surrounding matrix atoms are known as the matrix cage that has important spectral ramifications when studying molecules, as is discussed in the next section. Furthermore, as the isolated compound gets larger, so does its cage and the probability of isolation starts to decrease rapidly.

If one considers a molecule occupying a single substitution site, such as CO, one can calculate the probability that another CO is not part of its cage based on the matrix ratio (n):

$$n = [\text{matrix atoms}]/[\text{trapped species}] \quad (1.1)$$

By taking the reciprocal of the matrix ratio (r) and assuming 12 nearest neighbors, equation 1.2 can be used to calculate the probability of a species being isolated:²⁸

$$P = (1-r)^{12} \quad (1.2)$$

As the isolated molecule gets larger the probability of isolation decreases rapidly. Consider a species with a diameter three times that of a matrix atom so that it occupies a site produced by a central matrix atom and the 12 surrounding cage atoms. The cage of this species is now expanded to 122 neighbors and the probability that the species is not isolated becomes:²⁸

$$P = (1-r)^{122} \quad (1.3)$$

The calculation is even more complicated when considering species that have strong interactions such as atomic lithium. Lithium atoms have been shown to dimerize during matrix formation, which could not be explained by simple clustering statistics; instead their strong interactions allow them to readily dimerize before the matrix is completely frozen if they come within a next-nearest neighbor distance (18 sites) of each other.³⁴ Even at low lithium concentrations, perturbations were observed in the atomic electronic structure that could only be rationalized by long-range interactions between atoms that are up to 3-matrix atom distances away. This strong interaction allows 68 potential non-nearest neighbor sites in which a second Li atom can reside and still perturb the electronic bands of another Li atom,³⁴ making isolation predictions difficult. The probability of isolation for various matrix ratios is shown in Table 1.2.

Table 1.2 Probability of isolation (adapted from ref. 28)

Matrix ratio (dopant %)	100 (1%)	1000 (0.1%)	10000 (0.01%)
single site, weak interaction			
% non-isolated	11.4	1.2	0.1
% isolated	88.6	98.8	99.9
multiple site, weak interaction			
% non-isolated	70.7	11.5	1.2
% isolated	29.3	88.5	98.8
single site, strong interaction			
% dimerised	16.5	1.8	0.2
% perturbed	41.3	6.4	0.7
% isolated	42.1	91.8	99.1

It should be noted that the above isolation calculations are only valid after all atoms and molecules have been frozen. Depending on deposition parameters, diffusion can take place to a considerable extent in each new layer of the forming matrix which complicates this evaluation further. When running a series of experiments, it is common to start with a reasonable dopant concentration and adjust it for future experiments based on spectral results such as clustering.

1.2.3 Spectral effects

As stated above, RGM are free from adsorption, emission, and Raman bands, all the way down to vacuum-UV radiation, and contain no ESR spectra. Furthermore, both neon and argon have negligible polarizability, so interactions with trapped polar or ionic compounds are reduced and vibrational origins will be near those found in the gas-phase. Jacox has compared the positions of ground-state vibrational fundamental bands of reaction intermediates in the gas phase with those in neon and argon matrices and found most

spectral shifts to be less than 1.2%.³⁵ In general, there are larger shifts in argon compared to neon as well as large shifts for alkali metal halides due to higher polarizability.³⁵

The matrix cage has several important ramifications for trapped species. One of the more obvious effects of the cage is to restrict rotations. Only a few small molecules have been found to show some pseudorotation, such as HCl in Ar, Kr, and Xe³⁶ and OH in Ne.^{37,38} Likewise, a ro-vibrational spectrum is observed for trapped water, which rotates nearly freely in RGM (see review ref. 39 and citations contained therein). Interestingly, very recent studies suggest that even the water trimer displays some pseudorotation.⁴⁰ For the majority of molecules, the matrix restricts movement, which simplifies spectra compared to those in the gas-phase due to the loss of rotational fine-structure.

The cage can, however, make a spectrum more complicated due to site effects that occur when trapped species exist in several different local environments caused by the non-equilibrium freezing process. Site effects will often induce a different number of peaks, shift peak positions, and change the shapes of peaks when compared to gas-phase spectra. For larger species, this site effect can also be extended to other complexes trapped nearby, which leads to further perturbation to the spectrum. If multiple peaks arise from a single active IR mode due to the cage-effect, the less thermodynamically stable sites typically decrease when annealing while the most thermodynamically stable site increases in intensity, thus leading to a simplified spectrum. Although never proven, the site effect has been used to explain multiple absorbances that could not be explained otherwise.²⁸ One objection to this explanation is that a continuous number of sites should exist at the lower deposition temperatures, especially for large complexes, and very broad bands should be observed instead of sharp multiplets.

Although all the above spectral changes are consequences of the matrix cage, the cage effect will be used to distinguish a specific implication for photolysis. Since molecules are trapped, isomeric products can be formed by photo-destruction of a molecule followed by rearrangement within its cage. One example is the HCN molecule trapped in neon which photo-dissociates upon UV irradiation forming H + CN fragments.⁴¹ Because of the cage effect, one of three events can occur depending on how much energy is available to the system. With little available energy, the trapped system will reform HCN. Given a little more energy, photoisomerization can occur forming the product HNC. Finally, with enough energy the hydrogen atom can diffuse out of the matrix cage and bind to other trapped species, leaving behind the trapped CN molecule. This photolysis event has been observed by the spectral growth of HCNH⁺ and CN.⁴¹ This technique has also been used to yield the HO₂ radical by allowing O₂ molecules to react with H atoms formed by photolysis of precursors such as HBr and HI.⁴²

1.2.4 Energy dissipation

The rapid freezing conditions under which a matrix is formed causes non-equilibrium trapping (kinetic control) of deposited gas phase species. Many examples have shown that when a high temperature ratio of isomers has been formed in the gas-phase, this ratio is preserved by trapping in a matrix.⁴³ One example is the *cis/trans* methyl-nitrite system which contains a 10.8 kcal/mol barrier to interconversion. By populating the less thermodynamically stable *trans*-structure in the gas phase, Willner showed that an argon matrix provides enough energy dissipation to stabilize the high-temperature isomer ratio.⁴⁴ It has been estimated that matrices can stabilize species as long as barriers to products are greater than ~2.5 kcal/mol.^{45,46}

The rapid energy dissipation has also been used to trap transient intermediates formed in the matrix. A recent hallmark study comes from the Ault group in the formation and stabilization of Criegee intermediates. Through the reaction of ozone with cyclopentadiene in argon matrices three intermediates have been observed.⁴⁷ The stabilization of these species is so remarkable because each lies ~50 kcal/mol exothermic to the reactants and exist next to low barriers of 10-20 kcal/mol. This stabilization means that the matrix dissipated most of the 50 kcal/mol that was available to the system. This study is crucial to our development of freeze-frame spectroscopy because it shows that a large amount of energy can be removed sufficiently quickly in order to trap key intermediates that could not be stabilized by other methods.

It is also important to consider the energy of impinging ions as they collide with the top layer of the matrix. Metal clusters are known to break apart or even imbed in a surface if deposited at a high enough energy,⁷ which would negate the values of mass-selection. Deposition therefore needs to occur under a condition known as soft-landing in order to preserve their gas-phase geometry. As will be discussed in Chapter 2, the energy of the metal ions are kept low (<10 eV) in order to minimize destructive deposition for cluster studies. A theoretical study of small Na_n clusters ($n = 6, 7, 8$) impinging on Ar_m clusters ($m = 7, 43, 87$) held at 0 K shows a very fast energy transfer upon impact from the sodium cluster to the argon cluster.⁴⁸ Even for the smallest Ar_7 cluster, energy is quickly dissipated, so that the Na_n remains geometrically unchanged as long as the initial sodium-cluster energy is kept low. The transferred energy is dissipated through argon-atom rearrangement and large-scale oscillations with the largest argon cluster being most efficient at removing excess energy.⁴⁸ For a matrix-isolation experiment, greater energy

dissipation is afforded by the large argon surface which is a nearly infinite heat sink. A transient, warm matrix surface exists before freezing out⁴⁹ which would further aid in soft-landing when compared to the computational study carried out at 0 K.

Another reason for minimizing ion energy is to avoid charge transfer during deposition, which can occur when the deposition energy is sufficiently high to ionize the matrix or trapped species. Table 1.34 provides ionization potentials of common species that are used in matrix experiments. High-energy deposition has been used in previous studies in order to maintain charge balance making use of this secondary ionization process (see section 1.4.3 for more detail).⁵⁰ Although we typically maintain low ion energies during deposition, high-energy Ar⁺ bombardment has allowed our group to observe exotic molecules such (CO)₂⁺ (Ch. 6) and O₄⁺ (Ch. 7).

Table 1.3 Ionization potentials of common molecular species commonly found in matrices (values taken from NIST, ref. 51)

Formula	I.P. (eV)	Formula	I.P. (eV)
He	24.587	N ₂	15.581
Ne	21.565	CO	14.014
Ar	15.759	CO ₂	13.777
Kr	13.999	(CO) ₂ ^b	13.05
Ar (s) ^a	13.9	H ₂ O	12.621
Xe	12.130	O ₂	12.070
Kr (s) ^a	11.9	(O ₂) ₂ ^c	11.66
Xe (s) ^a	9.7		

^a solid values taken from ref. 52

^b value taken from ref. 53

^c value taken from ref. 54

1.3 Species identification

It is often difficult to characterize species in the matrix since the only “handle” one has on their identification is spectroscopy. Deposition temperature plays a large role in complexation (Chapter 3) and impurities in the matrix such as H₂O, N₂, CO₂, etc. can also complex with the species of interest. Indeed, early matrix examples formed under poor vacuum conditions often contained background contaminants of nearly equal concentrations to the system of interest.^{26,27} Even under the ultra-high vacuum conditions gained by our system with a baseline pressure of $\sim 10^{-10}$ Torr (Chapter 2) we still observe H₂O and CO₂ from background contamination, depending on sample preparation.

Due to the difficulty of peak assignment, there have been several wrongly assigned peaks in the literature such as that of the CO band at 2136.7 cm⁻¹. Dubost and Abouaf-Marguin originally assigned this peak to the CO-N₂ complex,⁵⁵ but it was later reassigned to a CO-dimer by two independent groups.^{56,57} This assignment was again called into question by Givan, who reassigned it to a CO-polymer.⁵⁸ Givan also noted that it may be a CO-monomer that is trapped in an unstable matrix site.⁵⁸ Finally, under careful experimental conditions Yamada has assigned this band to the CO-monomer that is undergoing librational motion (hindered-rotation).⁵⁹ It is clear, therefore, that careful control experiments are necessary to make sure that observed changes in spectra are attributed to the correct physical phenomena.

Species identification is often a synergy between multiple techniques including gas-phase comparison, isotopic substitution, *ab initio* calculations, and variations to deposition conditions. As was stated, matrix absorptions tend to be close to those observed in the gas phase; therefore, identification starts with gas-phase comparison whenever possible. After

gas-phase comparison, the best method is isotopic substitution. By substituting a heavier isotope for a naturally occurring one, the vibrational frequency shifts in a predictable way. Assuming the molecule acts as a harmonic oscillator, the vibrational frequency (ν) is given by equation 1.3:

$$\nu = \frac{1}{2\pi} \sqrt{\frac{k}{\mu}} \quad (1.3)$$

where k is the force constant, and μ is the reduced mass. Substituting $\omega = 2\pi\nu$, where ω is frequency in wavenumbers, and solving for the force constant we get:

$$k = \omega^2 \mu \quad (1.4)$$

Assuming the force constant doesn't change upon isotopic substitution, which holds true for most molecules, equation 1.4 can be solved when considering two isotopes:

$$\omega_2 = \omega_1 (\mu_1 / \mu_2)^{1/2} \quad (1.5)$$

where ω_2 is the frequency of the heavier species, ω_1 is the frequency of the lighter species, and μ_1 and μ_2 are the reduced masses of the light and heavy isotopes respectively. As an example consider ^{12}CO which absorbs at 2138.0 cm^{-1} in argon. The absorbance of ^{13}CO can then be predicted by using the reduced masses for ^{12}CO of 6.857 and ^{13}CO of 7.172 and substituting in to equation 1.4, ω_2 is predicted at 2090.5 cm^{-1} which is indeed where it absorbs in argon.

Isotopic substitution is also useful for determining the number of ligands bound to a metal center. This type of study is typically done by doping a matrix with a 50:50 mixture of two isotopes and observing the splitting and intensity patterns.⁶⁰ For example a

monocarbonyl with the formula MCO would give rise to two peaks of equal intensities in a mixed isotope experiment (one for $M^{12}\text{CO}$ and another for $M^{13}\text{CO}$). On the other hand, a linear dicarbonyl species would be expected to give rise to three peaks with the mixed isotopomer being twice as intense as each single isotope species. This is because both $\text{O}^{12}\text{C-M-}^{13}\text{CO}$ and $\text{O}^{13}\text{C-M-}^{12}\text{CO}$ must be considered as two possible structures that give rise to the same frequency, as each are chemically identical. The interpretation can get more complicated if both sides of the molecule exist in distinct sites in the matrix, thus chemically distinguishing which side of the metal atom the isotopic molecule is on. This difference in environment should lead to two discrete frequencies for the mixed isotopomer and split the isotopic dicarbonyl into a quartet with each frequency of equal intensity. Likewise, if the molecule contains a degenerate mode, the degeneracy may be broken leading to an intensity ratio that is not easily predicted, as in the case of a D_{3h} species which gives rise to a 5:3:3:5 pattern.⁶⁰

Deposition conditions can also be adjusted to add insight into new species. Clustering generally increases when the dopant concentration and deposition temperature are increased (Chapter 3). Likewise, neutralization increases at higher temperature depositions as well (Chapter 5). Identification of ions can be particularly challenging, especially when trying to identify charge. In general, anions are red shifted in relation to cations due to their stronger interaction with the matrix, which weakens chemical bonds.⁸ Although anions can sometimes be identified via photodetachment, the detached electrons often neutralize cationic species leading to the loss of both. A technique used in the past was to add small amounts of electron scavengers such as CCl_3 that preferentially bind electrons in the forming matrix layers before they can attach to species of interest, thereby

reducing the anionic peaks in question.⁶⁰ Because our species are already charged when deposited, this technique would probably not aid in our experiments; however, it has been shown that we can solely deposit anionic species which greatly simplifies identification (Chapter 4). Sometimes it is worth using high energy Ar⁺ to generate molecular ions from trapped species in the matrix, as we have done to identify the (CO)₂⁺ complex (Chapter 6).

1.4 Previous matrix-ion deposition methods

Studying charged species in rare gas matrices can pose a particular challenge; since the matrices are rather poor electrolytes, isolated charges are poorly screened and therefore there must be charge balance of anions and cations in order to accumulate sufficient number densities for spectroscopic studies. Many techniques have been employed to accomplish this task, including collisional or photoinduced charge transfer *in situ*, inherently neutral plasma sources, and high-energy mass deposition. Each of these techniques will be discussed below, as well as disadvantages of these methods. For a complete list of ions that have been spectroscopically observed in rare gas matrices, see Jacox's compilations.^{61,62}

1.4.1 Photoionization and chemiionization - *in situ* generation

The first ions in matrices were made from the interaction of deposited alkali metal atoms with small trapped molecules, a deposition process developed by Pimentel.⁶³ The first ionic species was identified by Andrews to be Li⁺O₂⁻ which is formed when Li atoms and O₂ molecules interact in the forming matrix.^{64,65} This complex is a Coulombically bound species which exists because electrostatic attraction makes up for the difference between the ionization potential of Li and the electron affinity of oxygen.⁶⁵ This complex

is bound within the same matrix cage, so the cation and anion cannot be considered isolated.

The first truly isolated ions were created independently by both Kasai and Jacox, who each used photoionization of trapped electron donors. Kasai used Na as an electron donor and upon irradiation observed the anion B_2H_6^- via ESR spectroscopy.⁶⁶ Similarly, Jacox observed the C_2^- anion by adsorption spectroscopy, which was formed by photoionization of acetylene. This band increased 30-fold when Ce atoms were added to the matrix as an electron source, also reaffirming this peak to be anionic.⁶⁷ Later, studies on the vacuum-UV photoionization of acetylene revealed that the C_2^- is stabilized as a Coulomb ion pair with the C_2H_2^+ cation existing separated by several argon layers such that the neither ion is perturbed by the other.⁶⁸ Photoionization was also applied to other molecules such as CCl_4 to reveal the CCl_3^+ , CCl_4^+ , and Cl_3^+ ions and the CCl_3 radical.^{69,70} Another method, developed by Ault and Andrews, was to deposit salt vapor with precursors in argon, leading to reactions during condensation. Deposition of NaCl with Cl_2 led to Na^+Cl_3^- while CsCl with HCl lead to $\text{Cs}^+\text{HCl}_2^-$ ion pairs.⁷¹⁻⁷³ This method has also been used to stabilize polyhalides such as Cs^+F_3^- and $\text{Cs}^+\text{BrF}_2^-$ and new compounds such as $\text{Cs}^+\text{SiF}_5^-$.⁷⁴⁻⁷⁶ One problem with the use of alkali metals is that they contain strong absorbances throughout the visible spectrum⁷⁷ though this can be avoided by using ESR and vibrational spectroscopy. Second, alkali metals tend to be very perturbing, making it hard to observe spectra due solely to anionic species. Finally, the wavelengths used for photoionization will often cause photodetachment of electrons from anionic centers before they can be spectroscopically observed.

1.4.2 Plasmas

Charge neutrality is also inherently satisfied by several techniques whereby ions are produced externally but in close proximity to the matrix and co-deposited with matrix gas. Microwave discharge involves excitation of a gas in a quartz tube with a small orifice directed toward the matrix. The majority of discharge gas leaving the tube remains in an excited metastable state.⁷⁸ The excited atoms relax by collisions with neutral precursors, leading to ionization of the precursor and ejection of an electron in a process called Penning Ionization.⁷⁸ The resulting cation gets trapped in the forming matrix while the electron is captured by other species present, thus maintaining charge balance. This method was applied early on by both Jacox and Andrews through the use of argon as a discharge gas.^{79,80} Using argon, however, introduced many difficulties for matrix isolation, including extensive atomization, isotopic scrambling, and matrix charge transfer, and could only be used for strongly bound diatomic and small polyatomic species such as C₂, N₂, CO, CN, and C₃.⁸ Jacox eliminated these problems by designing a new discharge setup using neon as the discharge gas and introducing the neutral precursors outside the discharge tube.⁸¹ Since all molecules besides He and Ne have ionization potentials below 16 eV, using excited neon atoms with first-excited states between 16.6 eV and 16.85 eV ensures that virtually any atom or molecule could be ionized by this method,^{81,82} even those with high ionization potentials such as BF₃ and HF.⁸ Furthermore, as the ion precursors were introduced downfield from the discharge tube, atomization and scrambling do not occur.

Another major breakthrough came with the application of laser ablation. This technique involves hitting a metal target with high energy laser pulses. The ensuing plasma plume consists of neutral metal atoms, a significant number of metal cationic species, and

an excess of electrons. Bondybey first applied this technique to study the gas-phase laser induced fluorescence spectrum of Pb_2 .⁸³ He later extended these studies to SiC_2 both in the gas phase and isolated in a neon matrix.⁸⁴ A more complete exploration of the possibilities of laser ablation was realized by Andrews, who has done extensive work on transition metals. By introducing the matrix gas doped with small reactive molecules such as O_2 , N_2 , CO , H_2 , etc., complexes form in or near the matrix surface and become trapped. Several reviews have been written on the transition-metal carbonyls,⁸⁵ transition-metal oxides,⁸⁶ transition-metal nitrosyls,⁸⁷ and transition-metal hydrides.⁸⁶

Charge balance is presumably achieved by both plasma sources because the ionization mechanisms also produce counter-ions in close proximity to the matrix, which are then trapped along with the ionic species of interest. Indeed, both cationic and anionic species can often be spectroscopically observed together in matrix samples produced using these types of sources.^{82,85,88} The disadvantage to these sources are that they afford little control as to the species formed and trapped. Furthermore, in order for them to operate, they must use high energy processes. Indeed for both cases a greater amount of reactive products are observed upon deposition when compared to the same metals vaporized by a Knudsen cell.⁸ Finally, due to the close proximity of the matrix, many unwanted reactions occur between species of interest and background gasses which also get trapped and can complicate spectral interpretation.

1.4.3 Mass-selected ion deposition

Beams of mass-selected ions generated in external ionization sources and guided to the deposition region have also been used for matrix isolation spectroscopy studies,⁸⁹⁻⁹² though in these cases the nature of the counter-ions are typically less clear.⁹³ The earliest

example of such work is from the Maier group, and featured deposition of small molecular cations generated by electron impact ionization of cyanogen and acetylene and probed by UV-visible spectroscopy;^{94,95} these studies were subsequently extended to larger molecules, notably cationic and anionic carbon chains.^{96,97} No specific counter-ions were observed, however the high estimated number density of cations in the matrix ($\sim 10^{16} \text{ cm}^{-3}$) could only be rationalized by the presence of a comparable density of counter-anions, which were assumed to have been produced by secondary ionization of the matrix or grounded sample holder during bombardment with the fairly high-energy cation beam ($\sim 150 \text{ eV}$).⁹⁸ A detailed investigation of the mechanisms by which negative counter-ions are generated during deposition of high-energy cation beams was reported by the Leroi group, where they directly observed CO_2^- radical anions formed by electron capture, confirming the earlier hypotheses.⁹³ The types of species able to be deposited with this method are limited to very robust molecules which can survive the high energy deposition process. It also relies on uncontrolled secondary ionization in order to maintain charge neutrality, which is not useful for catalytic studies where high levels of control are needed.

An alternative method for providing charge balance when using beams of mass-selected cations is to flood the deposition region with low-energy electrons. These electrons can attach either to impurity species to form counter-ions,^{90,99} or they can recombine with the cations to form neutral species.¹⁰⁰⁻¹⁰³ The latter method has proven particularly useful for generation of neutral metal atoms and clusters for matrix-isolation spectroscopic studies.¹⁰⁰⁻¹⁰³ More recently years, Moskovits has applied this technique to deposit mass-selected cation clusters such as Ag_5^+ ,¹⁰⁴ Fe_3^+ and Ag_3^+ ,¹⁰⁵ and Ag_7^+ ¹⁰³. Although no ions were observed, each of the neutral clusters were probed using resonance Raman

spectroscopy. He also used this technique to form iron cluster carbonyls^{102,106} and iron-dinitrogen compounds,¹⁰⁷ probed via FTIR, but in each case only neutral species were detected.

1.4.4 Ion-codeposition method

An alternative method for providing charge balance to stabilize matrix deposition of ions from mass-selected beams would be to simultaneously direct a second beam of oppositely charged ions into the same deposition region, adjusting the beam currents so that the overall deposited charge is zero. Indeed, this method was proposed and attempted by the Leroi group, using beams of CS_2^+ and Cl^- ions mass selected by two separate quadrupoles aimed toward the deposition window.¹⁰⁸ After 48 hours of deposition, no evidence of trapped ions was observed, even using high-sensitivity laser-induced fluorescence detection.¹⁰⁸ We have taken a similar approach by codeposition of metal anions with counter-cations; however, our ion beams mix and follow the same deposition path toward the matrix, which we attribute to the experiment's success. We have been the first group to deposit and isolate mass selected metal ions in a matrix through the use of specific counter-ions. Additionally we can selectively form anionic metal species at 10 K without their neutral or cationic counterparts, making spectral interpretation far simpler than previous studies. This new deposition method should be generally applicable and may shed light on many convoluted previous matrix experiments.

1.5 Dissertation outline

A large amount of time and effort has been spent on designing, building, testing, and modifying a custom-made apparatus that can perform the experiments that were

proposed. Chapter 2 is devoted to the experimental details about the system. Mass spectra of the ions used for experiments, along with their stopping potentials and how data is manipulated after being taken, is presented. Chapter 3 is a reproduction of the first article published using the counter-ion co-deposition method. The anionic copper carbonyl system was used to analyze this new technique and probe parameters such as deposition temperature, dopant concentrations, and neutralization events. Based on these preliminary results, Chapter 4 contains results performed by deposition at 10 K in the absence of ambient light and the subsequent “clean” spectra that is afforded by our new method. By isolating only anionic complexes, wavelength dependent photodetachment and subsequent electron capture C-C bond formation is monitored. Chapter 5 covers 20 K deposition in the absence of light and the resulting spectra which contain resolution limited peaks. Even more surprising are the transient neutral complexes, which are formed only after annealing the anionic system followed by photodetachment. These transients are then able to relax to a more stable geometry with gentle annealing.

All experiments presented use either Ar^+ or Kr^+ as the counter cation, though we were not able to definitively identify a cationic species in the matrix until recently. Chapter 6 addresses this problem with the identification of $(\text{CO})_2^+$ via high energy Ar^+ deposition experiments. This study is the first time this species has been identified in an argon matrix. Chapter 7 presents failed attempts to form copper oxide species; instead, we found what appears to be the lowest temperature example of chemical equilibrium, a conformational rearrangement of O_4^+ at 10 K. Finally, Chapter 8 describes the versatility of the deposition method through the use of the Ag^- and Ni^- carbonyl systems and the implications for this deposition method going forward.

Chapter 2

Experimental methodologies

2.1 Introduction

This chapter describes the experimental methods used for our matrix-isolation experiments. The apparatus design and assembly of vacuum components including all internal ion optics was completed by Dr. David Moore and a previous graduate student Alex Hunter. The first testing and modification of the magnetron source along with the first copper mass spectra taken using the system were also carried out by Alex Hunter. My contribution began with taking the first matrix-isolation data, detected using UV-vis spectra with help from Nathan Roehr, a graduate student from Dr. Polfer's group at the University of Florida. I then made several modifications to key components and determined the optimal working parameters for matrix-isolation experiments. These modifications led to the first IR data of matrix-isolated ions deposited with this system and all subsequent data presented in this dissertation.

The first section describes the matrix-isolation system, which has been custom built in-house to meet our requirements including metal generation and mass selection. In order to generate enough metal ions for spectroscopic observation, the magnetron sputtering source had to be significantly modified, as is discussed. These ions were then mass- and charge-selected and balanced by an equal current of counter-ions. Due to potential secondary ionization events⁹⁸ and destructive deposition for larger clusters,^{109,110} it is important to keep the energies of the both ion beams as they impede on the matrix as low as possible. This energy is measured by use of stopping potentials near the deposition

region. System modifications for both FTIR and UV-Vis spectroscopy employed in these experiments are also discussed.

Following a description of the instrument, a section is devoted to the gas-delivery system. This gas system was designed so that stock gases could be mixed at various concentrations and stored until their introduction to the matrix deposition chamber during an experiment. Finally, a section is devoted to data collection and manipulation. Data manipulation typically involves correcting the baseline and in some cases removing etaloning. Also, small daily fluctuations in atmospheric peaks (water and CO₂) must be taken out.

2.2 Matrix-isolation system

2.2.1 System overview

The apparatus for the experiments presented herein is a custom-built ultra-high vacuum (UHV) system shown in Figure 2.1. It combines ion-beam deposition with a spectroscopic cryostat for matrix-isolation studies. A UHV system was constructed in order to minimize contamination by background gas; in particular, H₂O and CO₂ levels must be kept low in order to reduce their interactions with species of interest. Likewise, their absorbances in the spectra can complicate spectral interpretation, especially carbon dioxide, which is a product of the reactions we aim to study. The system consists of four stages of differential pumping, a condition whereby differences in pressure are maintained between different stages of a vacuum system. This condition is created by using conductance limiting apertures between each of the chambers and maintaining UHV with magnetically levitated turbo molecular pumps (hereby referred to as “turbo-pumps”)

backed by oil-free scroll or rotary-vane pumps. For vacuum pump and gauge information, as well as typical pressures, see Table 2.1 in the Appendix.

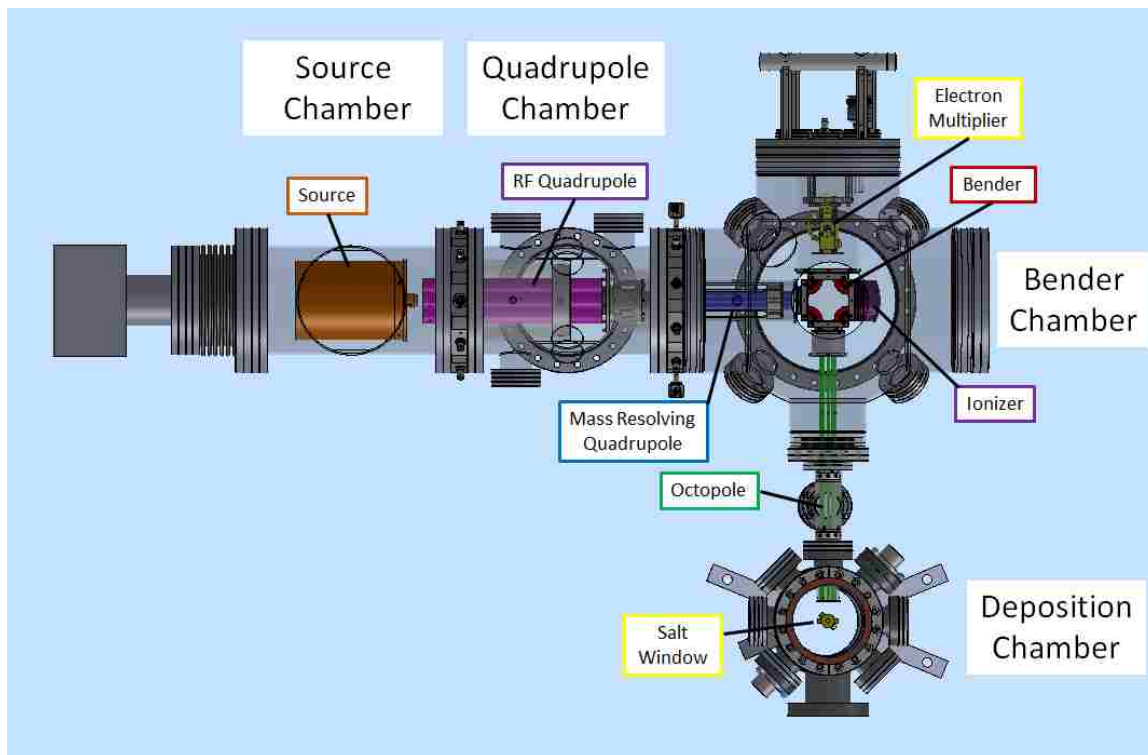


Figure 2.1 Ultra-high vacuum system for deposition of mass-selected ions into rare gas matrices. Some interior components, such as collars and housings, have been made transparent for clarity. The system stand, internal gas lines, and wires not shown.

The source chamber houses a magnetron sputtering source (customized version of NC200U-B from Oxford Applied Research) used to produce cluster anions. After being generated, the anions are extracted through a 6.25 mm diameter nozzle maintained at a potential up to +400 V and sent into the quadrupole chamber. This chamber houses a series of RF and DC ion optics, including a 22-mm RF-only quadrupole collimating ion-guide. This quadrupole sends the ion beam into a 9-mm resolving quadrupole mass filter contained at the entrance in the bender chamber. The resulting beam of mass-selected ions then enters a DC quadrupole bender, which turns the ions through an octopole ion guide

leading to the deposition chamber. An electron-impact ionization (EI) source is mounted to the opposite side of the quadrupole bender for the production of positive counter-ions. Each of the quadrupoles, octopole, and bender also contain entrance and exit plates that may also be used to guide ions.

All ion optics, including the quadrupoles, are controlled using a Tempus data system (Ardara Technologies). The EI source and electron multiplier are controlled by a Merlin data system (Extrel). High voltage is supplied to the EM by a high voltage power supply, capable of supplying up to 5000 V (Standard Research Systems, PS350/5000V-25W). Common settings on all optics for anionic metal deposition can be found in Table 2.2 (Appendix). Due to the unique requirement for mass-resolution of large metal clusters, a custom RF power supply for the 9-mm quadrupole was made. This supply allows one to readily change out the inductance coil, which is typically fixed in commercial instruments. For all data presented in this dissertation, a coil with an inductance of 24.4 μ H and frequency of 2.40 MHz was used. The Faraday plate is connected via a BNC cable to a preamplifier (Advanced Research Instruments, PMT-5R), which is then connected to the Tempus Data Controller for a digital current reading and mass-spectroscopy. The output of the preamplifier can also be connected to an analog electrometer for current readings (Kiethley Instruments, 610C).

All initial samples were deposited onto a KBr window (Koch Crystal Finishing) mounted on a 4K closed-cycle helium cryostat (Advanced Research Systems model CS204SF-X20B). Because of its low threshold for thermal stress, the KBr window cracked and needed to be replaced periodically; therefore, a CeI window has recently been installed due to its higher tolerance to thermal strain. The cryostat is mounted on a UHV rotating,

vertical translation stage (McAllister Technical Services), which allows optimal orientation of the window for deposition (0°) or spectroscopy (45°), and also for the sample window to be moved up out of the ion beam for current measurements on a Faraday detector, maintained at ground potential. Temperature control of the cryostat is achieved using a PID temperature controller (Lakeshore 331), monitoring a silicon diode sensor mounted directly on the sample holder window, and controlling a 50 W heating band wrapping the second stage of the cryostat. The matrix gas is introduced through a 1/16" stainless steel line aimed toward the window at a distance of about 2 inches.

Spectra are recorded using an FTIR (Thermo-Nicolet 6700) equipped with an externally-mounted, liquid-N₂-cooled MCT-A detector coupled into the cryostat chamber via a pair of KBr windows. All data were taken using Omnic, Thermo Nicolet Corporation software. The detector and external beam-path are contained in custom built boxes, which are constantly under a nitrogen purge to minimize atmospheric water and carbon dioxide in the spectra. Early studies were done with UV-Vis through the use of a tungsten filament lamp introduced through a series of fiber-optic cables and lenses, as is discussed in Section 2.2.4.

2.2.2 Metal-ion generation and mass selection

Motivated by Takagi, who was working on the deposition of large ionic clusters,¹¹¹ Haberland proposed a new type of source for formation of large clusters.¹¹² Haberland's source combined discharge sputtering with a gas aggregation technique and showed that an intense, continuous beam of metal clusters was possible.^{112,113} Our magnetron sputter source, shown in Figure 2.2, is a commercialized version based off Haberland's technique. It operates by bombarding a metal target with ionized argon. First, argon is continuously

flowed into a gas feed line between the cathode and the anode. A high voltage controller is used to ignite the argon in a small gap ($\sim 0.3\text{mm}$) between the cathode and anode forming an argon plasma. This plasma contains high amounts of Ar^+ which are accelerated toward the metal target sitting on the cathode. The argon ions bombard the metal target sputtering off metal atoms and small clusters. Electrons, which are in high yield in the plasma, become trapped by a permanent magnet also contained under the target. Following helical paths around the magnetic field lines, the electrons collide with neutral argon atoms near the target surface leading to further argon ionization and sputtering. Due to this enhanced ionization, sputtering rates are so high compared to previous methods. Furthermore, anywhere from 20% to 80% exist as ions.^{112,113} For the purpose of this dissertation, only the metal anions will be considered because the current counter-ion production method is restricted to cations.

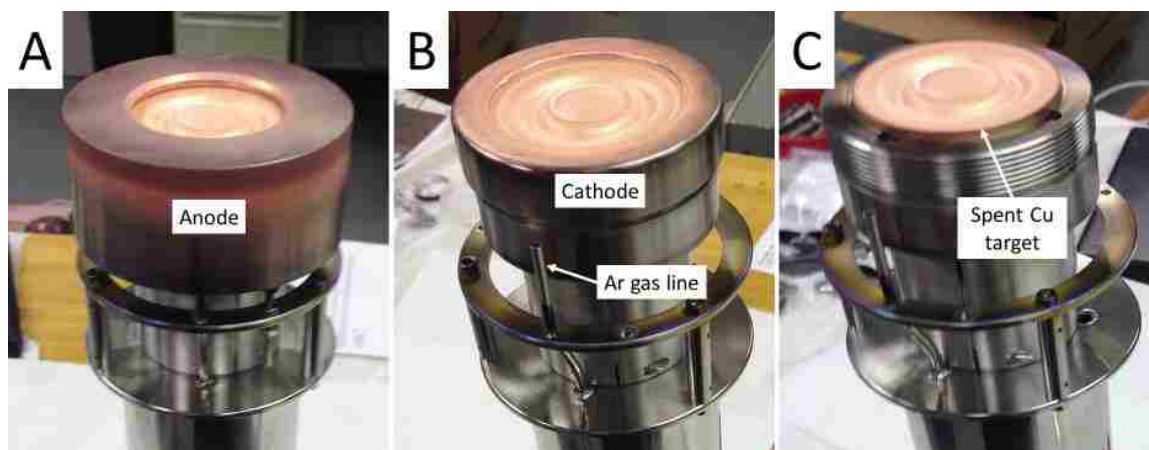


Figure 2.2 Magnetron sputter source containing a spent copper target: A) fully assembled, B) anode removed, and C) cathode removed.

In order to form clusters, a rare gas is introduced into a water-cooled aggregation tube which causes clustering through metal atom collisions. Theoretically, cluster size should be controlled by adjusting the length of the aggregation region, rate of gas flow, and

power supplied to the magnetron. Early studies on our system only yielded very large clusters with little mass resolution, requiring extensive modifications to be made to the system. The most important result of modification has been the improvement of the mass resolution in the region of interest. Another important upgrade has been to the front of the aggregation tube, which has been refit with a nozzle capable of maintaining a potential up to +400 V which extracts the metal ions from the plasma region. In order to insulate the voltage from the rest of the system, a double Teflon gasket was made. This split gasket design, one with a smaller inner diameter (Figure 2.3C) and one with a larger inner diameter (Figure 2.3D), have to be used together to avoid copper build up upon sputtering and grounding of the nozzle. The nozzle and gasket assembly are shown in Figure 2.3. A 6.25 mm diameter nozzle has been used for all experiments, maintained at a bias around +215 V.

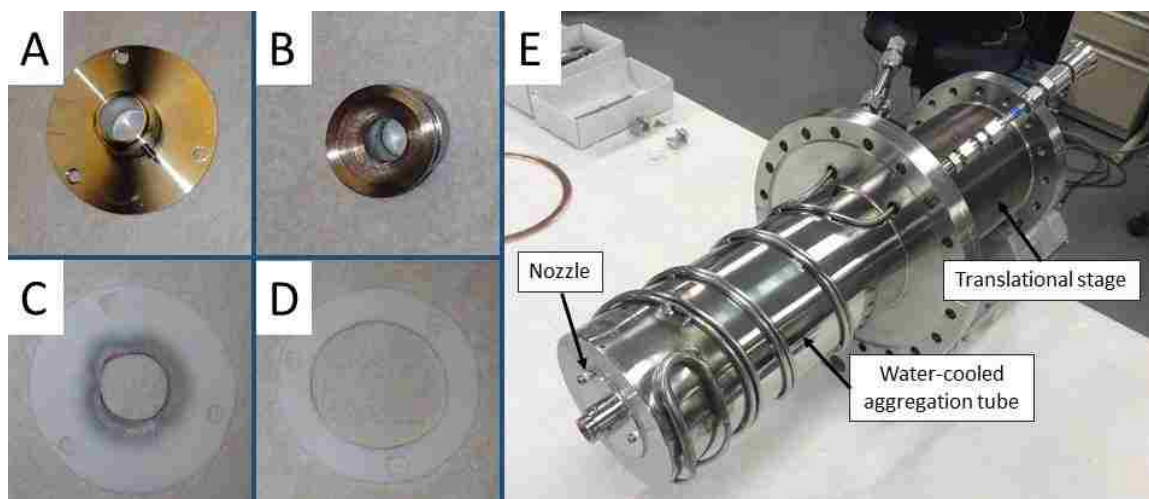


Figure 2.3 Extraction nozzle assembly, completely disassembled showing: A) nozzle attachment plate, B) nozzle with 6.25 mm opening, C) inner, sacrificial gasket, and D) outer gasket. Aggregation tube in E with nozzle completely assembled and attached.

All metal targets are standard 2” diameter sputter targets purchased from the Kurt J. Lesker Company. The three metals used so far have been copper, silver, and nickel. Both copper and silver targets with a 0.125” thickness and 99.99% purity are used while a thinner nickel target of 0.063” and purity of 99.9% is used. A new and spent copper target is shown in Figure 2.4. The track taken by electrons is roughly the same as where argon cations impinge on the target which can be seen on spent targets (Fig. 2.4B). Under appropriate magnetron sputtering conditions (4 sccm Ar, 113 mA discharge current at 250-300 V), ion currents of 4-11 nA are achievable depending on the target age and metal used. The expected target lifetimes, in terms of power absorbed, for copper, silver, and nickel are 1200, 800, and 400 W•h, respectively.

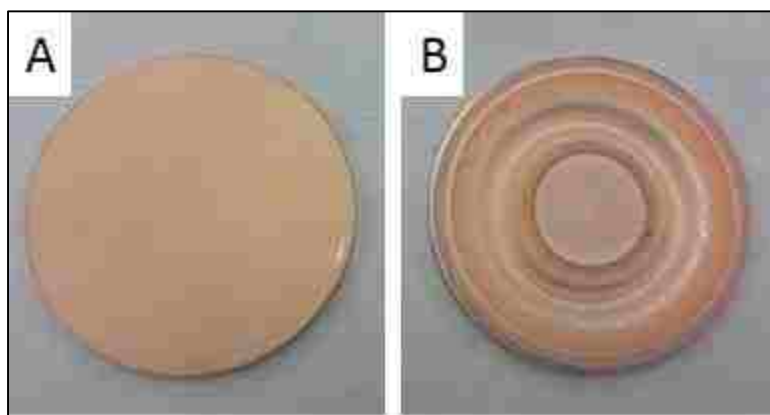


Figure 2.4 Copper sputtering target used for matrix isolation experiments: A) new B) after ~20 hours of sputtering.

Before depositing into a matrix, all sputtering conditions and optics must be optimized for the metal of interest, and the absence of contamination peaks must be confirmed. This is done by taking a mass spectrum of the anion beam on an electron

multiplier located in the bender chamber (Figure 2.1). A pure copper spectrum can be obtained (Figure 2.5A), where both the anionic copper monomer and dimer are isotopically resolved without any contamination peaks (see Appendix 2.12 for a spectrum with a contamination peak). Once the absence of contamination peaks has been verified, the resolution of the quadrupole mass spectrometer is detuned for maximum throughput for deposition during experiments (Figure 2.5B). See Figure 2.14 (Appendix) for resolved spectra of both silver and nickel anions and Table 2.3 for natural isotope abundances of copper, silver, and nickel.

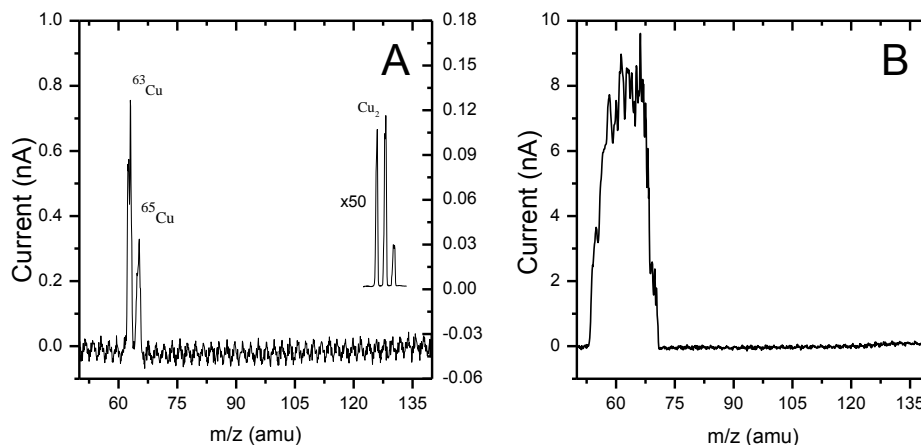


Figure 2.5 Mass spectra of copper anions from sputter source: A) high-resolution, isotopically resolved monomer and dimer, and B) high-throughput for matrix experiments.

2.2.3 Charge balance and ion-energy measurements

In order to deposit metal anions of interest, it is necessary to maintain charge balance through the use of counter cations. Once the anionic metal current is stable, a beam of counter-ions is produced by introducing a low flow (~ 0.3 sccm) of the desired gas into the EI source. Due to the lack of mass selection for counter-cations, only rare gasses, Ar or Kr, are used because only one product can be formed, Ar^+ or Kr^+ respectively. The

counter-cations are then bent into the octopole and combined with the anionic metal beam. In order to achieve a net current of zero as measured at the Faraday plate, several parameters may be adjusted. Since the metal anions represent our limiting reagent, i.e. the system optics have already been optimized for max throughput of anions, the only factors that are changed have to do with the cation beam. First, the flow rate of the counter-ion gas may be increased, however this also increases the background pressure, so is typically kept to 0.3 sccm. Instead the ionizer filament current is adjusted as a course control and the ion region bias in the ionizer is adjusted as a fine control.

Another consideration for deposition is the kinetic energy of the impinging beam upon the matrix which must be kept low, as stated in Chapter 1. This energy is measured on the Faraday plate by monitoring the total ion flux as a function of the voltage applied to the exit plate of the octopole. As the optical bias is scanned, the ion beam will begin to be rejected as its kinetic energy can no longer overcome the electric potential, known as a stopping potential. By taking the first derivative of the beam current at the Faraday plate versus the optic bias, the stopping potential can be determined.

Assuming an ion is not accelerated or retarded by an external field after being formed, its stopping potential is typically established by its birthing potential, which is the potential that the ion first “feels” once it is created. For the EI source, a small metal grid surrounds the region where cations are formed. Once neutral species are ionized, the birthing potential is established by the bias that is applied to the grid. The cation energies respond nearly linearly to the bias set inside the ionizer as measured by stopping potentials described above (Figure 2.15, Appendix). On the other hand, metal anions will not change their stopping potentials even if the extraction nozzle is adjusted between 0-400 V. This

strange behavior can only be explained by a low birthing potential that is not affected by the nozzle's bias. We hypothesize that there is a layer of gas-phase "sacrificial" ions either in or near the nozzle that shields an inner layer of ions from the applied bias. These inner ions, that survive to be detected, only feel the self-potential at the center of the beam. Anion energy distributions have been measured to be centered around -10 eV for copper anions, -5 eV for silver anions, and -4 eV for nickel anions (Figure 2.6). Cation energies are maintained at +60 eV during typical deposition experiments, which are somewhat higher than desired, but are required in order to balance the currents at the Faraday plate when the ion optics are tuned for maximum anion transmission as stated above. We later verified that the major features of the spectra and subsequent processing steps were unaltered when slower cations, ~30 eV, were used.

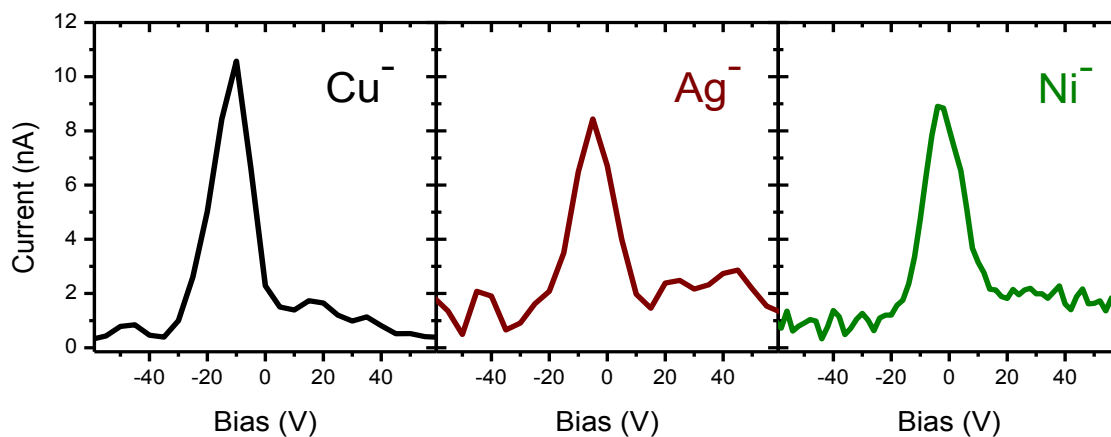


Figure 2.6 Ion energy distributions derived from stopping-potentials of metal-anion beams detected at the Faraday plate.

2.2.4 FT-IR and UV-Vis detection methods

Except for the very first data taken on the system, all data have been taken using FTIR spectroscopy using a Thermo-Nicolet 6700 spectrometer. The IR beam is sent out

the side of the commercial spectrometer by an internal mirror and directed toward the deposition chamber. An image of the beam path is shown in Figure 2.7. The beam is reflected off two flat mirrors mounted on an optics table and enters the deposition region through a differentially pumped KBr window. The deposition window is rotated so that the beam hits it at a 90° angle while taking a scan. The beam then leaves the chamber through another differentially pumped window and is focused by a parabolic mirror into a liquid nitrogen-cooled, MCT-A detector. Each of the optical tables are contained in plexiglass boxes (not shown in figure), which are continuously purged with nitrogen from a nitrogen generator (Parker Balston, 75-62).

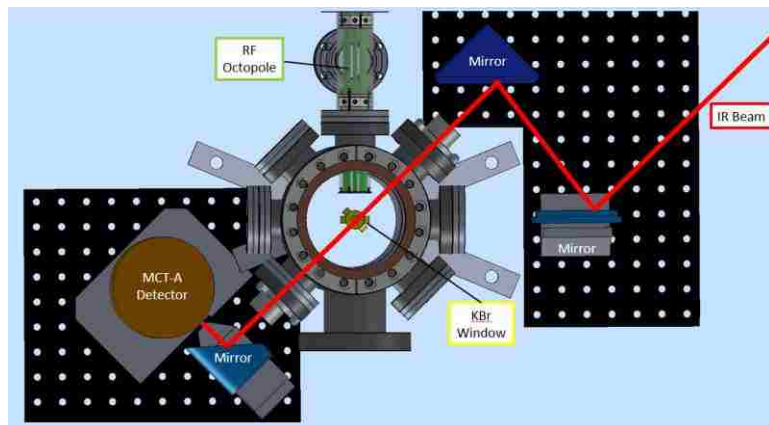


Figure 2.7 Close-up illustration of the deposition chamber showing the FTIR beam path. The beam is produced by a Nicolet 6700 spectrometer (not shown), directed into the vacuum chamber, through the matrix, and detected by an external MCT-A detector.

In order to obtain UV-Vis data, the mirrors and MCT-A detector are removed and replaced by a fiber optic system. A tungsten-filament lamp (Hamamatsu, L2192) is used to produce visible light, and UV is generated by a deuterium source (Analytical Instrument Systems, DT 1000). Light from both sources is collected through 100 μm diameter fiber

optic cables (Ocean Optics) and is sent through the deposition chamber via a dispersion lens sitting close to the differentially pumped KBr window. The light follows the same path as the FTIR beam through the deposition region, exits the other KBr window, and is collected by a collimator lens. Another fiber optic cable sends the collected transmitted light into a fixed-grating spectrometer, with a photodiode array detector (Ocean Optics, USB 2000).

2.3 Gas preparation and delivery

An in-house gas mixing and delivery system (Figure 2.8) has been designed so that nearly any matrix gas of varying dopant concentration may be premade and stored before the day of an experiment. Several stock gases (Praxair) are stored at high pressures and high concentrations including: argon (6.0 research grade), helium (6.0 research grade), carbon monoxide (10.2% in excess argon), and oxygen (10.4% in excess helium). The majority of experiments consist of a dilute solution of either CO or O₂ in excess argon however if a specialty gas mix is needed such as NO or an isotope, there are two open spots to attach these bottles. Mixes are made by opening one of the six aluminum gas-mix cylinders and using standard gas dosing techniques to dilute one of the stock mixes with argon. Aluminum bottles are used to avoid high-pressure mixes of CO from reacting with metals, namely nickel, in steel bottles. Three pressure gauges are contained on the rack: a Pirani gauge (1-1000 mTorr, Kurt J. Lesker-6000) used to monitor vacuum conditions when not in use, a piezo transducer gauge (1-1000 Torr, Kurt J. Lesker-902) used to measure dopant gasses for matrix mixes, and a Bourdon gauge (-0.1 to 0.5 MPa, Swagelok EN-837-1) used to measure high-pressure argon when making a matrix-gas mixture. The baseline pressure in the gas rack is normally 10 mTorr and gas mixtures are typically made

to a total pressure of 2000 Torr. Once made, the gas mixes may be stored indefinitely, but are usually consumed within a week before a new mix is made.

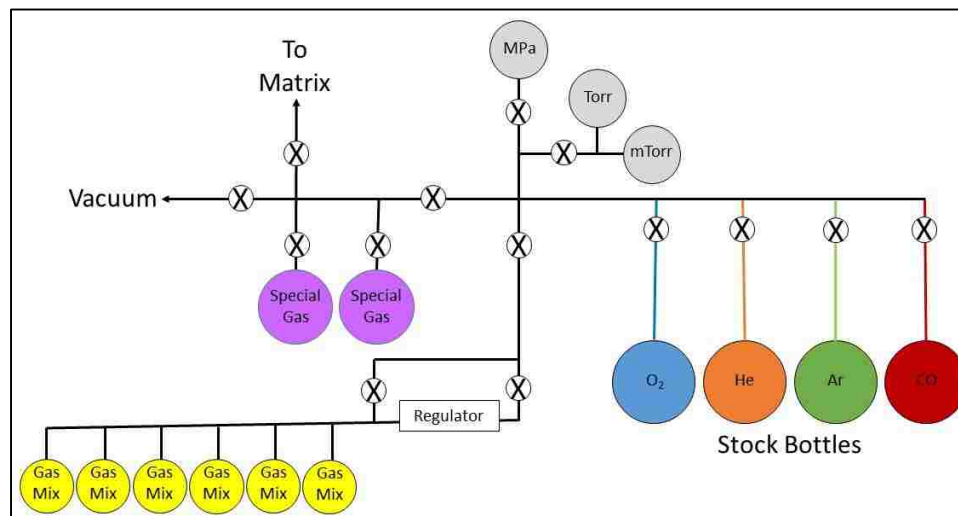


Figure 2.8 Gas rack used for making matrix gas mixtures. Stock solutions are diluted into aluminum gas mixing bottles and stored until needed for an experiment. Baseline pressure in the rack is measure by a Pirani gauge (mTorr) while low and high pressures during gas mixing are measured with a piezo transducer gauge (Torr) and Bourdon gauge (MPa), respectively.

Nearly all of the gas lines in the gas rack up to the deposition line are made from 1/4" copper in order to prevent CO gas mixes from pulling nickel and iron out of stainless steel lines; however, it is still necessary to purify the matrix gas before introducing it into the deposition region. This purification is done by making a cold ethanol bath using liquid nitrogen as a cooling agent inside a dewar (Figure 2.9). A section of copper tubing, which has been twisted into a spiral, is immersed in the 157 K bath removing any metal carbonyl impurities along with CO₂ and H₂O as the matrix gas flows through it. Initially, flow rate was controlled by a needle valve using approximately constant backing pressure maintained in two steel bombs on the gas rack (not shown in figure). The needle valve was shortly replaced by a mass flow controller (Allicat, MC-10sccm) capable of supplying gas

between 1 to 10 sccm. After being purified, the gas is introduced into the deposition chamber through a 1/16" stainless steel line aimed toward the deposition window. An ozone generation system, as well as an open line for secondary gas introduction, are hooked up near the deposition chamber, however, these were not used in any experiments presented.

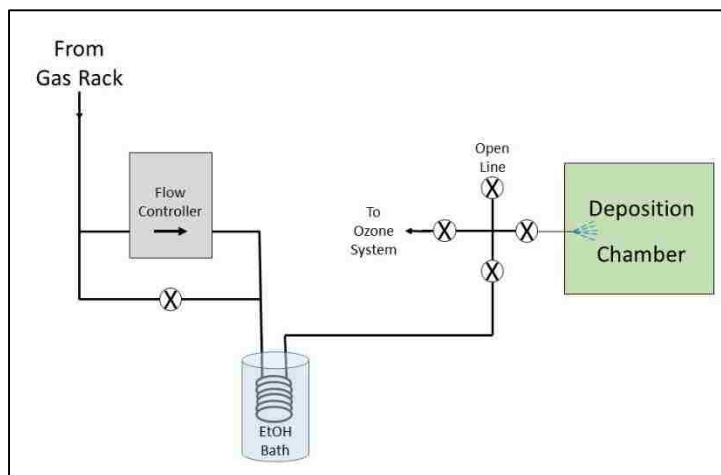


Figure 2.9 Matrix line used to introduce gas mixtures into the deposition region. The gas is sent from the gas to a mass flow controller which regulates the gas flow. The gas is dehydrated and purified by a liquid N₂, ethanol-bath before being introduced into the deposition region via a 1/16" tube.

An argon tank is devoted to both the magnetron sputter source and to the counter ion line. The magnetron line uses a mass flow controller capable of flow rates between 1-100 sccm (Alicat, MC-100sccm). The magnetron also has two other permanent lines for aggregation gases which are currently not in use. The counter-ion line uses a low flow controller capable of flow rates between 0.1-1sccm (Alicat, MC-1sccm) and can be easily switched to a number of gas cylinders for introduction of different cations.

2.4 Data collection and manipulation

Due to temperature-dependent absorptions from dilute impurities in the window material, it is necessary to not only take backgrounds with the window in the beam path but it must also be held at 10 K. A single-beam spectrum is taken by averaging 2500 scans with the window cold for resolutions of both 0.5 cm^{-1} and 0.125 cm^{-1} . The proper resolution background is then applied when taking data in absorption mode. Most scans at 0.5 cm^{-1} resolution require an average of 500 scans while 0.125 cm^{-1} resolution requires at least 1000 scans averaged due to the increase in noise. All FTIR data are initially taken through Omnic, Thermo Nicolet Corporation software and all post-data manipulations are done in Origin 8.0 software package. After being taken, it is necessary to correct the baseline which has a steep upward slope (Figure 2.10A). This slope is due to frequency-dependent scattering, presumably from polycrystalline domains in the matrix, as evidenced by a “foggy” appearance upon deposition (Figure 2.11). The baseline is corrected by applying a 9th-order polynomial fit (Figure 2.11B). Though a 9th-order fit is not strictly necessary, it is easily applied in Origin, does not affect any of the matrix peaks, and provides a baseline-corrected spectrum (Figure 2.10C).

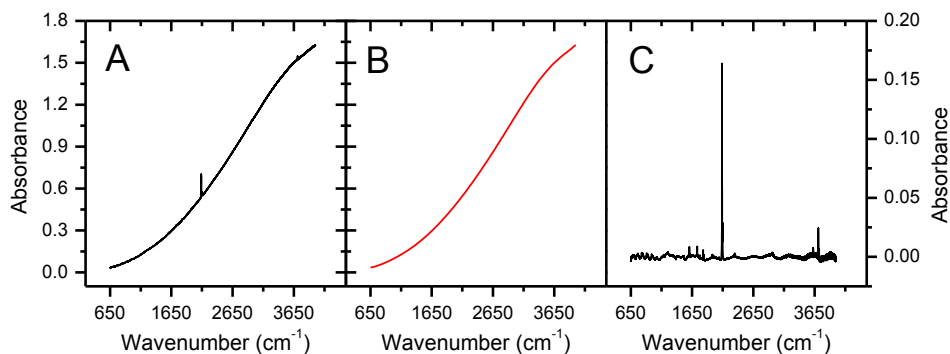


Figure 2.10 Baseline correction performed in Origin software: A) raw data is taken which contains an upward slope, B) a 9th-order polynomial is fit to the raw data, and C) the poly fit is subtracted from the raw data to give a baseline resolved spectrum.



Figure 2.11 Picture through Kodial glass viewport showing IR window after 4 hours of matrix deposition.

Another common problem is etaloning, which occurs when light reflects off two or more surfaces, causing interference between the multiple reflections and resulting in a standing-wave pattern. In matrix experiments, etaloning arises due to reflections off the deposition window as well as the thin matrix layer. The phase difference (δ) between two beams is dependent on a few factors, including the wavelength of light (λ), the angle of light through the material (θ), the thickness of the material (l), and the refractive index of the material (n) as seen by equation 2.1:

$$\delta = \left(\frac{2\pi}{\lambda}\right)2nl \cos \theta \quad (2.1)$$

By applying this equation to a 2-hour deposition, 10 sccm flow rate experiment and using the index of refraction of bulk argon (1.77^{114}), a matrix thickness of $\sim 60 \mu\text{m}$ is calculated. While useful for matrix thickness, etaloning can obscure data interpretation and makes

quantitative analysis very difficult. Furthermore, there are often several etaloning patterns that interfere with one another, causing drastic phase shifts as well as amplitude deviations making it challenging to subtract out of the data. To minimize etaloning a deposition window with a 0.5 degree wedge is used. Also, as more matrix is built up on the window, the etaloning increases in frequency and decreases in intensity, as seen in Figure 2.12. Because of this, four to six hour depositions are typically employed to minimize the need for post-collection manipulations. Finally, it is common to apply atmospheric suppression in Omnic, a quantitative model that reduces or removes the effects of water vapor and carbon dioxide on the collected spectra. Since backgrounds are infrequently collected, this takes care of minor atmospheric fluctuations from day to day.

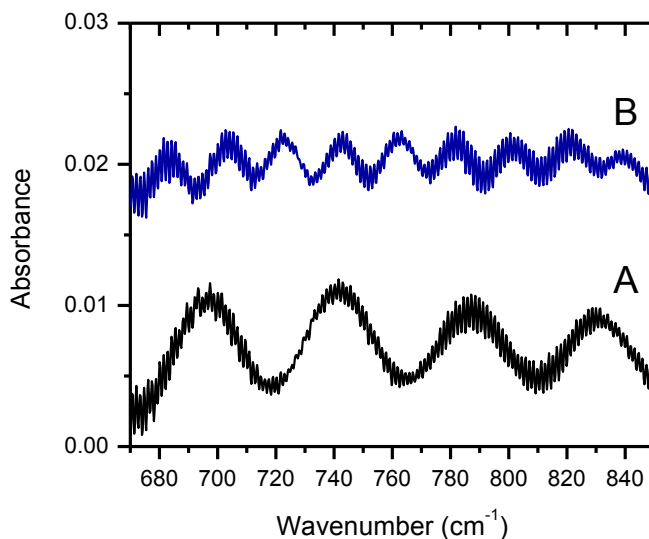


Figure 2.12 Argon only matrix deposited at 10 sccm, 20 K for: A) 2 hours, and B) 4 hours. As the matrix increases in thickness, the observed etaloning increases in frequency and decreases in amplitude.

2.5 Appendix

Table 2.1 Vacuum pump and gauge information

		Source Chamber	Quadrupole Chamber	Bender Chamber	Deposition Chamber
Turbo Pump	Make	Osaka	Osaka	Edwards	Osaka
	Model	TG1300 MCWB	TG900 MCAB	STP-A1303C	TG420 MCAB
	Speed	560 Hz	560 Hz	542 Hz	680 Hz
Backing Pump	Type	rotary vane	scroll*	scroll*	scroll*
	Make	Adixen	Edwards	Edwards	Edwards
	Model	ACP28	XDS 35i	XDS 35i	XDS 35i
Chamber Gauge	Type	compact full range	ion	ion	ion
	Make	Balzers	Lesker	Lesker	Lesker
	Model		G100K	G100K	G100K
Backing Gauge	Type	pirani	pirani	pirani	pirani
	Make	Lesker	Lesker	Lesker	Lesker
	Model	KJL-6000	KJL-6000	KJL-6000	KJL-6000
Baseline P		10^{-10} Torr	10^{-10} Torr	10^{-10} Torr	10^{-10} Torr
Operating P		10^{-4} Torr	10^{-5} Torr	10^{-5} Torr	10^{-5} Torr

* only one Edwards scroll pump is used to back all three chambers

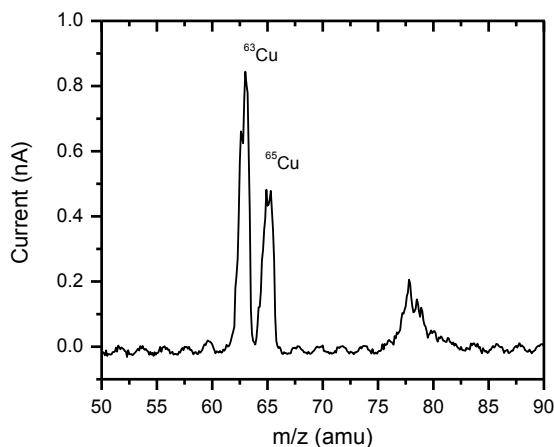


Figure 2.13 Baseline-resolved mass spectrum showing copper isotopes as well as a large contamination peak. This peak is likely due to Cu-O or Cu-H₂O which is slightly shifted from the calculated m/z due to improper spectrometer calibration.

Table 2.2 Typical parameters set on individual electronic optics for the deposition of copper, silver, and nickel anions

	Copper Anion	Silver Anion	Nickel Anion
Optic	bias (V)	bias (V)	bias (V)
nozzle	215	250	225
22 mm quad RF	76	98	76
22 mm quad DC	10	10	25
22 mm exit lens	0	0	0
prefilter	13	15	10
9 mm entrance lens	150	150	150
9 mm quad DC	30	17	30
9 mm exit lens	325	383	325
bender entrance lens	5	0	3
ionizer entrance	-10	-10	-10
bender inner pole	56	48	45
bender outer polder	-5	-5	-4
bender exit lens	0	0	0
bender top/bottom	60	60	60
octopole entrance lens	0	0	0
octopole RF	54	54	54
octopole DC	15	13	18
octopole exit lens	40	40	40
start mass	62	105	57
end mass	63	106	59

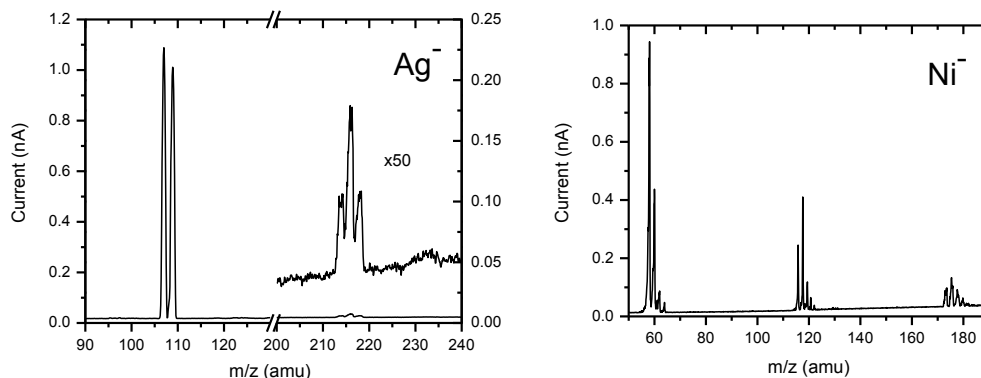


Figure 2.14 Silver and nickel high-resolution spectra. The silver anion is similar to copper in that single atoms are relatively easy to produce, but larger clusters are much more difficult. The nickel anion produced the most abundant dimer and trimer, both of which were easily baseline resolved.

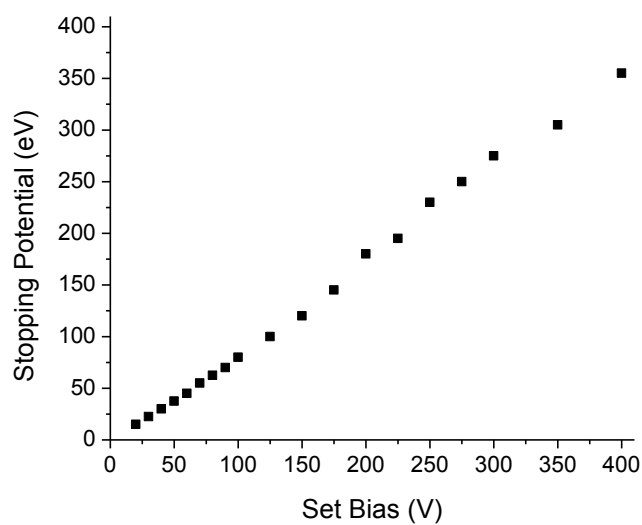


Figure 2.15 Measured stopping potentials for Ar^+ versus bias set on ionizer extraction plate. Measured cation energies vary nearly linearly with the applied bias.

Table 2.3 Natural isotopic abundances for copper, silver, and nickel

Symbol	Mole fraction
^{63}Cu	0.6915
^{65}Cu	0.3085
^{107}Ag	0.5184
^{109}Ag	0.4816
^{58}Ni	0.6808
^{60}Ni	0.2622
^{61}Ni	0.0114
^{62}Ni	0.0363
^{64}Ni	0.0093

Chapter 3

Formation of ionic complexes in cryogenic matrices:

A case study using co-deposition of Cu^- with rare gas cations in solid argon

Adapted with permission from Ludwig, R. M.; Moore, D. T. Formation of Ionic Complexes in Cryogenic Matrices: A Case Study using Co-Deposition of Cu^- with Rare Gas Cations in Solid Argon. *J. Chem. Phys.* **2013**, *139*, 1-9. Copyright 2013 AIP Publishing.

3.1 Abstract

Matrix-isolation spectra have been obtained for ionic species formed from a beam of mass-selected ions, with a coincident beam of externally generated counter-ions used to provide charge balance. Infrared spectra were obtained for copper-carbonyl complexes formed following deposition of Cu^- ions with rare-gas counter-cations into CO-doped argon matrices. Both anionic and neutral copper carbonyl complexes $\text{Cu}(\text{CO})_n^q$ ($n=1-3$; $q=0,-1$) were observed in the spectra, with peak positions corresponding to previously reported assignments; new partially resolved bands appearing in the range $1830-1845\text{ cm}^{-1}$ are assigned to larger $[\text{Cu}(\text{CO})_3 \cdot (\text{CO})_n]^-$ aggregates, having additional CO ligands in the second solvation shell. The experimental geometry ensures that all Cu^- centers initially arrive at the matrix as anions, so the relative abundance of anionic relative to neutral complexes is much higher than in previous studies employing alternative methods for ion deposition; this approach allows for monitoring of electron-transfer processes between anions and cations in the matrix. Comparison of time-dependent vs. temperature-dependent trends reveal two distinct mechanisms by which the population of anionic complexes is converted into neutral complexes: short-range electron transfer between a cation-anion pair following diffusion, and long-range electron transfer involving photodetachment of an electron from the anion into the conduction band of solid argon,

resulting in eventual recombination of the electron with a cation in a remote matrix site. The spectra also show a marked dependence on the deposition temperature and dopant concentration, in that 100-fold higher CO concentrations were required during deposition with the sample window at 10 K compared to that used at 20 K, in order to obtain a similar distribution of copper carbonyl complexes. Furthermore, although no carbonyl complexes are observed initially when low concentrations of CO are used at 10 K, upon warming the matrix to 15 K, the neutral di- and tricarbonyl peaks appear abruptly, which is attributed to energy released upon short-range recombination of Cu^- ions with cations.

3.2 Introduction

This chapter describes preliminary results on the system taken to test the new deposition method. The copper-carbonyl system was chosen for the first trials because it is well-studied in the literature, relatively easy to produce ions, and has strong oscillator strength in the infrared region. Due to a few initial failed FTIR attempts, UV-Vis spectroscopy was employed due to its higher sensitivity, which yielded the first matrix results. These trials are compared to the work of Ozin, who studied the absorption of the copper atom and dimer in argon, krypton, and xenon.¹¹⁵ The studies in this chapter focus on the $(4p)^2P \leftarrow (4s)^2S$ absorption in argon.

After the success of UV-Vis studies, FTIR was again employed. The neutral copper species were studied in the 1970s by Ozin through the use of a Knudsen cell at high metal concentrations.¹¹⁶ More recently, Andrews used laser ablation to observe the anionic and neutral copper mono-, di-, and tricarbonyl complexes, as well as the cationic monocarbonyl in argon,⁸⁸ and this study set the stage for experiments done on our new system. Though similarities exist, many improvements have been made in developing the codeposition

method. Namely, no cationic copper complexes exist, and there are roughly equal amounts of anionic and neutral complexes. In addition to demonstrating the viability and utility of this technique, the spectra also revealed insights into the formation and neutralization of the anionic copper carbonyls.

3.3 Experimental

The data in this chapter contain some of our first experiments carried out with the counter-ion method, and as such, some of the experimental details are different than what follows in subsequent chapters. Only differences from standard procedures and details directly affecting the experiments of this chapter are presented. For complete experimental details, see Chapter 2.

All matrix samples were prepared as follows, except where otherwise noted: 8-10 nA each of Cu^- and counter cations (Ar^+ or Kr^+) were co-deposited with Ar matrix gas doped with 0.02-2% CO, for 2 hours (54 mmol total gas exposure) at the specified deposition temperature (10 or 20 K). All spectra were recorded with the sample held at 10 K; annealing steps involved warming for 30 minutes to the specified temperature, then re-cooling to 10 K to take the spectrum. The spectra have been processed in software to remove etalon fringes due to the thin layer of the matrix.

Flow rate was controlled by maintaining a steady backing pressure behind a needle valve. The needle valve was adjusted so that pressure in the deposition chamber was maintained at a steady-state value of $\sim 3 \cdot 10^{-5}$ Torr, although fluctuations were inevitable since the gas rack was constantly depressurizing. Also unless explicitly stated, the matrix gas was not purified through an ethanol bath and metal carbonyl species, formed in the mixing bottles and gas lines, were deposited in many samples (see Results section and

Table 2.2). At every 15-20 minutes, deposition would be stopped and a short survey scan was taken. After deposition, different heights and rotations of the window were scanned in order to find the best area of the window for overlapping the IR beam with the highest concentration of deposited species.

For UV-Vis spectra, most lab lights were turned off in order to reduce the ambient light that reached the spectrometer. Both a “dark” spectrum (I_{dark}), taken by blocking the entrance of the spectrometer, and a background scan (I_{ref}), taken through the KBr window before any matrix was deposited, were collected. The incident light (I_0) was then calculated from $I_{\text{ref}} - I_{\text{dark}}$ and radiation coming from the sample (I) from $I_{\text{sample}} - I_{\text{dark}}$. Absorbance spectra could then be generated by plotting $-\log I/I_0$ versus wavelength. All UV-Vis scans were taken by averaging 500 scans at 0.5 s intervals. All samples were deposited at 20 K for a total of 60-90 minutes. Annealing was performed in 2 K steps by holding the sample at the set temperature for 5 minutes then cooling back to 10 K to take the spectrum.

3.4 Results

3.4.1 UV-Vis spectroscopy

These experiments depend on building up a sufficient density of ions in the matrix to enable absorption spectroscopy experiments. Initially, the more sensitive UV-vis spectroscopy was employed to verify the presence of copper species in the matrix. The first successful UV-Vis experiment of a neutral copper atom spectrum was performed by Nathan Roehr, a graduate student from Dr. Polfer’s group at the University of Florida. Soon after, I repeated these results and my data are presented in this chapter.

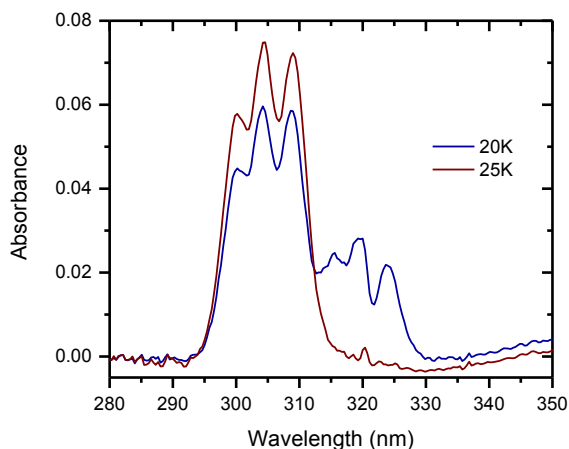


Figure 3.1. UV spectra of anionic copper monomer balanced by krypton cation deposited in a 20 K argon matrix for one hour. After deposition (blue) bands associated with neutral copper monomer are seen for both stable (300.2 nm, 304.6 nm, 309.0 nm) and secondary trapping sites (315.6 nm, 319.6 nm, 323.7 nm). Upon annealing to 25 K for 30 min (red), thermally unstable bands are irreversibly converted to the stable bands. Both spectra are taken at 10 K.

Figure 3.1 shows spectra obtained after co-depositing Cu^- and Kr^+ (~ 3 nA of each) with Ar matrix gas (~ 27 mmol/hr) at 20 K for 2 hours. The triplet of peaks at 299.8, 304.2 and 308.3 nm correspond closely with those assigned to neutral Cu atoms in an Ar matrix.¹¹⁵ Originally, this triplet was thought to arise by a simple symmetry breaking;^{117,118} however, it was later explained by Vala as the existence of simultaneous spin-orbit interaction in the Cu excited ^2P state to a Jahn-Teller distortion of the matrix cavity.¹¹⁹ The weaker triplet of peaks at 316.0, 319.3 and 323.7 nm is gone after annealing the matrix to 25 K (with concomitant increase of the intensity of the other bands) and does not reappear. This peak loss is consistent with the previous assignment of two of these bands (the band at 316.0 nm was not resolved in the previous study) to neutral Cu atoms kinetically trapped in a thermally unstable site.¹¹⁵ Similar results were obtained when Ar^+ was used as a counter-ion, though the band intensities were lower after the same deposition interval.

Experiments employing deposition at lower temperatures were also attempted, however the scattering background increased drastically even at 15 K, so that no absorption bands could be observed. We believe this was due to a higher degree of polycrystallinity in the matrices at the lower temperatures, as well as the higher propensity for scattering of the shorter wavelength UV light.

No direct spectroscopic evidence was obtained that indicate the presence of copper anions in the matrix; this absence is likely because the photodetachment threshold for Cu^- is in the near-IR ($\sim 1000 \text{ nm}$ ¹²⁰). Nonetheless, the source of the neutral atoms in the matrix must be the beam of copper anions because the sputtering source is over 2 m away from the cryostat, and the quadrupole bender insures that there is no line-of-sight pathway from the source to the sample window. The mechanism for neutralization of the Cu^- to neutral atoms is unclear from these data, however, it seems likely that it is either from photodetachment by photons from the UV-vis source (or ambient light), or from direct charge transfer with the counter-cations, either in the matrix or in the gas phase. These possibilities are explored further in the discussion section.

3.4.2 FTIR spectroscopy

The spectrum of the CO stretching region for a sample deposited at 20 K with a 0.02% mix and Kr^+ counter-ion is shown in Figure 3.2, along with spectra following annealing to 25, 30, 35 and 40 K; a krypton overlayer (27 mmol) was deposited over the matrix to inhibit sublimation at the higher temperatures. The spectra obtained here are somewhat reminiscent of the spectra of neutral and anionic copper carbonyls reported in the literature;^{88,116} a complete listing of the observed bands and their assignments is given in Table 3.1. Most of the major bands observed in the current study correspond closely

with those observed in previous work, however there are some significant differences that can be attributed to the different deposition method employed here, as discussed below. Specifically, it is clear from Figure 3.2 that the annealing steps lead to a net loss of intensity from the bands assigned to anionic species, with a concomitant increase of the bands assigned to neutral species. This “neutralization” phenomenon is different from what was observed in previous studies upon annealing, and is analyzed in detail below.

Table 3.1 Vibrational band positions (in cm^{-1}) for $\text{Cu}(\text{CO})_n^q$ [$n=1,2,3$; $q=-1,0$] species in argon matrices

Assignment	Deposition temp.		Ref. ^a	Assignment	Deposition temp.		Ref. ^a
	10 K	20 K			10 K	20 K	
$\text{Cu}(\text{CO})^-$	1733.7	1733.5	b	$\text{Cu}(\text{CO})$	2008.0 2010.2	2007.8 2010	b,c b,c
$\text{Cu}(\text{CO})_2^-$	1774.7 1780.9	— 1780.7	— b	$\text{Cu}(\text{CO})_2$	1891.3 (1876) ^d	1890 —	b,c b,c
$\text{Cu}(\text{CO})_3^-$	1823.6 — 1829.9	1823.4 1825.1 1829.9	— — b	$\text{Cu}(\text{CO})_3$	1975.7 — 1981.4 ^e —	1975.5 1977.4 — 1981.8	b,c — — —
$[\text{Cu}(\text{CO})_3 \cdot (\text{CO})_n]^-$	— — — — —	1832.6 1833.8 1835 1838.1 1843	— — — — —		1983.4 ^e 1985.5	1983.2 1985.9	b b,c

a) All references report peak positions within $\pm 0.3 \text{ cm}^{-1}$ of table values. b) ref. 88
c) ref. 116 d) additional site peaks were reported in refs, but not seen in this study
e) peak only observed on annealing above 20 K

The presence of bands corresponding to anionic species in our spectra provides direct experimental evidence that the explicit co-deposition of a controlled counter-ion flux does indeed allow matrix isolation of ionic species with number densities sufficient for infrared spectroscopic experiments. Control experiments carried out with the same Cu^- beam current but without counter-ions showed no evidence of any copper species

(Figure 3.6, Appendix), confirming that it is the cation beam that is acting to provide the necessary charge-balance. Although neutral complexes are also observed upon deposition, they must be the result of some secondary neutralization process occurring during matrix formation.

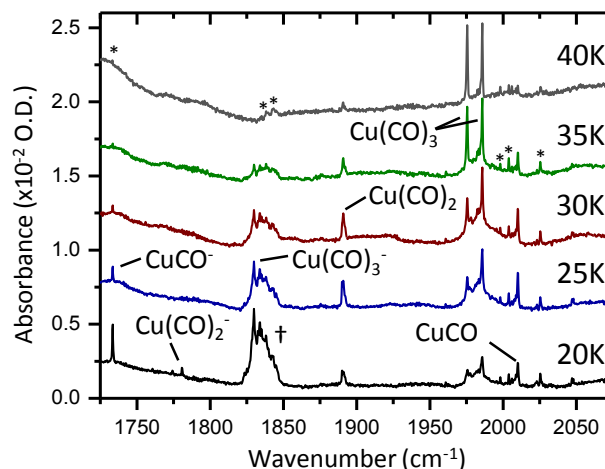


Figure 3.2. FTIR spectra obtained using co-deposition of Cu^- and Kr^+ ion-beams (8 nA each) for two hours with 0.02% CO in argon at 20 K, with subsequent annealing steps; all spectra recorded at 10 K. Broad feature marked with \dagger assigned to $[\text{Cu(CO)}_3 \cdot (\text{CO})_n]^-$ species. Peaks marked with * are assigned to metal-carbonyl impurities.

3.4.3 Peak assignments

The peaks at 1733.7, 1780.9 and 1829.9 cm^{-1} are assigned to the anionic mono-, di- and tri-carbonyl complexes, respectively, based on previous work reported by the Andrews group.⁸⁸ The relative intensities of these bands at 20 K are also generally consistent with the earlier study, including the curiously low intensity for the Cu(CO)_2^- species. However, the current spectra also contain several incompletely resolved bands (Table 3.1) extending to the high frequency side of the Cu(CO)_3^- peak, that were not observed in the previous argon matrix experiments (which employed deposition at 10 K). Although these bands are incompletely resolved (Figure 3.7, Appendix), their positions are reproducible from

experiment to experiment. Given the higher deposition temperature used here, which allows for more diffusion of small dopants prior to “freezing” of the matrix, it seems most reasonable to assign these additional features to larger $\text{Cu}(\text{CO})_3 \cdot (\text{CO})_n^-$ complexes, where the additional CO ligands beyond three are more weakly associated in a second coordination sphere, and thus only cause a small shift of the vibrational frequency. We note that analogous bands to these were observed (although not assigned) by the Andrews group after annealing to 8 K in neon matrices, lending credence to the notion that they arise from larger aggregates.⁸⁸ Furthermore, although the $\text{Cu}(\text{CO})_3^-$ complex has planar D_{3h} symmetry,⁸⁸ and thus is not sterically hindered from having additional ligands directly coordinated to the copper center, it is already an 18-electron coordination complex, and therefore further ligands would be expected to exist in a second solvation shell, consistent with the proposed assignment here.

As mentioned above, several bands corresponding to neutral copper carbonyl complexes are also observed upon deposition at 20 K (Figure 3.2): a doublet at 2008.0 and 2010.2 cm^{-1} for CuCO , a broad peak centered at 1891.3 cm^{-1} for $\text{Cu}(\text{CO})_2$, and a pair of peaks at 1975.7 and 1985.5 cm^{-1} for $\text{Cu}(\text{CO})_3$, all appearing within 0.3 cm^{-1} of their positions in previous studies employing both laser-ablation,⁸⁸ and Knudsen-type evaporation sources.¹¹⁶ It is interesting to note that in the current study, the relative intensities of the neutral and anionic bands are quite comparable, while in the laser-ablation work of the Andrews group, the neutral bands were several orders of magnitude more intense than the anionic peaks.⁸⁸ This is because while the laser-ablation method produces large fluxes of neutral species with relatively small amounts of ions,⁸⁵ in the co-deposition method employed in the current experiments the total copper flux is limited to the beam

current of Cu^- , so that any neutral species must be formed by secondary electron-transfer processes. Indeed, one of the advantages of counter-ion co-deposition is that it can provide insight into the possible neutralization mechanisms, as discussed below. All remaining bands in the spectra shown in Figure 3.2 arise from small amounts of transition metal carbonyls formed in the CO storage bottle; a table of the observed impurity transitions is given in the Appendix, Table 3.2.

3.4.4 CO concentration dependence

Figure 3.3 shows spectra taken with CO concentrations of 0.02%, 0.1% and 0.5% in Ar using ~ 10 nA of Cu^- balanced by Ar^+ counter-ions, deposited at 20 K for 2 hours (54 mmol total gas exposure); spectra taken following annealing to 30 K are also shown for each concentration. The first thing to note is the similarity of the spectra for 0.02% CO deposited at 20K with Ar^+ counter-ions (Fig. 3A), and the analogous spectrum taken using Kr^+ counter-ions (Fig. 3.2). The positions and relative intensities of all of the anionic and neutral copper carbonyl bands are practically identical (Figure 3.7, Appendix); even the partially resolved bands assigned to $\text{Cu}(\text{CO})_3 \cdot (\text{CO})_n^-$ are reproduced quite closely (Figure 3.8, Appendix).

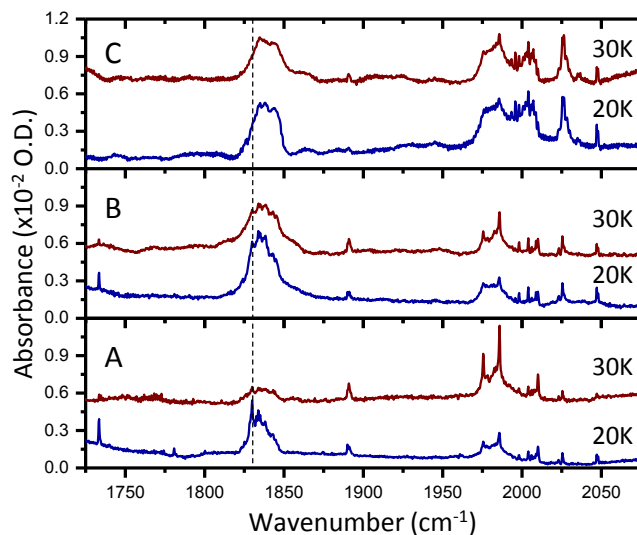


Figure 3.3 CO concentration dependence on copper carbonyl formation for varying CO concentrations: A) 0.02%, B) 0.1%, and C) 0.5%. Samples were deposited at 20 K for 2 hours with ~ 10 nA Cu^- balanced by Ar^+ ; all spectra recorded at 10 K.

Several interesting CO concentration-dependent trends are revealed in the spectra in Figure 3.3. The most obvious one is that the average coordination number of the complexes increases with CO concentration. In the anion region, bands for the mono-, di- and tricarbonyl complexes diminish monotonically with increasing CO concentration, while the bands assigned to $\text{Cu}(\text{CO})_3 \cdot (\text{CO})_n^-$ aggregates grow in, becoming more intense than the tricarbonyl peak in the 0.1% CO spectrum (Fig. 3.3B), and completely dominating the anion region of the spectrum at 0.5% CO (Fig. 3.3C). In the neutral manifold, the trends are similar but less pronounced; the dicarbonyl band persists even at the highest concentration, and the broad band grows in underneath the neutral tricarbonyl doublet between 1975 and 1985 cm^{-1} .

Another striking feature of these spectra is that the total intensity of the anionic and neutral copper carbonyl bands stays approximately constant across the 25-fold

concentration range explored. This result contrasts with the behavior of the impurity bands, e.g. the $\text{Fe}(\text{CO})_5$ peak at 2025 cm^{-1} , which show a linear increase in intensity with CO concentration. This confirms that copper is the limiting reagent in the formation of these clusters, and also indicates that essentially every Cu atom or ion has at least one CO molecule coordinated to it, even at the 0.02% concentration level. Finally, the spectra taken after 30K annealing for each concentration show the same general “neutralization” trend (diminishing anion bands with growth of neutral bands) as observed for the data in Figure 3.2, however the overall effect seems more muted as the CO concentration is increased.

3.4.5 Dependence on deposition temperature

Figures 3.4A and B show spectra recorded following 10 K deposition of 0.1% and 2% mixtures of CO in argon with Kr^+ counter-ions, respectively, including spectra obtained following annealing steps at 15, 20, and 25 K. It is immediately obvious that there is a drastic qualitative difference between the 0.1% sample deposited at 10 K vs 20 K (Figure 3.3B). After 10 K deposition, there are no bands whatsoever corresponding to anionic or neutral copper carbonyl complexes evident in the spectrum (all bands arise from impurities). Upon annealing however, bands for the neutral di- and tricarbonyl complexes appear abruptly, growing in intensity as the annealing temperature is increased from 15 to 25 K. There is no sign of anionic complexes, nor is the neutral monocarbonyl complex observed (though that region is overlapped by an impurity band, possibly concealing a weak absorption). The implication is that the copper is trapped as free Cu^- ions at 10 K, only forming complexes upon annealing to 15 K, with neutralization of the copper centers occurring either before or during the complexation process.

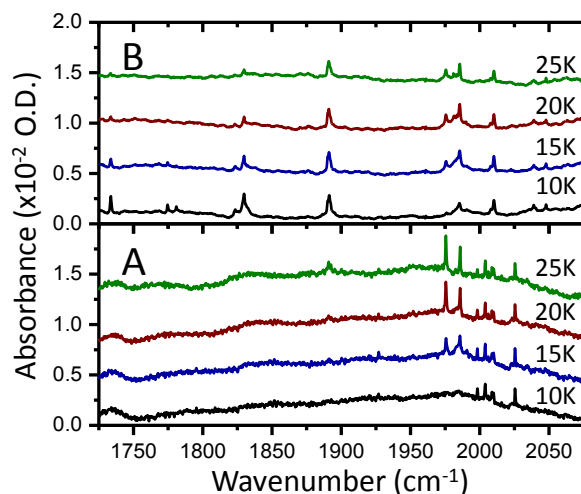


Figure 3.4 FTIR spectra obtained following 2 hours of co-deposition of Cu⁻ and Ar⁺ at 10 K with: A) 0.1% CO in argon, ~7 nA Cu⁻ & Ar⁺ and B) 2% CO in argon, ~3 nA Cu⁻ & Ar⁺; spectra for subsequent annealing steps are also shown. All spectra recorded at 10 K.

On the other hand, when the more CO rich 2% mixture is used for 10 K deposition (Figure 3.4B), the bands for the anionic and neutral mono-, di- and tricarbonyl complexes are clearly evident in the spectrum. In fact, the results are qualitatively similar to those measured following deposition of the 100-fold more dilute 0.02% CO mixture at 20 K (Figure 3.3A), except that the bands for the larger Cu(CO)₃•(CO)_n⁻ aggregates are missing, and the linewidths of the peaks are noticeably broader. All of these trends –the requirement of higher CO concentration to observe complexation, absence of larger clusters, and broader lines– are consistent with a much faster “freezing out” of the dopants during the matrix formation process at 10 K as compared to 20 K, as is discussed in detail below.

Although the spectra in Fig 3.4B are qualitatively similar to those in Figure 3.2, there are some small but significant differences. First, there is a slight but consistent and reproducible blue-shifting of most of the peaks by 0.2-0.3 cm⁻¹ in the 10 K spectrum (Table 3.1), with the exceptions being the Cu(CO)₃⁻ peak (not shifted) and the Cu(CO)₃

peak at 1985.5 cm^{-1} (redshifted by 0.4 cm^{-1} from 20 K spectrum). Additionally, there are new bands at 1774 cm^{-1} and 1824 cm^{-1} , which are tentatively assigned (based on proximity) to di- and tricarbonyl complexes trapped in different matrix sites at the lower deposition temperature. There are also partially resolved features at 1981.4 and 1983.4 cm^{-1} that grow in upon annealing to 20 K; although there is intensity in the corresponding region of the 20 K deposition spectrum (Figure 3.2), it is harder to identify individual bands. Note also that most of the impurity bands are absent from the spectra in Fig. 3.4B; the deposition gas for this sample was run through a liquid nitrogen/ethanol bath, in order to remove the metal carbonyl contaminants. The only remaining peaks in the region where impurities were observed are at 2039 cm^{-1} , which is from $^{13}\text{C}^{18}\text{O}$ (observable in this high-concentration CO mix at natural abundance), and at 2048 cm^{-1} , which is now assigned by our group to $(\text{CO})_2^+$. (Note: at time of publication the 2048 cm^{-1} assignment was not known. For spectroscopic details of this peak identification, see Chapter 6.)

3.4.6 Time-dependent vs. temperature-dependent neutralization

Figure 3.5A shows difference spectra for the data in Figure 3.2 (0.02% CO in argon deposited at 20 K with Kr^+ counter-ions), where each trace represents sequential changes in the spectra between “adjacent” scans taken after annealing at temperatures differing by 5 K; labels refer to the upper member of temperature pair (e.g. 25 K – 20 K difference spectrum is labeled 25 K). The principal effect upon annealing the sample to 25 K was a loss of intensity in all of the anionic bands, with a concomitant growth of the neutral bands. This effect is in contrast to the previous laser-ablation study, where annealing resulted in cluster growth of the anionic species, without an overall loss of intensity from the corresponding bands.⁸⁸ At higher annealing temperatures, the anionic bands continue to

decrease monotonically as the temperature is increased, with the larger clusters persisting the longest. However for the neutral complexes, only the tricarbonyl shows a consistently increasing trend up to 40 K; the mono- and dicarbonyl peaks start decreasing above 30 K, indicating complexation of additional CO ligands via diffusion of free CO molecules, to the extent that at 40 K virtually all of the intensity is in the doublet of peaks assigned to $\text{Cu}(\text{CO})_3$.

To address the question of whether the annealing is really required to observe neutralization, a time-lapse study was performed while maintaining the sample at 10 K, starting with a 0.02% CO in argon matrix (~ 7 nA each Cu^- and Ar^+) deposited at 20 K, yielding the results shown in Fig 3.5B (unsubtracted spectra shown in Figure 3.9, Appendix). Even though this sample was not heated, the spectra still show a clear depletion of the anionic peaks with concomitant growth of the corresponding neutral peaks over the 8 hour time-span investigated (which is approximately equal to the total time for all annealing experiments). Furthermore, the correlation of anion depletion to neutral growth seems more straightforward than for the annealing data; all anionic peaks show only depletion, and all neutral peaks show only growth. Even more striking is the tight correlation between the anionic and neutral peaks with a given stoichiometry: peaks for both dicarbonyl complexes disappear after 4 hours, and peaks for both monocarbonyls disappear after 6 hours. This suggests that whatever “time-dependent” neutralization process occurs is rather mild, such that it preserves the coordination number of the complexes during electron transfer.

Note that the partially resolved bands assigned to larger $\text{Cu}(\text{CO})_3 \cdot (\text{CO})_n^-$ aggregates show a clear decreasing trend in Fig. 3.5A and 3.5B, confirming their assignment to anionic

species. The trend in Fig. 3.5B seems to indicate that their neutral counterparts contribute to the broad absorption between 1975 and 1985 cm^{-1} , however the correlation is not as clear as it is for the mono-, di- and tricarbonyl species. This can be contrasted with the behavior of the sharp feature at 1975 cm^{-1} , which grows in with increasing temperature in the annealing series, but is not evident in the time-dependent series at 10 K, suggesting that there are (at least) two distinct processes contributing to the spectral changes observed upon annealing, as discussed below.

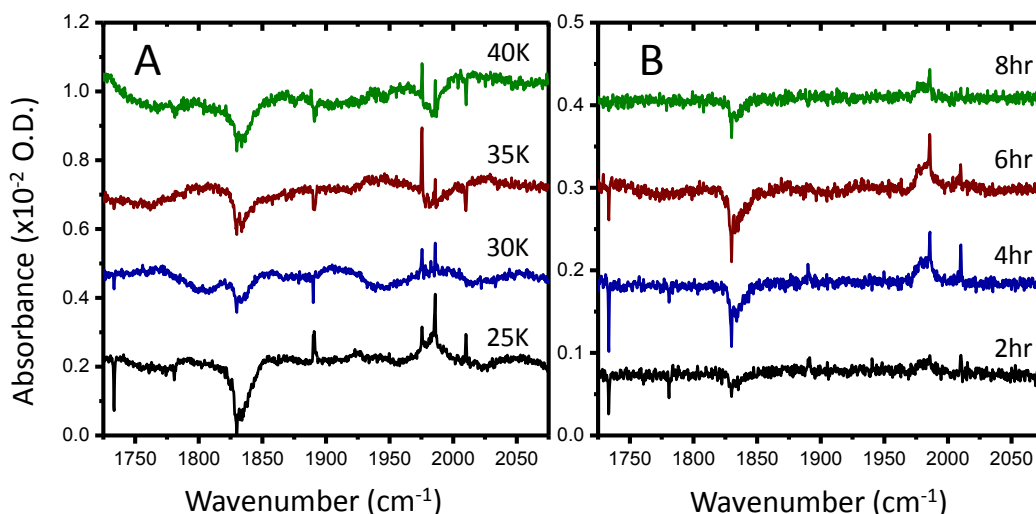


Figure 3.5 Difference spectra emphasizing changes during A) 5 K annealing steps for data shown in Figure 3.2, and B) time-dependent neutralization of a similarly prepared sample maintained at 10 K.

3.5 Discussion

The results obtained here demonstrate the feasibility of using a counter-ion beam to provide charge balance during matrix deposition of mass-selected ions, in order to accumulate sufficient number densities of ionic species for infrared absorbance

spectroscopy after only two hours of deposition. As mentioned in Chapter 1, previous, unsuccessful attempts to achieve this had been reported in the literature, even though much longer deposition times and more sensitive detection methods were employed.¹⁰⁸ Using the ion beam currents and the physical dimensions of the matrix, we can estimate the number density of ions in the matrix, assuming unity probability of ion trapping in a homogeneous matrix. Deposition at 10 nA for 2 hours corresponds to delivery of 4.6×10^{14} each of cations and anions; based on the etalon peaks in the infrared spectra (Figure 3.10, Appendix) the matrix thickness is estimated to be 60 μm , assuming this is uniform over the deposition area of 3.1 cm^2 yields a matrix volume of 0.018 cm^3 , corresponding to a number density of $\sim 2.5 \times 10^{16}$ ions/ cm^3 each for cations and anions. Using the bulk density of solid argon (~ 1.77 g/cm^3 at 20 K),¹¹⁴ this converts to a molar $\text{Cu}^+:\text{Ar}$ ratio of $\sim 1:10^6$, representing an upper limit for the ion concentration in the matrices presented here. Of course the actual ion abundance is likely significantly lower in practice, given expected losses due to phenomena such as “grounding out” of ions on the sample holder, as well as scattering in local high pressure of the deposition region. The spectra presented above also reveal significant populations of neutral species upon deposition, indicating that many of the ions undergo neutralization as the matrix is forming; possible electron transfer mechanisms underlying the neutralization are discussed below.

We believe that the success of the current efforts may be attributed to various features of the experimental design that are distinct from those reported in the earlier attempt by the Allison group.¹⁰⁸ Perhaps most significant is the use of an octopole ion-guide to transport the ions to the deposition window, ensuring that they travel on stable, non-divergent trajectories until they are within a few cm of the target, and minimizing the

field-free distance that must be traversed. Similarly, the use of the quadrupole bender to combine the cation and anion beams ensures that they travel along a common path, and it is assumed that this helps to produce a fairly homogeneous spatial distribution of ions in the deposition region, though this has not yet been measured explicitly. It must be noted that the choice to combine the ion beams necessitated the use of significantly higher energy for the cation beam (~60 eV) relative to the anion beam (~10 eV), in order to balance the current while maintaining a high anion flux. The anion energy is comparable to the 6-8 eV used for both ion beams in the earlier study;¹⁰⁸ it is not yet clear why such asymmetry in the ion beam energies might facilitate stabilization of high number-densities of ions in the matrix, but it cannot be ruled out as a potential contributing factor. Another potentially relevant point is that the matrix gas flow rates used here (~27 mmol/hour) are at least 10 times higher than those typically employed in matrix isolation studies,³³ and may be up to 50 times higher than what was used in the Allison study.^{108,121} The potential significance of the higher flow rate is that it likely leads to a lower probability of cation-anion “recombination” during deposition because it results in a lower ratio of ions to matrix atoms, and also a higher local gas pressure near the matrix surface, which in turn affords a more gradual slowing of the ions in the matrix region. Finally, the choice of metal carbonyls as the species of interest may have enhanced the detection efficiencies in the current work, owing to the high oscillator strengths of the molecular vibrations.

It must also be pointed out that the goal of the current work was somewhat different from that of the earlier Allison study, in that the aim here was to measure spectra of anionic complexes formed during the matrix deposition process, rather than to deposit and detect the specific ions produced in the external source. Indeed, as discussed below, the spectra

obtained here reveal information about other physical phenomena, such as the formation of the complexes, and electron-transfer processes leading to neutralization of ions, and allow some inferences to be drawn about the nature of the cations present in the matrix.

3.5.1 Complex formation

It has long been understood that a cryogenic matrix being formed via condensation of room temperature gas in a vacuum chamber will necessarily have a transient “surface region” that is warmer than the nominal sample temperature, and thus where fast diffusion of dopant species can occur.²⁸ For example, such a surface layer has been implicated to rationalize the aggregation of metal cluster carbonyls produced in argon matrices, which were much larger than could be explained by simple statistical models.^{49,122} The results of the current study are also consistent with this general picture of complex formation in matrices, and further provide insight into how the experimental parameters are correlated with average cluster size.

The picture of the complex formation process is as follows: first, the gas phase species (CO, Cu⁻, and counter-ions) are initially trapped in the surface region of the matrix where fast diffusion is occurring, so there is a reasonable probability of collisions between the very low concentration ions and the CO dopant molecules. Given that the calculated binding energies of CO ligands in anionic copper carbonyls are at least 2.5 kcal/mol,⁸⁸ and that the temperature in the surface region will be < ~80 K (the condensation point of liquid Ar), the complex formation will occur exclusively under kinetic control. Each ion-CO collision has a near-unity probability of increasing the coordination number of the copper centers, and dissociation of CO ligands from complexes already formed should not occur to any significant extent. This qualitative model is similar to the “quenched reaction”

mechanism that was found to best explain the experimental results for aggregation of metal cluster carbonyls in a previous study.⁴⁹ Note that collisions between anionic and cationic species resulting in neutralization via electron transfer are much less likely than ion-CO collisions due to the very low number densities of ions, and are assumed not to occur to any significant extent during the steady-state lifetime of the fluid layer (see section on neutralization below).

It is now straightforward to rationalize the differences between the spectra for deposition at 10 and 20 K in terms of the relative steady-state lifetimes of the surface layers in those cases. At 20 K, the dopants experience fast diffusion for a sufficiently long time that each copper ion experiences (on average) multiple collisions with CO ligands, resulting in a population of anionic copper carbonyls that is reflective of the relative CO concentration in the matrix gas (Figure 3.3). At the highest CO concentration (0.5%) at 20 K, only unresolved bands for the $\text{Cu}(\text{CO})_3 \cdot (\text{CO})_n^-$ aggregates persist at 20 K. At the other extreme, low (0.1%) CO concentration at 10 K, no copper carbonyl bands whatsoever were observed upon deposition. This reflects the much shorter steady-state lifetime of the surface layer, which does not allow for even a single collision between Cu^- and CO prior to “freezing out” of the dopant species. Only after increasing the CO concentration 20-fold to 2% are copper carbonyl complexes observed. Even so, the average coordination number of the complexes in this spectrum is lower than observed with 100-fold lower CO concentration at 20 K (compare Figures 3.4B and 3.2), and the anionic clusters with a second solvation shell of CO are not observed at all at 10 K.

So, it is clear that adjusting the dopant concentration and deposition temperature appropriately in these ion co-deposition experiments affords coarse control over the

complex formation process. At low temperature and low concentration, the average number of ion-dopant collisions is zero, such that free ions and CO ligands are trapped in the matrix. Higher deposition temperatures and dopant concentrations allow formation of progressively larger clusters, up to the point where the first coordination sphere is saturated and ligands are being added to the second solvation shell.

3.5.2 Neutralization

As mentioned above, the mass- and charge-selection enforced by the experimental setup ensures that all copper species must initially arrive at the deposition region as monatomic anions. Nonetheless, neutral copper complexes are observed both immediately after deposition, and later as a result of population transfer from the anionic bands. Mechanisms for neutralization of cations by electron transfer in cryogenic matrices have been studied by the Harbich group;¹²³ we draw upon their work to identify two distinct modes of electron transfer in the matrix samples studied here: “short-range” transfer between anions and cations that have diffused to proximate sites in the matrix, and “long-range” transfer occurring when electrons are photodetached from the anion into the conduction band of solid argon (~ 0.3 eV above the vacuum level,⁵²), whereupon they travel relatively long distances through the matrix to recombine with stationary cations. These recombination events are highly exothermic, each releasing >11 eV of energy, a portion of which goes into transient heating of the local matrix environment; it is this last phenomenon that provides the key to distinguishing the short- and long-range neutralization modes, since the local release of energy enables diffusion of free CO molecules. For the short-range case, the cations are necessarily close to copper centers, so the spectrum will reflect the increases in coordination number due to the attachment of

“transiently mobilized” CO ligands. Conversely, in the long-range case, the anionic copper species and the cation start much farther apart (recall the average ion:Ar ratio is only $\sim 1:10^6$), so the local heating around the cation center is unlikely to result in any changes in coordination number of the copper centers.

The clearest example of neutralization occurring via short-range electron transfer is upon annealing the low CO-concentration sample deposited at 10 K (Figure 3.4A). No copper carbonyl bands whatsoever were observed upon deposition, but after the 15 K annealing step the bands for the neutral tricarbonyl suddenly grew in, reflecting a change in coordination number from 0 to 3. Recall that in this case, we expect that most of the Cu^- centers are trapped as free ions upon deposition. The observed behavior on annealing is thus consistent with these centers diffusing under coulombic attraction until they can undergo short-range charge-exchange with a nearby cationic center. The precedent for diffusion of the Cu^- centers at 10-15 K is established by early work with alkali atoms, which do diffuse through argon matrices at these temperatures.⁷⁶ Note also that the doublet of peaks at 1975 and 1985 cm^{-1} in the 15 K spectrum is sharp and baseline-resolved, quite unlike their appearance in the analogous 15 K spectrum for the 2% CO mix (Figure 3.4B), but much more closely resembling the doublet after annealing the 0.02% 20K-deposition sample above 35 K (Figure 3.2), consistent with the proposed local-heating interpretation.

The best example supporting the long-range electron transfer picture is the time-dependent series of spectra (Fig. 3.5B) taken while holding the matrix sample at 10 K, at which temperature little or no diffusion through the solid matrix is expected.³³ These data show a very tight correlation between the disappearance of the anion bands and the growth of the neutral bands with no apparent changes in the corresponding coordination numbers.

Photodetachment from anionic copper carbonyl complexes upon irradiation with broadband visible light has been observed previously;⁸⁸ in our experiments the photon source is the constant, though diffuse, illumination of the sample region by visible radiation from the laboratory lighting, as well as Bayerd-Alpert ion gauges in the vacuum chamber. A similar long-range electron transfer mechanism was proposed to explain neutralization of mass-selected Cu_n^+ and Ag_n^+ ($n=1-3$) clusters during deposition in argon matrices, where photoelectrons released from the grounded metal sample support recombined with the cationic clusters.¹²³

For the other cases where neutralization is observed, after either deposition or annealing, it is harder to distinguish between the two mechanisms, and both may actually be contributing. The difference spectra in Fig. 3.2 seem to reflect more long-range neutralization between 20 and 25 K, since there is close correlation between depleted anionic and enhanced neutral bands for a given coordination number, but this correlation is then lost at higher annealing temperatures, suggesting short-range processes may play a larger role. Both mechanisms may also contribute to neutralization during deposition in principal, but the results seem more consistent with long-range electron transfer. Otherwise one would tend to expect much more neutralization during 20 K deposition than 10 K due to the longer surface diffusion period, and this is not the case; for example, the relative ratio of neutral to anionic species upon deposition is approximately the same between Figures 3.3B and 3.4B.

3.5.3 Nature of counter-cations

At the time of publication, we could not positively identify any cations in the matrix. Recently, we have assigned the peak at 2048 cm^{-1} to the $(\text{CO})_2^+$, as explained in

Chapter 6. Assuming comparable oscillator strength, the CO dimer cation cannot account for the entire charge balance in the spectra due to its low intensity compared to the anionic copper carbonyl bands. This suggests that other cations must be present, the precise nature of which remains an open question. No other clear spectroscopic evidence, neither direct nor indirect, was found to support the assignment of any bands to cationic molecules or complexes, and furthermore no differences in band positions were observed between spectra taken using Ar⁺ or Kr⁺ counter-cation beams (Figures 3.7 and 3.8, Appendix). A contributing factor is likely that the ionization potential (IP) of solid argon (13.9 eV^{52,124}) lies below that of both atomic Ar (15.8 eV¹²⁵) and Kr (14.0 eV¹²⁶), as well as CO (14.0 eV¹²⁷). This latter fact likely precludes the observation of molecular CO⁺ in argon;¹²⁸ indeed other authors have also noted its conspicuous absence in argon matrix spectra,^{88,129} whereas it is readily observable in neon matrices.⁸² There are also no bands assignable to CO molecules perturbed by a localized positive charge, which is expected to produce a significant blue-shift of the CO stretch.^{85,130} This absence is noteworthy because anionic CO complexes are readily observable, and the abundances of cations and anions in the matrix must be approximately equivalent.

It has been suggested that small cations may experience a strong interaction with the argon matrix, which effectively cages them against complexation;^{88,129} evidence to support this proposal is derived from the strong red-shifting of vibrational bands for species in solid argon.^{88,129,131} Thus it seems likely that the counter-cations in these experiments are localized either as Kr⁺ (when it is used for cation beam), or as Ar₂⁺, which is thought to be the charge carrier in ionized pure Ar matrices,^{124,132} but that a “caging” effect prevents them from interacting with other species in the matrix. Some circumstantial support for

this hypothesis is derived from the observation that the photoionization thresholds of both solid argon, as well as Kr dopants in solid argon (12.2 eV¹³³) are lower by ~1.8 eV from the gas phase atomic values, suggesting the ionic centers experience a strong stabilization from the matrix. This notion of “caged” cluster cations is also consistent with experimental data on the mobility of holes in pure solid argon, which is particularly low even for highly crystalline samples at temperatures near the triple point.¹³²

3.6 Conclusions

The results presented here represent the first time matrix-isolation spectra have been obtained for ionic species formed from a beam of mass-selected ions, with a coincident beam of externally generated counter-ions used to provide charge balance. Infrared spectra were obtained for copper carbonyl complexes formed following deposition of Cu⁻ ions with rare-gas counter-cations into a CO-doped argon matrix. Both anionic and neutral complexes were observed in the spectra, with most peak positions corresponding to previously reported assignments; new, partially resolved bands were assigned to larger [Cu(CO)₃•(CO)_n]⁻ aggregates with additional CO ligands in the second solvation shell.

The spectra obtained from this ion co-deposition technique provide insights into fundamental physical phenomena associated with ions in rare gas matrices, such as clustering and neutralization. Cluster formation appears to occur in the warmer surface region of the condensing matrix, therefore rough control over the complex formation process is afforded by varying the deposition temperature and dopant concentration. Spectra presented here show that roughly 100-fold higher CO concentration is required for deposition at 10 K relative to 20 K, in order to obtain a comparable distribution of anionic

and neutral copper carbonyls. Population transfer from anionic to neutral bands is observed in both time-lapse and temperature-dependent annealing studies, indicating that there are two distinct neutralization mechanisms: short-range electron-transfer between a proximate anion-cation pair following diffusion, and long-range electron transfer where the electron is first photodetached from the anion into the conduction band, then recombines with a spatially remote cation. Results for deposition using low CO concentration at 10K provide a striking example of short-range neutralization; all Cu^- are initially trapped as free ions, but upon annealing to 15 K, they are drawn through the matrix by Coulombic attraction to undergo electron exchange with cationic centers. The resulting energy release warms the matrix, allowing CO ligands to diffuse and form neutral copper carbonyl clusters.

3.7 Appendix

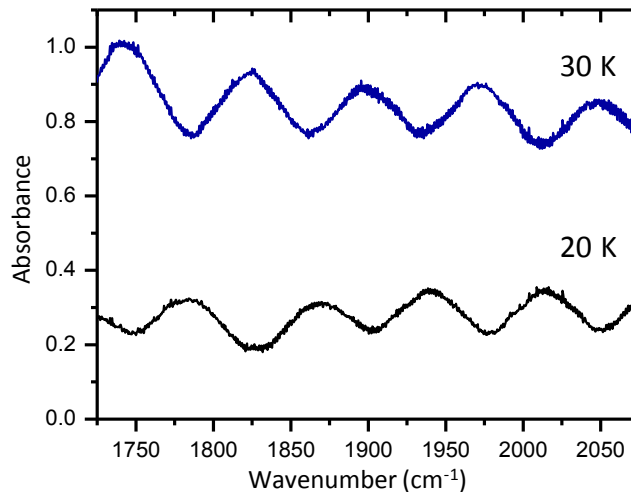


Figure 3.6 Control experiment of Cu^- deposition with no counter-ion in a 0.02% CO/Ar matrix deposited at 20 K. Note that there are no signs of copper complexes upon deposition at 20 K or upon annealing to 30 K showing the necessity of the counter-ion for the deposition process.

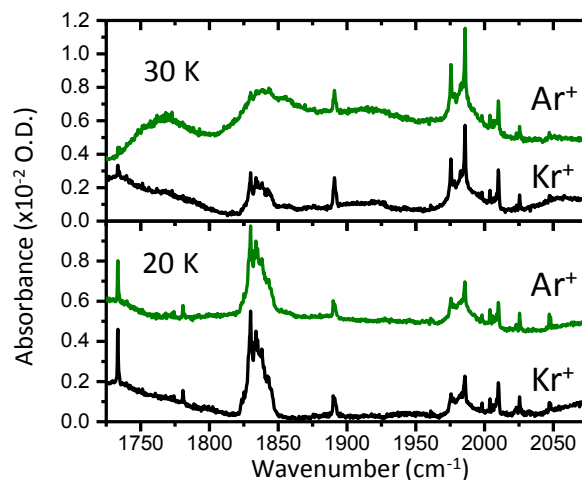


Figure 3.7 Deposition of Cu^- into a 0.02% CO in argon matrix at 20 K followed by 30 K annealing during two separate experiments using Kr^+ and Ar^+ as counter-ions as shown. Note that both counter-ions lead to virtually the same spectrum. The same neutralization events occur in both cases upon annealing with the exception of the larger $\text{Cu}(\text{CO})_3^-$ species persisting longer in the Kr^+ case.

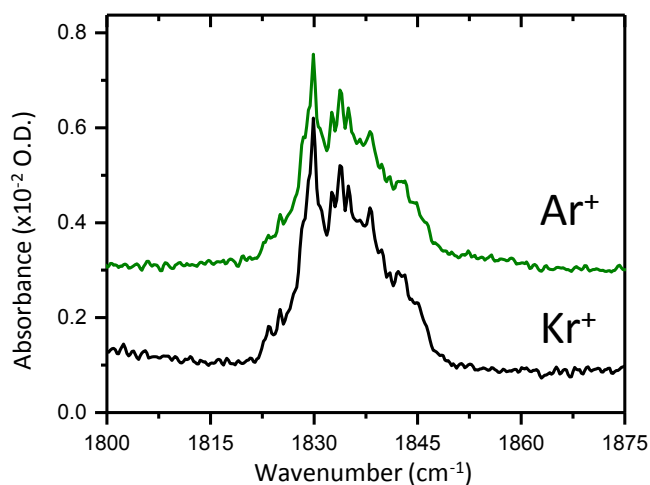


Figure 3.8 Deposition of Cu^- into a 0.02% CO in argon matrix at 20 K during two separate experiments using Kr^+ and Ar^+ as counter-ions as shown. Spectra are zoomed in on the $\text{Cu}(\text{CO})_3^-$ and $[\text{Cu}(\text{CO})_3 \cdot (\text{CO})_n]$ regions to emphasize the reproducibility of fine structure contained within the broad feature.

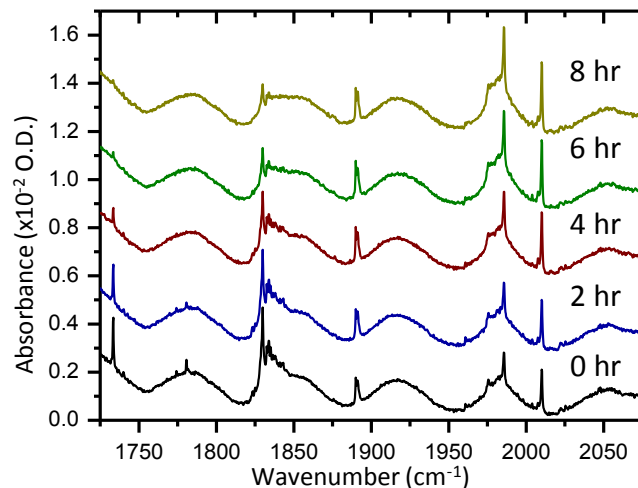


Figure 3.9 Time-lapse study using sample with ~ 7 nA Cu^- & Ar^+ co-deposited in a 0.02% CO in argon matrix at 20 K. Sample was maintained at 10 K over the course of 8 hours with scans taken every two hours. Spectra show neutralization attributed to long-range photodetachment mechanism (Figure 3.5B).

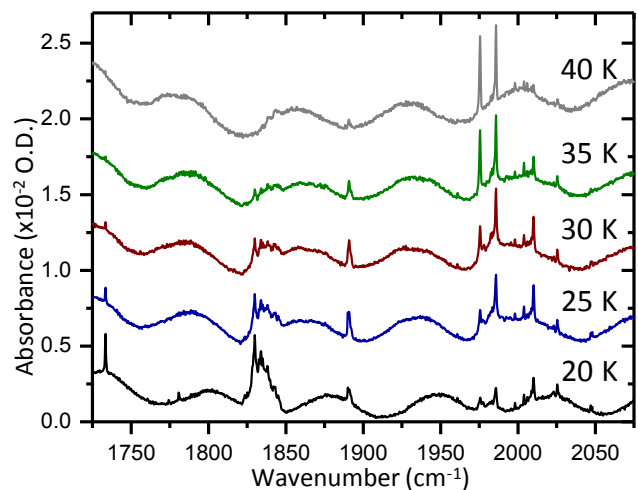


Figure 3.10 Unprocessed data from Figure 3.3 of main text showing low-frequency etaloning from interference in the matrix. Using index of refraction of bulk argon (1.77),¹¹⁴ fringes correspond to matrix thickness of ~ 60 μm .

3.7.1 Description of minor spectral differences for 10 K vs 20 K deposition

As stated in the main text, when the more CO-rich 2% mixture is used for 10 K deposition (Figure 3.4B), the results are qualitatively similar to those measured following deposition of the 100-fold more dilute 0.02% CO mixture at 20 K (Figure 3.2), however, there are some small but significant differences. First, there is a slight but consistent and reproducible blue-shifting of most of the peaks by 0.2-0.3 cm^{-1} in the 10 K spectrum (Table 3.1), with the exceptions being the $\text{Cu}(\text{CO})_3^-$ peak (not shifted) and the $\text{Cu}(\text{CO})_3$ peak at 1985.5 cm^{-1} (redshifted by 0.4 cm^{-1} from the 20 K spectrum). Additionally, there are new bands at 1774 cm^{-1} and 1824 cm^{-1} , which are tentatively assigned (based on proximity) to di- and tricarbonyl complexes trapped in different matrix sites at the lower deposition temperature. There are also partially resolved features at 1981.4 and 1983.4 cm^{-1} that grow in upon annealing to 20 K; although there is intensity in the corresponding region of the 20 K deposition spectrum (Figure 3.2), it is harder to identify individual bands. Note also that most of the impurity bands are absent from the spectra in Fig. 3.4B; the deposition gas for this sample was run through a liquid nitrogen/ethanol bath, in order to remove the metal carbonyl contaminants. The only remaining peaks in the region where impurities were observed are at 2039 cm^{-1} , which is from $^{13}\text{C}^{18}\text{O}$ (observable in this high-concentration CO mix at natural abundance), and at 2048 cm^{-1} , which has been assigned by our group as $(\text{CO})_2^+$ (Chapter 6).

3.7.2 Ion abundance calculation

Using the ion-beam currents and the physical dimensions of the matrix, we can estimate the number density of ions in the matrix, assuming unity probability of ion trapping in a homogeneous matrix. Deposition at 10 nA for 2 hours corresponds to delivery

of 4.6×10^{14} each of cations and anions; based on the etalon peaks in the infrared spectra (Figure 3.10) the matrix thickness is estimated to be 60 nm, assuming this is uniform over the deposition area of 3.1 cm^2 yields a matrix volume of 0.018 cm^3 , corresponding to a number density of $\sim 2.5 \times 10^{16}$ ions/ cm^3 each for cations and anions. Using the bulk density of solid argon ($\sim 1.77 \text{ g/cm}^3$ at 20 K),¹¹⁴ this converts to a molar Cu⁺:Ar ratio of $\sim 1:10^6$, representing an upper limit for the ion concentration in the matrices presented here. Of course the actual ion abundance is likely significantly lower in practice, given expected losses due to phenomena such as “grounding out” of ions on the sample holder, as well as scattering in local high pressure of the deposition region. The spectra presented in the main text also reveal significant populations of neutral species upon deposition, indicating that many of the ions undergo neutralization as the matrix is forming.

Table 3.2 Peaks assigned to transitions from metal carbonyl impurities (Figures 3.2-3.4), based on previous spectroscopic assignments (see references contained within 85 and 129). Peaks marked with ‘?’ do not correspond to any previously reported bands, but are still assigned to impurity species based on their absence when using an ethanol cooling bath, and insensitivity to annealing (note their absence in difference spectra in Figure 3.4B).

Impurity Peaks	
Absorption	Assignment
1998.2	?
2001.1	?
2003.95	Fe(CO) ₅ site
2006.12	Fe(CO) ₅
2008.8	?
2009.98	?
2023.2	?
2025.4	Fe(CO) ₅
2034.6	?
2051.7	Ni(CO) ₄

Chapter 4

Cold chemical reactions triggered using electrons photodetached from “clean” distributions of anions in cryogenic matrices via counter-ion co-deposition

Adapted with permission from Ludwig, R. M.; Moore, D. T. Chemical Reactions Triggered using Electrons Photodetached from "Clean" Distributions of Anions Deposited in Cryogenic Matrices Via Counterion Codeposition. *J. Phys. Chem. Lett.* **2014**, *5*, 2947-2950. Copyright 2014 American Chemical Society.

4.1 Abstract

Application of matrix-isolation spectroscopy to ionic species is typically complicated by the presence of neutral contaminant species related to the matrix deposition process. Here it is demonstrated that explicit deposition of balanced currents of counter-ions with the mass-selected ions of interest can be used to create “clean” distributions of matrix-isolated copper carbonyl anions, where only the anion bands are present in the CO-stretching region of the vibrational spectrum. Furthermore, photodetachment by mild irradiation with visible light is used to initiate complete conversion of the anions into their corresponding neutral species. Finally, it is demonstrated that the photodetached electrons initiate covalent chemistry in the van der Waals dimer of CO, which forms a C-C bond following electron capture to make trans-OCCO⁻. The clear connections that can be drawn between the spectral changes induced at each step in the experiment derive from the initial “clean” distribution of ions, demonstrating the potential of the counter-ion co-deposition technique to enable detailed studies of chemistry involving ions and electron-transfer in cryogenic matrices.

4.2 Introduction

While many matrix-isolation studies of ions have been reported,¹³⁴ the requirement that charge-balance be maintained throughout matrix deposition has limited the scope of ions that could be studied to those produced by intrinsically neutral sources such as laser ablation⁸⁵ and microwave discharge,⁸¹ or to robust ions such as carbon chains that can survive deposition at very high kinetic energies.⁸⁹ All previous methods for generation and deposition of matrix-isolated ions tend to be “dirty”, in that a large fraction of the species trapped in the matrix are neutrals species produced during ion generation, or formed by secondary processes such as fragmentation or auto-neutralization during deposition. Photodetachment – the process whereby an electron is released from a negatively charged atom or molecule following the absorption of a sufficiently energetic photon (in analogous fashion to photoelectron emission from neutrals) – is a standard method used to distinguish charged from neutral species in matrices.¹³⁵⁻¹³⁷ Irradiation of the matrix with broadband UV/visible radiation, induces selective depletion of the bands associated with ions; the interpretation is that anions are directly neutralized by photodetachment, and the electrons released then combine with and neutralize cations. Few matrix studies have gone beyond such simple diagnostic uses of photodetachment, however, due to the contamination issues mentioned above; there are some examples where wavelength filters were used to distinguish anionic species by their photodetachment thresholds, which tend to be significantly blue-shifted in matrices.^{135,137}

The coupling of a vibrational spectroscopy matrix isolation apparatus to the output of a mass-spectrometer to enable structural characterization of arbitrary ions of interest has long been recognized as an important goal in instrumental analytical and physical

chemistry.¹⁰⁸ Results from our group, presented in Chapter 3, demonstrated the feasibility of using co-deposition of rare-gas counter-cations for just such a purpose.¹³⁸ Anionic copper carbonyl complexes in sufficient number densities for FTIR spectroscopic characterization were produced by simultaneously directing low-energy beams of monatomic copper anions (Cu⁻) and rare gas cations (Ar⁺ or Kr⁺) into a CO-doped argon matrix.¹³⁸ That study demonstrated proof-of-concept for the technique, but still was not an ideally “clean” source of matrix isolated ions, since the neutral copper carbonyls were also produced during deposition.

It was clear from the early studies that two neutralization events can occur: one that followed annealing whereby excess energy was released local to the copper centers, and an event that occurred when holding the sample at 10 K characterized by minimal energy transferred to the copper. In response to these studies, additional experiments were performed in the absence of ambient light. All lab lights were kept off, ion gauges shut off, and the IR beam kept bent away from the deposition window until scans were being taken. This chapter presents the ensuing “clean” spectra of anionic carbonyls afforded by this method.

4.3 Experimental

For these studies, the deposition and subsequent processing steps were carried out under darkened conditions except where otherwise noted; all internal sources of light were turned off (ion gauges, RGA analyzer, etc.), and the lab lights were kept off throughout. Some light from the spectrometer necessarily reached the sample (the HeNe alignment laser for the interferometer) during spectral scans; the spectrometer beam was directed away from the deposition chamber when not recording spectra. For photodetachment

studies, broad-band visible irradiation was achieved using a tungsten filament bulb (Figure 4.5, Appendix) held outside the vacuum chamber and introduced through a Kodial glass viewport (Kurt J. Lesker Company). Wavelength-dependence studies were performed using several narrow-band LED sources (Thor Labs, spectra provided in Appendix 4.6). There was no direct line of sight from the tungsten source to the sample holder as the Faraday plate was in the light's path, therefore, any photons hitting the sample were reflected off the inside of the vacuum chamber.

Gas mixes were prepared by dilution of a purchased mixture of 10% CO in He (PRAXAIR) down to a 2% CO mix with Ar (PRAXAIR, 99.9999%). Isotopic gas mixtures were made using 99% ^{13}C O (< 5% ^{18}O , Sigma-Aldrich). All matrix gases were dehydrated by flowing through a copper tube immersed in ethanol-liquid nitrogen bath prior to deposition; this method also removed any gas contaminants (i.e. carbon dioxide, metal carbonyls, etc.). Between this cryogenic trapping and the use of UHV vacuum systems, the levels of common atmospheric contaminant gases such as H_2O and CO_2 were kept quite low; weak bands corresponding to the isolated monomers, as well as the H_2O -CO complexes seen in Figure 4.7 Appendix, were typically observed, but no evidence of any copper complexes of those species were found. Thus there is no evidence that those gases interfere with the experiments described in the main text in any major way, however, as mentioned in our previous paper, the possibility that they are cationic charge carriers cannot be completely ruled out.¹³⁸ Even if this were the case, it would not affect the conclusions of the current work in any significant way.

4.4 Results

4.4.1 Visible irradiation followed by annealing

Figure 4.1 shows an improved version of the experiment where the matrix deposition was conducted under completely darkened conditions at 10 K. The expected bands for the anionic mono-, di- and tricarbonyl complexes are observed at 1733, 1780 and 1829 cm^{-1} , respectively, as in previous studies,^{88,138} but now the neutral copper carbonyl peaks are conspicuously absent from the spectrum (the peak at 1774 cm^{-1} was not observed in the earlier work, but clearly arises from an anion, as demonstrated below). Evidently the removal of all sources of ambient light during the deposition phase protected the anions from premature photodetachment, so that neutral species were not produced. Note that this also implies that neutralization by electron transfer between adjacent pairs of oppositely charged ions does not occur to any significant extent. The implication is that the ions become trapped in matrix sites before they can diffuse together under the influence of Coulomb attraction; this is qualitatively consistent with previous 10 K studies for this system, which showed trapping of uncoordinated Cu^- ions at low CO concentrations.¹³⁸

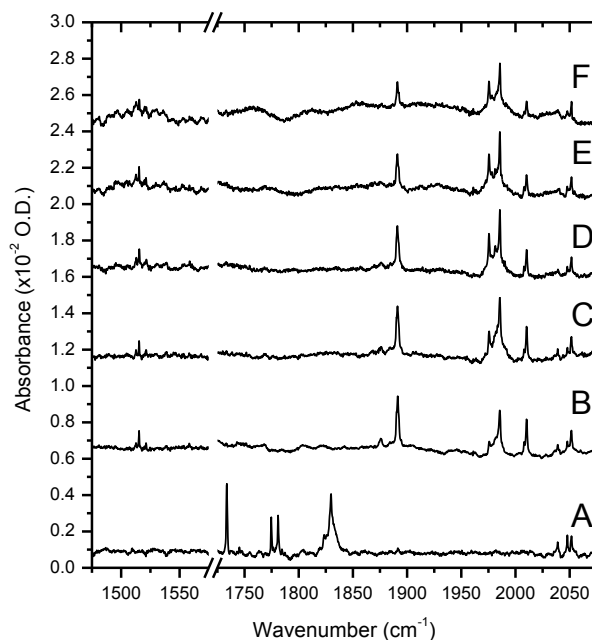


Figure 4.1 FTIR spectra from co-deposition of Cu^- and Ar^+ ion-beams (3 nA each) for two hours with 2% CO in argon at 10 K, with subsequent annealing steps; all spectra recorded at 10 K. A) Spectrum following deposition, showing only anionic copper carbonyl bands. B) Spectrum following photodetachment of the anions by visible irradiation; new bands correspond to neutral copper carbonyl complexes, as well as *trans*- OCCO^- near 1515 cm^{-1} . C-F) Spectra following annealing steps at 15, 20, 25 and 30 K, respectively.

The benefit of having a clean source of anions can be appreciated from Fig. 4.1B, which shows the spectrum following deliberate photodetachment of the anions using ~ 10 minutes irradiation with light from a tungsten-filament bulb. All of the bands corresponding to anionic species (including the new 1774 cm^{-1} band) have been completely depleted, and replaced in the spectrum by the corresponding neutral copper complexes, with peaks for the mono- and dicarbonyls at 2010 and 1890 cm^{-1} , respectively, and a broad feature centered at 1980 cm^{-1} with sharp peaks at 1975 and 1985 cm^{-1} representing the tricarbonyl.^{116,138} The photodetachment seems to be a gentle event, preserving the approximate relative intensities of the mono-, di- and tricarbonyls within the anionic and neutral manifolds. The dicarbonyl seems a bit more intense in the neutral spectrum,

relatively, but it is not clear whether this represents a difference in population or in oscillator strength. Furthermore, a peak at 1515.5 cm^{-1} which has been assigned to $(\text{CO})_2^-$ and 1512.6 cm^{-1} assigned to a $(\text{CO})_2^-$ site⁸⁸ appears along with a peak at 1521.8 cm^{-1} which has not been reported in the literature, the implications of which are discussed below. Annealing to higher temperatures (Fig 4.1C-F) does not cause any further significant changes in the spectrum.

4.4.2 Annealing followed by visible irradiation

Although long-range neutralization was shut-down, as shown above, due to lack of ambient light there exists the possibility of close-range ion recombination during annealing of the matrix. Since the top facile layer of the matrix during deposition should provide enough thermal diffusion to see any neutralization if it were to take place, neutralization due to annealing post-deposition seemed unlikely, however, was still necessary for completeness of study. Therefore, experiments were performed by annealing in 5 K increments after deposition and irradiated only after 30 K annealing (Figure 4.2). As seen in Figure 4.2A there is only a very small population of the neutral dicarbonyl copper complex upon deposition. This is likely due to a small amount of light given off by the electron impact ionizer filament in the bender region that still gets to the deposition surface. As will be discussed below, the anionic dicarbonyl is easily photodetached with visible light. Annealing to 15K decreases the 1733 cm^{-1} , 1774 cm^{-1} , and 1780 cm^{-1} bands while a broad feature to the blue of the 1830 cm^{-1} peak grows in (see subtraction spectra, Figure 4.8, Appendix). Although the neutral dicarbonyl gains slight intensity, no other neutralization occurs. It seems likely that this small growth is due to sharpening of the already present neutral dicarbonyl and not due to further neutralization of ionic precursors.

Annealing to higher temperature continues to decrease the anionic peaks. It is important to note here, that annealing to temperatures of 30 K does not cause any significant neutralization as was observed with previous studies,¹³⁸ even after sitting at 30 K for 6 hours. The loss of anionic complexes is due to overall matrix loss as observed by pressure spike in the vacuum chamber upon 30 K annealing.

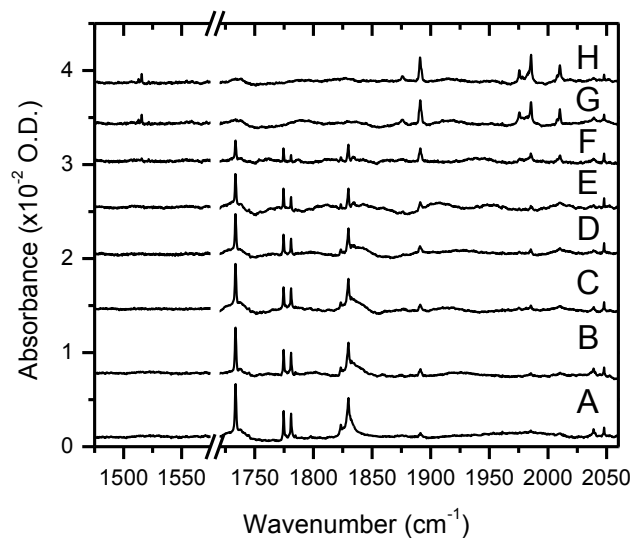


Figure 4.2 $\text{Cu}^- \text{Ar}^+$ co-deposited (4 nA each) for 4 hours with 2% CO in argon at 10 K. A) 10 K deposition, B) 15 K annealing, C) 20 K annealing, D) 25 K annealing, E) 30 K annealing, F) low intensity irradiation, G) high intensity irradiation, and H) 30 K annealing after irradiation. All spectra taken at 10 K.

Irradiation in this study was performed by first exposing the system to low intensity light for 30 min (Figure 4.2F) followed by exposure to full intensity light for another 30 min (Figure 4.2G). With the low intensity light, the anionic dicarbonyl species shows the greatest relative depletion followed by the anionic monocarbonyl. The higher intensity light is able to neutralize the rest of the anionic population as well as form the $(\text{CO})_2^-$ species at around 1515 cm^{-1} . Annealing to 30K after photodetachment leads to an increase in the tricarbonyl peaks and a sharpening of the dicarbonyl peak with no change to the mono

peak. One major difference observed between this study and the photodetachment before annealing study (Figure 4.1) is the persistence of the 1876.2 cm^{-1} band even after 30 K annealing.

4.4.3 Wavelength-dependent photodetachment

Another benefit to having a clean deposition is the ability to follow wavelength dependent photodetachment events as shown in Figure 4.3. Using narrow-band LEDs (Figure 4.6, Appendix) individual species can be neutralized based on their photodetachment thresholds. This allows another level of identification that was not possible by previous methods. It should be noted that the photodetachment events shown do not provide true thresholds, but instead show that photodetachment occurs at or above the wavelength of light by which it is being detached. The species to detach at the longest wavelength of 735 nm is the anionic dicarbonyl. This low threshold explains previous findings of this species having an anomalously low intensity upon deposition which certainly occurred with constant light hitting the window.^{88,138} It should also be noted that the 1774 cm^{-1} peak is detached along with the 1780 cm^{-1} and both seem to add to the intensity of the 1890 cm^{-1} band. This not only adds to the notion that this new peak is ionic, but also that it is a form of the anionic dicarbonyl as will be discussed. The anionic monocarbonyl is the next complex to photodetach using 660 nm light. The anionic tricarbonyl is harder to track due to its low appearance on this day but is completely neutralized with the shortest wavelength at 590 nm. It does appear however that a small population becomes detached at each of the wavelengths. These detachment events suggest that the photodetachment threshold might not be a sharp cutoff but instead either a continuum or multiple thresholds possibly due to differences in the local matrix

environment. It could also mean that the tricarbonyl is undergoing a more complicated process such as multiple “detach-reattach-detach” events leading to the eventual depletion.

Upon annealing after photodetachment, the 1975 and 1985 cm^{-1} tricarbonyl bands gain intensity while the mono and dicarbonyl species lose intensity. This is consistent with aggregation toward higher stoichiometries upon annealing. Finally, it should be noted that the $(\text{CO})_2^-$ species did not form this day. Possible explanations as to its absence are discussed below.

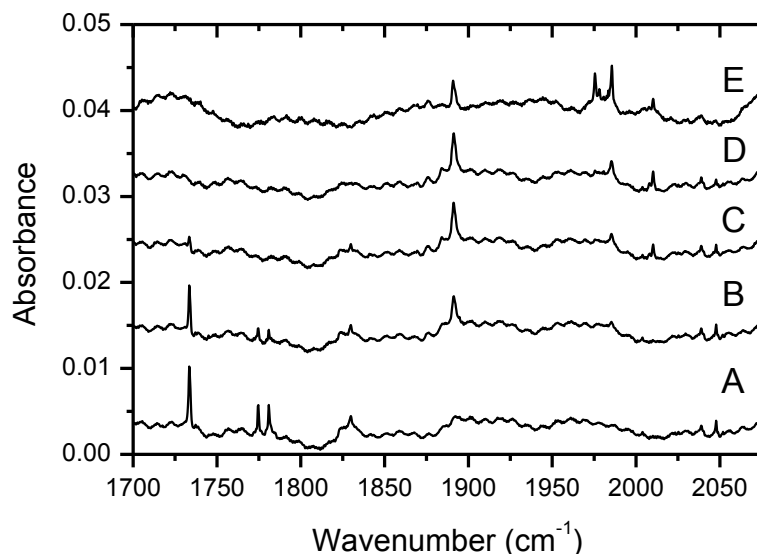


Figure 4.3 $\text{Cu}^- \text{Ar}^+$ co-deposited (4 nA each) for 4 hours with 2% CO in argon at 10 K. A) 10 K deposition, B) 735 nm light, C) 660 nm light, D) 590 nm light, and E) 30 K annealing. All spectra taken at 10 K.

4.5 Discussion

4.5.1 Electron-induced C-C bond formation

One thing to consider is the fate of the photodetached electrons in the matrix. Another pair of peaks at 1512.6 and 1515.5 cm^{-1} also appeared in the spectrum following the irradiation step (Figure 4.1B); these have previously been assigned the *trans*- OCCO^-

species in argon matrices.¹²⁹ Their appearance strongly suggests that some of the photodetached electrons ended up getting captured by neutral (CO)₂ van der Waals complexes, which were present in relatively high abundance due to the high CO concentration in the matrix (2140 cm⁻¹ band⁵⁹ in Figure 4.7, Appendix). This electron-capture event means that the photoelectrons initiated formation of a covalent C-C bond in the weakly bound neutral CO-dimers, and thus we have achieved the photo-triggered cryochemistry scheme shown in Figure 4.4.

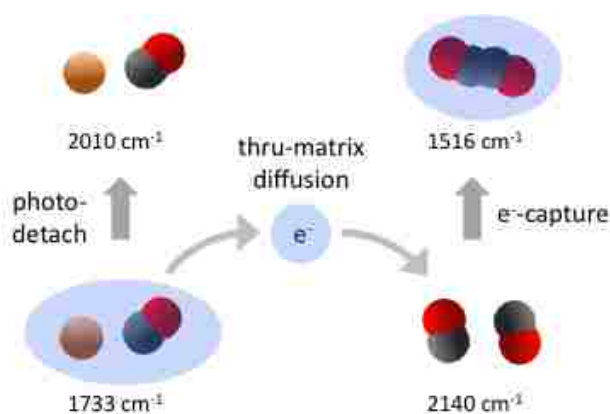


Figure 4.4 Cryochemistry scheme based on using electrons photodetached from the anionic monocarbonyl complex to induce formation of the *trans*-OCCO⁻ by electron attachment to the van der Waals CO-dimer, which results in C-C bond formation. Positions of corresponding IR bands in Fig. 4.1 and 4.7 are indicated.

There is obviously a significant driving force for photodetached electrons to recombine with cations trapped in the matrix, as observed by a small decrease in the 2048 cm⁻¹ peak assigned to (CO)₂⁺ (see full intensity irradiation subtraction spectrum Figure 4.8, Appendix); however, assuming the oscillator strength is near that of the anionic complexes, then the 2048 cm⁻¹ peak cannot account for all the cation species. The remaining cations are most likely rare-gas centers lacking vibrational bands,¹³⁸ making it impossible to directly observe them in the spectrum. However the apparent gentleness of the photodetachment results above indicates that this recombination cannot be happening

in close proximity to the anion complex that served as the source of the photoelectrons. Otherwise the huge amount of energy (>10 eV) released locally into the matrix would be expected to perturb the spectral bands of the (now neutral) copper carbonyl source complex, as was observed in our previous set of experiments when free Cu^- ions underwent diffusion and spontaneous neutralization, and the local energy released shifted the stoichiometry of the observed neutral complexes to larger clusters.¹³⁸ Even while irradiating the system during deposition during which local diffusion is occurring, the stoichiometry remained the same (Figure 4.9, Appendix). Instead, it seems that the cation neutralization is happening in remote sites following diffusion of the electron across multiple argon atoms in the matrix. This is consistent with the expected behavior of electrons flowing freely in the conduction band of the argon solid, which lies ~ 0.3 eV above the vacuum level.⁵² For the current case, the known gas-phase photodetachment thresholds of the anionic copper carbonyls are 0.95 and 1.02 eV for the di- and tricarbonyls, respectively.¹³⁹ Thus for the anionic copper carbonyls in the current study, long range diffusion following photodetachment is expected for visible light of wavelength < 939 nm (1.32 eV), which is certainly available with the broad-band source used here (Figure 4.5, Appendix).

4.5.2 Wavelength-dependent trends

Although we cannot obtain exact thresholds, the wavelength dependent trends follow that seen in the literature whereby the anionic copper dicarbonyl is detached before the anionic copper tricarbonyl¹³⁹ (for a complete list of photodetachment energies, see Table 4.1 in the Appendix). There has not been a gas-phase value determined for the anionic copper monocarbonyl, but the trends observed here suggest that it should be

somewhere between the dicarbonyl and tricarbonyl species (1216 nm to 1305 nm for gas-phase values).

Due to higher energy photons necessary in the matrix compared to the gas phase, it is clear that the argon cage plays a significant role in determining the energy necessary to detach an electron. The literature value of 0.3 eV above the vacuum level was found using a near perfect argon crystal,⁵² which is not close to our experiments deposited at 10 K. One can imagine then that the local argon structure can shift the exact energy needed to detach the electron into the conduction band of argon. This matrix effect could be one explanation as to why the tricarbonyl, which contains the largest cage and should have the greatest variation of cage structure, has a small population depleted with every wavelength used but a large neutral band isn't observed until annealing post-irradiation (compare this with Figures 4.1 and 4.2, where broad-band irradiation leads to a high neutral complex and annealing does not change the spectrum much). If the photodetachment and conduction band injection are two distinct events, then an electron that is photodetached with insufficient energy to be "lost" to the matrix may rattle around in the local cage environment. At this point, it may either reattach to form the original anion, or it's possible that it could get "stuck" in some intermediate dark state, such as a Rydberg anion. This "dark intermediate" can then release the electron upon annealing which would recombine with a cation in the matrix. Though this is very speculative at this point, it would be consistent with the data in Figure 4.3.

There is also an absence of $(\text{CO})_2^-$ upon irradiation this day, however, there is also no discernable neutral $(\text{CO})_2$ peak upon deposition. The lack of formation of this neutral dimer along with an anomalously low anionic tricarbonyl are both consistent with a lower

deposition temperature. This low deposition temperature could also provide an alternate explanation as to why annealing leads to such intense 1975 and 1985 cm^{-1} bands. It is possible that free- Cu^- centers were trapped upon deposition and undergo violent neutralization during annealing as was seen in the 10 K low concentration experiments in chapter 3. An alternate explanation as to why the $(\text{CO})_2^-$ does not form could be because of the “gentleness” of photodetachment in this case. With the broadband source, some electrons would be detached with a large amount of excess energy. It’s possible that this extra energy is needed to induce the C-C covalent bond in the neutral complex. During the wavelength dependent studies, photodetachment events may occur close to their threshold values so that the electrons do not contain sufficient energy to induce C-C bond formation.

4.5.3 New spectroscopic peak identification

As stated above, a new species at 1774.7 cm^{-1} is formed with equal intensity to the 1780.9 cm^{-1} peak, the latter of which has been previously assigned to a $\text{Cu}(\text{CO})_2^-$ species in argon. It is clear from the photodetachment studies that this species is ionic and due to its frequency is likely anionic. Isotope studies (Figure 4.10, Appendix) show that this species contains two equivalent CO molecules bound to a copper center, therefore we assign this peak to be a $\text{Cu}(\text{CO})_2^-$ species. Although both the 1774 and 1780 cm^{-1} peaks contain two CO units, the peak shape of the 1780.9 cm^{-1} mixed isotopomer is surprising. For the 1774 cm^{-1} species, the mixed isotopomer is as expected for a linear dicarbonyl, however, the 1780.9 cm^{-1} mixed isotopomer at 1753.7 cm^{-1} is inherently broad suggesting that the two CO ligands are not equivalent. This broadening could occur for several reasons such as the local environment being different around one side of the molecule in relation to the other. It could also be that this species is being perturbed by another molecule in the

matrix making the two ends of the molecule inequivalent. It is interesting that both the 1780 and 1774 cm^{-1} peaks are neutralized to the 1890 cm^{-1} peak suggesting that whatever perturbs the anionic complex, does not seem to have an effect on the neutral complex (Figure 4.3). It should also be pointed out that there are some minor peaks near the neutral dicarbonyl complex in the isotope studies, however, they are of low intensity and not resolved enough for interpretation at this time.

Preliminary DFT calculations in our group (carried out by Prof. Moore at the B3LYP/6-311+G(3df) level) suggest that the two species observed arise from both the triplet and singlet states of the anionic copper dicarbonyl. Although the ground state is predicted to be the triplet and was previously assigned by the Andrews group to the 1780 cm^{-1} species,⁸⁸ our calculations suggest that the 1780 cm^{-1} peak is due to the singlet state and that the 1774 cm^{-1} peak arises from the triplet. We predict the singlet state to lie ~10 kcal/mol higher in energy than the triplet state, which could be formed and stabilized under our deposition conditions which occur under a large degree of kinetic control. It is not certain at this time why the Andrews group did not observe this peak as well. It's possible that it was present but obscured by a large broad peak in this region.⁸⁸ Also, the 1780 cm^{-1} band deposited via laser ablation is about 20-fold lower in intensity than in our spectra, so it is possible that the 1774 cm^{-1} is just not concentrated enough to appear in Andrews' study. Further investigation on this species in our group is ongoing.

4.6 Conclusions

Looking ahead at the ramifications of the proof-of-concept study presented here, there are several aspects to be developed. Perhaps most obviously, the electron-induced bond-formation can be applied to a system that is a bit more interesting than the van der Waals dimer of CO. Adding tighter wavelength resolution to the photodetachment step will enable precise determinations of photodetachment thresholds in the matrix, which is interesting in its own right, but will also enable determination of the lower energy of the conduction band-edge, based on the separation of the measured values for anions with known gas-phase photodetachment thresholds. In terms of the photo-triggered cryochemistry scheme in Figure 2, the wavelength resolution will allow for precise control of the kinetic energies of the electrons in the matrix. It would be interesting to investigate the correlation between the electron energy in the matrix and the capture efficiency for the *trans*-OCCO⁻ formation; thresholds at both the upper and lower limits are certainly conceivable. It would also be interesting to use this scheme to investigate capture of electrons by molecular cations that could be monitored in the IR spectrum. Finally, it should be noted that in a general sense, the phenomenon demonstrated here represents an interesting opportunity for theorists to study a quintessential example of long-range electron transfer between donor and acceptor species trapped in a conducting medium (for electrons that are sufficiently above threshold), and one where detailed experimental control over many of the most relevant variables.

4.7 Appendix

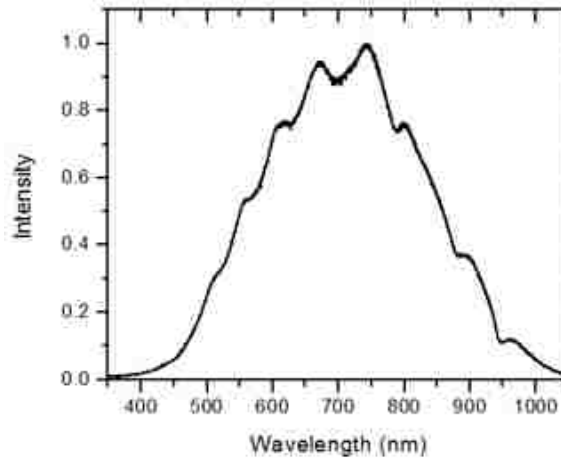


Figure 4.5 UV-visible spectrum of emission from tungsten-filament bulb used for broad-band photodetachment studies.

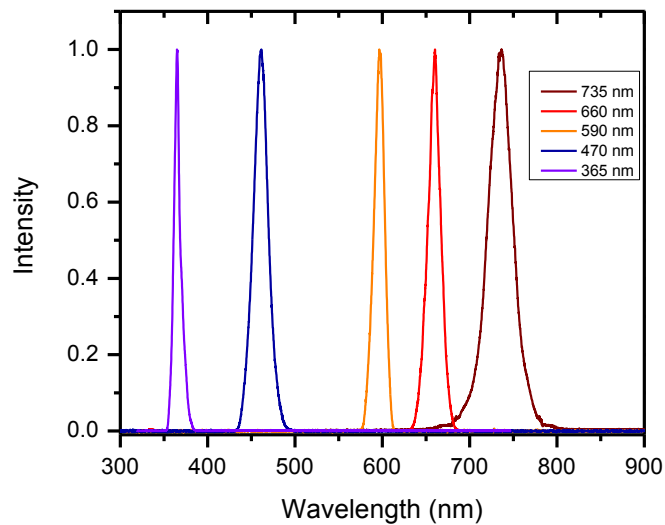


Figure 4.6 LED spectra used for narrow-band photodetachment studies. Neither the 470 nm nor the 365 nm centered LEDs were used in this study, but are used in later chapters and have been included for completeness.

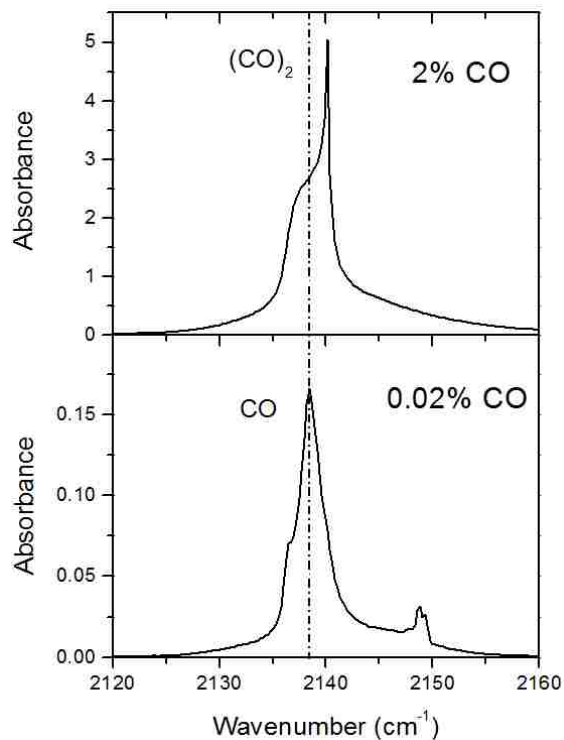


Figure 4.7 IR spectrum of the CO stretching region showing concentration dependence of the associated bands. Note the prevalence of the band at 2140 cm^{-1} for the van der Waals CO-dimer⁵⁹ in the more concentrated 2% CO matrix used for the current study. The peaks near 2150 cm^{-1} arise from $\text{H}_2\text{O}-(\text{CO})_n$ van der Waals complexes.^{140,141}

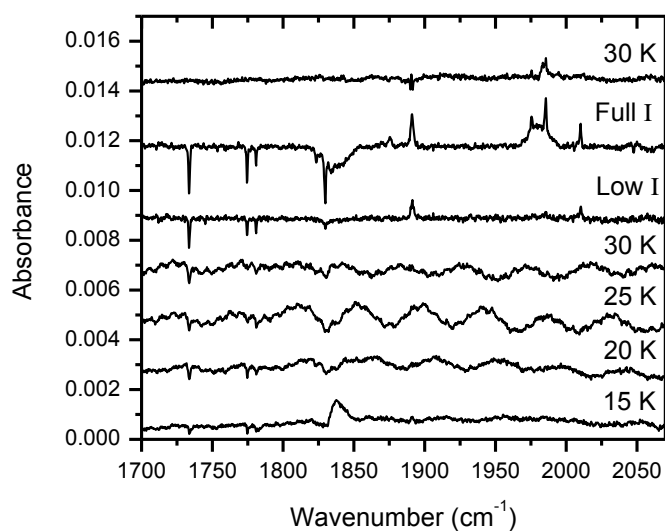


Figure 4.8 Difference spectra emphasizing changes during 5 K annealing steps and irradiation steps for data shown in Figure 4.1.

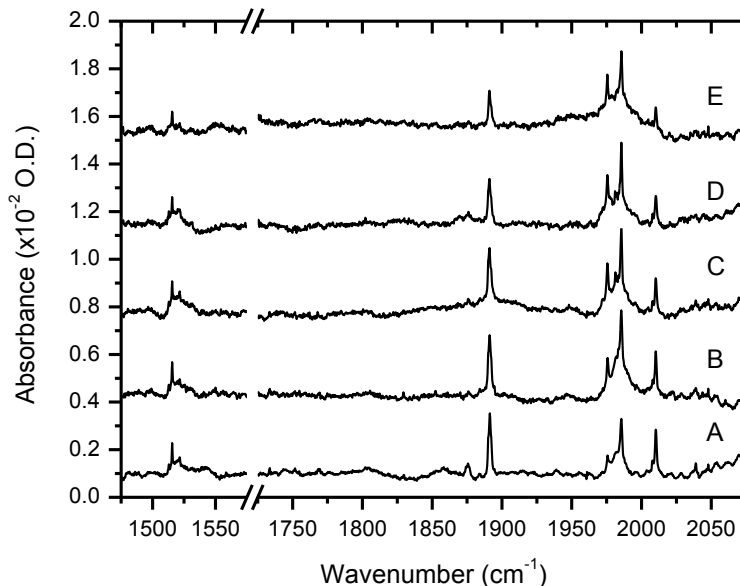


Figure 4.9 Tungsten-filament source on during deposition of 3 nA Cu^- balanced by Ar^+ in 0.02% CO doped argon matrix. As expected, no anionic copper compounds are observed after a 2 hour deposition: A) 10 K deposition, B) 15 K, C) 20 K, D) 25 K, and E) 30 K annealing. All spectra recorded at 10 K.

Table 4.1 Gas-phase photodetachment thresholds for anionic copper clusters and anionic copper carbonyls

Anionic Copper Clusters ^a	Energy		Anionic Copper Carbonyls ^b	Energy	
	eV	nm		eV	nm
Cu_1^-	1.2	1033	Cu^-	1.23	1008
Cu_2^-	0.9	1378	$\text{Cu}(\text{CO})^-$	NA ^c	NA ^c
Cu_3^-	2.4	517	$\text{Cu}(\text{CO})_2^-$	0.95	1305
Cu_4^-	1.5	827	$\text{Cu}(\text{CO})_3^-$	1.02	1216
Cu_5^-	1.9	653	$\text{Cu}(\text{CO})_4^-$	1.04	1192
Cu_6^-	2	620	$\text{Cu}_2(\text{CO})_4^-$	1.43	867
Cu_7^-	2.2	564	$\text{Cu}_2(\text{CO})_5^-$	1.25	992
Cu_8^-	1.5	827			

^avalues taken from ref. 142

^bvalues taken from ref. 139

^cno photoelectron value is available for the anionic copper monocarbonyl

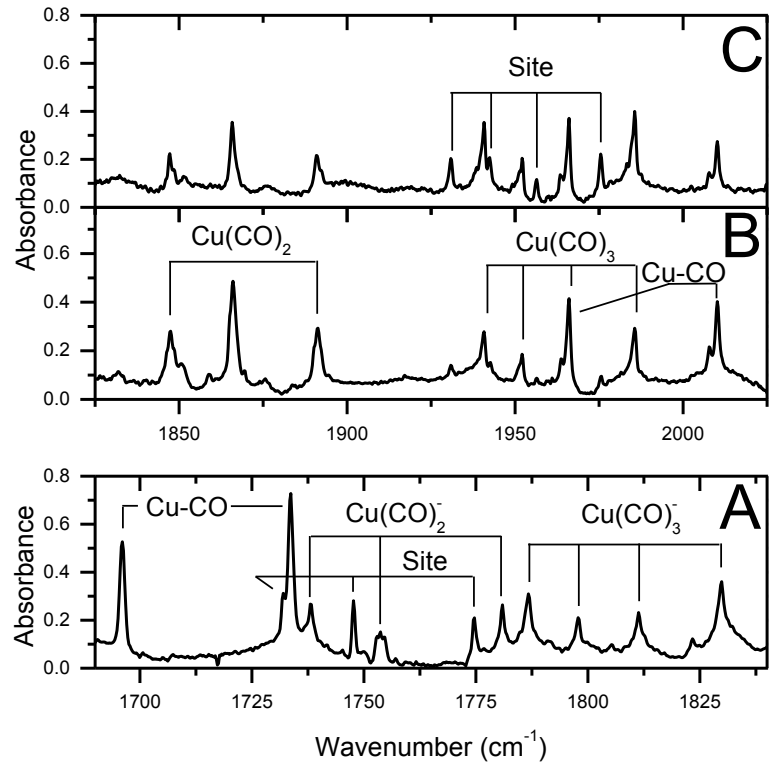


Figure 4.10 Cu⁻Ar⁺ codeposited with a 1% ¹²CO + 1% ¹³CO in Ar matrix at 10 K: A) deposition, B) visible irradiation, and C) 30 K annealing after irradiation.

Chapter 5

High-temperature deposition: intermediate anionic complex formation upon annealing and trapping of subsequent transient photodetachment products

5.1 Abstract

Since its early development, matrix isolation has been used to stabilize transient species. By using the counter-ion codeposition method, transient formation is observed for the simple copper-carbonyl system. After deposition of anionic copper carbonyl precursors at 20 K, annealing leads to many new sharp features in the anionic region. What makes this so remarkable is that oscillators which have nominally one vibrational frequency give rise to multiple peaks in the spectrum. The anionic monocarbonyl, for example, gives rise to at least five bands while the anionic tricarbonyl gives rise to over fifteen bands, most of which contain resolution limited line-widths. Upon irradiation with wavelengths above 470 nm, new transients are observed in the neutral copper carbonyl region that have not been observed in previous studies. These peaks clearly arise from precursors that must be annealed-in in the anionic region and subsequently photodetached. Due to the high level of control afforded by this new deposition method, neutralization events occur sufficiently far from the copper centers such that the neutral transients formed are stabilized and can be traced back to their anionic precursors. Annealing the system after irradiation gets rid of the neutral transients which seem to “relax” to previously assigned neutral copper carbonyl species. Some of these bands are reminiscent of long sought-after vertical detachment products as is discussed.

5.2 Introduction

As stated in Chapter 1, our new deposition method was developed with the goal of creating a technique called freeze-frame spectroscopy. We envisioned that transient species could be trapped in a matrix, driven over a barrier with the input of energy, and the subsequent transient product would also be trapped in the energy dissipating environment. Chapter 3 demonstrated the feasibility of depositing sufficient amounts of anionic metal into a matrix through the use of explicit counter-ions. Chapter 4 showed the power of this new method, whereby deposition in the absence of ambient light at 10 K allows for a “clean” deposition under which only the anionic carbonyl species are created and trapped. This study was important since it provided a level of control that cannot be afforded by any other method. However, annealing did not cause any changes in the relative intensities of the peaks, only an overall scaling of the spectrum, presumably from matrix loss. Furthermore, the anionic to neutral photodetachment occurred in an approximately 1:1 relation assuming that there isn’t much change in the relative oscillator strengths of the various anionic and neutral complexes.

With these studies in mind, 20 K deposition was reinvestigated. Due to the higher temperature, we expect facile diffusion in the top layer to persist for a longer time than that of our 10 K study and for there to be some neutralization. Indeed a small population is neutralized upon deposition but what was not expected was the increased complexity of the anionic region of the spectrum due to the appearance of a large number of new peaks upon annealing the sample. Many resolution-limited bands are observed for species having nominally one vibrational absorbance in the IR. Furthermore, the neutralization of these peaks through photodetachment leads to neutral species that were not observed before.

These new bands seem to arise from a “trapped” transient photodetachment product which can be “relaxed” upon annealing to previously assigned complexes. The spectra of such studies are presented here along with possible explanations as to what might give rise to the observed transients as well as their connection to possible vertical detachment products.

5.3 Experimental

All of the studies contained in this chapter were performed under darkened conditions, with all internal sources of light turned off (ion gauges, RGA analyzer, etc.), and the lab lights kept off as well. The spectrometer beam was directed away from the deposition chamber when not recording spectra. Irradiation was performed using narrow-band LED sources centered at 590 nm and 470 nm (Thor Labs, see spectra Chapter 4 Figure 4.6) held outside the vacuum chamber and introduced through a Kodial glass viewport (Kurt J. Lesker Company).

All matrix samples were prepared by deposition of 4 nA Cu^- and Ar^+ counter-ions in an Ar matrix gas doped with either 0.02% CO for 20 K deposition or 0.0002% CO for 30 K deposition for 4 hours at 20 K (108 mmol total gas exposure). Isotopic gas mixtures were made using 99% ^{13}CO (< 5% ^{18}O , Sigma-Aldrich). All matrix gases were purified by flowing through a copper tube immersed in an ethanol liquid-nitrogen bath prior to deposition. Annealing up to 30 K was carried out by holding the sample at the specified temperature for 30 minutes then cooled back to 10 K in order to record a spectrum. Annealing to 40 K was done by holding the sample at temperature for 5 minutes before cooling to 10 K. We have found that samples deposited at higher temperatures can generally withstand higher annealing temperatures. This is attributed to the matrices being annealed during deposition to a higher extent, making them more crystalline and thus

making them less prone to vacuum sublimation. Matrices formed at 20 K and 30 K can be annealed briefly to 40 K and 45 K, respectively, before significant loss occurs.

5.4 Results

5.4.1 Annealing followed by irradiation

Figure 5.1 presents deposition at 20 K in the absence of light. As was seen in earlier 20 K deposition experiments,¹³⁸ all anionic copper carbonyl species are present along with the secondary-shell cluster. Furthermore, a small amount of neutral species are present upon deposition as well, which is in contrast to the “clean” deposition afforded at 10 K under which only anionic copper species are present.¹⁴³ Presumably the transient warm layer of the matrix persists long enough for a small population of anions to come in close enough proximity with a cation and directly transfer charge. Qualitatively the deposition is similar to that seen in our previous study when all lights were left on (Chapter 3) with some minor quantitative differences such as an increased amount of anionic dicarbonyl.

A big difference between this study and our previous studies occurred when the matrix is annealed. Annealing the matrix to 25 K (Fig. 5.1B) and 30 K (Fig. 5.1C) depletes several of the anionic bands while several new sharp bands appear slightly blue shifted to those that annealed away (subtraction spectra have been included in order to emphasize changes). Specifically the CuCO^- band at 1733.5 cm^{-1} loses intensity while the 1745.0 cm^{-1} grows in. Likewise, the anionic dicarbonyl peak at 1774.2 cm^{-1} is annealed away while a peak at 1784.6 cm^{-1} anneals in. The implications of this apparent population transfer are discussed below. The main anionic tricarbonyl peak at 1829.9 cm^{-1} does not change even though there is a growth of peaks to the red of this peak at 1823.1 cm^{-1} and 1826.0 cm^{-1} as well as peaks to the blue which sharpen out of the solvation shell complexes.

This increased complexity is an odd phenomena for matrix studies which normally use annealing as a way to simplify spectra by annealing away site-effects into a single stable band; instead the anionic region is becoming much more complicated. Furthermore, a large amount of neutral complexes appear after annealing (for a full list of matrix peaks, see Table 5.1 in the Appendix). Since the overall area of the anionic complexes is conserved, it is unclear at this point where the neutral complexes originate. It is possible these arise from free Cu^- centers that become neutralized and form complexes upon annealing, or from a small population of anionic complexes that become neutralized and have greater oscillator strengths in their neutral forms.

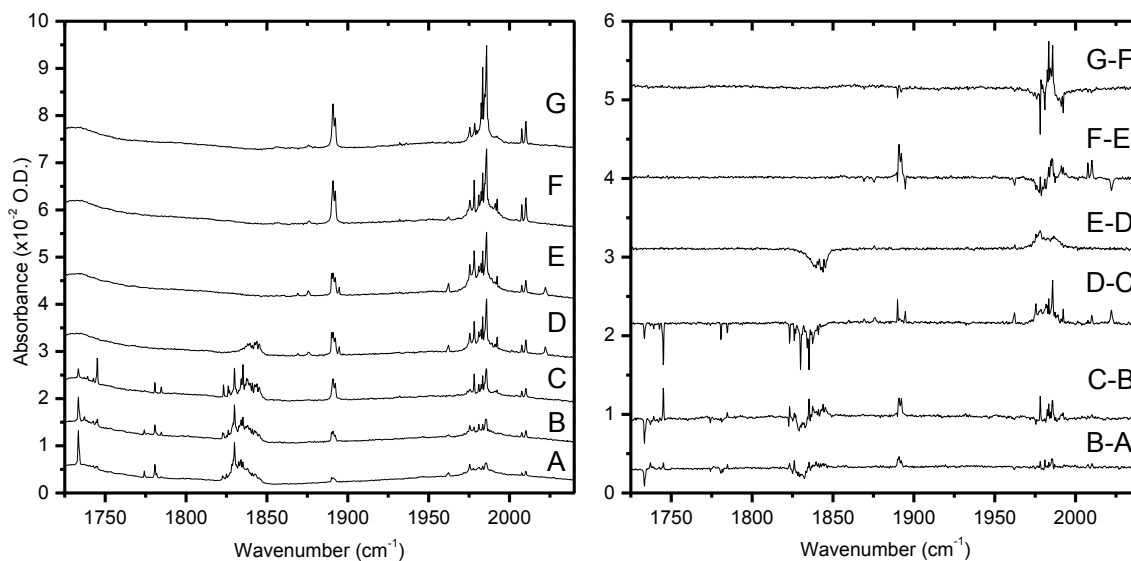


Figure 5.1 $\text{Cu}^- \text{Ar}^+$ co-deposited (4 nA each) for 4 hours with 0.02% CO in argon at 20 K: A) 20 K deposition, B) 25 K annealing, C) 30 K annealing, D) 590 nm irradiation, E) 470 nm irradiation, F) 30 K annealing, and G) 35 K annealing. All spectra taken at 10 K. Subtraction spectra included to emphasize changes.

Irradiation with a 590 nm centered, narrow-band LED causes photodetachment from all anions except for the $\text{Cu}(\text{CO})_3^-(\text{CO})_n^-$ species while their corresponding neutrals grow in. This result is consistent with previous photodetachment studies on the 10 K

deposition system with the exception of the solvated clusters which are not formed at the lower deposition temperature.¹⁴³ Further irradiation with 470 nm centered light depletes the remaining solvation shell anions. In addition to the expected neutral carbonyl species formed from photodetachment of the anionic precursors, new transient peaks also appear in the neutral copper carbonyl region. In particular, a transient monocarbonyl band at 2022.2 cm^{-1} and two transient dicarbonyl bands at 1889.9 and 1894.7 cm^{-1} are the focus of this study. There are also transient dicarbonyl bands at 1869.2, 1875.7, and 1876.2 cm^{-1} as well as tricarbonyl peaks at 1962.2, 1991.1, and 1992.3 cm^{-1} , none of which play a prominent role in the following discussion. These transient species are gone after 30K annealing with the exception of the 1991.1 cm^{-1} and 1992.3 cm^{-1} peaks which persist until 40 K annealing. These transients have important ramifications for our new deposition method and future studies as is discussed. In addition there is a large increase in the neutral intensities upon annealing after photodetachment. In particular, the dicarbonyl seems much larger than can be explained just from the initial intensity in the corresponding anion.

What is immediately obvious about most of the peaks observed is that they are sharp and baseline-resolved, causing us to take some high resolution (0.125 cm^{-1}) scans. Figure 5.2 shows the remarkable spectra with unprecedented resolution for peaks of ions deposition in argon. Most of these bands are resolution-limited and reveal how unique and clean this new deposition method is. It is also revealing to see how many peaks are present in each of these regions. The anionic monocarbonyl, for example, contains 5 absorbances while the anionic tricarbonyl contains at least 20 resolved bands. It is important to keep in mind that all these peaks arise from species with nominally one IR active mode. It is also revealing to see peaks which are inherently broad such as the neutral dicarbonyl bands at

1982.5 and 1983.4 cm^{-1} in comparison to the neutral dicarbonyl transient bands at 1890.0, 1894.3, and 1894.8 cm^{-1} , which are all resolution-limited.

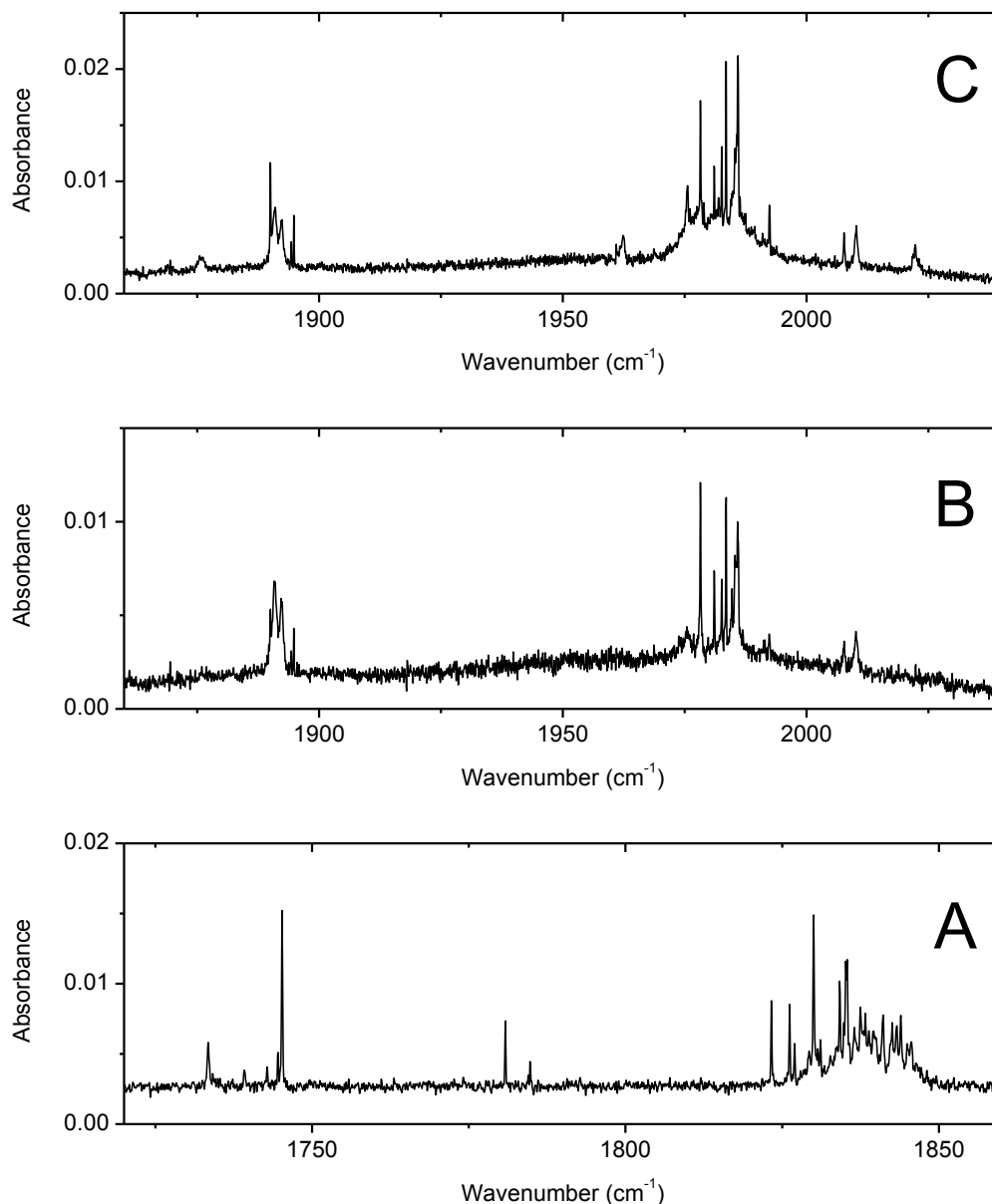


Figure 5.2 High resolution (0.125 cm^{-1}) spectra of Figure 5.1 after 30 K annealing of A) anionic region and B) neutral region. C) neutral region after 470 nm irradiation. In order to get spectrum A, the high resolution 30 K scan was subtracted from the irradiation scan in order to remove atmospheric water lines across this region. No anionic species remain after irradiation, so subtraction only removes water lines and does not affect the anionic spectrum. Since the atmospheric peaks are only present up to $\sim 1800 \text{ cm}^{-1}$, spectra B and C are both raw data with no background interferences.

5.4.2 Irradiation before annealing

A comparison experiment was performed whereby a matrix was deposited and irradiated before annealing. All deposition parameters remained the same as that in Figure 5.1 and therefore all species formed upon deposition remain the same (compare Figures 5.1A and 5.3A). However, when irradiation is performed before annealing, Figures 5.2B and 5.2C, several of the transient neutral species are never observed. In particular, the 2022.2 cm^{-1} and the 1894.7 cm^{-1} peaks no longer appear even after all anionic copper peaks are gone (see subtraction spectra in appendix Figure 5.8 for obvious differences). It is important to note here that since annealing was not performed while the anionic species were present, neither the 1745.0 cm^{-1} nor the 1784.8 cm^{-1} species are created. Their absence coincides with the absence of the neutral transient bands implying that the anionic species that are annealed in are precursors to the transient neutrals observed above as will be discussed in detail below.

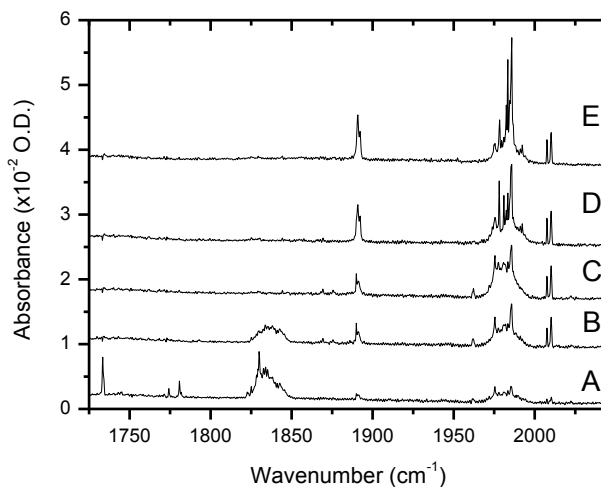


Figure 5.3 $\text{Cu}^- \text{Ar}^+$ co-deposited (4 nA each) for 4 hours with 0.02% CO in argon at 20 K: A) 20 K deposition, B) 590 nm irradiation, C) 470 nm irradiation, D) 30 K annealing, and E) 35 K annealing. All spectra taken at 10 K.

5.4.3 High-temperature assessment

Two experiments were performed to see if the new anionic species remain at higher temperatures. After forming the transient anionic peaks by annealing to 30 K (Figure 5.4B), the system was warmed to 40 K. As seen in Figure 5.4, both the 1745.0 and 1784.8 cm^{-1} peaks are annealed away, with the 1733.5 and 1780.8 cm^{-1} species regaining some of the lost intensity. In contrast, the peaks that sharpen out of the anionic tricarbonyl region remain at the higher temperature. Upon photodetachment, the neutral transient species are again absent, providing further support for the hypothesis that they arise from the anionic precursors (which were lost after 40 K annealing). Also, there are now clear differences in the tricarbonyl region after photodetachment. Only four bands are observed at 1975.5, 1982.5, 1983.4, and 1985.8 cm^{-1} and this spectrum did not change upon annealing. Furthermore, the overall population of neutral species did not change upon annealing after irradiation (compare this to Figures 5.1 and 5.2).

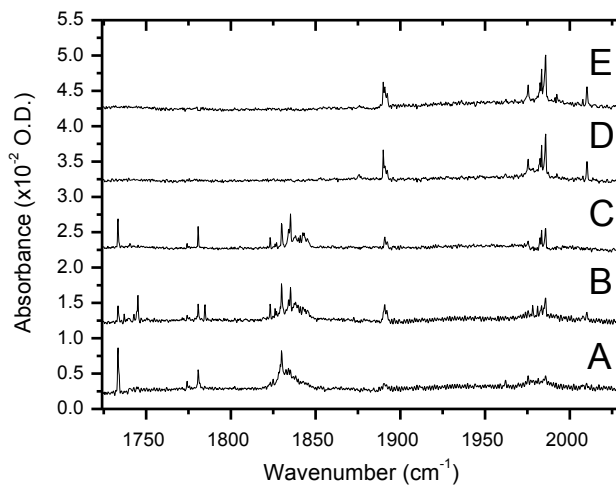


Figure 5.4 $\text{Cu}^- \text{Ar}^+$ co-deposited (4 nA each) for 2 hours with 0.02% CO in argon at 20 K: A) 20 K deposition, B) 30 K annealing, C) 40 K annealing, D) 470 nm irradiation, and E) 30 K annealing. All spectra taken at 10 K. (data taken by Michael Goodrich)

Since the anionic transients anneal in at 30 K, deposition was performed at 30 K to try and selectively deposit these transients (Figure 5.5). Due to increased clustering at the higher deposition temperature, a 2 ppm CO matrix was used, however this largely shifts the overall stoichiometry to the monocarbonyl. Upon deposition a large amount of 1745.0 cm^{-1} is present in comparison to 20 K, but none of the other transients are observed. There is also a new peak in the neutral region at 1970.2 cm^{-1} which has not been observed in previous studies. We observe previously assigned water complexes in our spectra at 2149.3 and 1572.9 cm^{-1} assigned in the literature to the CO-H₂O complex¹⁴⁰ and the Cu-H₂O species¹⁴⁴, respectively. Based on this observation, it is possible that the 1970 cm^{-1} band is due to a Cu-H₂O-CO complex. Furthermore, this species is lost upon 470 nm irradiation signifying that this could be an anionic species. An experiment using higher levels of 0.002% CO was attempted, but the increased clustering greatly shifts the complexation toward the tricarbonyl making it impossible to observe the 1745.0 or 2022.2 cm^{-1} bands (Figure 5.9, Appendix).

What is very interesting is the lack of the 2022.2 cm^{-1} peak which is suspiciously absent even though some 1745.0 cm^{-1} was present before irradiating. On the other hand, the 1962.5 cm^{-1} complex does appear even though the anionic tricarbonyl is very low. This 1962.5 cm^{-1} peak is annealed away at 40 K annealing. Using a 470 nm centered LED is able to get rid of the 1970.2 cm^{-1} peak. Unlike the previous studies, neutralization of these transients did not seem to add intensity to any other complex.

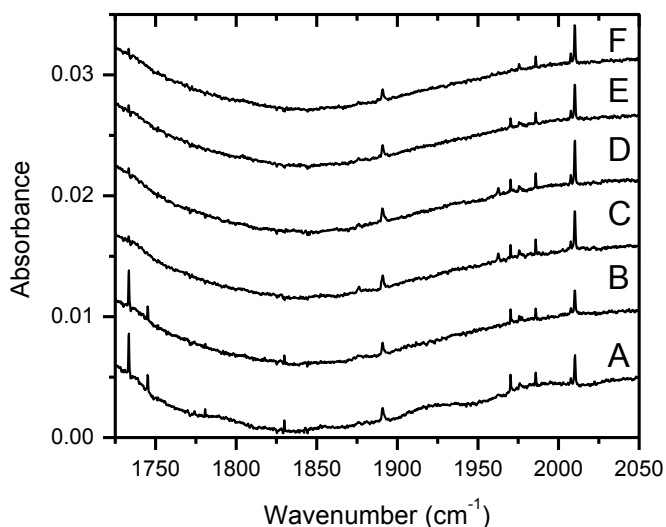


Figure 5.5 Cu⁻ Ar⁺ co-deposited (4 nA each) for 4 hours with 2 ppm CO in argon at 30 K: A) 30 K deposition, B) 35 K annealing, C) 590 nm irradiation, D) 30 K annealing, E) 40 K annealing, and F) 470 nm irradiation. All spectra taken at 10 K.

5.5 Discussion

Typically annealing a matrix leads to simplification of the spectrum, instead the anionic region presented here becomes much more complicated. All the copper species have nominally one infrared active mode yet give rise to multiple bands. Just as surprising, especially for argon, is that higher resolution scans show that most of these peaks contain resolution limited linewidths (see high resolution scan Figure 5.2). Upon annealing, the neutral complexes behave “normally” in that they move toward a more stable peak. As we do not understand why these changes are occurring, each of the mono-, di-, and tricarbonyl changes are discussed below in a phenomenological way. Possible explanations as to why these changes occur are also discussed as well as their connection to vertical-detachment products.

5.5.1 Cu-CO⁻ → Cu-CO

The easiest peak transitions to follow are those which arise from the monocarbonyl. The previously assigned anionic copper monocarbonyl at 1733.5 cm⁻¹ gives rise to a new peak at 1745.0 cm⁻¹ upon annealing to 30 K. A 50:50 ¹²CO:¹³CO doped matrix reveals this peak to arise from the copper monocarbonyl species (see isotopic spectrum, Figure 5.11.C). After irradiation, a peak at 2022.2 cm⁻¹ appears in the spectrum. Due to its broadness, it is difficult to assign this band in the isotope study although there seems to be another broad band at 2002.5 cm⁻¹ which may be the ¹³CO complex. The 2022.2 cm⁻¹ band is annealed away at 30 K with the concomitant 2-fold growth of the previously assigned neutral Cu-CO peaks at 2007.7 and 2010.2 cm⁻¹ (Figure 5.1F). If the system is not annealed when the anionic species are present such that the 1745.0 cm⁻¹ does not form, the 2022.2 cm⁻¹ does not appear upon neutralization. Likewise, annealing after neutralization does not lead to any increase in the 2007.7 or 2010.2 cm⁻¹ bands (Figure 5.8, Appendix). Finally, if the 1745.0 cm⁻¹ is annealed away at 40 K before irradiation (Figure 5.4C), the 2022.2 cm⁻¹ does not appear after neutralization and once again the 2007.7 and 2010.2 cm⁻¹ peaks do not gain intensity upon further annealing. We can therefore draw the following reaction scheme:

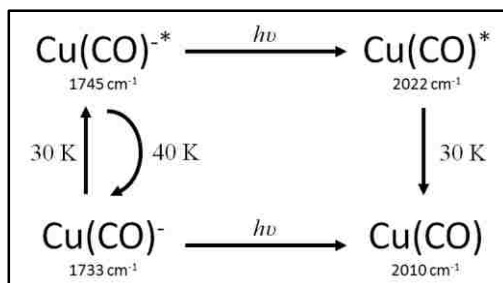


Figure 5.6 Reaction scheme for the copper carbonyl complex. The asterisks denotes a transient complex. A curved arrow is used to emphasize that the “back” process happens only at 40 K.

The 30 K deposition study is strange in that the 2022.2 cm⁻¹ is not formed even though a large fraction of 1745.0 cm⁻¹ is present upon deposition (see Figure 5.5). This makes sense upon deposition since any 2022.2 cm⁻¹ that is formed should be rapidly converted to the more stable 2010.2 cm⁻¹ at 30 K; however, irradiation should have led to a population of the 2022.2 cm⁻¹, which did not occur. Since we do not know precisely what mechanism gives rise to these peaks (see section 5.5.4), it is difficult to speculate about these high-temperature results at this time.

5.5.2 Cu(CO)₂⁻ → Cu(CO)₂

A similar situation exists for the dicarbonyl species. Two peaks are present for the anionic dicarbonyl upon deposition, at 1774.2 cm⁻¹ and 1780.7 cm⁻¹, both of which have been observed in our previous studies at 10 K deposition. Annealing to 30 K destroys the 1774.2 cm⁻¹ band and slightly decreases the 1780.7 cm⁻¹ peak while a new band at 1784.8 cm⁻¹ grows into that region (see subtraction data, Figure 5.1C-B). Just as in the anionic monocarbonyl system, 40 K annealing transfers the population from the 1784.8 cm⁻¹ species back to the 1780.7 cm⁻¹ signal (Figure 5.9C-B, Appendix). In isotopic studies, the 1784.8 cm⁻¹ peak is overlapped by the ¹³CO-tricarbonyl compound and its mixed isotopomer was not intense enough to observe in those studies.

The neutral dicarbonyl species consists of six peaks. Two peaks at lower wavenumbers of 1869.2 and 1875.7 cm⁻¹ are present upon irradiation and disappear upon subsequent annealing to 30 K. In the high temperature annealing study (Figure 5.4) the 1875.7 cm⁻¹ peak is present upon irradiation regardless of the fact that the 1784.8 cm⁻¹ precursor is not present. It is difficult to determine whether the 1869.2 cm⁻¹ species is also present due to its inherent broadness and weak intensity. It should also be noted that the

30 K deposition study does not have either of these two peaks but instead contains a new transient at 1876.2 cm^{-1} (Figure 5.5).

The other four neutral bands, all of which show expected isotope behavior for a dicarbonyl, are much more interesting to track and play a more prominent role toward the vertical detachment explanation below. Upon annealing the deposited matrix, two peaks at 1890.9 cm^{-1} and 1892.3 cm^{-1} anneal in (Figure 5.21C-B). On the other hand, irradiation leads to bands at 1889.9 cm^{-1} and 1894.7 cm^{-1} (Figure 5.1D-C). A high-resolution spectrum reveals that the 1894.7 cm^{-1} band is actually a doublet at 1894.3 and 1894.8 cm^{-1} but for clarity will be considered here as one peak. Upon annealing to 30 K after irradiation, both of the two “outer” transient bands anneal into the two inner bands (Figure 5.1F-E). Further annealing to 35 K, reduces more of the 1889.9 cm^{-1} band as well as the 1892.3 cm^{-1} band while the 1890.9 cm^{-1} peak gains some intensity. Although these are very minor changes compared to the rest of the processing steps, deposition at 30 K creates only the 1890.9 cm^{-1} peak; therefore, it seems as though the 1890.9 cm^{-1} species is the most stable form of the neutral dicarbonyl. When the matrix is processed at 40 K, irradiation leads only to the 1889.9 cm^{-1} species which is then annealed into the 1890.9 cm^{-1} band. It is difficult to tell if the 1892.3 cm^{-1} peak also increases since these changes are very small in the subtracted data (Figure 5.9E-D, Appendix). Based on the above observations, we can write the following dicarbonyl reaction for 20 K deposition:

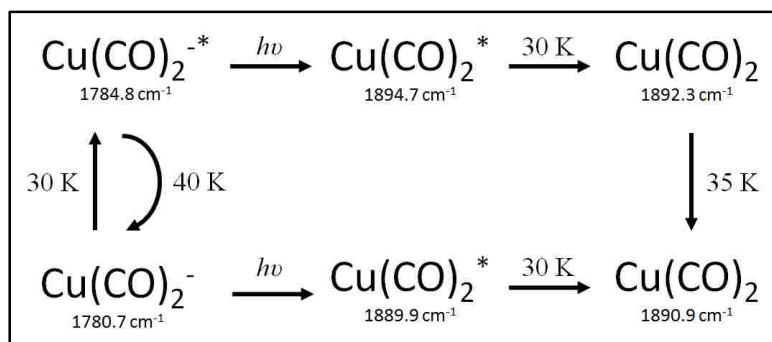


Figure 5.7 Reaction scheme for the copper dicarbonyl complex. The asterisks denote a transient complex. A curved arrow is used to emphasize that the “back” process happens only at 40 K .

5.5.3 $\text{Cu}(\text{CO})_3^- \rightarrow \text{Cu}(\text{CO})_3$

The tricarbonyl species is much more difficult to follow due to the number of peaks observed in this region and exact reactions cannot be made at this time, however, some points are worth mentioning. Throughout the annealing steps, the 1829.9 cm^{-1} band does not seem to change despite many sharp peaks arising from this area. This is interesting because both the anionic mono- and di-carbonyl systems lost intensity in their main bands which gave rise to anionic transients. Likewise, when annealing the anionic system to 40 K the new bands near the anionic tricarbonyl are relatively unchanged although some unresolved changes do take place (Figure 5.9C-B, Appendix). This again is in contrast to both the anionic mono- and di-carbonyl systems. The changes occurring in the tricarbonyl region do not appear to be due to transient species or at the very least are not due to the same phenomena that alter the other two systems. Since a large population of the anionic tricarbonyl contains some CO in an outer solvation shell, the changes observed could be due to these secondary molecules rearranging to create more stable structures. Besides two peaks at 1823.1 cm^{-1} and 1826.0 cm^{-1} that gain intensity to the red of the anionic tricarbonyl compound, all other changes occur to the blue in the solvation shell region. One feature

that is very prominent in the spectrum is a triplet at 1832.5, 1834.0, and 1835.2 cm^{-1} . Upon annealing, the 1832.5 cm^{-1} peak loses intensity while the 1835.2 cm^{-1} peak becomes more intense than the normal tricarbonyl band.

Irradiation with 590 nm centered light photodetaches most of the anionic tricarbonyl region with the exception of the larger solvation shell clusters. These are able to photodetach with UV light centered at 470 nm. One possible explanation is that the extra energy is needed for the electron to escape the surrounding CO-containing cage. The unresolved broad anionic feature clearly neutralizes into the unresolved broad region between the neutral tricarbonyl peaks (Figure 5.1E-D). The overall area of the broad region is roughly the same between the anionic and neutral spectra. This same trend is seen when irradiation is performed without annealing (Figure 5.8C-B, Appendix). The neutral tricarbonyl region has peaks which sharpen and gain intensity as the system is heated. It seems as though the entire system is annealing toward the 1985.8 cm^{-1} at the higher temperatures.

Although the overall trends cannot be followed at this time, there are a few differences between the different experiments that should be mentioned. First, one peak worth noting is the 1978.1 cm^{-1} band which is present whether the anionic system is annealed first or not, however, it is not there when the system has been heated to 40 K. Also, the 1975 cm^{-1} to 1985 cm^{-1} ratio is much greater when the anionic bands are annealed to 40 K before irradiation. Likewise deposition of 0.002% CO at 30 K (Figure 5.10, Appendix) leads to a large amount of both the 1975 and 1985 cm^{-1} bands. Both these studies and our previous studies are consistent with the 1975 cm^{-1} band being the $\text{Cu}(\text{CO})_4$ species however previous isotope studies (Chapter 4) suggest this peak contains three

equivalent CO ligands. It is possible that the fourth CO-ligand might show up somewhere else, but as of now we have no evidence for this. An isotope study at the higher temperature may be warranted for a future study. Finally the lowest CO concentration at 30 K (Figure 5.5) contains a new peak at 1970.2 cm^{-1} . This does not change upon annealing even up to 40 K but instead goes away upon 470 nm irradiation. Also, upon irradiating the anionic peaks with 590 nm light, a transient at 1962.5 cm^{-1} is present which anneals away at 40 K. The loss of these two peaks does not seem to add intensity to any other species and it is uncertain why they go dark under these conditions.

5.5.4 Possible explanations for anionic transient formation

One major point that is not understood is why the anionic transient peaks arise. Each individual species is presented below, but it seems as though the phenomenon which gives rise to these peaks should be generally the same for each species. A simple explanation is that the complex changes geometry upon annealing which would lead to a change in frequency. It is hard to imagine why this would occur spontaneously even with the matrix moving toward a more crystalline form. If structural geometry is changing, it seems as though this must be driven by another process occurring in the matrix. Another possibility is that another CO molecule gets close enough to perturb the vibrational frequency. Indeed we have assigned peaks that are blue shifted from the anionic tricarbonyl to such secondary shell molecules,¹³⁸ which would be consistent with these new transients also blue shifting. The problem with this explanation is that isotope studies do not show any unexplained peaks, i.e. all isotopic peaks can be explained based on their parent species. Also, this type of diffusion-like process should shift the complexes toward larger stoichiometries which does not seem to occur.

Since cations and anions must be present in order to maintain charge balance, these peaks could arise due to ion-ion interactions. Deposition at 20 K forms a portion of neutral species whereas 10 K deposition (Chapter 4) isolates only anionic complexes; therefore, anions and cations in the surface layer of the forming matrix must be getting close to each other at 20 K, close enough that some population is able to transfer charge. It is interesting to note here that these transients are not observed when processing a 10 K sample which is consistent with the ions getting trapped far enough apart at the colder deposition such that they cannot anneal close to each other. All of these explanations become very complicated when considering the high temperature annealing at 40 K before irradiation (Figure 5.4C) which transfers population from the transients back to their precursor anionic peaks. If secondary molecules were causing a change, higher temperature annealing should lead to clustering. Likewise if ion pairs create the observed shift, then high temperature annealing should lead to neutralization.

There is also a third possibility that should be mentioned: the spectral changes are due to a temperature-dependent change in the argon matrix. This change in the cage structure could induce the observed shifts. Although there is no precedent to believe that a temperature-dependent argon transition exists, it would explain the issues described above.

5.5.5 Vertical detachment products: an explanation for neutral transients

Regardless of what causes the anionic transient bands to form, the neutral transients must arise from the anionic transient precursors. These bands only form from irradiation of the anionic transient system. Furthermore, they anneal away to previously assigned bands.¹³⁸ It seems that whatever form they exist in as anions becomes trapped as neutrals

in the energy dissipating environment upon irradiation. They are then able to “relax” to stable geometries upon annealing. This behavior is very reminiscent of vertical detachment, which can arise when the geometry of an ion differs from that of the neutral molecule, as is often the case. A vertical detachment product is the result of an ion that has been neutralized or neutral molecule that has been ionized and the resulting complex remains trapped in the precursor geometry. This is in contrast to adiabatic ionization which is the lowest energy necessary to detach an electron and leads to the lowest, relaxed geometry of a system.¹⁴⁵ Furthermore, according to the Franck-Condon principle the vertical ionization energy is always greater than the adiabatic ionization energy.¹⁴⁵ This property could be used in future wavelength-dependent photodetachment studies experiments if selective wavelengths can be used to neutralize precursors *versus* transients.

5.6 Conclusions

The power of this new deposition method toward the formation and stabilization of transient bands has been presented. Though a small population of ions become neutralized upon deposition, this method is still much cleaner and under more control than previous ion deposition methods. Different combinations of heating and irradiation afford us the ability to follow reactions by forming intermediates and/or products. Indeed this is what we set out for with the development of freeze-frame spectroscopy. Future studies involving very-narrow wavelength filters should allow us to follow these reactions in greater depth. Furthermore, in-depth information should be gained by deposition of metal-cluster ions in future reaction studies.

Future studies will also involve deposition of spectroscopically active counter-cations such that ion-ion interactions in the matrix can be followed if any are occurring. Selection of such cations could afford us another level of control in that smaller mobile cations could be used to follow annealing changes or larger cations that should not diffuse readily can be deposited. Finally, many of the neutral transients stabilized here are reminiscent of vertical detachment products. Success of isolating such species is critical in moving forward with this project. It is proof that we not only can form such unstable intermediates, but we have the ability to move them along potential energy surfaces by the introduction of heat or light.

5.7 Appendix

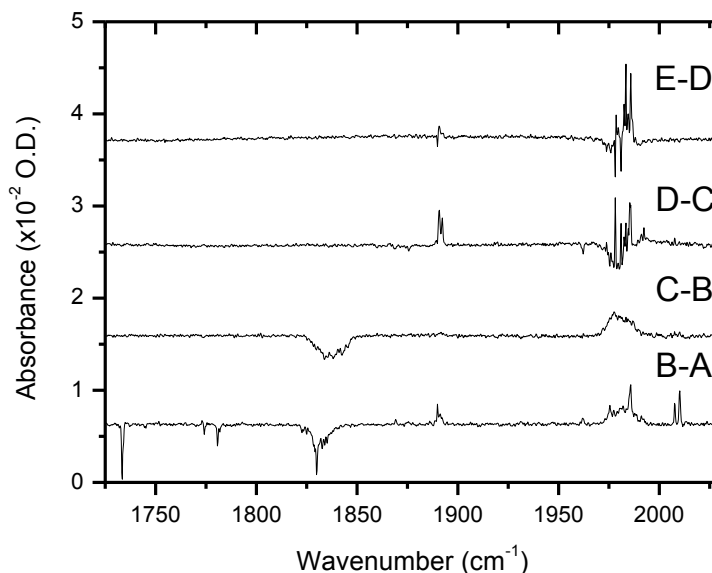


Figure 5.8 Subtraction data from Figure 5.3 showing differences for: B-A) 590 nm irradiation, C-B) 470 nm irradiation, D-C) 30 K annealing, and E-D) 35 K annealing.

Table 5.1 Peak assignment for high temperature, 20 K and 30 K, deposition. Wherever possible, peak position was based on high-resolution scan (0.125 cm^{-1})

Parent Species	Wavenumber (cm^{-1})		Parent Species	Wavenumber (cm^{-1})	
$\text{Cu}(\text{CO})^-$	1733.5	A	$\text{Cu}(\text{CO})$	2007.7	B
	1737.1	A		2010.2	B
	1739.2	B		2022.2	C
	1742.6	B			
	1745.0	B			
$\text{Cu}(\text{CO})_2^-$	1774.2	A	$\text{Cu}(\text{CO})_2$	1869.2	C
	1780.8	A		1875.7	C
	1781.9	A		1876.2	C
	1784.8	B		1889.9	C
				1890.9	B
				1892.3	B
				1894.7	C
$\text{Cu}(\text{CO})_3^-$	1823.1	B	$\text{Cu}(\text{CO})_3$	1962.2	C
	1825.1	A		1962.5	D
	1826.0	B		1970.2	D
	1827.0	B		1975.5	
	1830.0	A		1978.1	A
	1832.5	A		1981.0	A
	1834.0	A		1982.5	B
	1835.2	A		1983.4	B
	1836.6	B		1984.6	B
	1837.5	B		1985.8	B
	1838.1	B		1991.1	C
	1839.8	B		1992.3	C
	1841.0	B			
	1842.4	B			
	1843.1	B			
	1843.9	B			
	1845.3	B			

A – peak present upon deposition

B – peak annealed in

C – transient peak upon photodetachment

D – only present at 30 K deposition

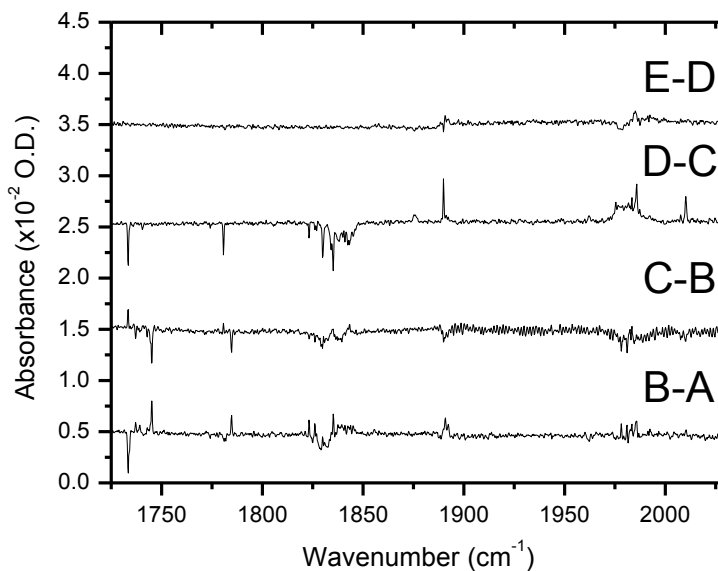


Figure 5.9 Subtraction data from Figure 5.4 showing differences for: B-A) 30 K annealing, C-B) 40 K annealing, D-C) 470 nm irradiation, and E-D) 30 K annealing.

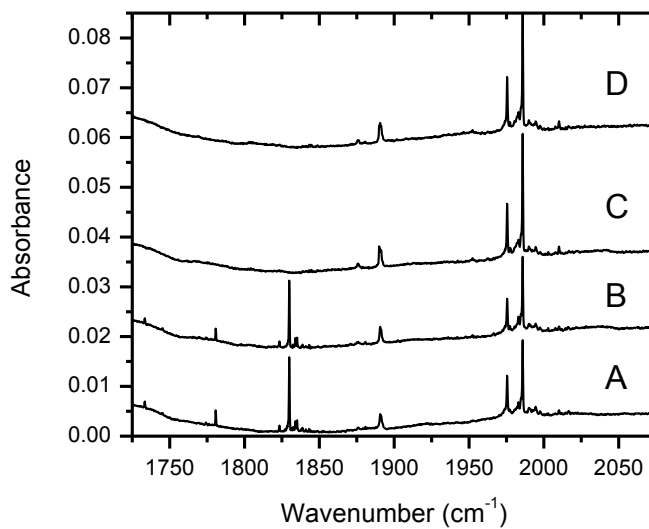


Figure 5.10 $\text{Cu}^- \text{Ar}^+$ co-deposited (4 nA each) for 4 hours with 0.002% CO in argon at 30 K: A) 30 K deposition, B) 35 K annealing, C) 590 nm irradiation, and D) 30 K annealing.

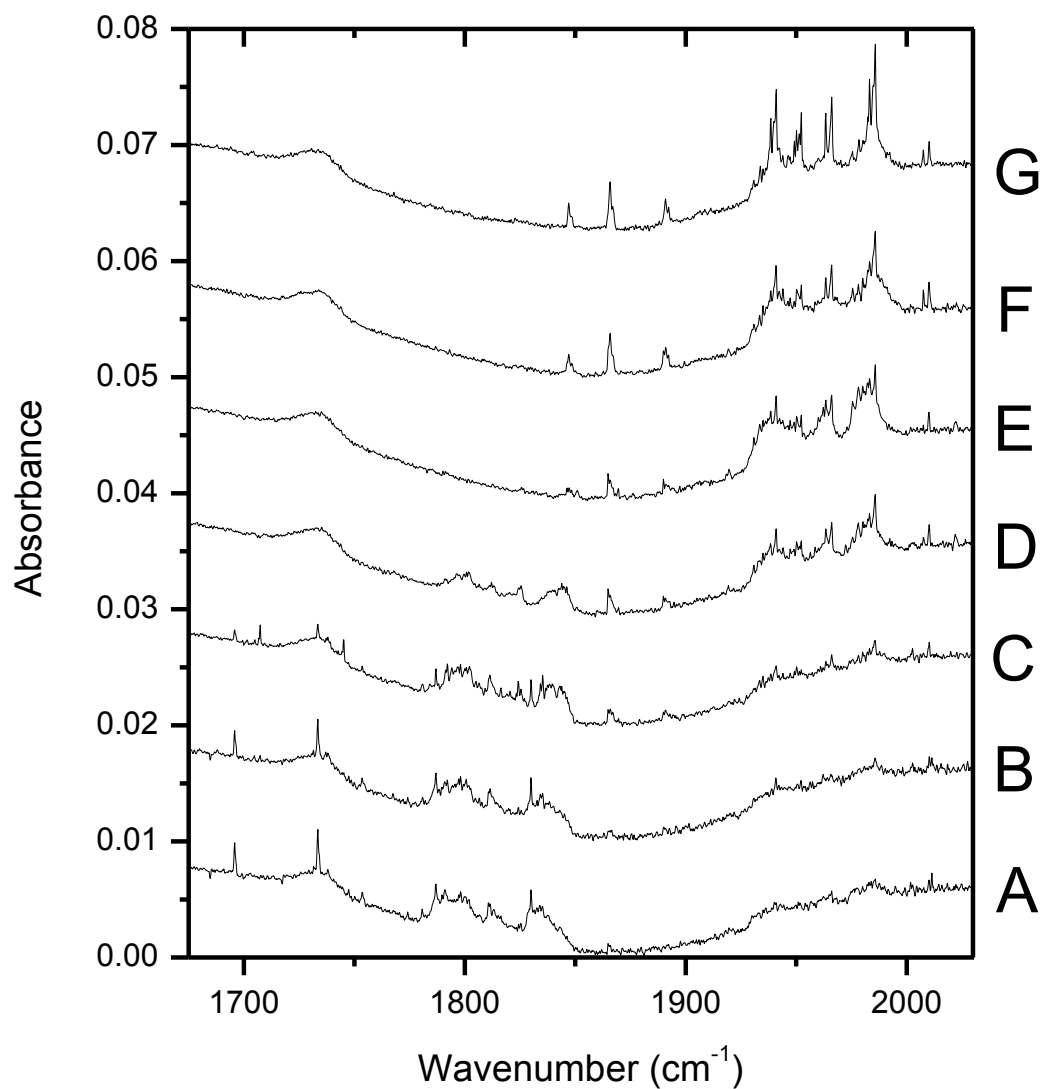


Figure 5.11 Cu⁻ Ar⁺ co-deposited (4 nA each) for 6 hours with 0.02% ¹²CO + 0.02% ¹³CO in argon at 20 K: A) 20 K deposition, B) 25 K annealing, C) 30 K annealing, D) 590 nm irradiation, E) 470 nm irradiation, F) 30 K annealing, and G) 35 K annealing.

Chapter 6

Identification of $(\text{CO})_2^+$ in argon matrices

Data in this chapter were collected with assistance of undergraduate research student, Jin Nam Ahn. All data workup presented here and analysis were performed by Ryan Ludwig.

6.1 Abstract

The CO^+ and $(\text{CO})_2^+$ species have been well-known ions in neon matrices where they are formed under plasma deposition techniques. Likewise, $(\text{CO})_2^-$ is also formed in these experiments by trapping of an electron by the $(\text{CO})_2$ cluster. The CO-dimer anion has also been observed in CO-doped argon matrices formed as a byproduct of laser ablated metals. In these studies, however, no CO or CO-cluster cations were observed. Using our deposition system under high energy Ar^+ settings, bombardment of CO-doped argon matrices forms several ionic CO species. Two bands near 1513 and 1516 cm^{-1} have been observed and assigned by previous groups to be the $(\text{CO})_2^-$ anion. We also observe a new peak in this region at 1522 cm^{-1} which is tentatively assigned to CO^- . In order for the matrix to maintain charge balance, cationic species are also formed. Two new peaks at 2047 and 2048 cm^{-1} are assigned to the $(\text{CO})_2^+$ complex based on isotopic shifts and our previous observations that these peaks are formed and contain the same behavior regardless of metal that is used. Finally, a peak is observed at 2181 cm^{-1} . This position is near the neon value for CO^+ and may be due to this ion; however, the frequency of any isotopically labeled molecule will be covered by the large, neutral CO bands and a definitive assignment cannot be made at this time.

6.2 Introduction

The CO dimer has long been known to be a stable molecule.¹⁴⁶ Even early matrix-isolation studies showed complexities in the vibrational spectrum of CO-doped matrices^{147,148} which Pimentel later proposed was due to CO clusters that are easily formed under typical deposition conditions.¹⁴⁹ The exact identification of these clusters was long debated,^{55-58,150-152} until Yamada's experiments in which both the 2136.1 and 2138.5 cm^{-1} bands were assigned to the CO monomer, the 2140.1 cm^{-1} signal to the CO-dimer, and a peak at 2149 cm^{-1} to the CO-H₂O complex.⁵⁹

The $(\text{CO})_2^+$ cation has also been studied in gas-phase experiments for many years. The CO-dimer cation was first observed through use of mass spectroscopic studies by the Franklin group, who showed that it readily forms with CO partial pressures below 100 Pa and low electron energies.¹⁵³ Franklin extended these studies to high pressure reactions of methane with CO^+ and $(\text{CO})_2^+$.¹⁵⁴ Using photoionization techniques, Linn measured the molecular dissociation energy for the formation of $\text{CO} + \text{CO}^+$ to be 0.97 eV,⁵³ which was in agreement with previous studies.¹⁵⁴⁻¹⁵⁶ More recently, the ground-state dissociation energy has been estimated to be greater than 1.29 eV.¹⁵⁷ In 1982 Knight and coworkers first isolated the CO^+ species in a neon matrix, detected *via* ESR spectroscopy,¹⁵⁸ and extended these studies to include the $(\text{CO})_2^+$ species.¹⁵⁹ This study also included *ab initio* calculations which predicted the charge to be delocalized with a planar *trans*, ground-state structure and CCO bond angles of 141°.¹⁵⁹ Weinhold later performed detailed calculations of the potential energy surface to account for the exceptionally high photodissociation energy which was consistent with the earlier prediction of the structure.^{160,161}

The $(\text{CO})_2^-$ was not observed in early mass-spectroscopic studies, however calculations predicted that the ground state should be bound and stable with respect to the separated $\text{CO} + \text{CO}^-$ molecules.¹⁶² Similar to the dimer-cation, the dimer-anion was predicted to have charge delocalization and adopt a planar *trans*-structure with CCO valance angles of 143° .¹⁶³ These calculations were supported by Schaefer, who predicted the ground state to be a *trans*-bent, C_{2h} structure with the bond angle near 150° .¹⁶⁴ The first experimental evidence came from Margrave who deposited CO and Li in cryogenic matrices which spontaneously formed a $\text{Li}^+\text{C}_2\text{O}_2^-$ complex observed by IR spectroscopy (Chapter 1).¹⁶⁵ Similarly, Silvia observed two IR bands for the $\text{Na}^+\text{C}_2\text{O}_2^-$ complex in argon which corresponded to calculations for the planar *trans* structure with angles near 170° .¹⁶⁶ Franklin has reported an electron affinity of 1.37 eV for CO, but definitive spectral data for CO^- have not yet been reported.¹⁶⁷

Using a microwave discharge source (see Chapter 1 for details), Jacox was able to create and stabilize CO^+ , C_2O_2^+ , and C_2O_2^- in a neon matrix.¹⁶⁸ They assigned a peak at 2194.4 cm^{-1} to the CO^+ species which was only shifted by 10.5 cm^{-1} from the gas-phase value of 2183.9 cm^{-1} . A peak at 2056.6 cm^{-1} was assigned to C_2O_2^+ redshifted from the CO frequency. This lower frequency was rationalized by bond lengths determined experimentally for CO and CO^+ to be 1.128 \AA and 1.115 \AA ,¹⁶⁹ respectively, and a calculated bond length of $\sim 1.14 \text{ \AA}$ for the *trans*- OCCO^+ species.^{159,160} Finally, a band at 1520 cm^{-1} was assigned to C_2O_2^- as well as a combination band at 2041 cm^{-1} from the ν_3 (bend) + ν_5 (CO stretch), though they could not rule out that the band at 2041 cm^{-1} was not due to CO^- .¹⁶⁸ The computational study by Schaeffer was in excellent agreement with Jacox's experiments, including isotopic predictions within a few wavenumbers.¹⁶⁸

Andrews also observed these species in neon, with similar frequencies to those observed by Jacox.¹²⁹ The laser-ablation source naturally generated such species as byproducts during the deposition of ablated metals. The CO^+ and $(\text{CO})_2^+$ species are formed near the highly energetic deposition region and the $(\text{CO})_2^-$ was assumed to form from capture of an electron by the van der Waals CO-dimers.¹²⁹ When CCl_4 was added to neon as an electron trap, both the CO^+ and $(\text{CO})_2^+$ bands doubled in intensity while the yield of $(\text{CO})_2^-$ was reduced. The cationic bands presumably increased in yield since there were not as many free electrons to neutralize these species whereas the anion decreased since fewer electrons were available for capture by the neutral CO-dimer compound. In Andrews' copper-CO study in argon, a peak at 1515.5 cm^{-1} was assigned to the $(\text{CO})_2^-$ and a peak at 1512.9 cm^{-1} was assigned to a site peak of the dimer anion, however, neither the CO^+ nor the $(\text{CO})_2^+$ were observed.

In this chapter, the $(\text{CO})_2^+$ resonance is assigned for the first time in argon. This species has been observed in all of our previous metal-CO experiments and does not change based on the metal in use (Figure 6.4). In order to rule out any metal perturbations, high energy Ar^+ bombardment is used to produce ionic CO species in the matrix without the use of explicit counter-ions such as a metals; therefore, all ionic peaks are believed to only contain CO-units.

6.3 Experimental

For these studies, the deposition and subsequent processing steps were carried out under darkened conditions. Irradiation studies were performed using several narrow-band LED sources (see spectra, Chapter 4). Gas mixtures were prepared by dilution of a purchased mixture of 10% CO in He (PRAXAIR) down to a 2% CO with Ar (PRAXAIR,

99.9999%) for 10 K deposition studies or 0.5% for 20 K deposition. Isotopic gas mixtures were made using 99% ^{13}C O (< 5% ^{18}O , Sigma-Aldrich). All matrix gases were purified by flowing through a copper tube immersed in an ethanol-liquid nitrogen bath prior to deposition. Ionic CO species were formed *in situ* by bombardment of ~60 nA of 400 eV Ar^+ throughout matrix deposition, which ionizes CO clusters, a process that occurs spontaneously, presumably due to the difference in ionization potentials and the high Ar^+ kinetic energies employed (Chapter 1). As far as we can tell, no other ionic species are formed other than those derived from CO units. We believe this is due to the low levels of contaminants in our system such as H_2O , CO_2 , and O_2 which should readily ionize under these conditions if present at sufficient concentrations.

6.4 Results

6.4.1 High energy Ar^+ bombardment

Figure 6.1A shows a high-resolution spectrum after a 4 hour deposition at 20 K of 400 eV Ar^+ into a 0.5% CO in argon matrix. Two spectral regions are shown: an anionic region near 1515 cm^{-1} and a cationic region near 2050 cm^{-1} . The anionic region contains two peaks around 1513 and 1516 cm^{-1} which are reminiscent of $(\text{CO})_2^-$ bands observed in previous argon experiments,^{88,129} and a new peak at 1522 cm^{-1} which has nearly equal intensity to the 1513 cm^{-1} species. There are also a few low intensity, broad peaks in that region as well (Figure 6.7, Appendix). A complete listing of the observed ionic bands and their assignments are given in Table 6.1.

Two other peaks that were not observed in the previous studies appear in our spectrum at 2047 and 2048 cm^{-1} and are assigned to the $(\text{CO})_2^+$ species. These bands were present in all our previous metal carbonyl experiments at 20 K as well, and had the same

vibrational frequency regardless of metal used (Figure 6.4, Appendix). Irradiation with wavelengths employed in this study longer than 470 nm, had no effect on the spectra. With 470 nm centered light (Figure 6.1F), all peaks, except the 1522 cm^{-1} band, began to decrease. The 1522 cm^{-1} peak seems to not be affected even with wavelengths down to 365 nm.

Table 6.1 Vibrational band positions (in cm^{-1}) for $(\text{CO})_2^q$ [$q=-1,+1$] species in argon matrices

Species	10 K (cm^{-1})	20 K (cm^{-1})
CO^+	2180.6	2180.6
$(\text{CO})_2^+$		2047.0
	2047.8	2047.9
$(\text{CO})_2^-$	1513.0	1513.1
		1514.7
	1515.5	1515.8
	1519.7	1519.9
CO^-	1521.8	1522.0
		1526.4

A weak band at 2180 cm^{-1} is also present in our spectra. This band has been observed in previous experiments by our group while studying metal carbonyl complexes, but has never been so clearly present as it is under high-energy deposition. This band also follows the general irradiation trends observed for the anionic and cationic species observed in Figure 6.1. Based on this trend and its location, we tentatively assign this band to a CO^+ species (see Discussion section for details).

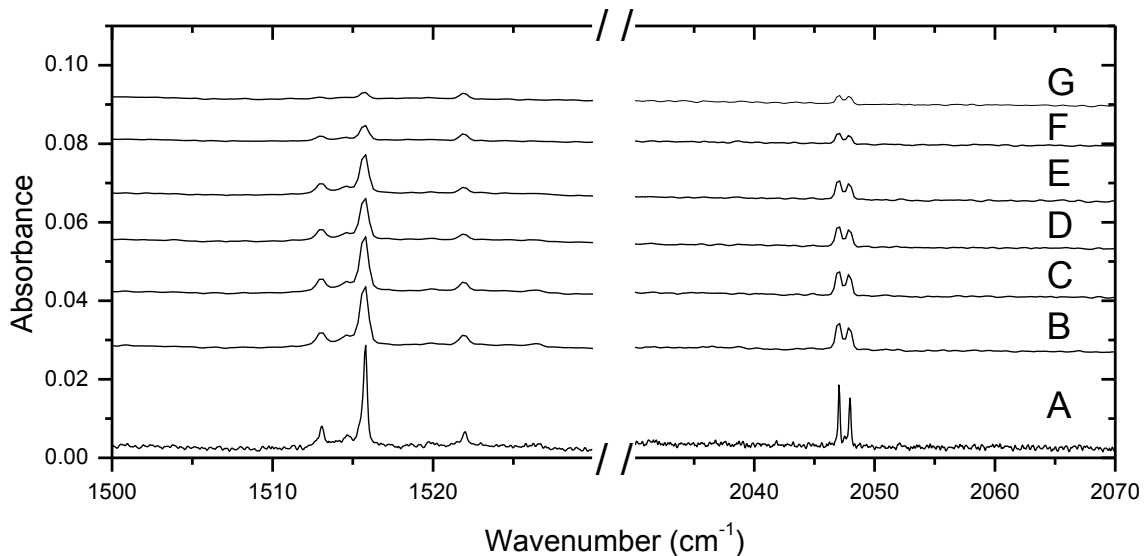


Figure 6.1 400 eV Ar⁺ deposition into 0.5% CO in excess Ar matrix, deposited for 4 hours at 20 K. A) 20 K, 0.125 cm⁻¹ resolution, B) 20 K, 0.5 cm⁻¹ resolution, C) 735 nm, D) 660 nm, E) 590 nm, F) 470 nm, and G) 365 nm. All spectra taken at 10 K. Irradiation performed for 5 minutes with specified LEDs while sample at 10 K.

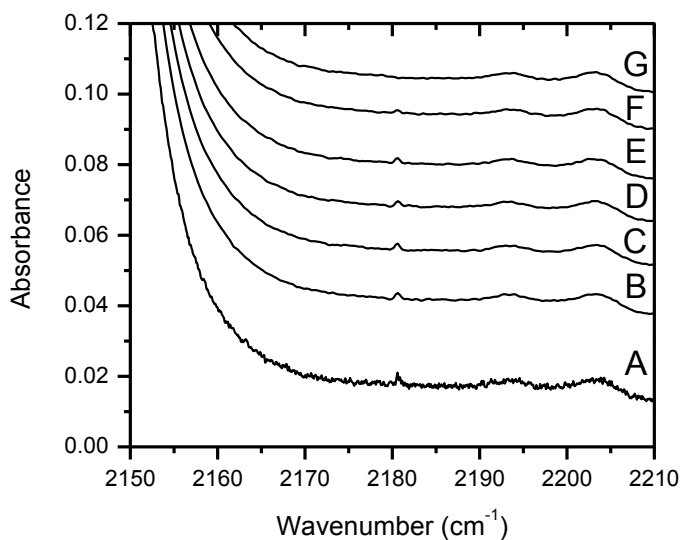


Figure 6.2 Same sample as Figure 6.1 showing a low intensity band blue-shifted from the main CO peak. This is near where CO⁺ should show up and follows the same irradiation trends as the other ionic peaks: A) 20 K, 0.125 cm⁻¹ resolution, B) 20 K, 0.5 cm⁻¹ resolution, C) 735 nm, D) 660 nm, E) 590 nm, F) 470 nm, and G) 365 nm. All spectra taken at 10 K.

6.4.2 Isotopic studies

An isotopic sample was prepared with high energy Ar^+ bombardment in a 0.5% ^{13}CO + 0.5% ^{12}CO in argon matrix (Figure 6.7). Both the 1516 and 1513 cm^{-1} bands show a 1:2:1 intensity ratio consistent with two chemically equivalent CO units. The new band at 1522 cm^{-1} is a bit more difficult to track due to its inherent broadness, however, there is a new peak in the anionic isotope spectrum at 1508.1 cm^{-1} which does not line up with any other bands. Furthermore, this has roughly the same intensity and broadness as observed for the 1522 cm^{-1} and is assigned to the all ^{13}CO species of the 1522 cm^{-1} band. Based on this 1:1 isotope ratio, the 1522 cm^{-1} peak is found to arise from a single-CO unit.

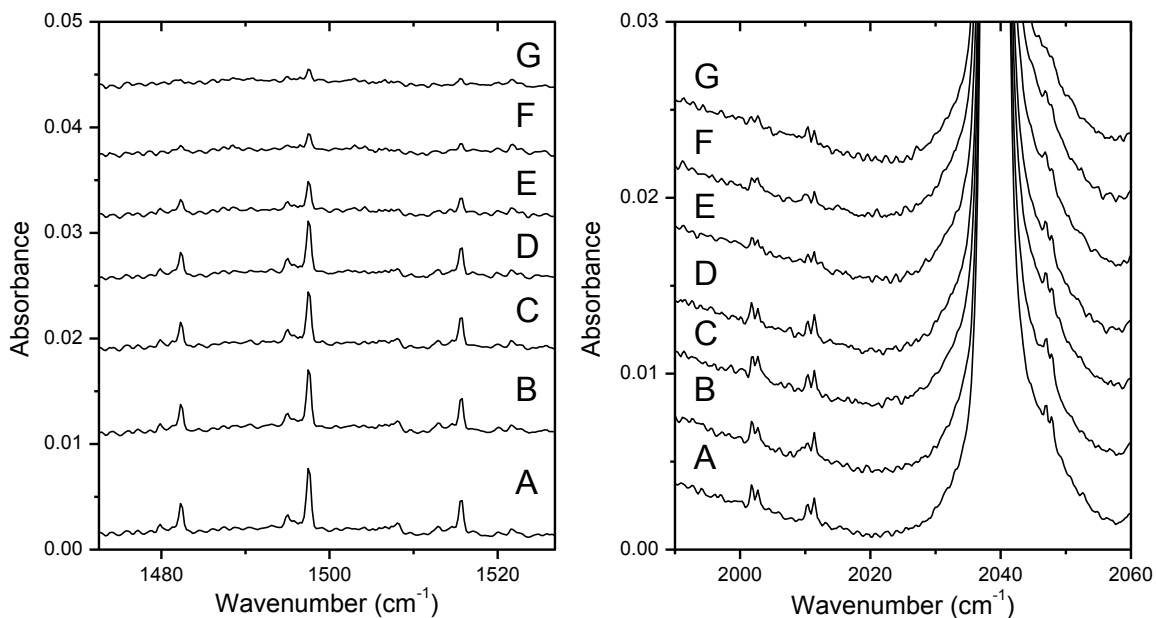


Figure 6.3 400 eV Ar^+ deposition into 0.02% ^{12}CO + 0.02% ^{13}CO in excess Ar matrix, deposited for 4 hours at 20 K: A) 20 K deposition, B) 735 nm, C) 660 nm, D) 590 nm, E) 470 nm, F) 365 nm, and G) 30 K annealing.

In the cationic region, a mixed isotopomer doublet at 2010.4 and 2011.4 cm^{-1} and a doublet for a completely substituted ^{13}CO species at 2001.7 and 2002.7 cm^{-1} are observed (Figure 6.3). This means that both the 2047.0 and 2047.9 cm^{-1} peaks contain two chemically equivalent CO units. It should be pointed out that there are some anomalies with the isotopic data. First, the frequency shift between the all ^{12}CO species to the mixed isotopomer is $\sim 36 \text{ cm}^{-1}$ whereas the mixed isotopomer to the all ^{13}CO species is only $\sim 9 \text{ cm}^{-1}$. Also, the relative intensity ratios between the two peaks of the doublet are reversed when comparing the mixed isotopomer to the all ^{13}CO substituted isotopomer. It is difficult to compare the ^{12}CO species in this context due to the large $^{13}\text{C}^{18}\text{O}$ absorption, however, comparing previous data to this experiment reveals that the all ^{12}CO doublet has an intensity ratio similar to that in the ^{13}CO species (Figure 6.8, Appendix). Finally a peak corresponding to isotopically equivalent band of the 2180 cm^{-1} cannot be observed due to the large CO peak which dominates this region. A future study is needed using a pure ^{13}CO in argon matrix to confirm that this peak is at least due to a CO unit.

6.4.3 Temperature dependent differences

Deposition at 10 K provides a very similar picture to that at 20 K; however, there is only one peak in the $(\text{CO})_2^+$ region at 2047.8 cm^{-1} (Figure 6.4). Also, the anionic region is missing the 1514.7 and 1526.4 cm^{-1} analogues seen upon 20 K deposition. Note, however, that the 10 K spectrum contains inherently broad peaks and it is hard to tell if the low intensity bands observed at 20 K are contained under broad features.

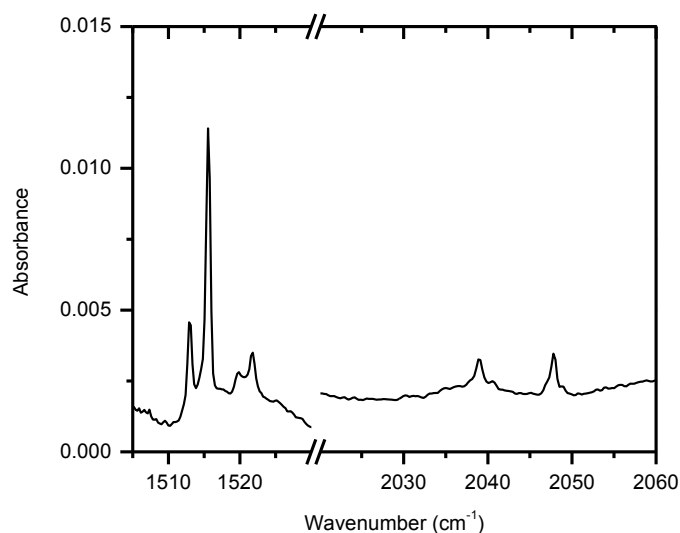


Figure 6.4 400 eV Ar⁺ deposition into 2% CO in excess Ar matrix, deposited for 4 hours at 10 K. Note that only one peak for the (CO)₂⁺ is present at 2047.8 cm⁻¹. Due to the high CO concentration, the ¹³C¹⁸O species is observable at 2038.9 cm⁻¹.

It is interesting that even though the 10 K spectrum has an much lower concentration of cationic species, the anionic (CO)₂⁻ still contains roughly the same intensity (see temperature comparison, Figure 6.5). This can be tested quantitatively by integrating the area of both regions. Integrating the area between the 1513 and 1516 cm⁻¹ peaks gives a value of 0.0152 for 20 K deposition and 0.0111 for 10 K deposition; however, integration across the 2048 cm⁻¹ region reveals areas of 0.00714 and 0.00112 for 20 K and 10 K respectively. Also, this “lost” intensity is not made up with the CO⁺ band. In fact the 2180 cm⁻¹ band shows the same anomalously low concentration at 10 K (Figure 6.9, Appendix). The implications of this are discussed below.

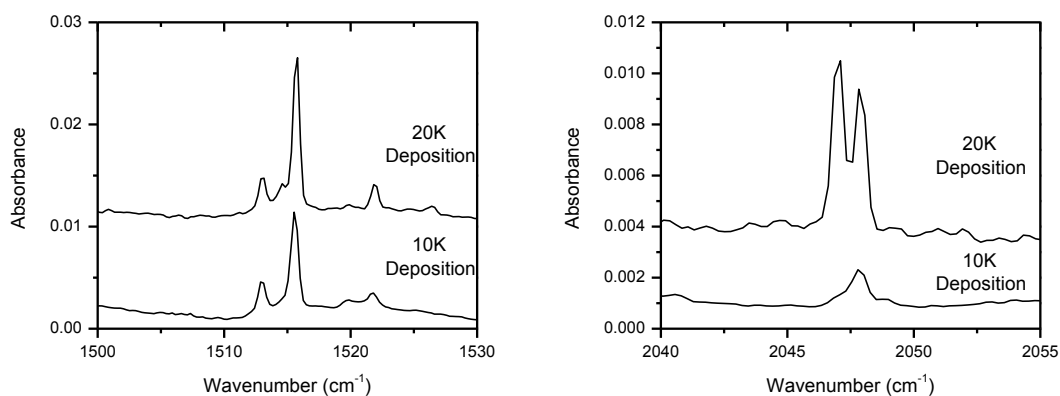


Figure 6.5 Deposition-temperature comparison. Both samples deposited under high energy argon for 4 hours using argon matrices doped with 2% and 0.5% CO for 10 K and 20 K deposition, respectively.

6.5 Discussion

6.5.1 Cationic dimer, $(\text{CO})_2^+$

Although matrix shifts are generally larger for species in argon compared to neon, neon values can be used to approximate where a compound might absorb in an argon matrix. The relative shift of an ionic species in relation to its neutral counterpart in neon can be used to estimate the ion's absorbance in argon assuming the shift from the neutral complex is the same. This approximation is of course an oversimplification since the higher polarizability of argon causes greater interaction with ionic compounds and therefore causes larger shifts when compared to the same ion in neon.¹⁷⁰ This estimation does, however, allow for a starting point for species identification.

The CO stretch appears at 2140.8 cm^{-1} in neon, whereas the $(\text{CO})_2^+$ appears at 2056.3 cm^{-1} (a shift of -84.5 cm^{-1}). Using this value for argon and noting that CO in argon is at 2138.2 cm^{-1} ,⁸⁸ the $(\text{CO})_2^+$ frequency should be near 2053.7 cm^{-1} . Indeed, the 2053.7 cm^{-1} prediction is fairly close to our peaks at $\sim 2049 \text{ cm}^{-1}$ with a slightly greater red-

shift due to a larger interaction with the argon as was discussed. The isotopic data show that two chemically equivalent CO molecules are involved and therefore we are left assigning these two bands to the $(\text{CO})_2^+$ complex in argon.

There are still a few points that are unclear at this time. First, two peaks are formed in the 20 K deposition. In previous annealing studies, we have shown that the lower frequency band anneals away (Figure 6.8, Appendix). It is possible that this is just a site affect whereby the lower frequency band is trapped in a less thermodynamically stable site. Typically if this is the case, annealing converts the less stable population into the more stable band and while the 2047 cm^{-1} anneals away, the 2048 cm^{-1} band does not gain intensity. Second, the splitting in the isotopic pattern is unusual. For completely symmetric molecules the relative frequency spacing between each of the isotopomers is the same (see $(\text{CO})_2^-$ isotope bands in Figure 6.3). The complete ^{13}CO species is not shifted nearly as far from the mixed isotopomer as the mixed isotopomer is from the complete ^{12}CO species. One possible explanation is that the positive charge is not evenly distributed between both CO units, as computational studies have suggested.¹⁵⁹⁻¹⁶¹ If the positive charge resides closer to one of the molecules, then a $(^{12}\text{CO})\cdots(^{13}\text{CO})^+$ versus $(^{13}\text{CO})\cdots(^{12}\text{CO})^+$ will be two chemically different species. In this case there should be a fourth doublet that is not observed; however, if this other doublet is shifted the same distance from the $(^{12}\text{CO})_2^+$ as the $(^{13}\text{CO})_2^+$ is from the observed mixed isotopomer, then this absorption would be masked by the large $^{13}\text{C}^{18}\text{O}$ peak at 2038 cm^{-1} . Finally, the relative intensities of the two peaks in the doublet isotopomer seem backwards based on the all ^{12}CO and all ^{13}CO complexes.

6.5.2 Cationic monomer, CO⁺

Using the same logic as above, the CO⁺ frequency in argon can be estimated from its absorbance in neon. CO⁺ has been assigned to 2194.3 cm⁻¹ in neon⁸⁸ (a shift of +53.5 cm⁻¹ in relation to the neutral CO frequency). Assuming again that this ion will interact with argon to the same extent as with neon, the CO⁺ frequency for argon should be near 2191.7 cm⁻¹. This estimation is somewhat close to our new peak at 2180 cm⁻¹. Furthermore, this peak does follow the same trends upon irradiation as the other ionic species giving credence to this species containing a charge. Because of this and its relative location we assign this band to the CO⁺. This assignment is very tentative, however since we cannot observe the corresponding isotopic peak due to the large CO peak which dominates the region where the ¹³CO-derived complex should show up. Other possibilities are that this is a larger (CO)_n⁺ cluster (n > 2). Though molecular beam studies have shown that additional CO units bind weakly to the (CO)₂⁺,^{53,171} this experiment is under kinetic control and formation of larger CO-clusters are very possible during the initial “warm surface layer” phase of deposition. Linn has measured an ionization potential of 12.91 eV for the (CO)₃⁺ which is below that of solid argon making it a possible candidate.⁵³ Finally, this peak could be a CO⁺ aggregated with a contaminant such as H₂O or CO₂, both of which are present in low amounts in the matrix.

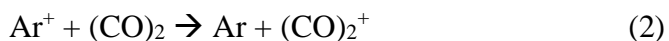
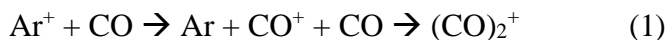
6.5.3 Anionic CO complexes

Upon deposition, both bands previously assigned to the (CO)₂⁻ are formed.¹²⁹ Our isotopic experiment are consistent with these assignments. We also observe a few new low intensity bands in the 20 K experiments as well. We cannot definitively assign them since they are of too low intensity to observe in the isotope experiments, but due to their location

they probably arise from $(\text{CO})_2^-$ anions. Another band not observed in the Andrews' study is at 1522 cm^{-1} . Due to its location and our previous observation of its formation upon electron capture (Chapter 4), we are left assigning this to an anionic CO compound. There also seems to be a 1:1 isotope splitting for this band which supports this assignment (Figure 6.3). Based on this data, it seems likely that the 1522 cm^{-1} band is due to the monomer, CO^- anion. Even using light down to 365 nm , the 1522 cm^{-1} band is not affected which is in agreement with the high electron affinity of 1.37 eV for CO^- observed by Franklin.¹⁶⁷

6.5.4 Complex formation and anomalous temperature concentrations

As was stated above, the 2047 and 2048 cm^{-1} peaks were present when anionic metals and 70 eV Ar^+ were deposited into the matrix. Our earlier studies also showed that these peaks scaled with the CO concentration.¹³⁸ In these studies, the $(\text{CO})_2^-$ was not observed presumably because the anionic copper complexes provided charge balance. In the experiments presented here, no explicit anion was deposited leaving the matrix to “self-neutralize” by forming the CO-dimer anion. It is interesting then to consider the formation process of these ionic species. For the cationic dimer two reactions can occur. Reaction one consists of an argon cation transferring charge to a neutral CO. The newly created CO-cation then clusters to form the cationic dimer. The second reaction involves the formation of a neutral CO-dimer which then becomes directly ionized by an argon cation.



There is precedence that reaction 2 leads to the formation of $(\text{CO})_2^+$. First, the ionization potential of solid argon lies slightly below that of CO whereas the CO-dimer lies below

that of solid argon (Chapter 1 and Table 1.4). Also once a cation is formed in the matrix it tends to become strongly solvated making it hard to cluster with other molecules. This solvation was used by Andrews to explain the lack of any cationic copper carbonyl complex larger than the monocarbonyl in argon, even though complexes up to the cationic tetracarbonyl were observed in neon.⁸⁸ In any case, both of these reactions are probably a significant oversimplification of a complicated ionization process occurring near the surface of the forming matrix.

The anionic complexes are a bit tougher to rationalize. We have shown that the van der Waals CO-dimer can readily trap free electrons in the matrix (Chapter 4). The source of the extra electrons is not obvious here. They cannot be directly from the depositing Ar^+ ; instead a secondary process must be occurring. One possibility is that the electrons are ejected from the sample holder when it is bombarded with the high energy argon cations. This explanation has been used in previous experiments to explain charge neutrality when specific counter-ions were not deposited.⁹³

With the above in mind the strange deposition temperature observations, whereby both 10 K and 20 K deposition contained roughly the same amount of anionic species whereas the 20 K deposition produced 6-fold more cationic species, can now be rationalized (section 6.4.3). At the 10 K deposition temperature, the warm top layer of the depositing matrix persists for a much shorter time compared to that at 20 K (section 3.5.1). Therefore, species are effectively “frozen out” before they have a chance to interact. This minimizes the interactions with CO species and the deposited Ar^+ , and therefore effectively reduces the probability of charge transfer between a CO complex and an argon cation. On the other hand, the anionic CO species do not need to interact with another molecule in

order for charge transfer to occur (although they do interact to an extent that dimer clusters are formed). Electrons that are released into the matrix (see above) can freely move and attach to a CO-dimer even if the dimer is some distance away from the place of the electron's origin (Chapter 4). In this way, deposition temperature only matters in so far as to cause clustering; it does not make a difference for electron capture events. Finally, because total anionic concentrations are the same in each case, the total cationic concentrations must be the same as well in order to maintain charge balance. This implies that there are a lot of cationic species in the 10 K sample that are "dark" in our spectrum. One likely possibility is that these "extra" cations exist as Ar_2^+ , which is thought to be the charge carrier in ionized pure Ar matrices.^{124,132} Indeed, we have used this explanation in the past to explain charge balance for our anionic copper carbonyl system¹³⁸ (section 3.5.3).

6.6 Conclusions

Through the deposition of high energy Ar^+ into a CO-doped argon matrix, ionic CO-complexes were formed. Two peaks previously assigned to the $(\text{CO})_2^-$ species are observed near 1515 cm^{-1} upon deposition. These peaks show a high threshold for photodetachment, with the onset of neutralization not beginning until use of 470 nm centered light. A new peak at 1522 cm^{-1} shows an even higher resistance toward photodetachment with the lowest wavelength of 365 nm used in this study not able to decrease this peak. Though the isotope experiment is not entirely clear at this point, it seems as though this peak may be the CO^- .

Two peaks near 2048 cm^{-1} are assigned to the $(\text{CO})_2^+$ in argon for the first time. These were readily formed in our previous studies of metal carbonyl systems and do not show any dependence on the counter-anion present in our previous studies. Finally, a peak

near 2180 cm^{-1} is in the correct region to be the CO^+ . Due to the large neutral CO band in this region, however, no isotopic peaks can be found. In future experiments employing mass-selected CO^+ , will eliminate the large neutral CO peak and should afford us with the ability to definitively assign this species.

6.7 Appendix

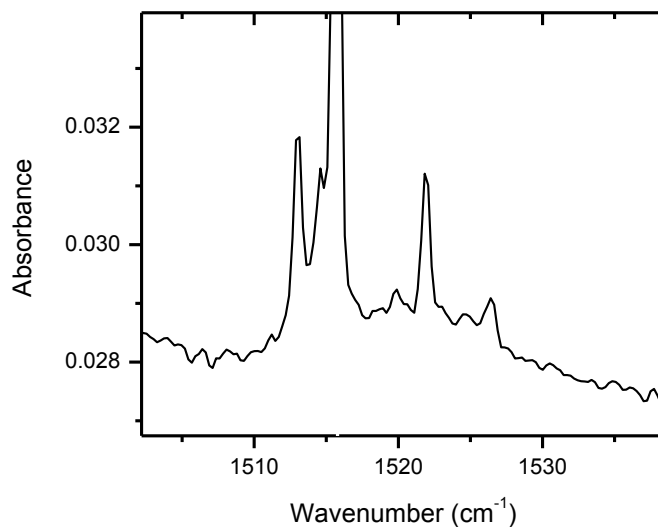


Figure 6.6 Anionic CO-dimer region from Figure 6.1B showing low-intensity peaks at 1514.7 , 1519.9 , and 1526.4 cm^{-1} .

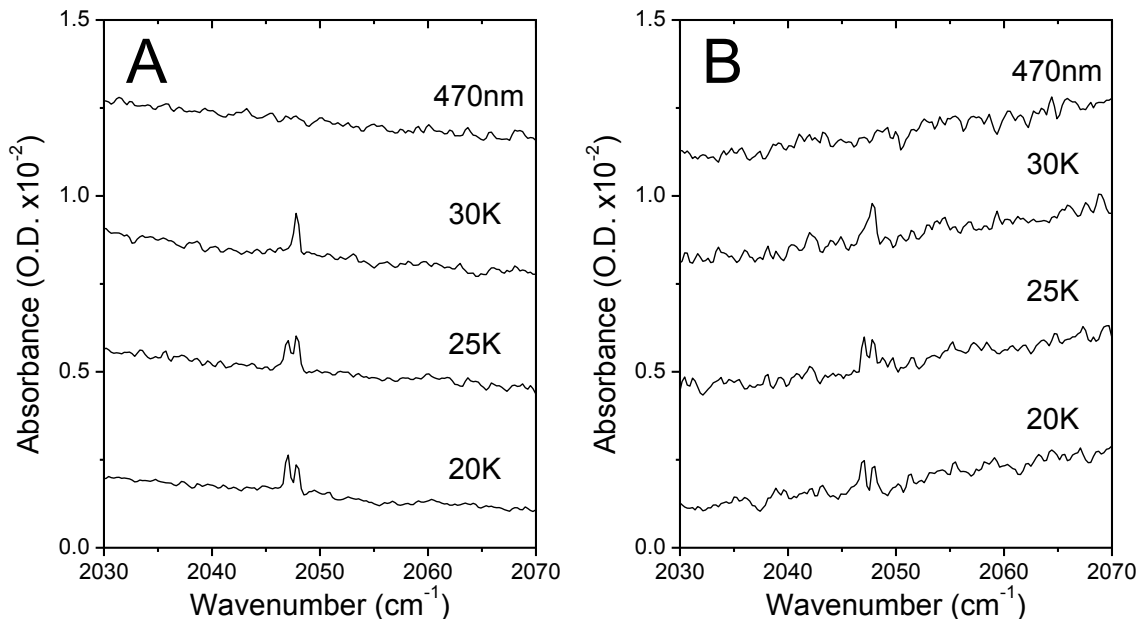


Figure 6.7 0.02% CO in argon matrix deposition at 20 K of 70 eV Ar⁺ balanced by A) Cu⁻ and B) Ag⁻. The (CO)₂⁺ behaves the same regardless of counter-ion. All spectra taken at 10 K.

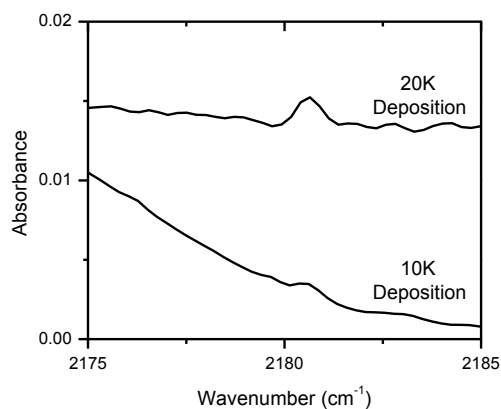


Figure 6.8 Deposition-temperature comparison of 2180 cm⁻¹ band. Both samples deposited under high energy argon for 4 hours using argon matrices doped with 2% and 0.5% CO for 10 K and 20 K deposition, respectively.

Chapter 7

The coldest example of chemical equilibrium: reversible conformational rearrangement of O_4^+ in an argon matrix at 10 K

7.1 Abstract

Thermodynamic equilibria are commonplace for chemical systems under standard conditions, but what is the lowest temperature at which chemical equilibrium can be observed? Matrix-isolation spectroscopy is typically the realm of kinetic control of chemical reactions, where non-thermal statistical distributions are “frozen-out” to allow characterization of metastable species. Nonetheless, FTIR spectroscopy of O_4^+ ions trapped in argon matrices has revealed a reversible exchange of intensity between two peaks assigned to *trans* and cyclic conformational isomers. Since the population can be driven back and forth between the two conformers by changing only the matrix temperature, we conclude that the system must be in thermodynamic equilibrium. The population trends are consistent with a weakly endothermic reaction, driven by increased entropy of the matrix for the cyclic product state. Problems encountered with quantitative van't Hoff analysis of the temperature-dependence for the equilibrium constant reveal that the assumptions underlying this standard analysis technique may break down at the very low temperatures of these experiments.

7.2 Introduction

The O_4^+ system is a complicated and still largely misunderstood compound, as shown by its long, complicated history in both experimental and theoretical work. Yang

and Conway first observed the complex using high-pressure mass spectroscopy. They found that the complex was stable by approximately 10 kcal/mol with respect to $O_2 + O_2^+$, which was attributed to an ion-induced dipole.¹⁷² Their later calculations showed that electron delocalization, presumably with the molecule in a rectangular structure, would cause additional stabilization.¹⁷³ Semi-empirical molecular orbital calculations suggested that the *trans*-bent structure was more stable than either the *cis* or rectangular structures but all were still found to be bound states.¹⁷⁴

The first IR spectrum was taken in 1989 when Jacox stabilized the molecule in a neon matrix through the use of a microwave discharge source.¹⁷⁵ Four bands were observed in that study, all of which showed isotopic substitution consistent with an O_4^+ species containing two-chemically equivalent O_2 -units: two strong bands at 1164 and 1320 cm^{-1} and two weak bands at 2808 and 2949 cm^{-1} . Based on isotopic splitting and previous calculations, the 1164 and 2808 cm^{-1} bands were assigned to the ν_5 (b_u) and $(\nu_1+\nu_5)$ (b_u) modes of *trans*- O_4^+ , respectively.¹⁷⁵ The other set of bands, however, presented a problem because the *trans*- O_4^+ should only have one IR-active, high-frequency O-O fundamental. Based on the lack of observation of a second isomer upon photolysis or annealing and an intensity anomaly observed for the heavy isotope species in isotopically enriched matrices, Jacox assigned the other two bands to the ν_5 mode of a perturbed *trans*- O_4^+ combination band, but noted the possibility of a second isomer.¹⁷⁵ In the same year, Knight used ESR to probe the molecule in neon and found the ground state to be nonlinear with three-unpaired electrons occupying π -type orbitals.¹⁷⁶

Using *ab initio* calculations, Peel found a rectangular ground-state structure with an unreasonably high stretching fundamental at 4331 cm^{-1} ,^{177,178} however Jacox pointed

out that even if the calculation yielded a realistic frequency, rectangular O_4^+ still only has one high-frequency, active-IR mode and could not explain the earlier experimental data.^{175,179} While studying electron transfer to O_4^+ from other species, Helm and Walter observed higher excited states with Rydberg character leading to dissociation patterns consistent with a rectangular structure. Using high theory *ab initio* calculations on the quartet-state, Lindh and Barnes showed that the *trans*- O_4^+ was the most stable structure but the rectangular structure exists at only 0.46 kcal/mol higher energy in agreement with experimental studies.¹⁸⁰ They also predicted ionization potentials of O_4 and O_2 to be 11.67 and 12.21 eV, respectively, which were in agreement with experimental values of 11.66 and 12.07 eV.¹⁸⁰ They also explained that earlier calculation problems were due to symmetry breaking. To date, this remains the best theoretical study on this system. In conjunction with Lindh and Barnes, Jacox was able to confirm the earlier 1164 and 2808 cm^{-1} band assignment of *trans*- O_4^+ and reassign the 1320 and 2949 cm^{-1} bands to the rectangular structure.^{179,180} This study also allowed her to justify the isotope anomaly whereby the greater zero point energy of the lighter isotope allowed that species to tunnel through the small isomerization barrier.¹⁷⁹

While studying laser ablated metals with oxygen in argon, Andrews observed O_4^- at 953.8 cm^{-1} and an 1118.6 cm^{-1} band assigned as the *trans*- O_4^+ .^{181,182} Through the use of electron impact and a Townsed discharge chemical ionization source, O_4^- and $(O_2)_n^+$ ($n=2-4$) ions were formed in argon as well as in oxygen-doped neon matrices through laser ablation of Co, Ni, and Cu.¹⁸³ Six argon peaks were observed due to O_4^+ cations. The band at 1119 cm^{-1} previously assigned to the *trans*- O_4^+ was present upon deposition while a band at 1186.1 cm^{-1} , which showed the same 16/18 ratio in isotope studies as *trans*- O_4^+ and

increased upon annealing at the expense of the 1119 cm^{-1} signal, was assigned to a *trans*- O_4^+ perturbed by an O_2 .¹⁸³ Four other bands were observed at 1302.1, 1310.6, 1328.9, and 1331.4 cm^{-1} and assigned to the cyclic- O_4^+ .¹⁸³ Finally, the argon experiment yielded bands at 1416.7 and 1490.4 cm^{-1} which were tentatively assigned to the cyclic- O_6^+ and O_8^+ , respectively.¹⁸³

This Chapter describes our studies with this complicated system. While trying to form copper oxides, large amounts of ionic oxygen-derived compounds were formed upon deposition. This was confirmed in our system by deposition of high energy Ar^+ with no metals present showing that the metal was only acting as a spectator ion to maintain charge balance but was not involved in the chemistry presented. In particular, this Chapter focuses on two sets of bands, each showing conformational equilibrium under different sets of conditions. The *trans*-1119 and cyclic-1310 cm^{-1} species show reversible thermal equilibrium while the *trans*-1186 and cyclic-1331 cm^{-1} bands show photochromic equilibrium. Both sets of equilibria occur independently from all other bands in the matrix. These findings call into question the current assignments in the literature as is discussed.

7.3 Experimental

For these studies, the deposition and subsequent processing steps were carried out under darkened conditions; all internal sources of light were turned off (ion gauges, RGA analyzer, etc.), and the lab lights were kept off throughout the experiment. Some light from the spectrometer necessarily reached the sample (the HeNe alignment laser for the interferometer) during spectral scans; the spectrometer beam was directed away from the deposition chamber when not recording spectra. Irradiation was performed either by narrow-band LED sources or through use of a tungsten filament bulb (see spectra,

Chapter 4). For irradiation scans, the sample was maintained at 10 K and a scan taken while the light was on (~13 min for a 500 scan average). After the scan, the light was turned off and a second scan taken under darkened conditions.

Temperature studies were achieved by cycling from 10 K to 18 K while stopping and scanning at all integer temperature values (i.e. 10 K, 11 K, ..., 18 K). The system was then cooled from 18 K to 10 K while stopping and scanning at all half integer values (i.e. 17.5 K, 16.5 K, ..., 10.5 K). Finally, quarter integer values were scanned at 0.5 K steps from 10 K back up to 16 K (i.e. 10.25 K, 10.75 K, ..., 17.75 K). This was done to rule out any anisotropy in the system. The $^{18}\text{O}_2$ system was only cycled to 16 K since the conformational transition occurs at a lower temperature (see below). Higher temperature processing was performed by annealing the system to the specified temperature at a rate of 4 K/min. Scans were taken at the higher temperature before cooling the system back to 10 K and taking another scan. Unless noted, all temperatures presented in this Chapter are the temperatures **at which** the scan is taken (this was not the case in previous Chapters where all scans were taken at 10 K).

Gas mixtures were prepared by dilution of a purchased mixture of 10.4% O_2 in He (PRAXAIR) with Ar (PRAXAIR, 99.9999%) down to a 2% O_2 mix for 10 K deposition or a 0.5% mix for 20 K deposition. Isotope gas mixtures were made using 99% $^{18}\text{O}_2$ (< 5% ^{17}O , Cambridge Isotope Laboratories). All matrix gases were purified by flowing through a copper tube immersed in ethanol-liquid nitrogen bath prior to deposition. Matrices were formed under a steady-state pressure of 10^{-5} Torr in the deposition chamber for 2 to 6 hours. Ionic oxygen species were formed in situ by bombardment of 400 eV Ar^+ throughout matrix deposition which transfers charge to the O_2 , a process that occurs spontaneously

presumably due to the difference in ionization potentials (see discussion). Charge balance was achieved by one of two methods: deposition of Cu^- with low Ar^+ energies or deposition of high energy (400 eV) Ar^+ through which anionic $(\text{O}_2)_2^-$ naturally forms to maintain charge neutrality.

7.4 Results

7.4.1 $\text{Cu}^- \text{Ar}^+$ deposition in a 0.5% O_2 matrix

Original experiments on this system were performed by depositing Cu^- counter-balanced by low-energy Ar^+ into O_2 -doped matrices in order to observe copper oxides; however, we only observed one copper-derived peak and many ionic oxygen peaks. Figure 7.1 shows the effects of such a deposition. All peaks were originally assigned based on the literature¹⁸³ and scrutinized by isotopic data performed by our group. Upon deposition at 20 K, a small band at 846.1 cm^{-1} was observed for the neutral $\text{Cu}(\text{O}_2)_2$ species. Interestingly, the O_4^- complex was also observed at 953.9 cm^{-1} , even though Cu^- should be present in the matrix as a counter-ion. Two bands due to the *trans*- O_4^+ were observed at 1118.5 and 1186.2 cm^{-1} as well as three cyclic O_4^+ bands at 1309.9 , 1329.0 , and 1331.8 cm^{-1} . Figure 1 was taken at 10 K, so the band at 1186.1 cm^{-1} is very weak, but this species plays an important role in the thermal equilibrium described below. Finally, the cyclic- O_6^+ complex was also observed at 1416.2 cm^{-1} . With high O_2 concentrations, a broad band at 1548.1 cm^{-1} was observed and assigned to an $(\text{O}_2)_n$ cluster (Figure 7.21, Appendix).

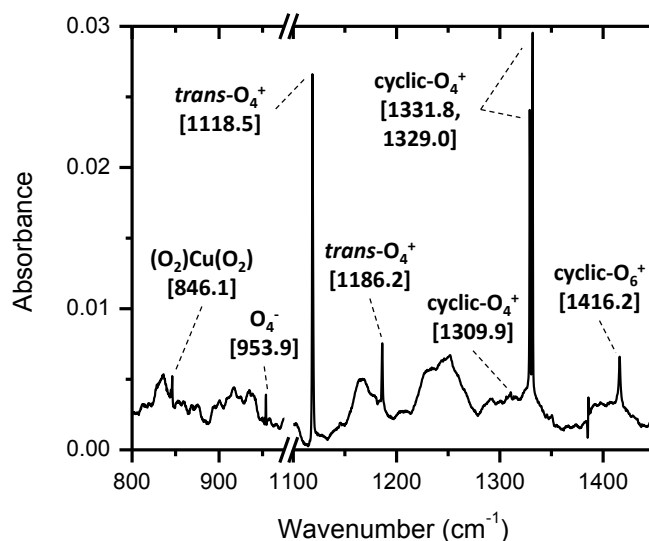


Figure 7.1 $\text{Cu}^- \text{Ar}^+$, 20 K deposition in a 0.5% O_2 in Ar matrix showing a survey scan of ionic complexes formed upon deposition. Note that the $\text{Cu}(\text{O}_2)_2$ is the only copper derived peak formed. The sharp line in the baseline near 1385 cm^{-1} is due to a difference in the background and the irregular baseline is due to the KBr window cracking from repeated use.

7.4.2 Isotopic study

A 50:50 $^{16}\text{O}_2$: $^{18}\text{O}_2$ isotopic experiment was performed using 0.5% of each oxygen isotope in argon with Cu^- and Ar^+ deposited at 20 K for 6 hours. The results for the *trans*- and cyclic region are shown in Figure 7.2. Both *trans*- species at 1119 and 1186 cm^{-1} show typical isotopic patterns for two chemically equivalent O_2 molecules. This data is similar to findings in previous experiments, however, we did not observe another O_2 coupled to the species at 1186 cm^{-1} and annealing did not lead to an increase in this peak; therefore, we believe the 1186 cm^{-1} band arises from a pure O_4^+ complex and not an $\text{O}_4^+ \cdots \text{O}_2$ as had been assigned.¹⁸³ The reason we believe this band is perturbed from the 1119 cm^{-1} band is explained below.

The cyclic doublet at 1329 and 1332 cm^{-1} each show the same splitting that indicates two equivalent O_2 molecules. The 1310 cm^{-1} peak is interesting in that it shows a splitting into four bands with a ratio of 1:1:1:1. This pattern means that the mixed isotopomer is perturbed so that instead of adding into a single band, the intensity is split between two bands. One possible explanation for this result would be that the positive charge resides on one O_2 molecule versus the other, whereby the $^{16}\text{O}_2^+ \dots ^{18}\text{O}_2$ and $^{18}\text{O}_2^+ \dots ^{16}\text{O}_2$ complexes would no longer be chemically equivalent. Another possibility is that there is a coupling to the matrix cage in such a way that both sides of the molecule are distinguishable. Finally, both the 846 and 954 cm^{-1} peaks show splitting due to two equivalent O_2 molecules (Figure 7.24, Appendix).

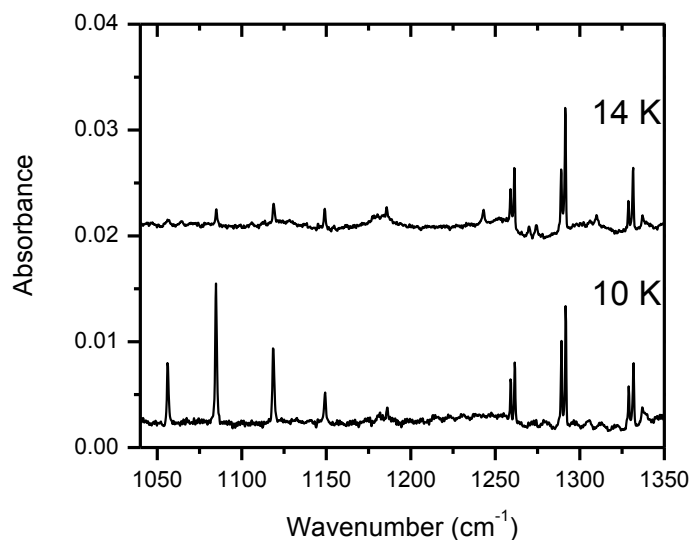


Figure 7.2 $\text{Cu}^- \text{Ar}^+$ deposition for 6 hours at 20 K in a 0.5 % $^{16}\text{O}_2$ + 0.5% $^{18}\text{O}_2$ in argon showing *trans*- O_4^+ and cyclic- O_4^+ . Spectra are taken with sample at 10 K and 14 K, respectively. A peak at 1337.2 cm^{-1} is due to an isotope of the O_6^+ complex

7.4.3 High energy Ar⁺ formation

The O₄⁺ complexes can also be formed from high energy (400 eV) Ar⁺ deposition without the use of specific counter-ions. Figure 7.3A shows a deposition through the use of 70 eV Ar⁺ with Cu⁻ while 7.3B shows 400 eV Ar⁺ with no intentionally deposited counter-ions. What is immediately obvious is that both systems are the same with respect to the O₄⁺ derived bands. This result is confirmed in both our temperature and irradiation studies (see below). The Cu⁻ is primarily a spectator ion only present to maintain charge balance. A small amount of copper, however, also reacted with O₂, as seen by the band at 846 cm⁻¹. Note that this peak is absent in the high-energy case, adding evidence that this peak involves a copper atom. In the case of the high-energy deposition, the system must remain neutral through secondary processes. The “self” neutralization is observed by the presence of a large O₄⁻ band that is not present in the low-energy deposition with Cu⁻. Also, the overall concentration of O₄⁺ complexes is lower for the high-energy deposition. This probably occurs due to the formation process whereby free electrons must be available in the matrix to bind to a neutral O₄ to form the anion. This is the same process we observed for the (CO)₂⁺ complex, described in Chapter 6. There is a large Coulomb potential for free electrons to bind to an already-formed O₄⁺ over a neutral complex, and this process probably leads to a final, lower cation formation. Furthermore, O₂ must be used to form the O₄⁻ which effectively lowers the concentration available to form cations.

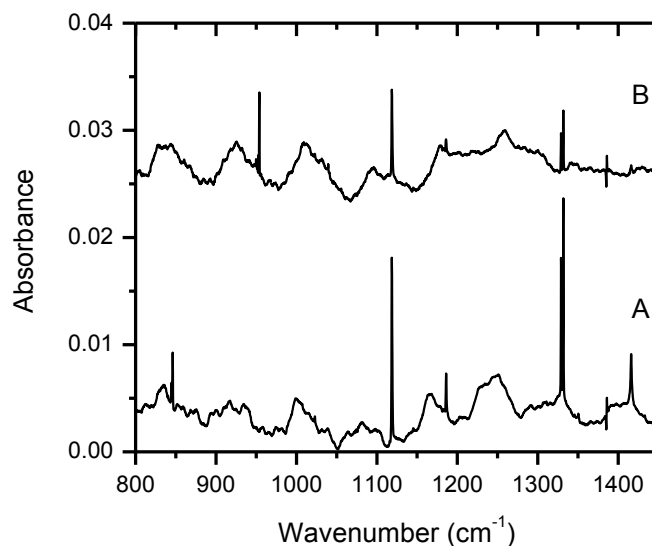


Figure 7.3 Deposition condition comparison for 0.5% O₂ in argon at 20 K formed from deposition of A) 70 eV Ar⁺ with Cu⁻ and B) 400 eV Ar⁺ only. Note the lack of the O₄⁻ in the high-energy deposition.

7.4.4 Dependence on deposition temperature

Deposition temperature had the effect of shifting the relative populations of the different cationic conformers observed. At 10 K, Figure 7.4A, a very intense band was observed for the *trans*- complex at 1119 cm⁻¹. As deposition temperature increased, the cyclic doublet near 1330 cm⁻¹ was selectively deposited while the *trans*- complex was decreased. At 25 K deposition the *trans*- structure was not formed at all (Figure 7.4C). This result aids in studying some complex physical phenomena that occur in our matrices, as will be discussed below. It is interesting to point out that the amount of O₄⁻ anion is approximately the same at each temperature, maybe even a little smaller at 10 K, though the peak is broader so overall area may be conserved. This result is in contrast to the O₄⁺ species, which seem to be much more concentrated in the sample deposited at 10 K. Assuming the oscillator strengths of the *trans*- and cyclic species are roughly the same,

other cationic species must exist at 20 K, and a lot more at 25 K that are dark in the IR spectra. One potential candidate would be O_2^+ , which does not have an active IR-mode. It is difficult, however, to understand why higher deposition temperatures, which should cause increased clustering, instead favor monomeric units.

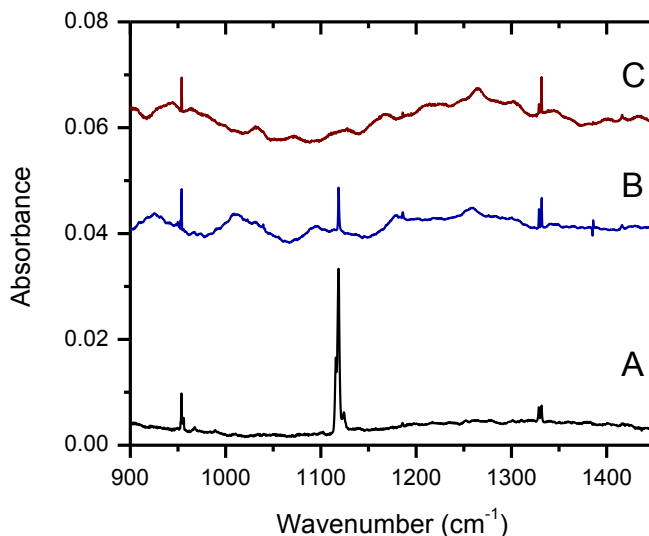


Figure 7.4 Temperature deposition comparison using 400 eV Ar^+ for: A) 10 K deposition of 2% O_2 , B) 20 K deposition of 0.5% O_2 , and C) 25 K deposition of 0.02% O_2 .

We note that the band at 1119 cm^{-1} has two shoulder peaks upon deposition at 10 K (Figure 7.22, Appendix). Both of these shoulder bands anneal away at 20 K, while both bands at 1416 , O_6^+ , and 1548 cm^{-1} , $(O_2)_n$, gain significant intensity (Figure 7.21, Appendix). There was also a small increase in the 1186 cm^{-1} band. We suspect that these shoulder peaks may be what Andrews observed in his data at 1119 cm^{-1} . This interpretation would explain why he observed an increase in the band at 1186 cm^{-1} and did not see the thermal trends explained below. Because of these shoulders, all samples deposited at

10 K were first annealed to 20 K for 15 minutes, so that they did not interfere with the quantitative data assessment given below.

7.4.5 Thermally-induced reversible conformational change

The central focus of this temperature study was how the spectrum in Fig 7.5A responded to changes in the temperature of the matrix. Fig 7.5B shows traces taken for temperature steps of 1 K between 11 K to 18K; all of the peaks show non-negligible changes with temperature, however, the thermal study was focused on just two of them, near 1119 cm^{-1} (peak A) and 1310 cm^{-1} (peak B), previously assigned to *trans*-planar and cyclic O_4^+ conformers, respectively, based on isotopic substitution¹⁸³ and comparison with theory.^{174,178,180} It is immediately apparent that these two peaks have opposite intensity trends, with A dying out and B growing in as the temperature is increased. What is even more striking is that upon cooling the sample back to 10 K, the original spectrum was restored, as shown in Fig 1C, indicating that these thermal trends are reversible. In fact, these trends proved to be completely reproducible over several temperature cycles.

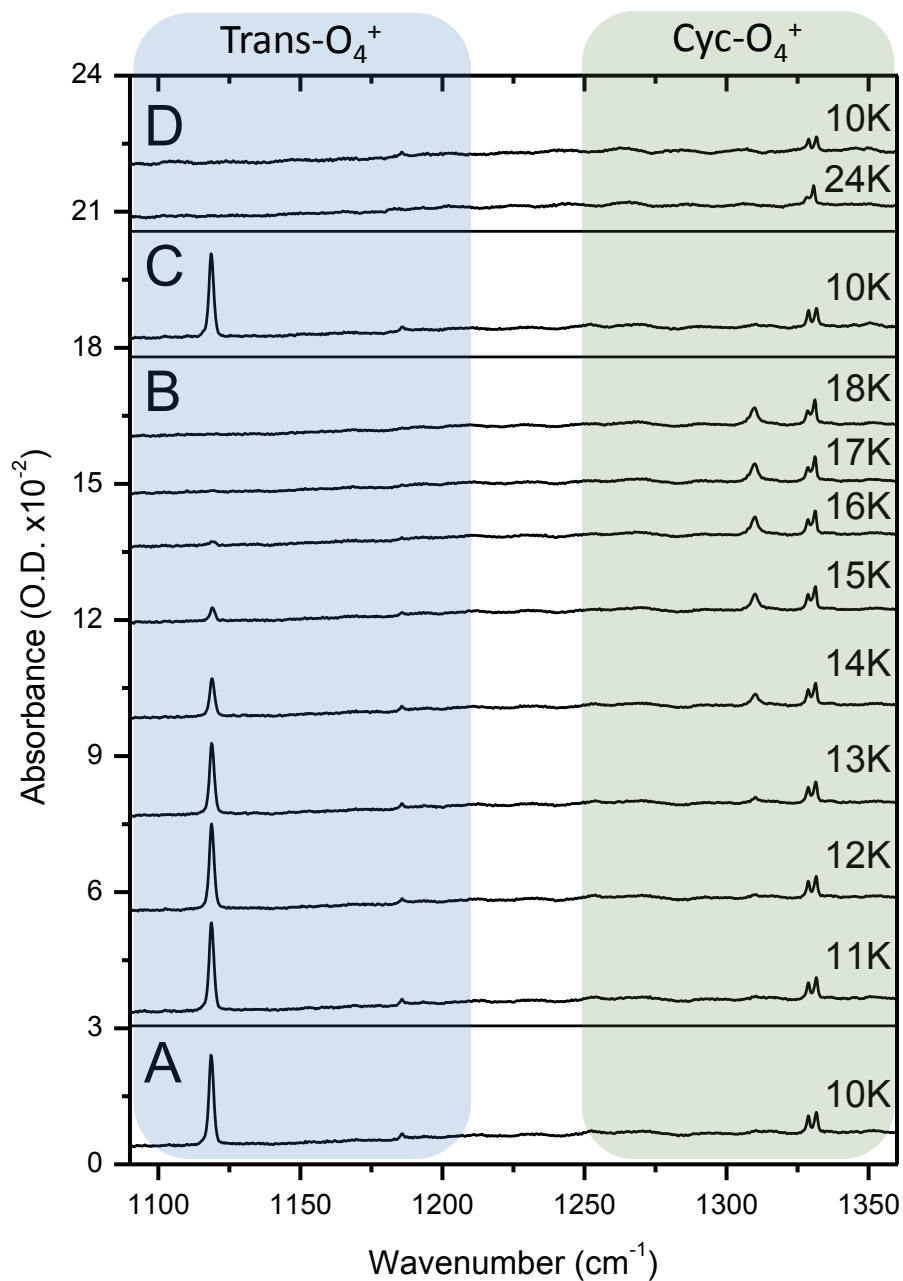


Figure 7.5 FTIR spectra of O_4^+ in argon matrices: A) spectrum recorded at 10 K following 10 K deposition, showing bands assigned to *trans*- (1119 and 1186 cm^{-1}) and cyclic (1329 and 1331 cm^{-1}) conformers; B) growth of new cyclic conformer band (1310 cm^{-1}) and concomitant loss of *trans* band (1119 cm^{-1}) upon warming from 11-18 K. Note that only whole-integer temperature values are shown, but scans were taken at 0.25 K intervals, see text; C) Restoration of initial spectrum upon re-cooling to 10 K, demonstrating reversible nature of spectral changes; D) Loss of both 1119 cm^{-1} and 1310 cm^{-1} bands following heating to 24 K.

7.4.6 Radiation-induced reversible conformational change

Figure 7.7 shows an FTIR spectrum taken after 4 hours of deposition at 20 K. For the irradiation studies, two peaks are once again the focus, one near 1186 cm^{-1} (peak C) and one near 1332 cm^{-1} (peak D), previously assigned to a *trans*-(O_4)⁺··· O_2 complex and a cyclic O_4^+ respectively.¹⁸³ These two bands showed a qualitative equilibrium trend in the annealing data above, Figure 7.5 (see also Figure 7.15 in the Appendix for a clearer thermal trend for the $^{18}\text{O}_2$ system), but their interconversion becomes clear in the presence of light. When a scan was taken with a 735 nm centered LED on, the peaks did not change; however, when 660 nm light was used, peak C gains some intensity while D loses some. Both peaks returned to their original intensities when the light was turned off. This same reversible population transfer occurred with the 590 nm light and reached the maximum conversion in these studies with 470 nm light. Furthermore, the cyclic-to-*trans* conversion (light on) seemed to be instantaneous on the timescale of our study; however, the “relaxation” back to the original state was slow enough to observe when taking a quick spectrum (16 scans averaged, ~30 s). We are working on a method to track this conversion quantitatively in order to derive kinetics data. Use of shorter-wavelength light, 365 nm light, again induced this change but to a lesser extent than the 470 nm light. In studies employing a broadband visible source (tungsten bulb used in Chapter 4), the reaction proceeded in the opposite direction, with peak C completely losing intensity while peak D gained intensity (Figure 7.14, Appendix). Once again, this change was reversible once the light was turned off. Apparently, a wavelength longer than 735 nm, which is produced by the broadband source, caused the D-to-C conversion.

It should also be made clear that peaks A and B described above **were not** affected by the irradiation studies (Figure 7.14, Appendix). Furthermore, the described changes occurred regardless of deposition temperature or the nature of the counter-anion and took place, even if peaks A and B were not present (see 25 K deposition, Figure 7.20, Appendix). Because of these trends, we conclude that the two *trans*-peaks, A and C, and the two cyclic-peaks, B and D, cannot be due to the same species as has been reported in the literature. Potential species assignments are presented in the Discussion section. Finally, the peak at 1329 cm^{-1} appears to be a spectator throughout both sets of experiments, but nonetheless is clearly an O_4^+ species. These irradiation results make it clear that this species cannot be a simple “site” peak, given its completely different qualitative response to visible irradiation.

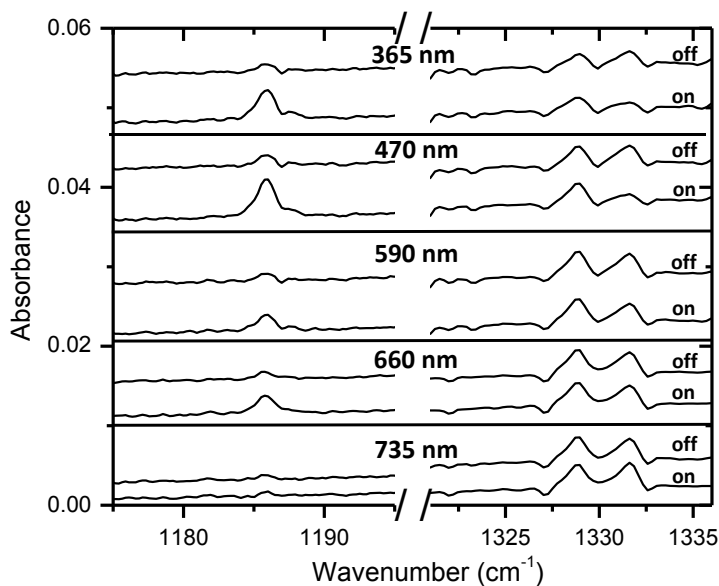


Figure 7.7 Irradiation series showing photochromism between the cyclic- 1331 cm^{-1} and *trans*- 1186 cm^{-1} conformers using different narrow-band LEDs. Spectra are taken at 10 K either with the light on or off as specified.

7.5 Discussion

Five peaks play a pivotal role in the studies presented above. Peaks at 1119 (A) and 1186 cm^{-1} (C) have been assigned by Andrews¹⁸³ to the *trans*-O₄⁺ while bands at 1310 (B), 1329, and 1332 cm^{-1} (D) have been assigned by Andrews¹⁸³ to the cyclic O₄⁺. All of these complexes have been assigned to the quartet spin state, based on theory.¹⁸⁰ Interestingly, the cyclic structure has been assigned in the gas-phase by Douberly and Duncan¹⁸⁴ at 1323 cm^{-1} whereas Jacox¹⁷⁹ assigned it at 1320 cm^{-1} in neon and Andrews¹⁸³ at 1330 cm^{-1} in argon. That is a neon value redshifted from the gas phase while the argon value is blueshifted! This odd apparent discrepancy suggests that some more complicated process is occurring other than simply site peaks or simple conformer conversion.

7.5.1 Thermodynamic equilibrium at 10 K

In general, cryogenic spectroscopy techniques involving chemically inert condensed materials such as rare gases are the realm of kinetic control, where owing to the low temperature and fast energy dissipation afforded by condensed matrices, the species observed tend to be those that form the fastest, rather than those that are the most energetically stable. Indeed, this was largely the goal when Pimentel developed matrix-isolation spectroscopy for the study of transient molecules many years ago; metastable species such as radicals or ions generated *in situ* in the matrices or deposited from gas-phase sources have their internal degrees of freedom rapidly quenched before they can rearrange or react to more stable forms.²⁶ Contrast this situation with the case of thermodynamic control, whereby chemical systems in thermodynamic equilibrium tend to favor the most stable state with the lowest free energy. The principle of detailed balance states that for a chemical system to be in equilibrium, the forward and reverse reactions

must be occurring with equal rates, such that the free energy difference between the reactants and products is reflected in the relative populations of those states. Thus while it is technically possible for a matrix-isolated chemical system to be in thermodynamic equilibrium, it requires unlikely conditions to be satisfied, namely that the free-energy difference between reactants and products is <1 kJ/mol. From a practical point of view, the barrier separating products and reactants must be also comparably low in order for the equilibrium to be achieved on the timescale of the experiment, but this is a kinetic, rather than thermodynamic, consideration.

Thermodynamic equilibrium has been shown below 30 K before by the Wight group while studying the difluoronitroxide radical system.¹⁸⁵ This system exhibits dynamic equilibrium between the F--FNO and F_2NO species when the system is annealed from 17 to 30 K.¹⁸⁵ In what follows, we present experimental evidence that the O_4^+ ion, (a covalently bound dimer of molecular oxygen with a single electron removed)^{179,183,186} exhibits a conformational equilibrium while trapped in an argon matrix at temperatures down to 10 K.

Under normal circumstances, it would be completely natural to attribute annealing behavior to thermodynamic equilibrium between the two conformers, but as the process occurs in a cryogenic matrix between 10 and 18 K, such behavior would be surprising to say the least! However, there are several aspects of the data that suggest that species A and B do actually represent two distinct chemical species in thermodynamic equilibrium. In such a case, the populations of species A and B (P_A and P_B) must sum to 1, so the summed intensity of both peaks (I_{tot}) at all temperatures should be represented by the linear equation $I_{\text{tot}} = \sigma_A P_A + \sigma_B P_B$, where σ_A and σ_B are constant scaling factors. Indeed, we find

a strong linear relationship between the integrated areas of peaks A and B for all the different temperatures (Figure 7.10, Appendix). Furthermore, when the sample is warmed to temperatures higher than 23 K, **both** species A and B are irreversibly lost from the spectrum. Figure 7.5D shows spectra both during heating to 24K (~ 30 min) and after cooling to 10 K; species B is clearly absent from the 24 K spectrum, and species A is also missing after cooling, yet the other 3 O₄⁺ peaks are still present with their original intensities. The implication is that, above 23 K, the cyclic conformer (species B), which dominates at higher temperatures can either dissociate irreversibly into O₂ and O₂⁺, both of which are undetectable in the infrared spectra, or gain another O₂ unit to form the O₆⁺ cluster which increases slightly upon annealing (Figures 7.12 and 7.13, Appendix).

7.5.2 Quantitative assessment

Thus, the spectral trends described above for species A and B reveal that the *trans*-planar and cyclic conformers of O₄⁺ are in thermodynamic equilibrium in the temperature range between 10 and 20 K. As such, it is sensible to convert the normalized peak intensities to relative populations and use them to track the temperature dependence of the equilibrium constant for the conversion of *trans*- to cyclic-O₄⁺; these data are collected in Table 7.1 of the Appendix. Figure 7.3A plots the relative populations of *trans*-planar and cyclic O₄⁺, which show near-perfect inverse correlation, as expected from the linear trend found in Fig. 7.5. The sigmoidal shapes of the curves are consistent with the reaction (*trans* to cyclic) being endothermic (positive ΔH), balanced by a positive entropy change that is sufficiently large to shift the reaction from favoring reactants to favoring products over the fairly narrow observed temperature range. Note however that at these temperatures, there can be little difference in the vibrational entropies of the O₄⁺ conformers, because the

probability of having significant population in vibrationally excited states is very small. Similarly, rotational degrees of freedom are not likely to contribute since the molecules are frozen inside a solid matrix. Therefore the entropic driving force must arise from differences in the way the two conformers interact with the surrounding argon matrix. Indeed, the Wight group used this explanation to account for the large entropy measured when forming an F₂ bond in the F₂NO molecule.¹⁸⁵ Likewise, this result is somewhat akin to solvent-driven processes occurring under more typical conditions, for example the inverted helix-coil transition of poly-benzyl-glutamate in mixed dichloroethylene dichloroacetic acid solvent, where going from helix to coil induces a positive entropy change in the solvent that compensates for the small (< 1 kcal/mol) endothermicity of the reaction.¹⁸⁷

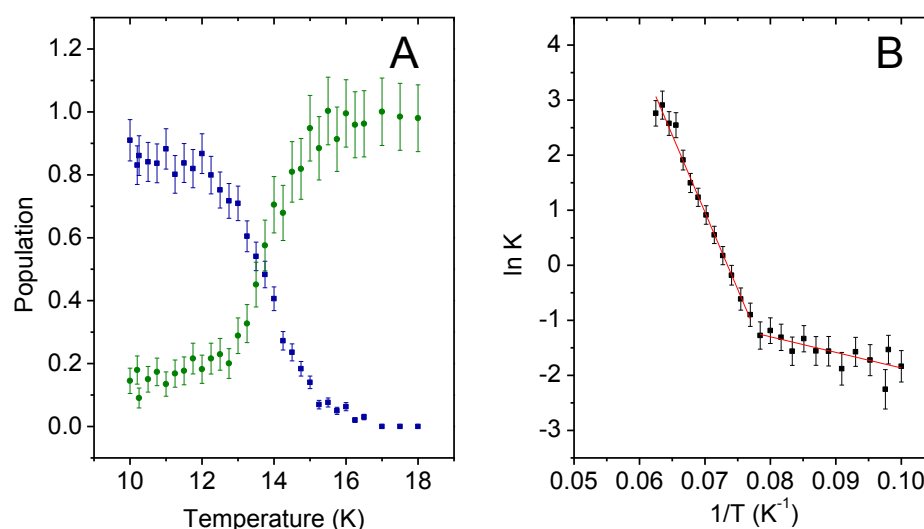


Figure 7.8 A) Temperature dependence of normalized populations in peaks A (1119 cm⁻¹) and B (1310 cm⁻¹). B) van't Hoff plot reflecting temperature dependence of K_{eq} for *trans*-to-cyclic conversion, derived from population data in part A. The higher temperature line was fit with a linear equation of $y = -280 \pm 8 x + 20.6 \pm 0.5$ with an R^2 value of 0.9886. The lower temperature line was fit with a linear equation of $y = -28.4 \pm 7 x + 0.969 \pm 0.6$ with an R^2 value of 0.5690.

Quantitative values for standard enthalpy and entropy can be obtained from a van't Hoff plot of the natural log of the equilibrium constant *versus* inverse temperature, as shown in Fig 7.3B. The negative slope of the plot is consistent with an endothermic reaction, and the linearity of the points in the higher temperature region (points corresponding to 13-16 K) indicates that ΔH° and ΔS° are constant in this temperature range, and can be extracted from the slope and intercept of a linear fit (shown), respectively. The plot clearly deviates from linearity for larger values of $1/T$ (points corresponding to 10-12.75 K), so these points were fit by a second line; possible explanations for the non-linearity of these points are considered below. The values obtained from the higher-temperature (13-16 K) linear fit are $\Delta H^\circ = 2.33 \pm 0.06 \text{ kJ mol}^{-1}$ and $\Delta S^\circ = 171 \pm 5 \text{ J mol}^{-1} \text{ K}^{-1}$. The former value is consistent with the calculations of Barnes and Lindh, which predicted the cyclic conformer to be $\sim 2.2 \text{ kJ mol}^{-1}$ higher in energy than the *trans*.¹⁸⁰ The latter value is surprisingly large for a conformational rearrangement; for comparison, the standard entropy of vaporization of argon is $79.1 \text{ J mol}^{-1} \text{ K}^{-1}$ at 87 K.¹⁸⁸ In terms of the Boltzmann definition of statistical entropy, $S = k_B \ln W$, the ΔS° value obtained from the van't Hoff analysis here would mean that the products have $\sim 9 \times 10^8$ times higher configurational entropy (W) than the reactants. Even considering participation from some degrees of freedom of the argon matrix (i.e., those associated with the shell of atoms surrounding the O_4^+), this large entropy seems hard to rationalize at the low temperatures of these reactions. The fit from the lower temperature line (10-12.75 K) are $\Delta H = 0.236 \pm 0.06 \text{ kJ mol}^{-1}$ and $\Delta S = 8.06 \pm 5 \text{ J mol}^{-1} \text{ K}^{-1}$. The entropy change in this case is more consistent with that observed for a simple molecular rearrangement.

7.5.3 Qualitative assessment

Figure 7.9 shows a simple model for the coupling between the argon matrix and the O_4^+ that captures the qualitative aspects of the measured trends. The argon atoms are locked in an FCC crystal structure at the known spacing of 375 pm,²⁸ and the geometrical parameters for the O_4^+ conformers are taken from the equilibrium geometries predicted by Lindh and Barnes.¹⁸⁰ The *trans*-planar conformer fits almost perfectly into a double-substitution site (Fig. 7.4A), whereas the cyclic conformer is much more compact, leaving a significant amount of free space inside the cavity. It has been shown experimentally that creation of a cavity inside solid argon is associated with a positive entropy change,²⁸ and the translational modes associated with the motion of the smaller cyclic conformer inside the cavity will contribute additional degrees of freedom that further increase the entropy of the product species relative to the reactant. This crude model is certainly an oversimplification, since it neglects the relaxation of the matrix cavity to accommodate the geometric change of the O_4^+ (and vice versa). Nonetheless, it is at least qualitatively consistent with the experimentally observed phenomena. A more quantitative analysis would require molecular dynamics simulations using a highly accurate potential energy surface describing the interaction between the argon and the O_4^+ dopant, allowing for the possibility that quantum nuclear tunneling plays a role in determining the relative conformer energies, all of which lies beyond the scope of the current work.

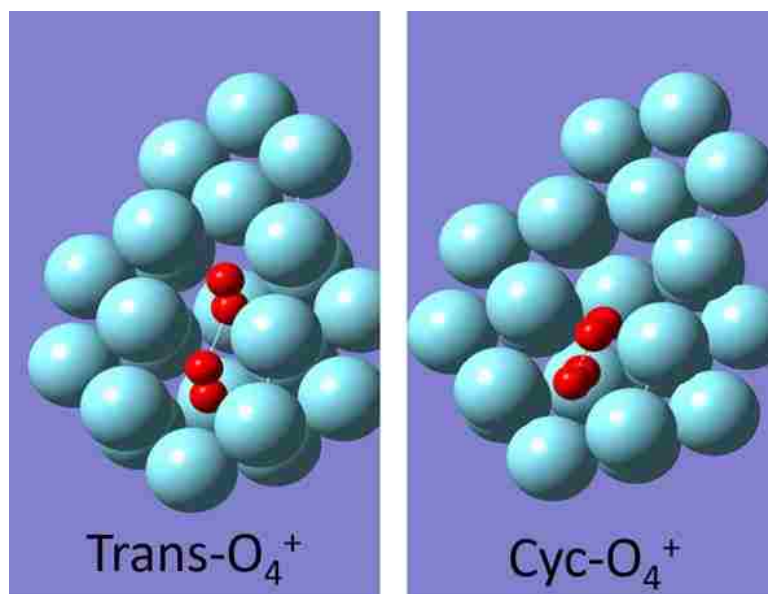


Figure 7.9 Simple schematic showing *trans* and cyclic conformers of O_4^+ in double substitution sites in a rigid fcc argon matrix (figure created by David Moore).

7.5.4 Isotopic substitution

As a final experimental test of the system, we repeated the set of experiments using pure $^{18}O_2$, and the results were completely analogous to the initial experiments with $^{16}O_2$, as shown in Figures 7.15-7.18 and Table 7.2 of the Appendix. The spectral series shows the same general trends for all of the O_4^+ bands (appropriately shifted) with temperature (Figure 7.15, Appendix), and the peaks corresponding to the *trans* and cyclic conformers (at 1056 and 1243 cm^{-1} , respectively) display reversible population transfer. Some of the quantitative details are different, for example there is more of the cyclic conformer present at 10 K for the $^{18}O_4^+$, as reflected in the thermal population data shown in Figure 7.17. Furthermore the van't Hoff plot shows an even greater deviation from linearity at the lower temperatures (Figure 7.18, Appendix), and the thermodynamic parameters extracted from the linear fit are $\Delta H^\circ = 1.8 \pm 0.1 \text{ kJ mol}^{-1}$ and $\Delta S^\circ = 136 \pm 8 \text{ J mol}^{-1} \text{ K}^{-1}$, both about 15% lower than for the $^{16}O_4^+$ case. Finally, the bands corresponding to both the *trans* and cyclic

conformers disappear irreversibly when the matrix is heated above 23 K (Figure 7.19, Appendix), just as with the $^{16}\text{O}_4^+$ case. The fact that the same phenomenology is exhibited by both isotopomers confirms that this behavior is characteristic of O_4^+ trapped in argon matrices in this temperature range. Furthermore, the small quantitative differences observed for the $^{18}\text{O}_4^+$ case indicate that quantum effects such as zero point energy, and possibly tunneling, are affecting the measured properties of the system. There is a problem there as well however, since it is very hard to conceive of a tunneling model where the **heavier** species has a **higher** population in the **higher** energy state at **lower** temperature.

7.5.5 Photochromic conformational changes at 10 K

It is clear that a second type of equilibrium exists in the system, between species C and D. These peaks are also assigned in the literature to *trans*- O_4^+ and cyclic- O_4^+ ,¹⁸³ however, based on the irradiation results they must be independent from species A and B. Not only do these peaks show photochromic changes, C and D must also be in thermodynamic equilibrium which is why they can re-establish the original populations when the lights are turned off. As was mentioned, qualitative evidence of this equilibrium exists in the thermal behavior presented in Figure 7.5 (see also Figure 7.15 in the Appendix for a clearer thermal trend for the $^{18}\text{O}_2$ system).

Based on all the data presented, it seems probable that all five O_4^+ peaks represent distinct species. It is easy to rationalize the thermal conversion between A and B as a conformational change, but C and D also present a conformational change. It is hard, then, to rationalize the existence of 5 distinct, well-separated spectral features that somehow correspond to only two different structural isomers. Therefore we are left with the hypothesis that different electronic states must also be involved. The quartet state of O_4^+

is the lowest energy electronic structure and as such all previous work, both experimental and theoretical, have been based on the study of the quartet; however, the system can also exist in a doublet state. With this in mind, it seems likely that the A-B and C-D pairs may be tracking the trans-cyclic isomerization of two different electronic states. There is still the problem of the 1329 cm^{-1} peak which does not appear to be coupled to any of the other bands, yet isotope data clearly shows that this is another O_4^+ species (Figure 7.2). This fifth species suggests that there is another distinct combination of structural and electronic states of the O_4^+ stabilized in argon, but an assignment as to which one cannot be made without further investigation.

7.6 Conclusion

It is clear that the experimental data unambiguously support the qualitative interpretation that the *trans* and cyclic conformers of O_4^+ are in thermodynamic equilibrium over the range 10-16 K in argon matrices, which gives rise to the reversible exchange of intensity between peaks A and B observed in the spectrum. To our knowledge, this is the lowest temperature for which a chemical equilibrium has been characterized; as mentioned in the Introduction, matrix isolation normally involves the realm of kinetic, rather than thermodynamic, control of chemical reactions, and it appears that this work may be the first time a reversible chemical equilibrium has been observed in a matrix isolation experiment.

The thermal trends in the populations of the two conformers are consistent with an endothermic, entropy driven reaction taking the system from *trans*-to-cyclic, and this can be rationalized in terms of a simple cavity-coupling model where the more compact structure of the cyclic *conformer* has more low-lying translational states than the more

extended *trans*-conformer. The quantitative van't Hoff analysis of equilibrium constants derived from the thermal population data proved harder to understand, however, predicting unphysically large values for ΔS° . This result raises the question of whether it is reasonable to apply van't Hoff analysis to a chemical equilibrium at such an unprecedentedly low temperature.

This system requires a careful treatment with high-level theoretical methods, but that is not without its own set of difficulties. The isolated O_4^+ system is extremely difficult to treat theoretically, as its inherently multi-configurational and multi-reference nature makes it extremely prone to symmetry-breaking in electronic structure calculations. Indeed, the 1994 paper by Lindh and Barnes remains the most thorough treatment of this system,¹⁸⁰ and even those results have been called into question in light of the symmetry-breaking problem.¹⁸⁹ Of course here, the O_4^+ is just part of the system; modeling of the chemical equilibrium would require including the degrees of freedom of the argon matrix in some fashion as well.

7.7 Appendix

7.7.1 Peak fitting and error analysis

In order to extract quantitative data, the peaks of interest must first be integrated. A program was written by DTM in order to perform high-throughput peak fitting for multiple peaks and multiple spectra in Origin computer software. For each of the peaks to be fit, a starting point and ending point are selected near the baseline of the peak. The program then integrates the area between the points chosen down to the spectral baseline. These areas are taken to be the signal (S) and become the basis for the rest of the

quantitative analysis. Error is estimated by running area statistics (a preloaded feature in Origin) over a region of ~150 data points where the spectral baseline is relatively flat. The standard deviation found by this method is then taken to be the noise level (N). The error can then be calculated as the $\sqrt{N/S} \cdot S$.

Once error was determined for the raw data, the areas of the two peaks were normalized. As was discussed above, the populations of species A and B (P_A and P_B) must sum to 1, so the summed intensity of both peaks (I_{tot}) at all temperatures should be represented by the following linear equation, where σ_A and σ_B are constant scaling factors:

$$I_{tot} = \sigma_A P_A + \sigma_B P_B \quad (1)$$

A plot is made of area of peak A *versus* area of peak B (Figure 7.10). The two peaks in equilibrium should have a linear relationship; therefore, a linear line is fit to the data. If plotted so that the slope is negative, the y-intercept becomes σ_B and the given error becomes the absolute error. We can then calculate σ_A by equation 2 where m is the slope:

$$\sigma_A = -\sigma_B/m \quad (2)$$

Absolute error can then be calculated through standard error analysis. Normalized intensities can then be calculated according to equation 1 and absolute error can be calculated using standard error analysis.

7.7.2 $^{16}\text{O}_2$ system

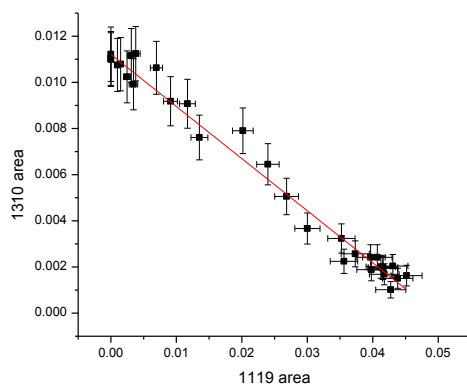


Figure 7.10 Integrated area of peak A (1119 cm^{-1}) *versus* integrated area of peak B (1310 cm^{-1}). There is a highly linear dependence between the two peaks across the temperature range with an R-squared value of 0.9749.

Table 7.1 Normalized peak areas with calculated errors for the calculation of an equilibrium constant for the $^{16}\text{O}_2$ system

Temp (K)	1119 norm	1119 abs err	1310 norm	1310 abs err	K norm	K err	1/T	ln K	ln K err
10.00	0.9099	0.0656	0.1451	0.0401	0.1594	0.0456	0.1000	-1.8360	0.2858
10.25	0.8611	0.0630	0.0905	0.0316	0.1050	0.0375	0.0976	-2.2534	0.3573
10.50	0.8412	0.0619	0.1501	0.0408	0.1785	0.0503	0.0952	-1.7234	0.2817
10.75	0.8365	0.0617	0.1735	0.0439	0.2074	0.0547	0.0930	-1.5732	0.2635
11.00	0.8825	0.0642	0.1346	0.0386	0.1526	0.0452	0.0909	-1.8801	0.2960
11.25	0.8015	0.0598	0.1682	0.0432	0.2098	0.0561	0.0889	-1.5615	0.2676
11.50	0.8376	0.0618	0.1766	0.0443	0.2109	0.0551	0.0870	-1.5565	0.2614
11.75	0.8199	0.0608	0.2159	0.0490	0.2633	0.0629	0.0851	-1.3346	0.2388
12.00	0.8674	0.0633	0.1819	0.0450	0.2097	0.0540	0.0833	-1.5619	0.2577
12.25	0.7993	0.0597	0.2158	0.0490	0.2700	0.0645	0.0816	-1.3094	0.2390
12.50	0.7518	0.0571	0.2294	0.0505	0.3051	0.0711	0.0800	-1.1871	0.2330
12.75	0.7172	0.0552	0.2003	0.0472	0.2792	0.0692	0.0784	-1.2757	0.2479
13.00	0.7093	0.0548	0.2885	0.0567	0.4067	0.0859	0.0769	-0.8997	0.2113
13.25	0.6046	0.0490	0.3271	0.0605	0.5410	0.1092	0.0755	-0.6143	0.2019
13.50	0.5407	0.0455	0.4511	0.0712	0.8343	0.1492	0.0741	-0.1812	0.1788
13.75	0.4831	0.0422	0.5754	0.0806	1.1910	0.1966	0.0727	0.1748	0.1651
14.00	0.4060	0.0376	0.7050	0.0895	1.7364	0.2730	0.0714	0.5518	0.1572
14.25	0.2723	0.0293	0.6790	0.0878	2.4935	0.4196	0.0702	0.9137	0.1683
14.50	0.2356	0.0269	0.8094	0.0961	3.4358	0.5660	0.0690	1.2343	0.1647
14.75	0.1836	0.0232	0.8190	0.0967	4.4605	0.7721	0.0678	1.4953	0.1731
15.00	0.1402	0.0199	0.9482	0.1043	6.7623	1.2158	0.0667	1.9114	0.1798
15.25	0.0694	0.0136	0.8845	0.1006	12.7432	2.8854	0.0656	2.5450	0.2264
15.50	0.0763	0.0143	1.0030	0.1074	13.1401	2.8348	0.0645	2.5757	0.2157
15.75	0.0497	0.0114	0.9132	0.1023	18.3625	4.6840	0.0635	2.9103	0.2551
16.00	0.0630	0.0129	0.9952	0.1070	15.8084	3.6585	0.0625	2.7605	0.2314
16.25	0.0202	0.0072	0.9592	0.1050	47.5589	17.6578	0.0615	3.8620	0.3713
16.50	0.0300	0.0088	0.9623	0.1051	32.1218	10.0290	0.0606	3.4695	0.3122

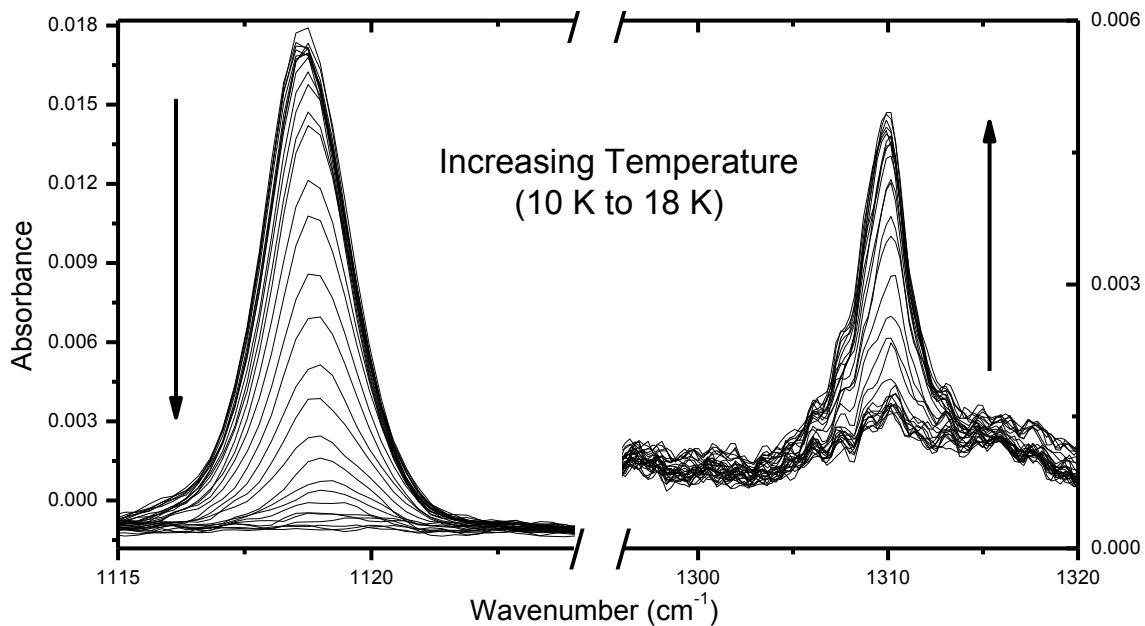


Figure 7.11 Conversion from 1119 to 1310 cm^{-1} upon increasing temperature. High density plot of data condensed in Figure 7.1.

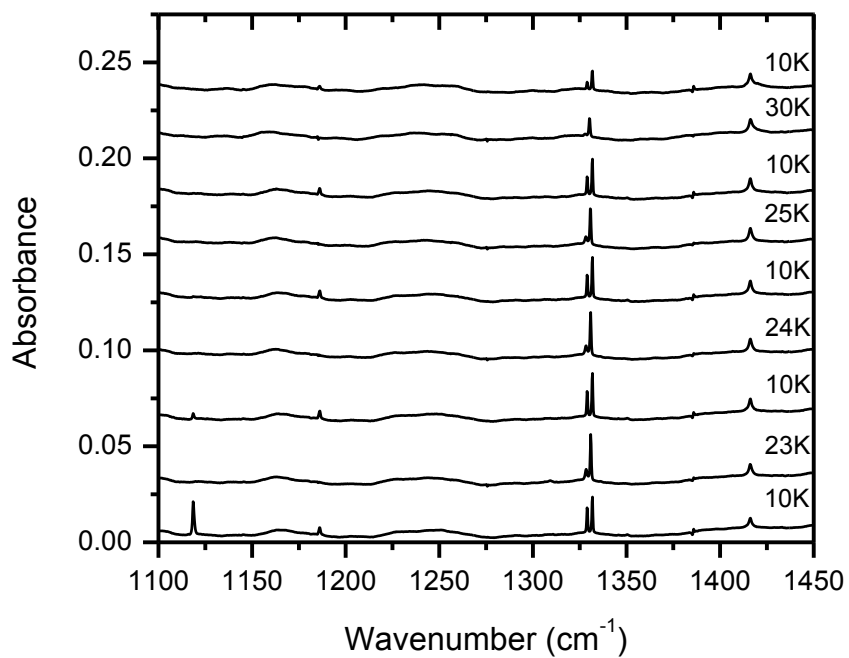


Figure 7.12 High temperature annealing for $^{16}\text{O}_2$ system. Note the loss of 1119 and 1310 cm^{-1} above 22 K as well as growth of the $(\text{O}_2)_3^+$ species at 1416 cm^{-1} .

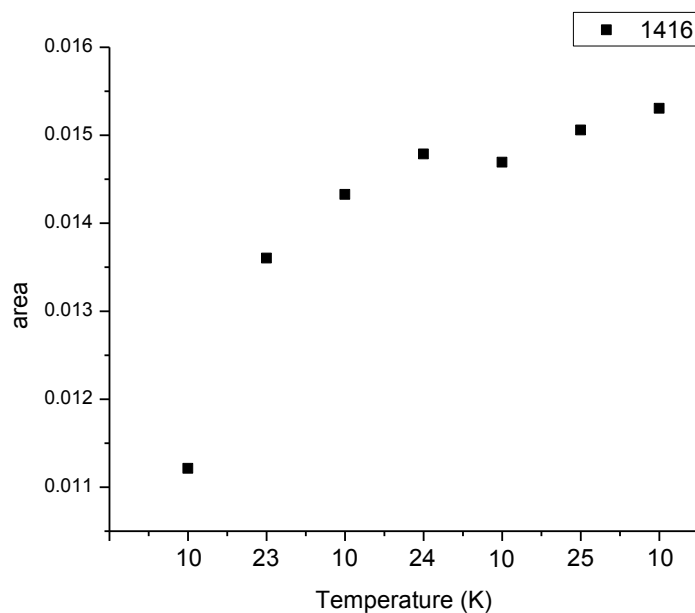


Figure 7.13 Area of 1416 cm^{-1} , O_6^+ , as a function of temperature. Integrated area from peaks in Figure 7.7.

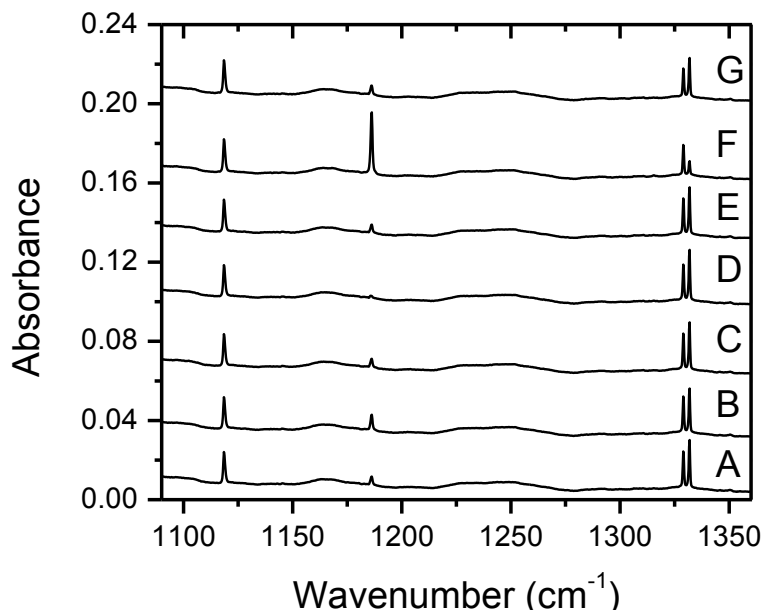


Figure 7.14 FTIR spectra of O_4^+ in argon matrices: A) spectrum recorded at 10 K following 20 K deposition, showing bands assigned to *trans*- (1119 and 1186 cm^{-1}) and cyclic (1329 and 1331 cm^{-1}) conformers, B) 590 nm centered LED, C) dark spectrum, D) broad band visible source, E) dark spectrum, F) 470 nm centered LED, and G) dark spectrum.

7.7.3 $^{18}\text{O}_2$ system

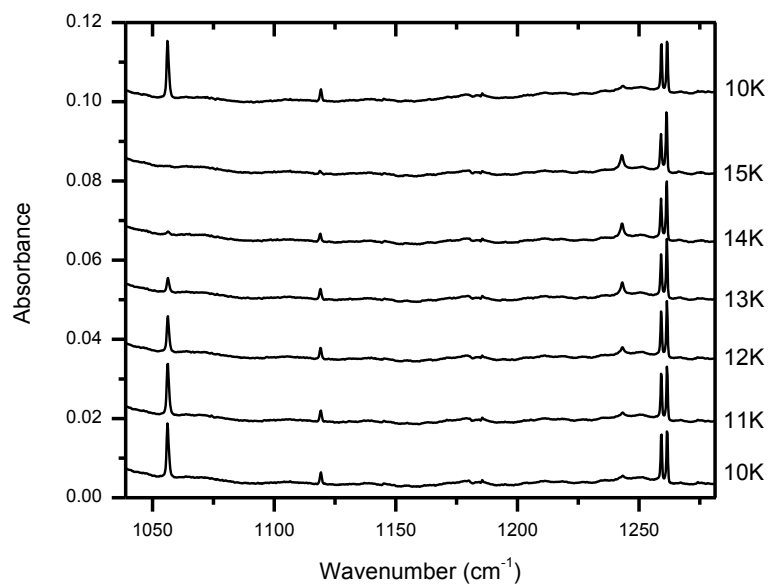


Figure 7.15 Cu- Ar⁺ deposited into a 0.5% $^{18}\text{O}_2$ in argon matrix. Note that the Cu⁻ is used here for the sole purpose of charge balance.

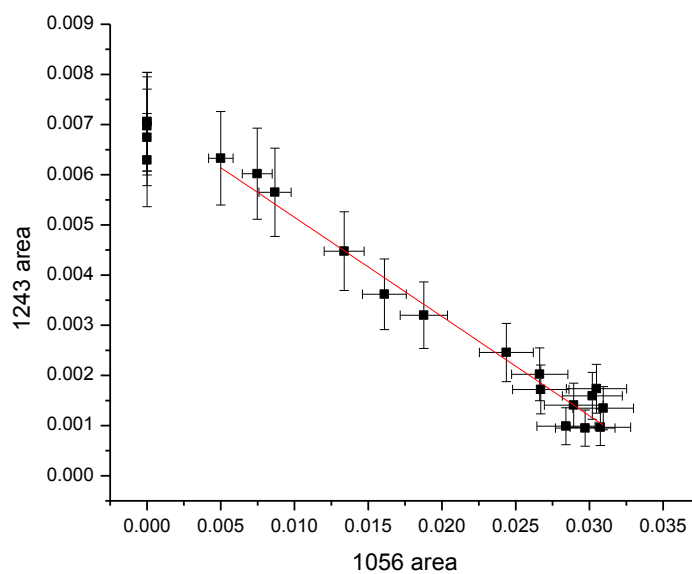


Figure 7.16 Two interconverting peaks for the $^{18}\text{O}_4^+$ system. Isotopic substitution shows the same linearity as that of the $^{16}\text{O}_4^+$ system. R-squared value is 0.9317.

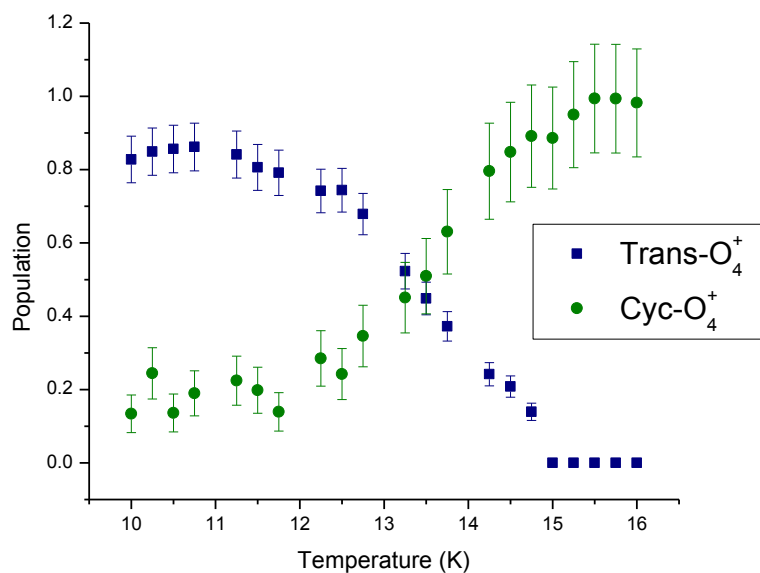


Figure 7.17 Thermal population of the $^{18}\text{O}_4^+$ system. There is more cyclic- O_4^+ at 10 K for the 18-isotope species.

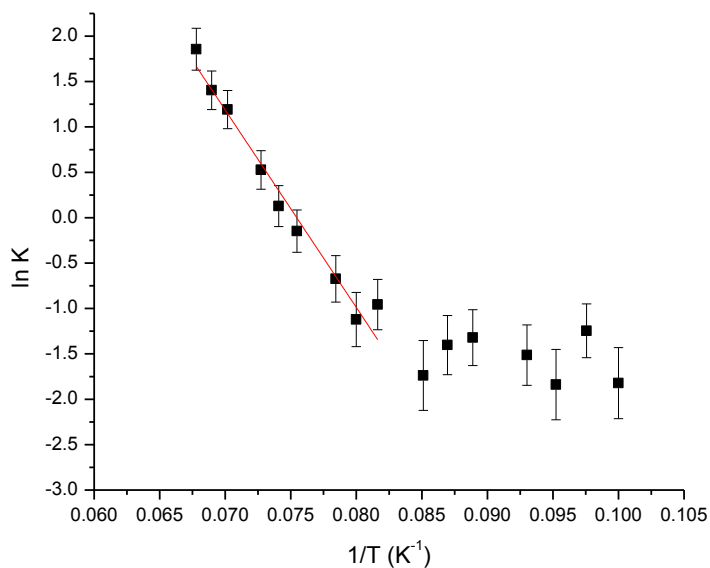


Figure 7.18 Van't Hoff plot for the $^{18}\text{O}_4^+$ system. Note the lower ΔH and ΔS values compared to the $^{16}\text{O}_4^+$ system as well as the divergence from linearity at 10 K and 11 K.

Table 7.2 Normalized peak areas with calculated errors for the calculation of an equilibrium constant for the $^{18}\text{O}_2$ system

Temp (K)	1056 norm	1056 abs err	1243 norm	1243 abs err	K norm	K err	1/T	ln K	ln K err
10.00	0.8278	0.0636	0.1339	0.0514	0.1617	0.0633	0.1000	-1.8219	0.3912
10.25	0.8492	0.0646	0.2443	0.0699	0.2877	0.0852	0.0976	-1.2459	0.2961
10.50	0.8563	0.0649	0.1362	0.0518	0.1590	0.0617	0.0952	-1.8387	0.3879
10.75	0.8618	0.0652	0.1897	0.0614	0.2201	0.0731	0.0930	-1.5137	0.3323
11.25	0.8413	0.0642	0.2244	0.0669	0.2667	0.0821	0.0889	-1.3216	0.3078
11.50	0.8061	0.0626	0.1981	0.0628	0.2458	0.0802	0.0870	-1.4033	0.3261
11.75	0.7914	0.0619	0.1392	0.0524	0.1759	0.0676	0.0851	-1.7380	0.3844
12.25	0.7419	0.0595	0.2849	0.0757	0.3841	0.1066	0.0816	-0.9570	0.2776
12.50	0.7439	0.0596	0.2423	0.0696	0.3257	0.0972	0.0800	-1.1218	0.2983
12.75	0.6787	0.0565	0.3460	0.0838	0.5098	0.1306	0.0784	-0.6737	0.2561
13.25	0.5229	0.0485	0.4508	0.0963	0.8620	0.2008	0.0755	-0.1485	0.2330
13.50	0.4484	0.0444	0.5096	0.1029	1.1363	0.2555	0.0741	0.1278	0.2248
13.75	0.3725	0.0400	0.6306	0.1154	1.6929	0.3592	0.0727	0.5265	0.2122
14.25	0.2418	0.0316	0.7959	0.1310	3.2920	0.6921	0.0702	1.1915	0.2102
14.50	0.2082	0.0292	0.8480	0.1357	4.0724	0.8663	0.0690	1.4042	0.2127
14.75	0.1393	0.0236	0.8914	0.1395	6.3976	1.4759	0.0678	1.8559	0.2307

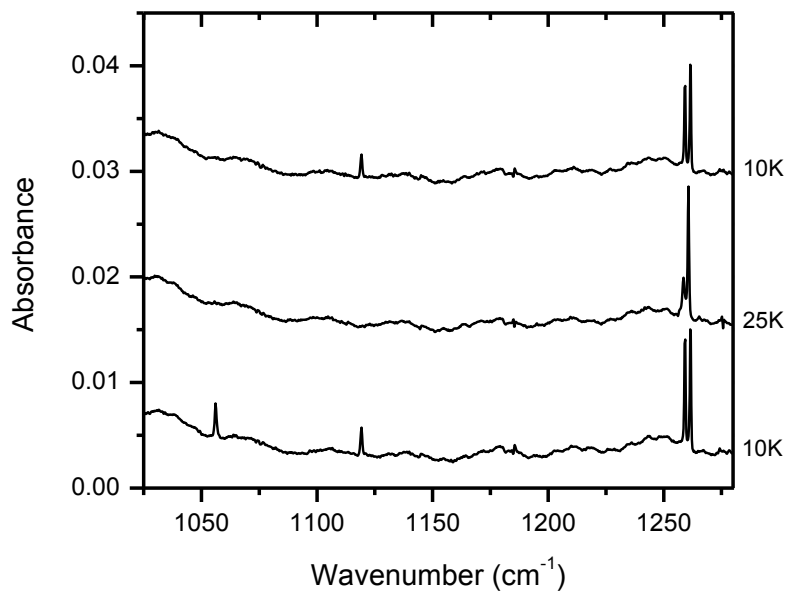


Figure 7.19 Higher temperature annealing of the $^{18}\text{O}_4^+$ system. Upon heating to 25 K, both the 1056cm^{-1} and 1243cm^{-1} peaks are destroyed irreversibly analogous to the $^{16}\text{O}_4^+$ system.

7.7.4 Deposition temperature anomalies

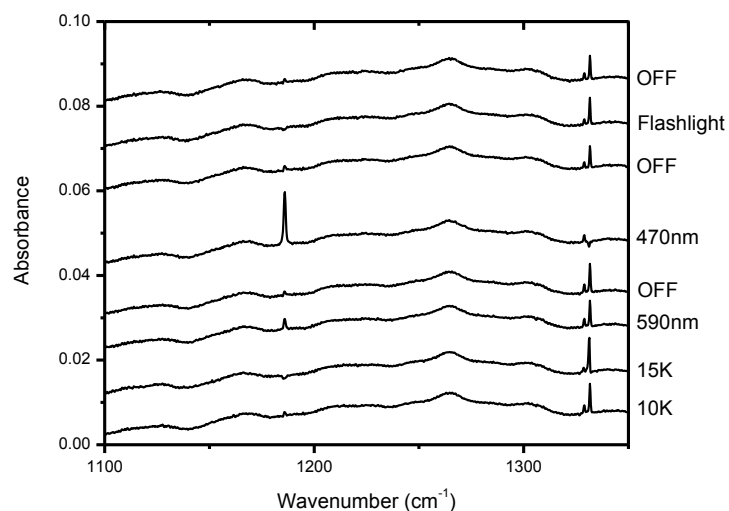


Figure 7.20 Deposition at 25K. Notice the absence of 1119 and 1310 cm^{-1} both upon deposition and at 15 K. Photochromism still occurs between the 1186 and 1332 cm^{-1} bands that are still present.

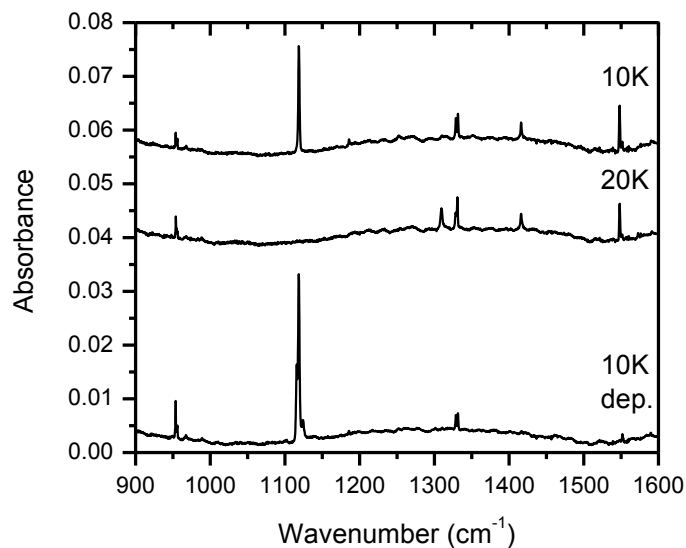


Figure 7.21 Deposition at 10 K with initial annealing to 20 K (before temperature series). Both the O_6^+ and $(\text{O}_2)_n$ clusters at 1416 and 1548 cm^{-1} , respectively, anneal in with the loss of a small population of *trans*- O_4^+ .

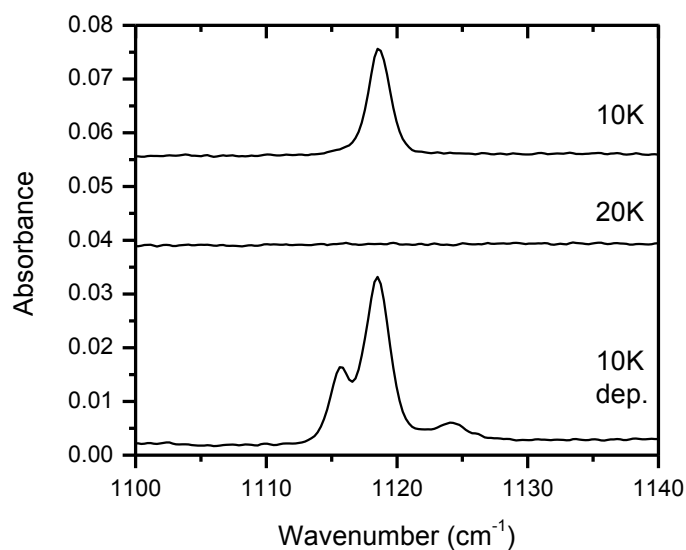


Figure 7.22 Expansion of *trans*-O₄⁺ band from Figure 7.21 showing two shoulder bands upon deposition at 10 K. Both bands are annealed away after initial warming of the system to 20 K along with a small population of the main 1119 cm⁻¹ peak.

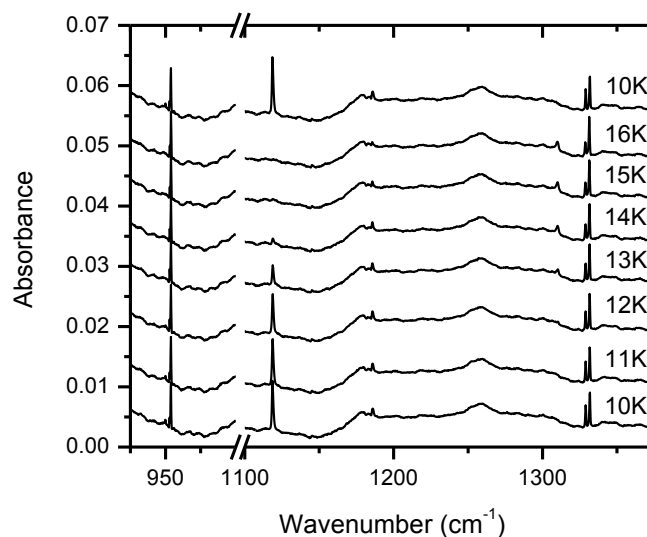


Figure 7.23 Deposition of high energy Ar⁺ (300 eV) into a 0.5% doped argon matrix with no explicit deposited anion. Note the large O₄⁻ peak at 953 cm⁻¹ formed upon deposition to maintain charge balance.

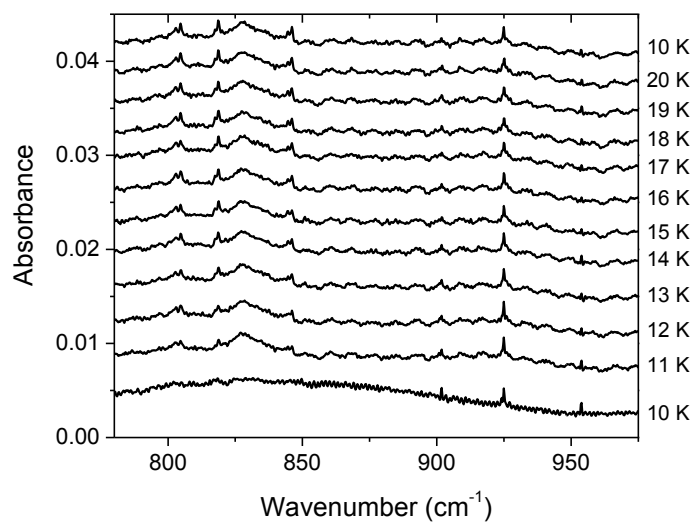


Figure 7.24 Cu⁻ Ar⁺ deposition for 6 hours at 20 K in a 0.5 % ¹⁶O₂ + 0.5% ¹⁸O₂ in argon showing Cu-O₄ and O₄⁻. Spectra are taken with sample at temperature shown. Note that this region does not have any temperature dependent trends.

Chapter 8

Silver and nickel anionic carbonyl systems: an investigation of the counter-ion codeposition method versatility

8.1 Abstract

The counter-ion codeposition method has been shown in previous chapters to successfully form and stabilize the anionic copper carbonyl system. In order to test whether some of the new behavior observed is unique to that system or whether it is more general and extends to other metal carbonyl systems, both anionic nickel and anionic silver were deposited in CO-doped matrices counter-balanced by argon cations. These metals were chosen due to their relationship to copper, namely silver being another coinage metal and nickel being in the same row next to copper. The anionic nickel system yields results very similar to those observed for the copper system. Both the anionic system, $\text{Ni}(\text{CO})_{1-3}^-$, and the neutral system, $\text{Ni}(\text{CO})_{1-4}$, are readily formed upon deposition and provide a wealth of peaks upon annealing and irradiation. The anionic silver system produced very few bands upon deposition with none that could be assigned to an anionic species, consistent with results from previous matrix isolation studies on the silver carbonyl system. After irradiation and post-irradiation annealing, many bands were observed including those assigned to the $\text{Ag}(\text{CO})_{1-3}$ in the literature. Both systems exhibit IR features that have been previously reported as well as several new ones that are observed here for the first time.

8.2 Introduction

This chapter presents studies on both the nickel and silver carbonyl systems to test the versatility of this new deposition method. Both systems have been studied in argon by previous groups and our results are compared to these studies for comparison and initial assignment of peaks. The studies presented here were performed at 20 K due to the large wealth of peaks observed with the copper system (Chapter 5). The following results are analyzed in light of our copper experiments.

Neutral nickel atoms were first deposited into a CO-doped argon matrix in 1969 yielding the tri- and tetra-carbonyl compounds as studied by IR.¹⁹⁰ These initial studies were later extended to the observation of all four carbonyl species Ni(CO)₁₋₄.^{191,192} In the late 1990's Manceron reinvestigated the nickel monocarbonyl system to include overtones and combination bands in argon.¹⁹³ The dicarbonyl system was then reinvestigated and twelve overtone, combination and fundamental bands, including seven of the nine fundamental vibrations, were assigned.¹⁹⁴ Based on these findings, they reassigned the dicarbonyl to a bent structure and not a linear structure as was previously thought.¹⁹⁴ Finally, Andrews investigated the nickel carbonyl system in argon *via* laser ablation.¹⁹⁵ In addition to the observation of all four neutral carbonyls, these studies also created the anionic Ni(CO)₁₋₃.¹⁹⁵ Though the cationic species were not observed in this study, Andrews' use of laser ablation applied to a neon matrix proved useful for the formation of the anionic, neutral, and the cationic system, Ni(CO)₁₋₄⁺.¹⁹⁶

Ogden first showed IR evidence for silver carbonyl formation in an argon matrix in 1971.¹⁹⁷ Using both IR and UV-Vis studies, Ozin observed peaks which were identified as the mono-, di-, and tri-carbonyl silver complexes.¹⁹⁸ The identification of the

monocarbonyl was later called into question by ESR studies which suggested that the monocarbonyl does not form.^{199,200} This observation is supported by calculation of the Ag-CO⁻ anion potential energy surface which found no bound states at the MP4 level.²⁰¹ Likewise, the neutral Ag-CO system has been calculated to have an extremely small binding energy of ~0.114 kcal/mol.^{202,203} Andrews has applied his laser ablation technique to this system in neon and observed Ag(CO)₂₋₃ and Ag(CO)₁₋₄⁺.²⁰⁴ He noted the absence of any silver or gold based anionic compounds in this study.²⁰⁴ Anionic metal species were absent even though free electrons still existed in the system as demonstrated by (CO)₂⁻, whose formation coincided with the formation of metal anions in all other transition metal studies.^{85,204} To date, no anionic silver carbonyl complexes have been observed in any matrix material and no cationic silver carbonyls have been observed in argon.

8.3 Experimental

All of the studies contained in this chapter were performed under darkened conditions with all internal sources of light turned off (ion gauges, RGA analyzer, etc.), and the lab lights kept off as well. The spectrometer beam was directed away from the deposition chamber when not recording spectra. Irradiation was performed using narrow-band LED sources centered at 735, 670, 560, 470, and 365 nm (Thor Labs, see spectra Figure 4.6) held outside the vacuum chamber and introduced through a Kodial glass viewport (Kurt J. Lesker Company).

Most of the ion optics remained the same as that for copper anion deposition with a few minor changes. First, the magnetron source was run at a current of 108 mA for silver and 81 mA for nickel (down from 117 mA for Cu). Also, the 22 mm quadrupole DC-bias was turned up to 25 V (up from 10 V) for nickel anion deposition. Finally, the inner pole

was turned down to ~45 V for both Ni⁻ and Ag⁻. All settings remained the same for the octopole ion guide (for a complete list of ion optic settings, see Table 2.2). It should also be mentioned that the Ni⁻ and Ag⁻ ion energies were slightly lower than that for copper anions at -4 and -5 eV, respectively.

All matrix samples were prepared by deposition of either 4 nA Ni⁻ or Ag⁻ with Ar⁺ counter-ions in an Ar matrix gas doped with 0.02% CO at 20 K deposition for 4 hours under a steady-state pressure of 10⁻⁵ Torr (~108 mmol total gas exposure). All matrix gases were purified by flowing through a copper tube immersed in an ethanol liquid-nitrogen bath prior to deposition. Annealing was carried out by holding the sample at the specified temperature for 15 minutes then cooling back to 10 K in order to record a spectrum. Isotope experiments have not been performed on either system yet, therefore all assignments are tentatively based on literature values and reaction to post-deposition manipulations.

8.4 Results and discussion

8.4.1 Anionic nickel deposition

Figure 8.1 shows data for deposition of anionic nickel in a CO-doped matrix using Ar⁺ as the counter-ion. This system is very similar to what we observed for the copper carbonyl (Chapter 5) in that a wealth of peaks are present, some of which have the same trends as the transients observed for copper. Many of these peaks are reminiscent of those observed in previous laser ablation studies;¹⁹⁵ a complete listing of all peaks observed is given in Table 8.1. In general the anionic nickel carbonyl species exist in the range of 1700-1900 cm⁻¹ while the neutrals are found between 1900-2050 cm⁻¹.

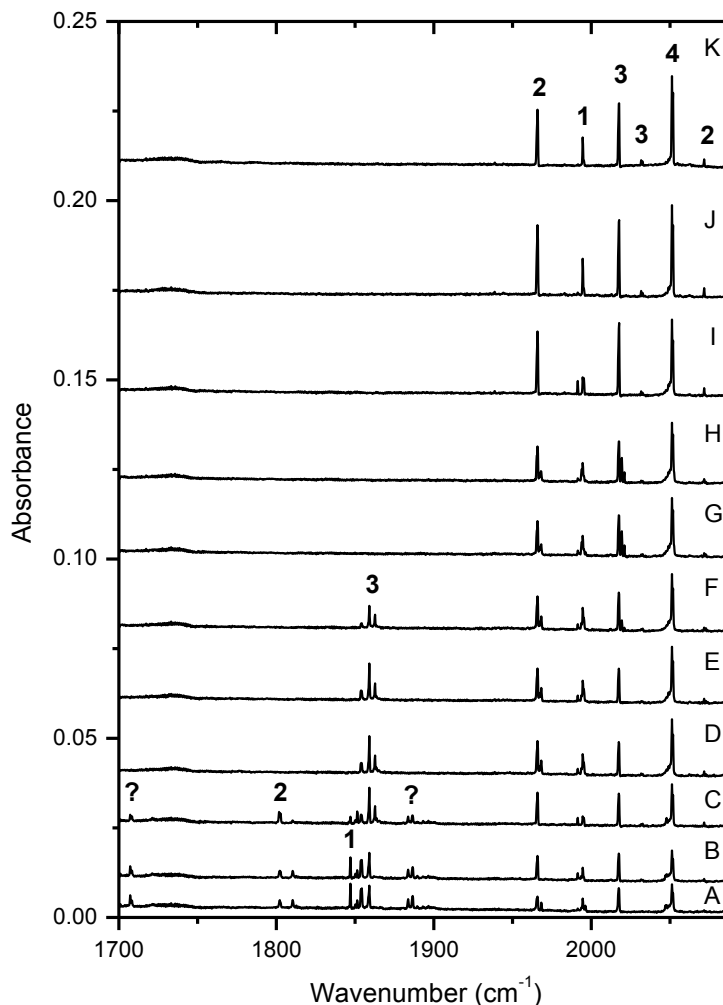


Figure 8.1 Ni⁻ Ar⁺ co-deposited (4 nA each) for 4 hours with 0.02% CO in argon at 20K: A) 20 K deposition, B) 25 K annealing, C) 30 K annealing, D) 735 nm irradiation, E) 670 nm irradiation, F) 560 nm irradiation, G) 490 nm irradiation, H) 365 nm irradiation, I) 30 K annealing, J) 35 K annealing, and K) 40 K annealing. All spectra taken at 10 K. Major bands labeled for the mono- (1), di- (2), tri- (3), and tetra-carbonyl (4) complexes and unknown species (?).

The anionic mono- and tri-carbonyl frequencies are very close to one another near 1850 cm⁻¹, which convoluted some of the early assignments of these bands.¹⁹² We observe bands at 1847.0 and 1850.2 cm⁻¹ which have been assigned to the anionic monocarbonyl as well as bands at 1854.0 and 1859.1 cm⁻¹ assigned to the anionic tricarbonyl.¹⁹⁵ We also observe the previously assigned anionic dicarbonyl at 1801.7 cm⁻¹.¹⁹⁵ Similar to our copper

system, there are many other bands in this region that increase or decrease upon annealing (Figure 8.2). Without assignment of these new bands, it is difficult to tell whether the observed annealing changes are due to clustering or due to a more complex mechanism such as transient formation. There are also two other groups of bands that are not near any of the peaks assigned in the literature, namely near 1700 cm^{-1} and 1890 cm^{-1} (see Table 8.1 for specific frequencies). With the exception of five bands including the two assigned to the anionic tricarbonyl, all peaks below 1900 cm^{-1} are destroyed upon 735 nm light including the new bands near 1700 cm^{-1} and 1890 cm^{-1} (Figure 8.1D). Based on their location and depletion with 735 nm light, these new bands are likely anionic. The 735 nm irradiation also gives rise to bands near 1966, 1995, and 2051 cm^{-1} assigned to the neutral di-, mono-, and tetracarbonyl systems respectively. This behavior adds further insight toward the new anionic bands observed, that they are likely one of these three systems. Furthermore the neutral tetracarbonyl increases, yet this was not one of the assigned anionic bands that were lost. It is likely that one or both of our new anionic regions is due to the anionic nickel tetracarbonyl, however, it is too early to definitively assign this without isotope experiments. Likewise, the bands assigned to the $(\text{CO})_2^+$ (Chapter 6) are present as shoulder bands to the tetracarbonyl (see Figure 8.2 for depletion upon annealing to 30 K and irradiation at 735 nm).

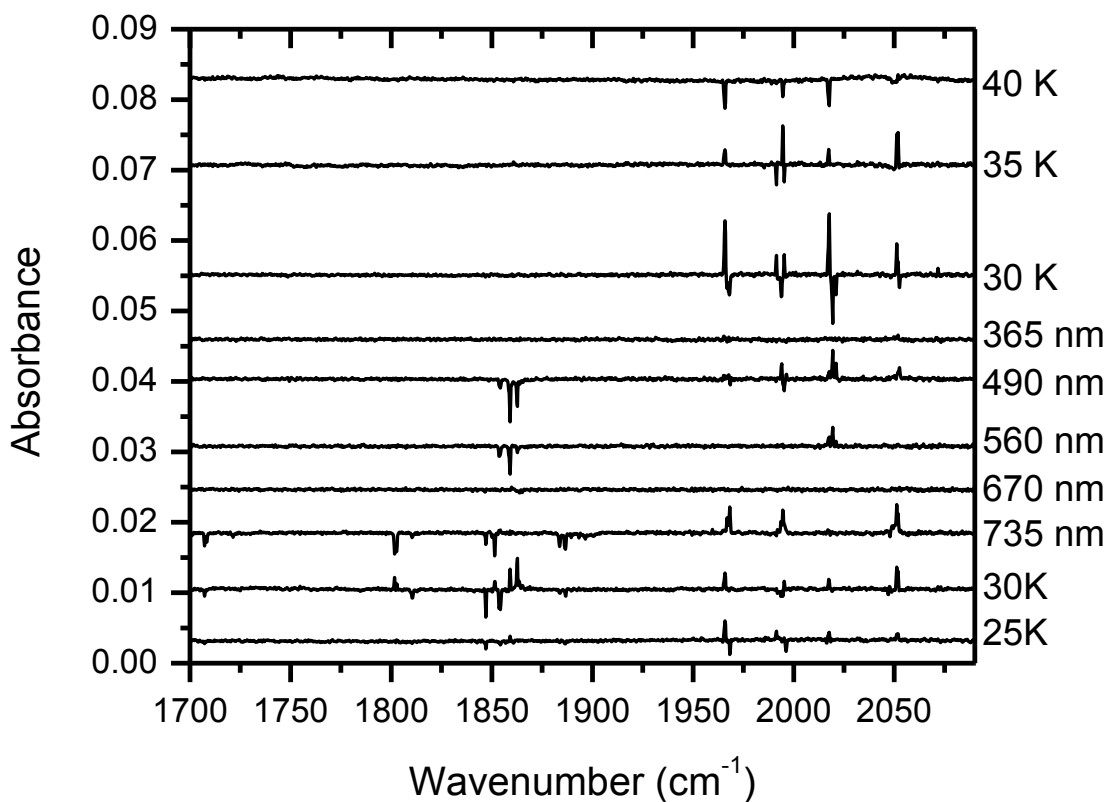


Figure 8.2 Subtraction data from Figure 8.1, $\text{Ni}^- \text{Ar}^+$, showing stepwise differences that occurred at each processing step labeled accordingly.

The other five anionic bands, which include the two assigned to the anionic tricarbonyl, are decreased with 560 nm light (Figure 8.1F). Likewise the neutral tricarbonyl bands near 2017.4 cm^{-1} increase adding credence to all these new bands belonging to the tricarbonyl system. Irradiation with 490 nm light completely destroys what's left of the anionic tricarbonyl bands (Figure 8.1G). Now, however, instead of just the neutral tricarbonyl growing in, the monocarbonyl is affected and the tetracarbonyl gains intensity as well (see subtraction Figure 8.2). Since the more energetic UV light does not affect the neutral bands further (Figure 8.1H), it seems likely that the neutral-complex

changes with 490 nm light stem from the anionic tricarbonyl precursor which may be undergoing photolysis or clustering at that wavelength, although it cannot be ruled out that any “reactions” occurring have not gone to completion which is why no change occurs with UV light.

Annealing at 30 K after irradiation has the same outcome as observed for copper whereby population transfer is observed presumably from less stable matrix-sites to more stable sites. This effect is seen with the di-, tri-, and tetracarbonyl, all of which show the depletion of one or more bands with the concomitant growth of a single, sharp, intense peak (compare spectra 8.1H with 8.1I; see also subtraction spectra, Figure 8.2). The monocarbonyl displays anomalous behavior in that four peaks are interconverted depending on what process is applied to the sample. Upon 460 nm irradiation, the 1993.8 cm^{-1} band increases while the 1995.3 cm^{-1} decreases. Annealing at 30 K increases the 1991.4 and 1995.3 cm^{-1} while decreasing the 1993.8 cm^{-1} . Annealing to 35 K once again decreases both the 1991.4 and 1995.3 cm^{-1} while 1994.5 cm^{-1} increases. Finally, at 40 K the 1994.5 cm^{-1} band decreases with no growth in any of the other bands. This system is very reminiscent of that observed for the copper dicarbonyl (see Chapter 5).

With the exception of the monocarbonyl bands just described, peaks associated with the other three carbonyl species increase upon annealing to 35 K. This growth is interesting since no depletion is observed in the carbonyl region (with the exception of the monocarbonyl described). It is possible this is due to aggregation although the small amount of monocarbonyl that is lost does not seem like it could give rise to the large growth of the other three species that is observed, unless it has a very low oscillator strength in relation to the other species. Finally, 40 K annealing leads to a loss of the mono-, di-, and

tri-carbonyl species which is consistent with our previous observation of overall sample loss through argon matrix sublimation.

It is worth briefly discussing the strange trends in the various vibrational frequencies with cluster size. The Ni-CO is anomalously blue shifted similar to what we observed for the Cu-CO system; however, the copper and nickel trends arise from two separate phenomena. The copper monocarbonyl blue shift has been explained due to the odd electron existing almost entirely in a 4s character, thus containing almost no back bonding as observed by a blue shifted monocarbonyl from what would be expected based on the di and tricarbonyl trends.¹⁹⁸ The nickel carbonyl, on the other hand, has been found to contain substantial vibrational coupling between the Ni-C and C-O stretching coordinates which effectively blue-shifts the vibration.¹⁹³ The nickel dicarbonyl also shows a strange vibrational pattern with two modes separated by $\sim 100\text{ cm}^{-1}$. Originally, this compound was believed to exist in a linear geometry¹⁹¹ with the 1966 cm^{-1} band belonging to the strong asymmetric stretch (note that the 2071 cm^{-1} band was not observed in this earlier study). The observation of a weak band at 2071 cm^{-1} could only be described by the symmetric vibrational mode of a bent dicarbonyl structure containing more Ni-C movement than C-O.¹⁹⁵ Furthermore, Andrews calculations found that the linear molecule is 2.7 kcal/mol higher in energy and contains an imaginary frequency signifying that the bent structure is the stable structure and its existence in the matrix is not simply due to matrix effects. Both the nickel tricarbonyl and tetracarbonyl species show typical behavior for the asymmetric stretch.¹⁹⁵ The anionic anomalies arise for the same reasons as the neutral complexes. Again, the anionic monocarbonyl vibration contains a high amount of

Ni-C character while the dicarbonyl contains a slight bent geometry in the ground state.¹⁹⁵ Finally, the anionic tricarbonyl shows typical behavior for a D_{3h} molecule.

8.4.2 Anionic silver deposition

The anionic silver carbonyl system only yielded four weak bands upon deposition at 1786.4, 1803.0, 1940.8, and 1959.1 cm^{-1} , Figure 8.2A, none of which are in the literature (a complete listing of peaks can be found in Table 8.2). This is in stark contrast to the anionic copper and nickel studies where we observed peaks for $M(\text{CO})_n^q$ ($M = \text{Ni}$ or Cu , $n = 1-3$ & 4 for nickel, $q = -1, 0$) including many new sharp bands not previously assigned. Even initial annealing up to 30 K only anneals three bands at 1841.7, 1951.6, and 1957.9 cm^{-1} , all of which are relatively weak (Figure 8.3C). Interestingly, these three bands match assignments in the literature.²⁰⁴ Five peaks have been assigned in an argon matrix, but only two can be definitively assigned to peaks we observe (Table 8.2). The first two bands at 1841.7 and 1951.6 cm^{-1} correspond to the dicarbonyl and tricarbonyl respectively.¹⁹⁸ The band at 1957.9 cm^{-1} is near an absorbance for both the mono- and tri-carbonyl bands in previous work¹⁹⁸ and cannot be definitively assigned at this time, although its increase upon each annealing step lends credence to this being another tricarbonyl band.

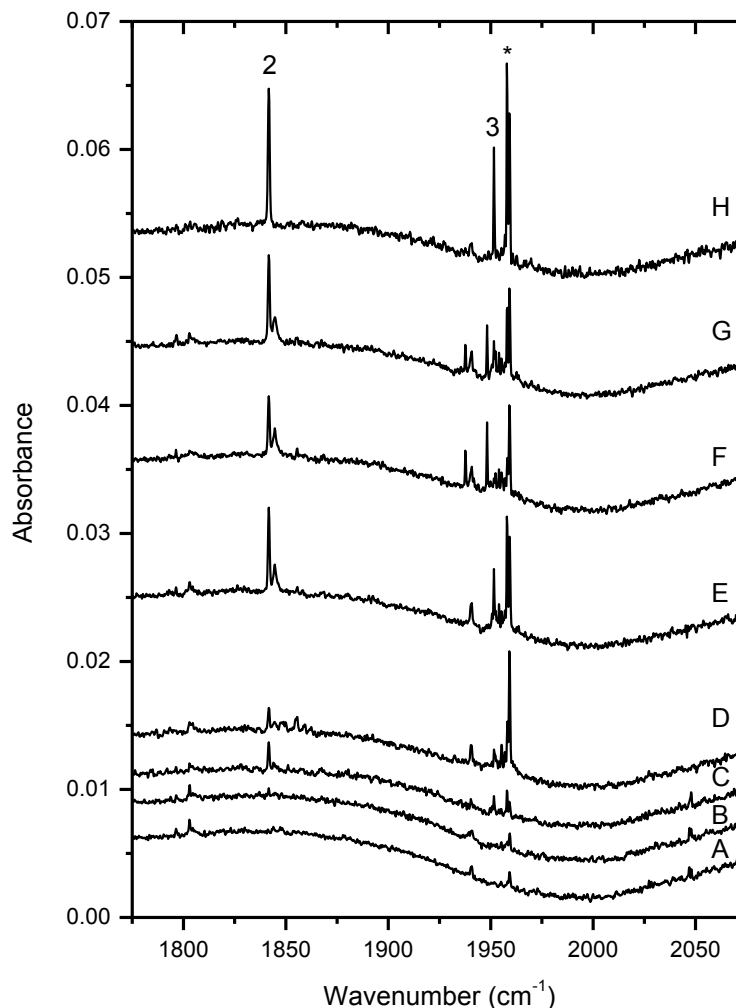


Figure 8.3 $\text{Ag}^- \text{Ar}^+$ co-deposited (4 nA each) for 4 hours with 0.02% CO in argon at 20 K: A) 20 K deposition, B) 25 K annealing, C) 30 K annealing, D) 470 nm irradiation, E) 30 K annealing, F) 365 nm irradiation, G) 30 K annealing, and H) 40 K annealing. All spectra taken at 10 K. Literature peaks labeled for di- (2) and tri-carbonyl (3). The * denotes a peak near a literature assignment for a mono- and tri-carbonyl species separated by 0.2 cm^{-1} .

It is not until irradiation with 470 nm centered light that large changes are observed in the spectrum (Figure 8.3D). One peak in particular becomes in very intense at 1959.1 cm^{-1} . A few lower intensity bands are also irradiated into the spectrum (see Table 8.2). It should be noted that no peaks are diminished from irradiation at this wavelength, so it is unclear at this time how these compounds are made and any attempted

explanation would be purely speculative at this point however, the $(\text{CO})_2^+$ does go away with the 470 nm light insinuating that electrons are being photodetached in the matrix (Figure 8.4, Appendix). It's possible that there are free Ag^- atoms trapped that become photodetached or some anionic silver carbonyls that are dark in their ionic state, but both situations are hard to rationalize. Just as interesting, annealing to 30 K after the initial irradiation step, yields even more growth in several peaks with only small depletions of very weak bands.

Because of these results, a second irradiation step was performed using 365 nm light. Five bands are clearly affected by the UV light (see subtraction data, Figure 8.4); an increase is seen for the 1937.6 and 1948.2 cm^{-1} bands while a decrease is observed for the bands assigned in the literature at 1841.7, 1951.6, and 1957.7 cm^{-1} .¹⁹⁸ All of these changes are reversible by annealing to 30 K. Finally, 40 K annealing seems to simplify the spectrum in that minor peaks are annealed away while four intense peaks ensue: 1841.7, 1951.6, 1957.9, and 1959.1 cm^{-1} . Once again the first three of these bands are the ones assigned in the literature study. This system's response to high energy light is reminiscent of the Cu-NO study performed by the Manceron group. They showed a photoconversion between two low-lying states of Cu-NO in an argon matrix monitored by a shift in the NO vibrational mode.²⁰⁵ After excitation into a nearly isoenergetic electronic state with 632 nm light, the system relaxes back to its original state over the course of ~5 minutes.²⁰⁵ Low-lying electronic states, such as in the Manceron study, could be important in identifying some of the new bands that are observed in our carbonyl complexes.

8.6 Conclusion

The versatility of the counter-ion codeposition method has been presented here. Both the nickel and silver carbonyl systems were investigated by deposition of Ni^- or Ag^+ counter-balanced by Ar^+ . These systems were chosen in order to do “short” survey scans on a metal both in the same row and in the same family as copper; however, the complexity of both systems warrant further investigations.

Both metals here were studied under the same deposition conditions as that of the anionic copper carbonyl system. It was assumed that the two systems studied would behave the same as the copper system both upon deposition and upon post-deposition manipulations. This is definitely an oversimplification since factors such as interaction with the argon matrix, diffusion during deposition, and M-CO_n reactions are different for each of the systems. Future studies on these systems will include manipulation of parameters such as deposition temperature and CO concentration. Finally, due to the wealth of peaks observed for both systems that was not observed in the literature, careful isotope experiments are necessary for complete characterization of each system.

8.7 Appendix

Table 8.1 Vibrational frequencies observed for the anionic and neutral nickel carbonyl system. Changes at various processing steps are shown accordingly.

Peaks	Pre-Irr. Annealing		Irradiation		Post-Irr. Annealing		Tentative Assignments	Ref.
	Increase	Decrease	Increase	Decrease	Increase	Decrease		
1702.2		30 K		735 nm				
1708.2				735 nm				
1801.7	30 K			735 nm			Ni(CO) ₂ ⁻	e
1802.7	30 K			735 nm				
1810.4		30 K		735 nm				
1847.0		30 K		735 nm			Ni(CO)-	e
1850.2				735 nm			Ni(CO)-	e
1851.4	30 K			735 nm				
1854.0		30 K		560, 490 nm			Ni(CO) ₃ ⁻	e
1858.3				560, 490 nm			Ni(CO) ₃ ⁻	
1859.1	30 K			560, 490 nm			Ni(CO) ₃ ⁻	e
1862.7	30 K			560, 490 nm			Ni(CO) ₃ ⁻	
1863.7	30 K			560, 490 nm			Ni(CO) ₃ ⁻	
1883.7		30 K		735 nm				
1886.6		30 K		735 nm				
1889.4				735 nm				
1893.3				735 nm				
1896.7				735 nm				
1965.9	25 K				30, 35 K	40 K	Ni(CO) ₂	b,c,d,e
1968.3		25 K	735 nm	490 nm		30 K		
1991.4	25 K				30 K	35 K	Ni(CO)	e
1993.8			490 nm			30 K	Ni(CO)	
1994.5		30 K	735 nm		35 K	40 K	Ni(CO)	c,e
1995.3	30 K			490 nm	30 K	35 K	Ni(CO)	a
1996.2		25 K					Ni(CO)	b
2017.4	30 K				30, 35 K	40 K	Ni(CO) ₃	b,d,e
2019.4			560, 490 nm			30 K	Ni(CO) ₃	
2021.1			560, 490 nm			30 K	Ni(CO) ₃	
2031.7	30 K						site	e
2032.6	30 K							
2047.8		30 K						
2049.0			735 nm					
2050.2			735 nm					
2051.2	30 K		735 nm		30, 35 K		Ni(CO) ₄	e
2051.9	30 K				35 k	30 K	Ni(CO) ₄	a,b
2071.7	30 K				30 K		Ni(CO) ₂	d,e

a reference 192

b reference 191

c reference 193

d reference 194

e reference 195

Table 8.2 Vibrational frequencies observed for the anionic and neutral silver carbonyl system. Changes at various processing steps are shown either by an increase in the peak (\uparrow) or a decrease in the peak (\downarrow). Assignments based on ref. 198.

Peaks	20 K	30 K		Post-470 nm				Post-365 nm				Tentative Assignment		
		\uparrow	\downarrow	\uparrow	\downarrow	Annealing	\uparrow	\downarrow	\uparrow	\downarrow	30 K		40 K	
1796.4	\dagger													
1803.0	\dagger													
1841.7		x				x			x	x				Ag(CO) ₂
1844.6					x	x							x	
1848.9					x		x							
1855.4					x		x							
1859.3					x		x							
1862.4					x		x							
1937.6								x			x		x	
1940.8	\dagger				x									
1948.2								x			x		x	
1951.6		x				x			x	x		x		Ag(CO) ₃
1952.3					x								x	
1954.0						x							x	
1955.2					x		x							
1956.9					x									
1957.9		x				x			x	x		x		*
1959.1	\dagger				x		x					x		

\dagger denotes peaks present upon deposition at 20 K

*two peaks at 1958.0 and 1958.2 cm⁻¹ were assigned to the Ag(CO) and Ag(CO)₃ species respectively in ref. 198

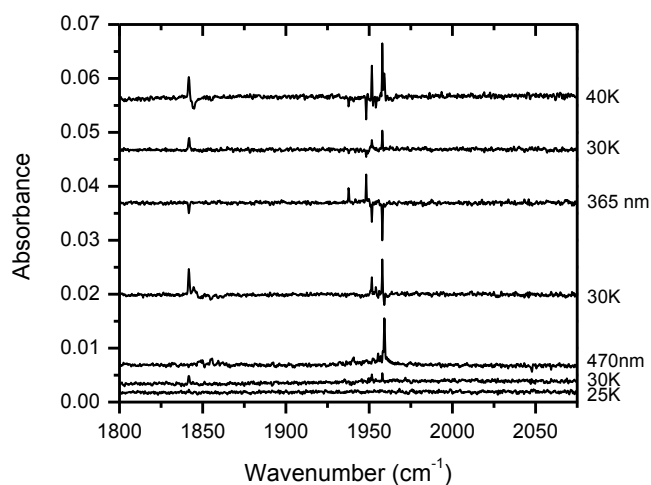


Figure 8.4 Subtraction data from Figure 8.2, Ag⁻ Ar⁺, showing stepwise differences that occurred at each processing step labeled accordingly.

Chapter 9

Conclusions and future directions

9.1 Conclusions

The results presented in this dissertation have demonstrated a new method for deposition of ions into an argon matrix, namely a counter-ion codeposition technique. This approach uses mass-selected metal anions, generated from a magnetron sputter source, that are codeposited with a beam of counter-cations into rare-gas matrices. By balancing the current of both ion beams such that the overall net-charge is zero, sufficient number densities of ions are built up in the matrix. Furthermore, by doping an amount of reactive gas into the matrix such as CO, metal-ligand complexes can be spectroscopically observed.

We have proven the feasibility of this technique through intensive studies of the copper carbonyl system by deposition of Cu^- balanced by either Ar^+ or Kr^+ into CO-doped matrices. Our initial studies (Chapter 3) show that compound-formation is strongly dependent upon both dopant concentration and deposition temperature. At the lowest temperature, 10 K, CO concentrations of 2% are necessary to form sufficient carbonyl concentrations upon deposition, whereas only 0.02% CO is necessary to produce roughly the same spectrum when deposited at 20 K. At 30 K only 2 ppm are necessary, very close to a $\text{Cu}^-:\text{CO}$ ratio of 1:1 yet di- and tri-carbonyl complexes are still observed. Likewise when a high CO concentration of 0.5% is deposited at 20 K, only large clusters of the type $[\text{Cu}(\text{CO})_3 \cdot (\text{CO})_n]^{-1,0}$ are formed. This is the first time these secondary shell species have been identified in matrices.

One hallmark of this new technique occurred when deposition was carried out at 10 K in the absence of any ambient light (Chapter 4). Under these conditions, **only** the anionic copper carbonyl species were observed upon deposition. This presents a huge advancement from the literature where ion deposition methods typically produce anions, cations, and neutrals of both the system of interest and from contaminant species trapped in the matrix. Our new method not only allows the selective isolation of anionic metal compounds but it is also gentle enough that secondary reactions and uncontrolled processes do not occur. This works to our advantage in that wavelength dependent photodetachment events can be carried out and monitored. Furthermore, because of the “clean” deposition spectrum the fate of this detached electron can be followed. In this study it attaches to the van der Waals CO-dimer and induces a covalent C-C bond. The ability to deposit under such control and monitor reaction processes has promise moving forward with future studies of catalytically relevant systems.

The power of this new deposition method toward the formation and stabilization of transient bands is demonstrated with 20 K deposition under darkened conditions (Chapter 5). Here, annealing diminishes several anionic bands with the concomitant growth of new anionic peaks. By photodetachment of these newly formed species, peaks appear in the neutral region which can be directly linked to the previously induced anionic bands. These bands are very reminiscent of vertical detachment products predicted by computational ionization studies. Further annealing of the neutral system diminishes several transient neutral bands while adding intensity to previously observed neutral bands. Based on these results, multiple reaction pathways can be drawn based upon the input of energy either in the form of heat or light. This is directly related to our goal of a new

technique called “freeze-frame” spectroscopy whereby reaction intermediates are trapped in a matrix and then driven over reaction barriers by the input of external energy. The reactions drawn from data in Chapter 5 present the first example of the “freeze-frame” technique using this new deposition method. Furthermore, high resolution spectra show that most of the bands contain instrument-limited linewidths at the maximum 0.125 cm^{-1} resolution setting which is not typical for matrix isolation in general and very rare for argon matrices.

In our attempts to study the copper oxide system, a fundamental discovery was made: the coldest example of chemical equilibrium (Chapter 7). We have shown a reversible conformational rearrangement from the *trans*- O_4^+ to cyclic O_4^+ by annealing between 10-16 K. Quantitative analysis on this system is consistent with an endothermic, entropy-driven reaction taking place which is rationalized in terms of a simple cavity-coupling model. Two other peaks, also assigned to *trans*- and cyclic O_4^+ species, show photochromic behavior in that different wavelengths of light drives reversible changes between the two conformers. The only way we can rationalize these two sets of peaks at this time is that one set is due to the quartet spin state while the other arises from the less-stable doublet which is able to be trapped in the matrix. Again, the level of control in this new deposition method affords us with the ability to study fundamental phenomena which were not studied using previous deposition methods.

Finally, the robustness of this new technique was studied through the deposition of both nickel and silver anions into CO-doped matrices. Nickel deposition provided both anionic and neutral carbonyl complexes similar to that observed with the copper system. Silver on the other hand contained almost no complexes upon deposition. This observation

was in line with literature studies which also noted the lack of any ionic complexes and very low amounts of the neutral mono-, di-, and tri-carbonyl complexes. Silver eventually did react with CO after irradiation and annealing. Both systems provided many new IR bands which have not been observed by previous methods which is in line with our copper system.

The unique control afforded by this new deposition technique should add insight into fundamental ion-reactions in future experiments. Though the studies presented here have all been anionic metal species, this technique should be generally applicable to any ions of interest that can be easily introduced in the gas phase. It is our hope that this method will inspire the chemistry community as a whole to revive the matrix isolation technique as a way of studying fundamental reactions under a high levels of control.

9.2 Future directions

9.2.1 Mass-selected cations

An obvious next step in future experiments is to deposit mass selected cations. Up to this point, all counter-cations have been Ar^+ or Kr^+ due to their ease of formation. Beside the formation of a small amount of $(\text{CO})_2^+$, we are spectroscopically blind to any other cations in the matrix. It's of vital importance that we have an IR active compound as a counter-cation moving forward. This will afford us the ability to not only monitor anionic metal complexes but also gives us a handle as to what the cation is doing during post-deposition matrix manipulations. For example, we still do not know if any of the new peaks observed upon annealing are due to ion-ion interactions. A spectroscopically active cation should afford us valuable information if such an events occurring. A few attempts

were made to deposit IR active cations such as CO^+ and SF_5^+ formed by electron impact ionization in the bender chamber, however the background gas was sufficiently high that enough neutral gas contaminated the spectrum. Furthermore, we do not know what cations, if any, were being generated.

We are currently in the process of installing a chemical ionization (CI) source which is coupled to a second quadrupole bender as well as another quadrupole mass-filter. This will give us the opportunity to form a beam of either mass-selected cationic or anionic species. Furthermore these species are generated in a new, differentially pumped chamber so that background gas necessary to form the ions does not contaminate the matrix. The setup and initial testing of this source is largely being carried out by Michael Goodrich and has been used thus far to generate mass selected beams of Ar^+ and Ar^{2+} .

An early experiment to be carried out with this source will be Cu^- counter-balanced by CO^+ and $(\text{CO})_2^+$ with **no** neutral CO deliberately doped into the matrix. Assuming one or both of these cations can be stabilized during deposition in the matrix, a number of important findings should come from this. First, definitive assignments of the cation peaks derived from CO species can be made. In particular, the CO^+ molecule can be assigned since no neutral CO should be present to obscure its frequency. Also fundamental reaction and diffusion kinetics should be gained by adjusting deposition conditions and observing $\text{Cu}^- + \text{CO}^+$ reactions which should lead to the neutral monocarbonyl complex. Since the copper and CO concentrations will be fixed in these studies, deposition temperature and matrix flow rate can be changed to study such kinetics.

As was explained in Chapter 1, high energy deposition has been used in previous studies as a way to maintain charge balance making use of secondary ionization

processes.⁵⁰ Indeed using Ar⁺ even at lower energies is able to create (CO)₂⁺ clusters upon deposition (see Chapter 6 for complete details). One potential method to shut down charge transfer events would be to deposit cations that have a much lower IP than that of argon. For example, SF₅ has an IP of 9.60 eV.⁵¹ This should be low enough that charge transfer to the matrix is completely shut down. Finally as was laid out in detail in Chapter one, complex formation in matrices occurs in a transient “surface region” that is warmer than the nominal sample temperature, and thus where “fast diffusion” of dopant species can occur.²⁸ Using cations of various sizes, we may be able to control and study some counter-ion size dependent diffusion and clustering trends.

9.2.2 Ionic-cluster deposition

Another logical step is the study of metal clusters. Indeed this was one of the original goals of this project. The magnetron source, however, has made it difficult to produce useful currents of anionic metal clusters for matrix isolation studies. A modification to the magnetron source in the future may be use of an ion funnel in place of or in combination with the nozzle that is currently being used. Ion funnels use a series of cylindrical ring electrodes to which radio frequency potentials of opposite polarity are applied on adjacent electrodes. Their main application has been to reduce losses that occur at the interface of high pressure ion sources of mass spectrometers.²⁰⁶ The use of such a source at the end of the aggregation tube may lead to a high extraction of ions in general including cluster ions.

One attempt at the deposition of the anionic copper dimer is shown in Figure 9.1. There are several peaks near the 1800 cm⁻¹ region that were not observed previously in our atomic copper studies, specifically at 1817.8, 1839.0, and 1865.6 cm⁻¹. Surprisingly, the

most intense peaks in the spectrum are those assigned to the neutral tricarbonyl species of monatomic copper at 1975 and 1985 cm^{-1} . There also appear to be peaks at 1938.6, 1961.0, and 2009.7 cm^{-1} however these are very low intensity and may not be due to copper species in the matrix. Irradiation with 590 nm light eliminates all three of the bands in the 1800 cm^{-1} region adding credibility to these being ionic species, although no corresponding neutral bands seemed to appear in the spectrum. Unfortunately the band assigned by Moskovits²⁰⁷ to the Cu_2CO at 2116 cm^{-1} is covered this day by atmospheric water bands from a failure in the nitrogen purge system. As of now it is uncertain why the bands for the neutral tricarbonyl species are so intense. Most likely, the copper dimer is breaking apart upon deposition although other factors cannot be ruled out, such as a copper dimer carbonyl cluster giving rise to the same absorbances as the monatomic copper tricarbonyl. Much more work is needed on this system to definitively assign any bands, although it is promising that our system is sensitive enough to detect such a low concentration of metal carbonyls ($\sim 3.6 \times 10^{13}$ total metal ions assuming 100% sticking probability).

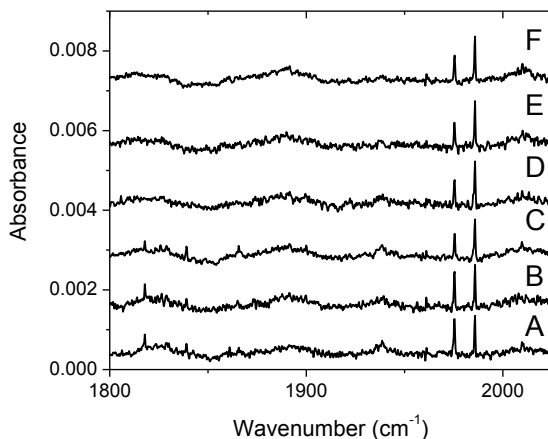


Figure 9.1 $\text{Cu}_2^- \text{Ar}^+$ co-deposited (~ 400 pA each) for 4 hours with 0.02% CO in argon at 20 K: A) 20 K deposition, B) 25 K annealing, C) 30 K annealing, D) 590 nm irradiation, E) 490 nm irradiation, and F) 30 K annealing. All spectra recorded at 10 K.

It should be noted here that cationic clusters are much easier to form with the magnetron source. Michael Goodrich has worked with optimizing beams of cationic metal atoms and clusters in the gas-phase. These provide higher currents of cation clusters and have promise for future matrix isolation experiments. The newly installed CI source will give us the ability to generate mass-selected counter-anions so that cationic metal clusters can be studied.

9.2.3 Formation and deposition of gas-phase carbonyls

Another interesting prospect is the deposition of metal carbonyls that have been formed in the gas phase. By formation and mass selection of a single anionic copper carbonyl species, its spectrum can be conclusively assigned. Also, by adjusting the kinetic energy of the impinging complex, dissociation energies can be found when the complex breaks apart upon collision with the matrix. This would be observed by the loss of parent species and the growth of a lower coordinated species.

The formation of such clusters is a difficult task. One possibility is to generate them *via* the magnetron sputtering source. There is a spare gas inlet for introduction of reactive gas that leads to the aggregation region of the magnetron source. We have tried introducing a 10.2% CO in He in this region but were unsuccessful in generating a large current of carbonyls. A low concentration was formed, however the electron multiplier was needed in order to detect these compounds. One problem that occurred was that the sputtering power became unstable when gas was introduced in the aggregation tube. We have observed this for pure He introduction into this region as well. It seems as though sputtering dynamics are very delicate and a slight change in the high pressure region can disturb this balance. Future attempts may have greater success by using a pure CO stream

such that the additional gas is low enough to aggregate but not disrupt the magnetron plasma. Also, mixes of varying concentrations of CO in He or Ar may be able to not disturb the plasma while allowing enough gas phase collisions for the CO to bind to copper atoms.

9.2.4 Wavelength dependent studies

As shown in Chapter 4, the anionic bands show wavelength dependent photodetachment events. It would be useful to have tighter wavelength control over such events so that photodetachment thresholds can be measured. Future plans include a monochromator in order to only allow very narrow band wavelengths to the sample. Also, the use of a pulse generator may lead to some photobleaching that can be quantitated. Figure 9.2 shows preliminary results of anionic band depletion through the use of 470 nm LED light pulsed at 1 second intervals. All four anionic species are found to follow roughly the same curve while using this light. These kinetics should change however once the wavelength of light is changed. For example, the anionic dicarbonyl readily photodetaches under 735 nm light whereas the anionic monocarbonyl only loses a small amount of intensity (Chapter 5).

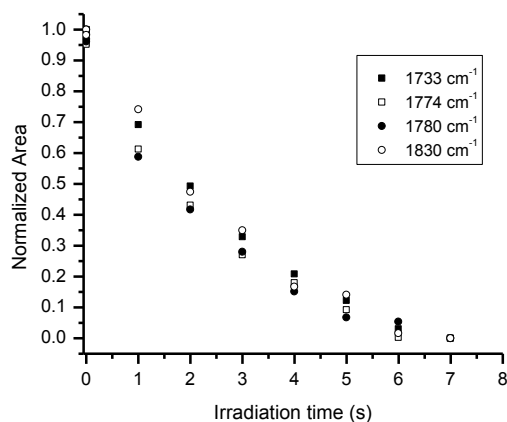


Figure 9.2 Normalized area of anionic copper carbonyl complexes at 10 K, subjected to 1 s pulses of 470 nm centered light.

Another wavelength dependent trend worth pursuing is that of the photochromic peaks in the O_4^+ system (Chapter 7). As was stated, these instantaneously convert from the cyclic to the *trans* form under 590 nm light under the timescale of our studies. The back conversion, however, is slower and kinetic data may be extracted. By taking rapid scans, quantitative conversion data may be obtained. The problem with this is that rapid scans must be done with a low number of averaged scans which leads to lower signal to noise. It should be possible to sync the pulse generator, mentioned above, to the spectrometer so that many cycles of this photochromic event can be scanned and precise scan times over multiple events can be averaged together to increase signal to noise.

9.2.5 Pump-probe technique

One of the initial goals for this project was to use a new technique called pump-probe. This would be a new complimentary technique to the freeze-frame spectroscopy method developed here. The basis is simple: once pre-reactive complexes are trapped in the matrix a burst of energy, such as from a laser, can be used to excite frequency-specific vibrational modes and move select reactants over activation barriers. In this way thorough mechanistic analysis can be drawn about product formation based upon specific reactant species. The results discussed above and throughout this dissertation in general, warrant the use of such lasers to this system. Indeed it was the long-term intention of this deposition method to study catalytically relevant species. As a final promising experiment, Figure 9.3 shows different length of time exposure to 365 nm light. At each length of exposure, the neutral dicarbonyl is decreased. When the UV LED is kept on for a minute or longer, the neutral tricarbonyl complex increases. What's more exciting is that upon 5 minute and 15 minute irradiation, CO_2 increases in the spectrum. There are many possibilities as to

where the carbon dioxide is coming from, such as desorption from the sample holder, however it is exciting to see the growth of a potential chemical product, CO_2 , with the concomitant decrease of a potential reactant, $\text{Cu}(\text{CO})_2$. It should be noted that there is precedence for this type of reaction in what's known as the Boudouard reaction.²⁰⁸ This reaction involves the disproportionation of carbon monoxide into carbon dioxide and graphite. It would make sense for this reaction then to occur from a "catalyst" with two CO units such as the dicarbonyl.

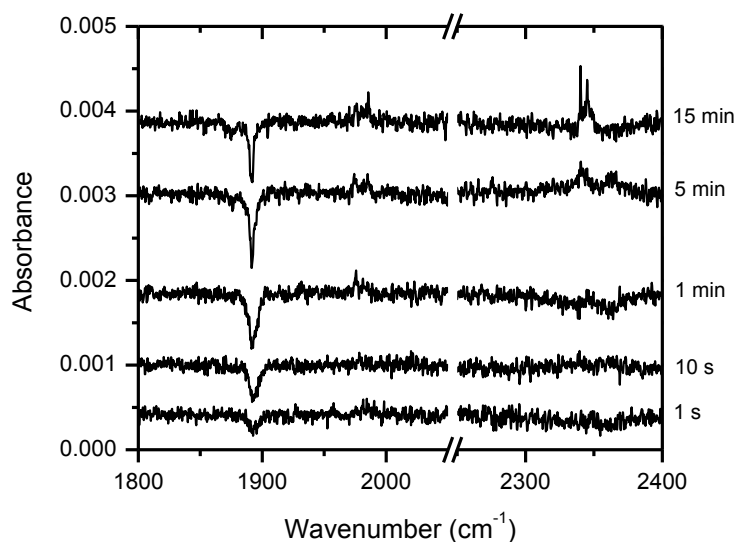


Figure 9.3 Subtraction data showing changes upon different length exposures to 365 nm light. Note the large decrease of the dicarbonyl complex with the concomitant increase of both the copper tricarbonyl and CO_2 .

Chapter 10

List of references

- (1) Spinoza, R. L.; Coville, N.; Schulz, H.; van Steen, E. Fischer-Tropsch Synthesis on the Eve of the XXI Century. *Catal. Today* **2002**, 71, 225-446.
- (2) Kaspar, J.; Fornasiero, P.; Hickey, N. Automotive Catalytic Converters: Current Status and Some Perspectives. *Catal. Today* **2003**, 77, 419-449.
- (3) Venuto, P. B.; Habib Jr., E. T. *Fluid Catalytic Cracking with Zeolite Catalysts*; Ponc, V., Bond, G. C., Eds.; In *Catalysis and Surface Properties of Liquid Metals and Alloys*; **1987**, Vol. 95.
- (4) Rostrup-Nielsen, J.; Sehested, J.; Norskov, J. Hydrogen and Synthesis Gas by Steam- and CO₂ Reforming. *Adv. Catal.* **2002**, 47, 65-139.
- (5) Schauermaun, S.; Hoffmann, J.; Johaneck, V.; Hartmann, J.; Libuda, J. Adsorption, Decomposition and Oxidation of Methanol on Alumina Supported Palladium Particles. *Phys. Chem. Chem. Phys.* **2002**, 4, 3909-3918.
- (6) Anderson, J. A.; Fernández Garcia, M. *Supported Metals in Catalysis*; Catalytic Science Series; London: Hackensack, NJ, **2005**; Vol. 11.
- (7) Heiz, U.; Landman, U., Eds.; *Nanocatalysis*; Nanoscience and Technology; Berlin: Springer, **2007**.
- (8) Jacox, M. E. The Spectroscopy of Molecular Reaction Intermediates Trapped in the Solid Rare Gases. *Chem. Soc. Rev.* **2002**, 31, 108-115.
- (9) Bamwenda, G.; Tsubota, S.; Nakamura, T.; Haruta, M. The Influence of the Preparation Methods on the Catalytic Activity of Platinum and Gold Supported on TiO₂ for CO Oxidation. *Catal. Lett.* **1997**, 44, 83-87.
- (10) Hammer, B.; Norskov, J. Why Gold is the Noblest of all the Metals. *Nature* **1995**, 376, 238-240.
- (11) Bond, G. C.; Thompson, D. T. Gold-Catalysed Oxidation of Carbon Monoxide. *Gold Bulletin* **2000**, 33, 41-51.
- (12) Thompson, D. New Advances in Gold Catalysis Part I. *Gold Bulletin* **1998**, 31, 111-118.
- (13) Thompson, D. New Advances in Gold Catalysis Part II. *Gold Bulletin* **1999**, 32, 12-19.

- (14) Kozlov, A.; Kozlova, A.; Liu, H.; Iwasawa, Y. A New Approach to Active Supported Au Catalysts. *Appl. Catal., A* **1999**, *182*, 9-28.
- (15) Bond, G. C.; Thompson, D. T. Catalysis by Gold. *Catal. Rev. Sci. Eng.* **1999**, *41*, 319-388.
- (16) Bollinger, M. A.; Vannice, M. A. A Kinetic and DRIFTS Study of Low-Temperature Carbon Monoxide Oxidation over Au-TiO₂ Catalysts. *Appl. Catal., B* **1996**, *8*, 417-443.
- (17) Boccuzzi, F.; Chiorino, A. FTIR Study of CO Oxidation on Au/TiO₂ at 90 K and Room Temperature. An Insight into the Nature of the Reaction Centers. *J. Phys. Chem. B* **2000**, *104*, 5414-5416.
- (18) Green, I. X.; Tang, W.; Neurock, M.; Yates, J. T., Jr. Spectroscopic Observation of Dual Catalytic Sites during Oxidation of CO on a Au/TiO₂ Catalyst. *Science* **2011**, *333*, 736-739.
- (19) Widmann, D.; Behm, R. J. Activation of Molecular Oxygen and the Nature of the Active Oxygen Species for CO Oxidation on Oxide Supported Au Catalysts. *Acc. Chem. Res.* **2014**, *47*, 740-749.
- (20) Green, I. X.; Tang, W.; McEntee, M.; Neurock, M.; Yates, J. T. Inhibition at Perimeter Sites of Au/TiO₂ Oxidation Catalyst by Reactant Oxygen. *J. Am. Chem. Soc.* **2012**, *134*, 12717-12723.
- (21) Kimble, M. L.; Castleman, A. W., Jr.; Mitric, R.; Burgel, C.; Bonacic-Koutecky, V. Reactivity of Atomic Gold Anions Toward Oxygen and then Oxidation of CO: Experiment and Theory. *J. Am. Chem. Soc.* **2004**, *126*, 2526-2535.
- (22) Kimble, M. L.; Moore, N. A.; Johnson, G. E.; Castleman, A. W., Jr.; Burgel, C.; Mitric, R.; Bonacic-Koutecky, V. Joint Experimental and Theoretical Investigations of the Reactivity of Au₂O_n⁻ and Au₃O_n⁻ (n=1-5) with Carbon Monoxide. *J. Chem. Phys.* **2006**, *125*, 1-14.
- (23) Kimble, M. L.; Castleman, A. W.; Burgel, C.; Bonacic-Koutecky, V. Interactions of CO with Au_nO_m⁻ (n ≥ 4). *Int. J. Mass Spectrom.* **2006**, *254*, 163-167.
- (24) Burgel, C.; Reilly, N. M.; Johnson, G. E.; Mitric, R.; Kimble, M. L.; Castleman, A. W., Jr.; Bonacic-Koutecky, V. Influence of Charge State on the Mechanism of CO Oxidation on Gold Clusters. *J. Am. Chem. Soc.* **2008**, *130*, 1694-1698.
- (25) Johnson, G. E.; Reilly, N. M.; Tyo, E. C.; Castleman, A. W.; Castleman, A. W., Jr. Gas-Phase Reactivity of Gold Oxide Cluster Cations with CO. *J. Phys. Chem. C* **2008**, *112*, 9730-9736.

- (26) Whittle, E.; Dows, D. A.; Pimentel, G. C. Matrix Isolation Method for the Experimental Study of Unstable Species. *J. Chem. Phys.* **1954**, *22*, 1943.
- (27) Becker, E. D.; Pimentel, G. C. Spectroscopic Studies of Reactive Molecules by the Matrix Isolation Method. *J. Chem. Phys.* **1956**, *25*, 224-228.
- (28) Cradock, S.; Hinchcliffe, A. J. *Matrix Isolation: A Technique for the Study of Reactive Inorganic Species*; Cambridge University Press: New York, NY, **1975**.
- (29) Hagele, W.; Probst, W.; Dellian, K.; Hingsamm, J.; Luscher, E. HCP Argon Single Crystals: Growth and Measurement of Birefringence. *Z. Naturforsch., A: Phys. Sci.* **1971**, *A 26*, 419-422.
- (30) Ahmad, S.; Kieft, H.; Clouter, M.; Whitmore, M. Determination of the Elastic Constants of Single Crystals of FCC and HCP Argon Alloys by Brillouin Scattering. *Phys. Rev. B* **1982**, *26*, 4239-4261.
- (31) Strzemechny, M.; Prokhvatilov, A.; Yantsevich, L. Excess Impurity Volumes in Binary Mixtures of Cryosolids. *Physica B* **1994**, *198*, 267-289.
- (32) Knozinger, E.; Babka, E.; Hallamasek, D. Cage Structure and Long Range Order in Solid Rare Gas Matrixes: A Combined FTIR and XRD Study. *J. Phys. Chem. A* **2001**, *105*, 8176-8182.
- (33) Dunkin, I. R. *Matrix Isolation Techniques: A Practical Approach*; Oxford University Press: Oxford; New York, **1998**.
- (34) Andrews, L.; Pimentel, G. Visible Spectra of Lithium in Inert-Gas Matrices. *J. Chem. Phys.* **1967**, *47*, 2905-2910.
- (35) Jacox, M. E. The Vibrational Energy Levels of Small Transient Molecules Isolated in Neon and Argon Matrices. *Chem. Phys.* **1994**, *189*, 149-170.
- (36) Berghof, V.; Martins, M.; Schmidt, B.; Schwentner, N. Vibrational Overtones and Rotational Structure of HCl in Rare Gas Matrices. *J. Chem. Phys.* **2002**, *116*, 9364-9373.
- (37) Tinti, D. Absorption and Emission Spectra of OH and OD in Solid Ne. Evidence for Rotation. *J. Chem. Phys.* **1968**, *48*, 1459-1464.
- (38) Brus, L.; Bondybey, V. Pseudorotational Local Mode Participation in OH and OD($A^2\Sigma^+$) Vibrational Relaxation in a Ne Lattice. *J. Chem. Phys.* **1975**, *63*, 786-793.
- (39) Ceponkus, J.; Engdahl, A.; Uvdal, P.; Nelander, B. Structure and Dynamics of Small Water Clusters, Trapped in Inert Matrices. *Chem. Phys. Lett.* **2013**, *581*, 1-12.

- (40) Ceponkus, J.; Uvdal, P.; Nelander, B. On the Structure of the Matrix Isolated Water Trimer. *J. Chem. Phys.* **2011**, *134*, 1-9.
- (41) Forney, D.; Thompson, W. E.; Jacox, M. E. The Vibrational-Spectra of Molecular-Ions Isolated in Solid Neon. IX. HCN^+ , HNC^+ , and CN^- . *J. Chem. Phys.* **1992**, *97*, 1664-1674.
- (42) Jacox, M. E.; Milligan, D. Spectrum and Structure of HO_2 Free Radical. *J. Mol. Spectrosc.* **1972**, *42*, 495-513.
- (43) Haas, Y.; Samuni, U. Reactions in Rare Gas Matrices: Matrix and Site Effects. *Progress in Reaction Kinetics* **1998**, *23*, 211-280.
- (44) Bodenbinder, M.; Ulic, S. E.; Willner, H. A Gas-Phase and Matrix Isolation Study of the Equilibrium CH_3ONO (Cis) \leftrightarrow CH_3ONO (Trans) by FTIR Spectroscopy. *J. Phys. Chem.* **1994**, *98*, 6441-6444.
- (45) Braathen, G. O.; Gatial, A.; Klaeboe, P.; Nielsen, C. J. IR Matrix-Isolation Studies of the Conformations of 1,3-Dichloro-2,2-Dimethylpropane and 2-Chloromethyl-2-Methyl-1,3-Dichloro-Propane. *J. Mol. Struct.* **1990**, *218*, 67-72.
- (46) Elbindary, A. A.; Klaeboe, P.; Nielsen, C. J. The IR Matrix Isolation Spectra and Conformation Energies of Eight Haloacetylhalides ($\text{CH}_2\text{X-COY}$; X, Y=F,Cl,Br). *J. Mol. Struct.* **1990**, *218*, 73-80.
- (47) Hoops, M. D.; Ault, B. S. Matrix Isolation Study of the Early Intermediates in the Ozonolysis of Cyclopentene and Cyclopentadiene: Observation of Two Criegee Intermediates. *J. Am. Chem. Soc.* **2009**, *131*, 2853-2863.
- (48) Dinh, P. M.; Fehrer, F.; Bousquet, G.; Reinhard, P.-G.; Suraud, E. Shape Dynamics during Deposit of Simple Metal Clusters on Rare-Gas Matrices. *Phys. Rev. A* **2007**, *76*, 1-7.
- (49) Moskovits, M.; Hulse, J. Cluster Formation in Rare-Gas Matrices - Models for Aggregation Processes. *J. Chem. Soc., Faraday Trans. 2* **1977**, *73*, 471-484.
- (50) Leutwyler, S.; Maier, J.; Spittel, U. The Electronic Absorption-Spectrum of I-C=C-C=C-I^+ in a Ne Matrix. *Chem. Phys. Lett.* **1983**, *96*, 645-648.
- (51) Lias, S. G.; Bartmess, J. E.; Liebman, J. F.; Holmes, J. L.; Levin, R. D.; Mallard, W. G. *Ion Energetics Data*; Linstrom, P. J., Mallard, W. G., Eds.; In **NIST Chemistry WebBook, NIST Standard Reference Database Number 69**; National Institute of Standards and Technology: Gaithersburg, MD, 20899.
- (52) Schwentner, N.; Skibowski, M.; Steinmann, W. Photoemission from Valence Bands of Solid Rare-Gases. *Phys. Rev. B* **1973**, *8*, 2965-2968.

- (53) Linn, S. H.; Ono, Y.; Ng, C. Y. Molecular-Beam Photo-Ionization Study of CO, N₂, and NO Dimers and Clusters. *J. Chem. Phys.* **1981**, *74*, 3342-3347.
- (54) Linn, S. H.; Ono, Y.; Ng, C. Y. A Study of the Ion-Molecule Half Reactions $O_2^+(a^4\Pi_u, v)\dots(O_2)_m \rightarrow O_{2m+1}^+ + O$, $m=1, 2$, or 3 , using the Molecular Beam Photoionization Method. *J. Chem. Phys.* **1981**, *74*, 3348-3352.
- (55) Dubost, H.; Abouaf-Marguin, L. Infrared-Spectra of Carbon-Monoxide Trapped in Solid Argon - Double-Doping Experiments with H₂O, NH₃ and N₂. *Chem. Phys. Lett.* **1972**, *17*, 269-273.
- (56) Diem, M.; Tso, T. L.; Lee, E. K. C. Some Observations on Molecular-Complexes of Carbon-Monoxide in Argon and Oxygen Matrices. *Chem. Phys.* **1982**, *73*, 283-289.
- (57) Han, H. S.; Kim, K. Optimum Geometry of CO Dimer and FT-IR Spectra of CO in Solid Argon. *THEOCHEM* **1997**, *418*, 1-10.
- (58) Givan, A.; Loewenschuss, A.; Nielsen, C. J. FTIR Studies of CO-Water Complexes in Argon Matrices and in Porous Ices. *J. Chem. Soc., Faraday Trans.* **1996**, *92*, 4927-4933.
- (59) Abe, H.; Takeo, H.; Yamada, K. Infrared Spectroscopy of CO Trapped in an Argon Matrix Revisited. *Chem. Phys. Lett.* **1999**, *311*, 153-158.
- (60) Darling, J.; Ogden, J. Spectroscopic Studies on Matrix-Isolated Metal Carbonyls. Part I. Use of C¹⁸O Enrichment to Obtain Characteristic Frequency and Intensity Patterns. *J. Chem. Soc., Dalton Trans.* **1972**, *22*, 2496-2503.
- (61) Jacox, M. Vibrational and Electronic Energy Levels of Polyatomic Transient Molecules. Supplement A. *J. Phys. Chem. Ref. Data* **1998**, *27*, 115-393.
- (62) Jacox, M. Vibrational and Electronic Energy Levels of Polyatomic Transient Molecules. Supplement B. *J. Phys. Chem. Ref. Data* **2003**, *32*, 1-441.
- (63) Andrews, L.; Pimentel, G. C. Infrared Spectrum Structure and Bonding of Lithium Nitroxide, LiON. *J. Chem. Phys.* **1966**, *44*, 2361-2369.
- (64) Andrews, L. Matrix Infrared Spectrum and Bonding in Lithium Superoxide Molecule, LiO₂. *J. Am. Chem. Soc.* **1968**, *90*, 7368-7370.
- (65) Andrews, L. Infrared Spectrum, Structure, Vibrational Potential Function, and Bonding in Lithium Superoxide Molecule, LiO₂. *J. Chem. Phys.* **1969**, *50*, 4288-4299.

- (66) Kasai, P.; McLeod, D. Electron Spin Resonance Study of Molecular Anions Generated in Argon Matrix at 4°K: ESR Spectrum of $B_2H_6^-$. *J. Chem. Phys.* **1969**, *51*, 1250-1251.
- (67) Milligan, D. E.; Jacox, M. E. Studies of Photoproduction of Electrons in Inert Solid Matrices . The Electronic Spectrum of the Species C_2^- . *J. Chem. Phys.* **1969**, *51*, 1952-1955.
- (68) Brus, L.; Bondybey, V. Molecular Ions and Electron Transport in Rare Gas Lattices: C_2^- Formation Mechanism and $X^2\Sigma_g^+ \leftrightarrow B^2\Sigma_u^+$ Spectroscopy. *J. Chem. Phys.* **1975**, *63*, 3123-3129.
- (69) Andrews, L.; Grzybowski, J.; Allen, R. Infrared Spectra of Molecular Ions and Radicals Produced by Proton Radiolysis of Carbon Tetrachloride in Argon during Condensation at 15°K. *J. Phys. Chem.* **1975**, *79*, 904-912.
- (70) Prochaska, F.; Andrews, L. Matrix Photodissociation and Photoionization of Carbon Tetrahalides with Noble-Gas Resonance Radiation. *J. Chem. Phys.* **1977**, *67*, 1091-1098.
- (71) Ault, B. S.; Andrews, L. Matrix Reactions of Alkali-Metal Chloride Salts and HCl and DCl - Infrared Spectra of $M^+HCl_2^-$ and $M^+DCl_2^-$ Ions Pairs. *J. Chem. Phys.* **1975**, *63*, 2466-2472.
- (72) Ault, B. S.; Andrews, L. Salt-Molecule Matrix Reactions - Infrared-Spectra of $M^+HCl_2^-$ and $M^+Cl_3^-$ Ion Pairs in Solid Argon. *J. Am. Chem. Soc.* **1975**, *97*, 3824-3826.
- (73) Ault, B. S.; Andrews, L. Infrared and Raman-Spectra of $M^+Cl_3^-$ Ion-Pairs and their Chlorine Bromine Counterparts Isolated in Argon Matrices. *J. Chem. Phys.* **1976**, *64*, 4853-4859.
- (74) Tevault, D. E.; Andrews, L. IR Spectra of Ca^+NO^- and $Ca^+NO_2^-$ in Solid Argon at 15 K. *Chem. Phys. Lett.* **1977**, *48*, 103-106.
- (75) Miller, J. H.; Andrews, L. Infrared Spectra of the $M^+BrF_2^-$ Ion and $M^+IF_2^-$ Ion Pairs in Solid Argon. *Inorg. Chem.* **1979**, *18*, 988-992.
- (76) Andrews, L. Spectroscopy of Molecular Ions in Noble Gas Matrices. *Annu. Rev. Phys. Chem.* **1979**, *30*, 79-101.
- (77) Halasinski, T.; Hudgins, D.; Salama, F.; Allamandola, L.; Bally, T. Electronic Absorption Spectra of Neutral Pentacene ($C_{22}H_{14}$) and its Positive and Negative Ions in Ne, Ar, and Kr Matrices. *J. Phys. Chem. A* **2000**, *104*, 7484-7491.
- (78) Berry, R. S. Theory of Penning Ionization. *Radiat. Res.* **1974**, *59*, 367-375.

- (79) Wight, C. A.; Ault, B. S.; Andrews, L. Microwave-Discharge Sources of New Chemical Species for Matrix-Isolation Spectroscopy and Identification of Charged Species. *J. Chem. Phys.* **1976**, *65*, 1244-1249.
- (80) Jacox, M. E. Matrix Isolation Study of Products of Interaction between Metastable Ar and Kr Atoms and Chloroform. Photodecomposition of HCCl_2^+ and HCCl_2 . *Chem. Phys.* **1976**, *12*, 51-63.
- (81) Jacox, M. E.; Thompson, W. E. The Production and Spectroscopy of Molecular Ions Isolated in Solid Neon. *Res. Chem. Intermed.* **1989**, *12*, 33-56.
- (82) Thompson, W.; Jacox, M. E. The Vibrational Spectra of CO_2^+ , $(\text{CO}_2)_2^+$, CO_2^- , and $(\text{CO}_2)_2^-$ Trapped in Solid Neon. *J. Chem. Phys.* **1999**, *111*, 4487-4496.
- (83) Bondybey, V. E.; English, J. H. Laser Induced Fluorescence of Metal Clusters Produced by Laser Vaporization: Gas Phase Spectrum of Pb_2 . *J. Chem. Phys.* **1981**, *74*, 6978-6979.
- (84) Bondybey, V. E. Laser Vaporization of Silicon Carbide: Lifetime and Spectroscopy of SiC_2 . *J. Phys. Chem.* **1982**, *86*, 3396-3399.
- (85) Zhou, M.; Andrews, L.; Bauschlicher, C. W. Spectroscopic and Theoretical Investigations of Vibrational Frequencies in Binary Unsaturated Transition Metal Carbonyl Cations, Neutrals, and Anions. *Chem. Rev.* **2001**, *101*, 1931-1961.
- (86) Andrews, L. Matrix Infrared Spectra and Density Functional Calculations of Transition Metal Hydrides and Dihydrogen Complexes. *Chem. Soc. Rev.* **2004**, *33*, 123-132.
- (87) Andrews, L.; Citra, A. Infrared Spectra and Density Functional Theory Calculations on Transition Metal Nitrosyls. Vibrational Frequencies of Unsaturated Transition Metal Nitrosyls. *Chem. Rev.* **2002**, *102*, 885-911.
- (88) Zhou, M.; Andrews, L. Infrared Spectra and Density Functional Calculations of $\text{Cu}(\text{CO})_{1-4}^+$, $\text{Cu}(\text{CO})_{1-3}$, and $\text{Cu}(\text{CO})_{1-3}^-$ in Solid Neon. *J. Chem. Phys.* **1999**, *111*, 4548-4557.
- (89) Maier, J. P. Spectroscopic Characterization of Mass Selected Ions. *Mass Spectrom. Rev.* **1992**, *11*, 119-135.
- (90) Bondybey, V.; Lorenz, M. Mass Selected Ions in Solid Neon: Matrix Damage and Site Effects. *J. Low Temp. Phys.* **2001**, *122*, 509-525.
- (91) Harbich, W. 'Soft Landing' of Size-Selected Clusters in Chemically Inert Substrates. *Philos. Mag. B.* **1999**, *79*, 1307-1320.

- (92) Fedrigo, S.; Harbich, W.; Buttet, J. Soft Landing and Fragmentation of Small Clusters Deposited in Noble-Gas Films. *Phys. Rev. B* **1998**, *58*, 7428-7433.
- (93) Godbout, J. T.; Halasinski, T. M.; Leroi, G. E.; Allison, J. Matrix Isolation of Mass-Selected Cations: Are Counterions Present and How are They Formed? *J. Phys. Chem.* **1996**, *100*, 2892-2899.
- (94) Leutwyler, S.; Maier, J.; Spittel, U. Electronic Absorption-Spectra of Dihaloacetylene Cations in Neon Matrices. *Mol. Phys.* **1984**, *51*, 437-444.
- (95) Leutwyler, S.; Maier, J.; Spittel, U. Electronic Absorption Spectra of the Halogenocynoacetylene Cations in Neon Matrices. *J. Chem. Soc., Faraday Trans. 2* **1985**, *81*, 1565-1572.
- (96) Freivogel, P.; Grutter, M.; Forney, D.; Maier, J. Infrared Bands of Mass-Selected Carbon Chains C_n ($n = 8-12$) and C_n^- ($n = 5-10, 12$) in Neon Matrices. *Chem. Phys.* **1997**, *216*, 401-406.
- (97) Freivogel, P.; Fulara, J.; Jakobi, M.; Forney, D.; Maier, J. Electronic Absorption Spectra of Linear Carbon Chains in Neon Matrices. II. C_{2n}^- , C_{2n} , and $C_{2n}H$. *J. Chem. Phys.* **1995**, *103*, 54-59.
- (98) Forney, D.; Jakobi, M.; Maier, J. Absorption Spectroscopy of Mass-Selected Ions in Neon Matrices. *J. Chem. Phys.* **1989**, *90*, 600-601.
- (99) Rabin, I.; Schulze, W.; Ertl, G.; Felix, C.; Sieber, C.; Harbich, W.; Buttet, J. Absorption and Fluorescence Spectra of Ar Matrix Isolated Ag_3 Clusters. *Chem. Phys. Lett.* **2000**, *320*, 59-64.
- (100) Felix, C.; Sieber, C.; Harbich, W.; Buttet, J.; Rabin, I.; Schulze, W.; Ertl, G. Fluorescence and Excitation Spectra of Ag_4 in an Argon Matrix. *Chem. Phys. Lett.* **1999**, *313*, 105-109.
- (101) Sieber, C.; Buttet, J.; Harbich, W.; Felix, C.; Mitric, R.; Bonacic-Koutecky, V. Isomer-Specific Spectroscopy of Metal Clusters Trapped in a Matrix: Ag_9 . *Phys. Rev. A* **2004**, *70*, 1-4.
- (102) Fedrigo, S.; Haslett, T.; Moskovits, M. A New Binary Carbonyl of Iron: The Synthesis of $Fe_4(CO)_{14}$ by Co-Deposition of Mass-Selected Fe_4 with CO. *Chem. Phys. Lett.* **1999**, *307*, 333-338.
- (103) Bosnick, K.; Haslett, T.; Fedrigo, S.; Moskovits, M.; Chan, W.; Fournier, R. Tricapped Tetrahedral Ag_7 : A Structural Determination by Resonance Raman Spectroscopy and Density Functional Theory. *J. Chem. Phys.* **1999**, *111*, 8867-8870.

- (104) Haslett, T.; Bosnick, K.; Moskovits, M. Ag₅ is a Planar Trapezoidal Molecule. *J. Chem. Phys.* **1998**, *108*, 3453-3457.
- (105) Haslett, T.; Bosnick, K.; Fedrigo, S.; Moskovits, M. Resonance Raman Spectroscopy of Matrix-Isolated Mass-Selected Fe₃ and Ag₃. *J. Chem. Phys.* **1999**, *111*, 6456-6461.
- (106) Fedrigo, S.; Haslett, T.; Moskovits, M. Direct Synthesis of Metal Cluster Complexes by Deposition of Mass-Selected Clusters with Ligand: Iron with CO. *J. Am. Chem. Soc.* **1996**, *118*, 5083-5085.
- (107) Haslett, T.; Fedrigo, S.; Bosnick, K.; Moskovits, M.; Duarte, H.; Salahub, D. Binary Iron-Dinitrogen Compounds Synthesized by Co-Deposition of Mass-Selected Fe, Fe₂, and Fe₃ with N₂. *J. Am. Chem. Soc.* **2000**, *122*, 6039-6044.
- (108) Sabo, M.; Allison, J.; Gilbert, J.; Leroi, G. Bridging the Gap between what Mass Spectrometrists Want and What Spectroscopists Can Do: An Instrument for Spectroscopic Investigation of Matrix-Isolated, Mass-Selected Ions. *Appl. Spectrosc.* **1991**, *45*, 535-542.
- (109) Cheng, H. P.; Landman, U. Controlled Deposition, Soft Landing, and Glass-Formation in Nanocluster-Surface Collisions. *Science* **1993**, *260*, 1304-1307.
- (110) Kaiser, B.; Bernhardt, T.; Rademann, K. Deposition of Size-Selected Clusters at Hyperthermal Energies Investigated by STM. *Appl. Phys. A* **1998**, *66*, S711-S714.
- (111) Yamada, I.; Usui, H.; Takagi, T. The Formation and Kinetics of Ionized Cluster Beams. *Z. Phys. D: At. Mol. Clusters* **1986**, *3*, 137-142.
- (112) Haberland, H.; Karrais, M.; Mall, M. A New Type of Cluster and Cluster Ion-Source. *Z. Phys. D: At. Mol. Clusters* **1991**, *20*, 413-415.
- (113) Haberland, H.; Karrais, M.; Mall, M.; Thurner, Y. Thin Films from Energetic Cluster Impact: A Feasibility Study. *J. Vac. Sci. Technol., A* **1992**, *10*, 3266-3271.
- (114) Beaumont, R. H.; Chihara, H.; Morrison, J. A. Thermodynamic Properties of Krypton. Vibrational and Other Properties of Solid Argon and Solid Krypton. *Proc. Phys. Soc.* **1961**, *78*, 1462-1481.
- (115) Ozin, G. A.; Mitchell, S. A.; Garciaprieto, J. Fluorescence Spectroscopy and Photoprocesses of Cu and Cu₂ in Rare Gas Matrices. *J. Phys. Chem.* **1982**, *86*, 473-479.
- (116) Huber, H.; Kundig, E. P.; Moskovits, M.; Ozin, G. A. Binary Copper Carbonyls: Synthesis and Characterization of Cu(CO)₃, Cu(CO)₂, CuCO, and Cu₂(CO)₆. *J. Am. Chem. Soc.* **1975**, *97*, 2097-2106.

- (117) Gruen, D. M.; Gaudio, S. L.; McBeth, R. L.; Lerner, J. L. Application of Matrix-Isolation Spectroscopy to Quantitative Sputtering Studies. I. Energies and Oscillator Strengths of Resonance Transitions of Gold Atoms Isolated in Noble-Gas Matrices. *J. Chem. Phys.* **1974**, *60*, 89-99.
- (118) Forstmann, F.; Kolb, D. M.; Leutloff, D.; Schulze, W. Analysis of Matrix Induced Changes in Optical-Spectra of Matrix-Isolated Noble-Metal Atoms. *J. Chem. Phys.* **1977**, *66*, 2806-2813.
- (119) Zeringue, K. J.; Shakhsemampour, J.; Rivoal, J. C.; Vala, M. Atom-Matrix Interactions: An MCD Study of Copper Atoms in Argon. *J. Chem. Phys.* **1983**, *78*, 2231-2239.
- (120) Wu, X.; Qin, Z.; Xie, H.; Cong, R.; Wu, X.; Tang, Z.; Fan, H. Photoelectron Imaging and Theoretical Studies of Group 11 Cyanides MCN (M = Cu, Ag, Au). *J. Phys. Chem. A* **2010**, *114*, 12839-12844.
- (121) Godbout, J.; Halasinski, T.; Leroi, G.; Allison, J. Matrix Isolation of Mass-Selected Cations: Are Counterions Present and how are they Formed? *J. Phys. Chem.* **1996**, *100*, 2892-2899.
- (122) Moskovits, M.; Ozin, G. A. *Matrix Cryochemistry Using Transition Metal Atoms*; Moskovits, M., Ozin, G. A., Eds.; In *Cryochemistry*; John Wiley & Sons, Inc. **1976**, 261-394.
- (123) Harbich, W.; Sieber, C.; Meiwes-Broer, K.; Felix, C. Electronic Excitations Induced by the Impact of Coinage Metal Ions and Clusters on a Rare Gas Matrix: Neutralization and Luminescence. *Phys. Rev. B* **2007**, *76*, 1-10.
- (124) Schwentner, N.; Koch, E. E.; Jortner, J. *Energy Transfer in Solid Rare Gases*; Bartolo, B., Ed.; In *Energy Transfer Processes in Condensed Matter*; Plenum: New York, **1983**, Vol. 114.
- (125) Weitzel, K.; Mahnert, J.; Penno, M. Z.-P. Investigations of Dissociation-Energies in Ionic Reactions. *Chem. Phys. Lett.* **1994**, *224*, 371-380.
- (126) Wetzel, R.; Baiocchi, F.; Hayes, T.; Freund, R. Absolute Cross-Sections for Electron-Impact Ionization of the Rare-Gas Atoms by the Fast-Neutral-Beam Method. *Phys. Rev. A* **1987**, *35*, 559-577.
- (127) Erman, P.; Karawajczyk, A.; Rachlewskallne, E.; Stromholm, C.; Larsson, J.; Persson, A.; Zerne, R. Direct Determination of the Ionization-Potential of CO by Resonantly Enhanced Multiphoton Ionization Mass-Spectroscopy. *Chem. Phys. Lett.* **1993**, *215*, 173-178.

- (128) Bondybey, V. E.; Miller, T. A. *Vibronic Spectroscopy and Photophysics of Molecular Ions in Low Temperature Matrices*; Bondybey, V. E., Miller, T. A., Eds.; In *Molecular Ions: Spectroscopy, Structure, and Chemistry*; North Holland: New York, **1983**.
- (129) Zhou, M.; Chertihin, G.; Andrews, L. Reactions of Laser-Ablated Iron Atoms with Carbon Monoxide: Infrared Spectra and Density Functional Calculations of Fe_xCO , $\text{Fe}(\text{CO})_x$, and $\text{Fe}(\text{CO})_x^-$ ($x = 1,2,3$) in Solid Argon. *J. Chem. Phys.* **1998**, *109*, 10893-10904.
- (130) Blyholder, G. Molecular Orbital View of Chemisorbed Carbon Monoxide. *J. Phys. Chem.* **1964**, *68*, 2772-2777.
- (131) Zhou, H.; Yang, R.; Jin, X.; Zhou, M. Infrared Spectra of the OH^+ and H_2O^+ Cations Solvated in Solid Argon. *J. Phys. Chem. A* **2005**, *109*, 6003-6007.
- (132) Lecomber, P.; Loveland, R.; Spear, W. Hole Transport in Rare-Gas Solids Ne, Ar, Kr, and Xe. *Phys. Rev. B* **1975**, *11*, 3124-3130.
- (133) Ophir, Z.; Raz, B.; Jortner, J.; Saile, V.; Schwentner, N.; Koch, E. E.; Skibowski, M.; Steinmann, W. Photoemission from Doped Solid Rare-Gases. *J. Chem. Phys.* **1975**, *62*, 650-665.
- (134) Jacox, M. E. Vibrational and Electronic Energy Levels of Polyatomic Transient Molecules. Supplement B. *J. Phys. Chem. Ref. Data* **2003**, *32*, 1-441.
- (135) Forney, D.; Jacox, M. E.; Irikura, K. K. Matrix Isolation Study of the Interaction of Excited Neon Atoms with CF_4 . Infrared Spectra of CF_3^+ and CF_3^- . *J. Chem. Phys.* **1994**, *101*, 8290-8296.
- (136) Forney, D.; Thompson, W. E.; Jacox, M. E. The Vibrational Spectra of Molecular-Ions Isolated in Solid Neon. XI. NO_2^+ , NO_2^- , and NO_3^- . *J. Chem. Phys.* **1993**, *99*, 7393-7403.
- (137) Jacox, M. E. *Photoexcitation of Free Radicals and Molecular Ions Trapped in Rare Gas Matrices*; Khriachtchev, L., Ed.; In *Physics and Chemistry at Low Temperatures*; Pan Stanford: **2011**, 1-23.
- (138) Ludwig, R. M.; Moore, D. T. Formation of Ionic Complexes in Cryogenic Matrices: A Case Study using Co-Deposition of Cu^- with Rare Gas Cations in Solid Argon. *J. Chem. Phys.* **2013**, *139*, 1-9.
- (139) Stanzel, J.; Aziz, E. F.; Neeb, M.; Eberhardt, W. Photoelectron Spectroscopy on Small Anionic Copper-Carbonyl Clusters. *Collect. Czech. Chem. Commun.* **2007**, *72*, 1-14.

- (140) Abe, H.; Yamada, K. M. T. Infrared Spectra of the CO–H₂O 1–1 Cluster Trapped in an Argon Matrix. *J. Chem. Phys.* **2001**, *114*, 6134-6141.
- (141) Abe, H.; Yamada, K. M. T. Spectroscopic Identification of the CO-H₂O 2-1 Cluster Trapped in an Argon Matrix. *J. Chem. Phys.* **2004**, *121*, 7803-7812.
- (142) Gantefor, G.; Cha, C.; Handschuh, H.; IckingKonert, G.; Kessler, B.; Gunnarsson, O.; Eberhardt, W. Electronic and Geometric Structure of Small Mass Selected Clusters. *J. Electron Spectrosc. Relat. Phenom.* **1995**, *76*, 37-45.
- (143) Ludwig, R. M.; Moore, D. T. Chemical Reactions Triggered using Electrons Photodetached from "Clean" Distributions of Anions Deposited in Cryogenic Matrices Via Counterion Codeposition. *J. Phys. Chem. Lett.* **2014**, *5*, 2947-2950.
- (144) Kauffman, J. W.; Hauge, R. H.; Margrave, J. L. Studies of Reactions of Atomic and Diatomic Cr, Mn, Fe, Co, Ni, Cu, and Zn with Molecular Water at 15 K. *J. Phys. Chem.* **1985**, *89*, 3541-3547.
- (145) NIST Computational Chemistry Comparison and Benchmark Database, NIST Standard Reference Database Number 101 Release 16a, August 2013, Editor: Russell D. Johnson III <http://cccbdb.nist.gov/>
- (146) Staudinger, H.; Anthes, E. Oxalyl Chloride. V. Oxalyl Bromide and Attempts to Prepare Di (Carbon Oxide). *Ber. Dtsch. Chem. Ges.* **1913**, *46*, 1426-1437.
- (147) Ewing, G. E.; Pimentel, G. C. Infrared Spectrum of Solid Carbon Monoxide. *J. Chem. Phys.* **1961**, *35*, 925-930.
- (148) Vu, H.; Atwood, M. R.; Vodar, B. 1–0, 2–0, 3–0, Absorption Bands of Dense Forms of Pure CO and its Solutions in N₂ and Ar. *J. Chem. Phys.* **1963**, *38*, 2671-2677.
- (149) Leroi, G. E.; Ewing, G. E.; Pimentel, G. C. Infrared Spectra of Carbon Monoxide in an Argon Matrix. *J. Chem. Phys.* **1964**, *40*, 2298-2303.
- (150) Davies, J. B.; Hallam, H. E. Infrared Cryogenic Studies. Part 8. Carbon Monoxide in Matrices. *J. Chem. Soc., Faraday Trans. 2* **1972**, *68*, 509-512.
- (151) Jiang, G. J.; Person, W. B.; Brown, K. G. Absolute Infrared Intensities and Band Shapes in Pure Solid CO and CO in some Solid Matrices. *J. Chem. Phys.* **1975**, *62*, 1201-1211.
- (152) Dubost, H. Infrared Absorption Spectra of Carbon Monoxide in Rare Gas Matrixes. *Chem. Phys.* **1976**, *12*, 139-151.

- (153) Munson, M. S. B.; Field, F. H.; Franklin, J. L. High-Pressure Mass Spectrometric Study of Reactions of Rare Gases with N₂ and CO. *J. Chem. Phys.* **1962**, *37*, 1790-1799.
- (154) Chong, S. L.; Franklin, J. L. High-Pressure Ion-Molecule Reactions in Carbon Monoxide and Carbon Monoxide-Methane Mixtures. *J. Chem. Phys.* **1971**, *54*, 1487-1495.
- (155) Saporoschenko, M. Mobility of CO⁺, CO₂⁺, and C₂O₂⁺ Ions in Carbon Monoxide Gas. *J. Chem. Phys.* **1968**, *49*, 768-774.
- (156) Meot-Ner, M.; Field, F. H. Kinetics and Thermodynamics of Association Reactions of CO⁺ and HCO⁺ with CO and of N₂⁺ and N₂H⁺ with N₂ between 120 and 650°K. *J. Chem. Phys.* **1974**, *61*, 3742-3749.
- (157) Norwood, K.; Guo, J. H.; Luo, G.; Ng, C. Y. A Photoion-Photoelectron Coincidence Study of (CO)₂ and (CO)₃. *J. Chem. Phys.* **1989**, *90*, 6026-6033.
- (158) Knight, L. B.; Steadman, J. An Experimental Procedure for ESR Studies of Rare Gas Matrix Isolated Molecular Cation Radicals: ¹²CO⁺, ¹³CO⁺, ¹⁴NH₃⁺, and ¹⁵NH₃⁺. *J. Chem. Phys.* **1982**, *77*, 1750-1756.
- (159) Knight, L. B.; Steadman, J.; Miller, P. K.; Bowman, D. E.; Davidson, E. R.; Feller, D. ESR and *ab initio* Theoretical Studies of the Cation Radicals ¹²C₂¹⁶O₂⁺, ^{12,13}C₂¹⁶O₂⁺, ¹³C₂¹⁶O₂⁺, ¹²C₂^{16,17}O₂⁺, ¹²C₂¹⁷O₂⁺, and ^{12,13}C₂^{16,17}O₂⁺ Isolated in Neon Matrices at 4 K. The use of Matrix-Isolation for Trapping Ion-Neutral Reaction Products. *J. Chem. Phys.* **1984**, *80*, 4593-4604.
- (160) Blair, J. T.; Weisshaar, J. C.; Carpenter, J. E.; Weinhold, F. Photodissociation of (CO)₂⁺: Theoretical Studies of Ground 2_{bu} and Excited 2_{bg} Potential Energy Surfaces. *J. Chem. Phys.* **1987**, *87*, 392-410.
- (161) Blair, J. T.; Weisshaar, J. C.; Weinhold, F. The 2_{ag} Excited State of (CO)₂⁺. *J. Chem. Phys.* **1988**, *88*, 1467-1468.
- (162) Vercauteren, D. P.; Fripiat, J. G.; Andre, J. M. Symmetry Dilemmas in Oxocarbons. *Int. J. Quantum Chem.* **1981**, *57*, 219-224.
- (163) Olivella, S.; Pericas, M. A.; Serratos, F.; Messeguer, A. A Mindo-3 Study on the Mono-electronic Reduction of Carbon Monoxide: The Acetylenediolate Dianion as the 1st Member and as the Common Precursor of all the Cyclic Oxocarbon Dianions. *THEOCHEM* **1983**, *14*, 91-97.
- (164) Thomas, J. R.; DeLeeuw, B. J.; O'Leary, P.; Schaefer, H. F.; Duke, B. J.; O'Leary, B. The Ethylenedione Anion: Elucidation of the Intricate Potential Energy Hypersurface. *J. Chem. Phys.* **1995**, *102*, 6525-6536.

- (165) Krishnan, C. N.; Hauge, R. H.; Margrave, J. L. Studies of Carbon Monoxide Activation with Atomic Lithium: IR Spectra of LiCO, LiOC, LiC₂C₂ and Li₂C₂O₂ in Cryogenic Matrices. *J. Mol. Struct.* **1987**, *157*, 187-196.
- (166) Ayed, O.; Manceron, L.; Silvi, B. Reactivity of Na and K with Carbon Monoxide in Solid Argon: An Infrared and Ab Initio Study. *J. Phys. Chem.* **1988**, *92*, 37-45.
- (167) Refaey, K. M. A.; Franklin, J. L. Endoergic Ion Molecule Collision Processes of Negative Ions. 3. Collisions of I⁻ on O₂, CO, and CO₂. *Int. J. Mass Spectrom. Ion Processes* **1976**, *20*, 19-32.
- (168) Thompson, W. E.; Jacox, M. E. The Vibrational Spectra of Molecular Ions Isolated in Solid Neon. 7. CO⁺, C₂O₂⁺, and C₂O₂⁻. *J. Chem. Phys.* **1991**, *95*, 735-745.
- (169) Huber, K. P.; Herzberg, G. *Molecular Spectra and Molecular Structure. IV. Constants of Diatomic Molecules*; Van Nostrand Reinhold: New York, **1979**.
- (170) Jacox, M. E. Comparison of the Ground State Vibrational Fundamentals of Diatomic Molecules in the Gas Phase and in Inert Solid Matrices. *J. Mol. Spectrosc.* **1985**, *113*, 286-301.
- (171) Bae, Y. K.; Cosby, P. C.; Lorents, D. C. Observation of Shell Structures in the Growth of Microcluster Ions. *Chem. Phys. Lett.* **1989**, *159*, 214-220.
- (172) Yang, J.; Conway, D. C. Bonding in Ion Clusters. I. O₄⁺. *J. Chem. Phys.* **1964**, *40*, 1729-1735.
- (173) Conway, D. C.; Yang, J. H. Bonding in Homomolecular Ion Clusters O_{2n+2}⁺. *J. Chem. Phys.* **1965**, *43*, 2900-2902.
- (174) Conway, D. C. Geometries of O₄⁺, O₄⁻, and N₄⁺ by an Approximate SCF-MO Theory which Considers Intermolecular Differential Overlap. *J. Chem. Phys.* **1969**, *50*, 3864-3867.
- (175) Thompson, W. E.; Jacox, M. E. The Vibrational-Spectra of Molecular-Ions Isolated in Solid Neon. 2. O₄⁺ and O₄⁻. *J. Chem. Phys.* **1989**, *91*, 3826-3837.
- (176) Knight, L. B.; Cobranchi, S. T.; Petty, J. Electronic Ground State Assignment for O₄⁺: Neon Matrix Electron-Spin Resonance Investigation. *J. Chem. Phys.* **1989**, *91*, 4423-4424.
- (177) Peel, J. The Geometry of the Ground State Oxygen Dimer Ion (O₂)₂⁺: Trans-Planar or Rectangular? *J. Chem. Phys.* **1991**, *94*, 5774-5775.
- (178) Carnovale, F.; Peel, J. B.; Rothwell, R. G. Photoelectron Spectroscopy of the Oxygen Dimer and Clusters. *Org. Mass Spectrom.* **1991**, *26*, 201-207.

- (179) Jacox, M. E.; Thompson, W. E. Evidence for the Stabilization of Rectangular O_4^+ in Solid Neon. *J. Chem. Phys.* **1994**, *100*, 750-751.
- (180) Lindh, R.; Barnes, L. The Fraternal Twins of Quartet O_4^+ . *J. Chem. Phys.* **1994**, *100*, 224-237.
- (181) Chertihin, G.; Saffel, W.; Yustein, J.; Andrews, L.; Neurock, M.; Ricca, A.; Bauschlicher, C. Reactions of Laser Ablated Iron Atoms with Oxygen Molecules in Condensing Argon. Infrared Spectra and Density Functional Calculations of Iron Oxide Product Molecules. *J. Phys. Chem.* **1996**, *100*, 5261-5273.
- (182) Chertihin, G.; Andrews, L. On the Spectrum and Structure of the Isolated O_4^- Anion in Solid Argon. *J. Chem. Phys.* **1998**, *108*, 6404-6407.
- (183) Zhou, M.; Hacaloglu, J.; Andrews, L. Infrared Spectra of Cyclic- O_6^+ and *Trans*- O_6^+ in Solid Neon and Argon. *J. Chem. Phys.* **1999**, *110*, 9450-9456.
- (184) Ricks, A. M.; Douberly, G. E.; Duncan, M. A. IR Photodissociation Spectroscopy of O_4^+ , O_6^+ and O_8^+ Cluster Ions. *Int. J. Mass Spectrom.* **2009**, *283*, 69-76.
- (185) Misochko, E. Y.; Akimov, A. V.; Goldschleger, I. U.; Boldyrev, A. I.; Wight, C. A. Endothermic Formation of a Chemical Bond by Entropic Stabilization: Difluoronitroxide Radical in Solid Argon. *J. Am. Chem. Soc.* **1999**, *121*, 405-410.
- (186) Lugez, C.; Thompson, W.; Jacox, M. E. Matrix Isolation Study of the Interaction of Excited Neon Atoms with O_3 : Infrared Spectrum of O_3^- and Evidence for the Stabilization of $O_2 \cdots O_4^+$. *J. Chem. Phys.* **1996**, *105*, 2153-2160.
- (187) Kagemoto, A.; Fujishiro, R. Enthalpy Change of the Coil-Helix Transition of Poly(γ -Benzyl L-Glutamate) in Dichloroacetic Acid-1,2-Dichloroethane Mixtures. *Biopolymers* **1968**, *6*, 1753-1758.
- (188) Haynes, W. M., Ed.; (*Internet Version Released 2015*) *CRC Handbook of Chemistry and Physics*; CRC Press/Taylor and Francis: Boca Raton, FL., **2015**; Vol. 95.
- (189) Sherrill, C. D.; Krylov, A. I.; Byrd, E. F. C.; Head-Gordon, M. Energies and Analytic Gradients for a Coupled Cluster Doubles Model using Variational Brueckner Orbitals: Application to Symmetry Breaking in O_4^+ . *J. Chem. Phys.* **1998**, *109*, 4171-4181.
- (190) Rest, A. J.; Turner, J. J. Photolysis of Tetracarbonylnickel, $Ni(CO)_4$, in Rare-Gas Matrices at 15°K: Evidence for Tricarbonylnickel, $Ni(CO)_3$. *J. Chem. Soc. D* **1969**, *18*, 1026.
- (191) DeKock, R. L. Preparation and Identification of Intermediate Carbonyls of Nickel and Tantalum by Matrix Isolation. *Inorg. Chem.* **1971**, *10*, 1205-1211.

- (192) Kundig, E. P.; McIntosh, D.; Moskovits, M.; Ozin, G. A. Binary Carbonyls of Platinum, $\text{Pt}(\text{CO})_n$ (Where $n = 1-4$). A Comparative Study of Chemical and Physical Properties of $\text{M}(\text{CO})_n$ (Where $\text{M} = \text{Ni}, \text{Pd}, \text{Or Pt}; n = 1-4$). *J. Am. Chem. Soc.* **1973**, *95*, 7234-7241.
- (193) Joly, H.; Manceron, L. Complete Vibrational Spectrum of NiCO Isolated in Solid Argon. *Chem. Phys.* **1998**, *226*, 61-70.
- (194) Manceron, L.; Alikhani, M. E. Infrared Spectrum and Structure of $\text{Ni}(\text{CO})_2$: A Matrix Isolation and DFT Study. *Chem. Phys.* **1999**, *244*, 215-226.
- (195) Zhou, M.; Andrews, L. Matrix Infrared Spectra and Density Functional Calculations of $\text{Ni}(\text{CO})_x^-$, $x = 1-3$. *J. Am. Chem. Soc.* **1998**, *120*, 11499-11503.
- (196) Liang, B.; Zhon, M.; Andrews, L. Reactions of Laser-Ablated Ni, Pd, and Pt Atoms with Carbon Monoxide: Matrix Infrared Spectra and Density Functional Calculations on $\text{M}(\text{CO})_n$ ($n = 1-4$), $\text{M}(\text{CO})_n^-$ ($n = 1-3$), and $\text{M}(\text{CO})_n^+$ ($n = 1-2$), ($\text{M} = \text{Ni}, \text{Pd}, \text{Pt}$). *J. Phys. Chem. A* **2000**, *104*, 3905-3914.
- (197) Ogden, J. S. Infrared Spectroscopic Evidence for Copper and Silver Carbonyls. *J. Chem. Soc. D* **1971**, *16*, 978-979.
- (198) McIntosh, D.; Ozin, G. A. Synthesis using Metal Vapors. Silver Carbonyls. Matrix Infrared, Ultraviolet-Visible, and Electron Spin Resonance Spectra, Structures, and Bonding of $\text{Ag}(\text{CO})_3$, $\text{Ag}(\text{CO})_2$, $\text{Ag}(\text{CO})$, and $\text{Ag}_2(\text{CO})_6$. *J. Am. Chem. Soc.* **1976**, *98*, 3167-3175.
- (199) Kasai, P. H.; Jones, P. M. Silver Carbonyls, $\text{Ag}(\text{CO})$ and $\text{Ag}(\text{CO})_3$: Matrix Isolation ESR Study. *J. Phys. Chem.* **1985**, *89*, 1147-1151.
- (200) Chenier, J. H. B.; Hampson, C. A.; Howard, J. A.; Mile, B. Spectroscopic Study of the Reaction of Silver Atoms with CO in a Rotating Cryostat. *J. Phys. Chem.* **1988**, *92*, 2745-2750.
- (201) Watanabe, K.; Nagashima, U.; Hosoya, H. An *ab initio* Study of Interactions of Carbon Monoxide and Metal Electrodes. *Chem. Phys. Lett.* **1993**, *209*, 109-112.
- (202) Marian, C. M. Stability and the CO Stretching Vibrational Frequency of Molecular AgCO. *Chem. Phys. Lett.* **1993**, *215*, 582-586.
- (203) Schwerdtfeger, P.; Bowmaker, G. A. Relativistic Effects in Gold Chemistry. V. Group 11 Dipole Polarizabilities and Weak Bonding in Monocarbonyl Compounds. *J. Chem. Phys.* **1994**, *100*, 4487-4497.

- (204) Liang, B.; Andrews, L. Reactions of Laser-Ablated Ag and Au Atoms with Carbon Monoxide: Matrix Infrared Spectra and Density Functional Calculations on $\text{Ag}(\text{CO})_n$ ($n = 2,3$), $\text{Au}(\text{CO})_n$ ($n = 1,2$) and $\text{M}(\text{CO})_n^+$ ($n = 1-4$; $\text{M} = \text{Ag}, \text{Au}$). *J. Phys. Chem. A* **2000**, *104*, 9156-9164.
- (205) Krim, L.; Wang, X.; Manceron, L.; Andrews, L. Absorption Spectra of Ground-State and Low-Lying Electronic States of Copper Nitrosyl: A Rare Gas Matrix Isolation Study. *J. Phys. Chem. A* **2005**, *109*, 10264-10272.
- (206) Kelly, R. T.; Tolmachev, A. V.; Page, J. S.; Tang, K.; Smith, R. D. The Ion Funnel: Theory, Implementations, and Applications. *Mass Spectrom. Rev.* **2010**, *29*, 294-312.
- (207) Moskovits, M.; Hulse, J. Interaction of CO with Very Small Copper Clusters. *J. Phys. Chem.* **1977**, *81*, 2004-2009.
- (208) Sihvonen, V. The Kinetics of the Boudouard Reaction. *Ann. Acad. Sci. Fenn.* **1931**, *33A*, 1-14.

Ryan M. Ludwig

Curriculum Vitae

Institutional Address:
Lehigh University
Chemistry Department
6 East Packer Avenue
Bethlehem, PA 18015
ryanludwig411@gmail.com
(610) 758-5877
rml210@lehigh.edu

Home Address:
916 North 32nd Street
Allentown, PA 18104
(610) 823-8427

EDUCATION

Ph.D., Physical Chemistry, Lehigh University, Chemistry Department Research Advisor: Dr. David T. Moore	2015
B.S., Chemistry, DeSales University, Chemistry Department	2010

DISSERTATION

Simultaneous counter-ion codeposition: A technique enabling matrix isolation spectroscopy studies using low-energy beams of mass-selected ions

TEACHING EXPERIENCE

DeSales University

General Chemistry Laboratory (adjunct professor, Fall 2014)

Lehigh University

Physical Chemistry Laboratory	(teaching assistant, Spring 2011, Spring 2014)
Advanced Chemistry Laboratory	(teaching assistant, Fall 2011, Spring 2012)
General Chemistry Laboratory	(teaching assistant, Fall 2010, Summer 2011)

PUBLICATIONS

Journal Articles (Peer Reviewed)

- 2014 Ludwig, R.M.; Moore, D.T. Chemical reactions triggered using electrons photodetached from “clean” distributions of anions deposited in cryogenic matrices via counter-ion co-deposition. *J. Phys. Chem Lett.* 2014, 2947.
- 2013 Ludwig, R.M.; Moore, D.T. Formation of ionic complexes in cryogenic matrices: A case study using co-deposition of Cu⁻ with rare gas cations in solid argon. *J. Chem. Phys.* 2013, 139, 244202.

Manuscripts in Preparation

Ludwig, R.M.; Goodrich, M.E.; Smith, A.N.; Moore, D.T. The coldest example of chemical equilibrium: reversible conformational rearrangement of O_4^+ in an argon matrix at 10 K.

Ludwig, R.M.; Ahn, J.N.; Watanabe, N.; Moore, D.T. Infrared spectrum of $(CO)_2^+$ formed by high energy Ar^+ deposition in CO-doped argon matrices.

Ludwig, R.M.; Goodrich, M.E.; Moore, D.T. Evidence for vertical detachment products: Trapping transient complexes formed by annealing and irradiating anionic copper carbonyl precursors.

AWARDS AND HONORS

- 2014 Lehigh University Chemistry Departmental Scholarship
- 2013 Richard A. Schaeffer Memorial Fund Travel Scholarship
- 2012 Sigma Xi Grant-in-Aid of Research
- 2012 Dean's Summer Award

CONFERENCE PARTICIPATION

Oral Presentations

- 2014 Ryan M. Ludwig, David T. Moore. "Simultaneous counter-ion codeposition: a technique enabling matrix isolation spectroscopy studies using low-energy beams of mass-selected ions." 69th Meeting: International Symposium on Molecular Spectroscopy, Champaign-Urbana, Illinois, June 16-20, 2014.
- 2014 Ryan M. Ludwig, David T. Moore. "Controlled neutralization of anions in cryogenic matrices by photodetachment." 69th Meeting: International Symposium on Molecular Spectroscopy, Champaign-Urbana, Illinois, June 16-20, 2014.

Poster Presentations

- 2014 Ryan M. Ludwig, David T. Moore. "Controlled neutralization of "clean" distributions of anions stabilized in cryogenic matrices." Vibrational Spectroscopy Gordon Research Conference, Biddeford, ME, August 3-8, 2014.
- 2013 Ryan M. Ludwig, Alex D. Hunter, Nathan P. Roehr, David T. Moore. "Counter ion-mediated formation of weakly interacting ionic complexes in rare gas matrices as probed by FTIR." 61st ASMS Conference on Mass Spectrometry and Allied Topics, Minneapolis, MN, June 9-13, 2013.
- 2012 Ryan M. Ludwig, Alex D. Hunter, Nathan P. Roehr, David T. Moore. "Matrix isolation FTIR and UV studies of anionic copper atoms interacting with CO in rare gas matrices." Fall ACS National Meeting, Philadelphia, PA, August 19-23, 2012.

2012 Ryan M. Ludwig, Alex D. Hunter, Nathan P. Roehr, David T. Moore. "Matrix isolation FTIR and UV studies of anionic copper atoms interacting with CO in rare gas matrices." Vibrational Spectroscopy Gordon Research Conference, Biddeford, ME, August 5-10, 2012.

RESEARCH EXPERIENCE

Dissertation Research

Developed a new analytical technique for depositing mass-selected ions in cryogenic matrices using co-deposition of counter ions under ultra-high vacuum conditions

Discovered method for triggered C-C bond formation following capture of photodetached electrons in solid argon

Measured the coldest example of chemical equilibrium at 10 K and designed a software script through Origin to quantitatively analyze data and error analysis

Aligned optical systems for use in both FTIR and UV-Vis spectroscopy

Designed a high pressure gas mixing rack for isotopic mixes, gas purification, and controlled flowrate deposition

Characterized beams of metal ions, produced by magnetron sputtering, via mass spectrometry

Proposal Research

Assembled and characterized a previously working helium droplet instrument

Implemented a new mounting system for the vacuum components based on a design created in SolidWorks

Wrote a proposal for a new method to form novel metal catalysts and magnetic core-shell clusters

Helped write an ACS-PRF grant aimed toward surface analysis of deposited metal species via TEM, HAADF-STEM, XPS, and LEIS

Rebuilt multiple types of oil and dry vacuum pumps

Undergraduate Research

Synthesized ionic liquids for use as "green" organic solvents for the nitration of guaiazulene

Characterized nitrated products through FTIR and NMR

PROFESSIONAL AFFILIATIONS

2013 American Society for Mass Spectrometry

2012 Sigma Xi, Associate Member

2008 American Chemical Society